

國立交通大學  
電子物理系

博士論文

量子與光學同調波之研究：  
利用微晶體雷射研究空間模態與極化奇異點特徵

Study of Quantum and Optical Coherent Waves: Pattern Formation  
and Polarization Singularities Generated from Microchip Laser Cavity

研究生：陸亭樺

指導教授：陳永富 教授

中華民國九十七年五月

量子與光學同調波之研究：  
利用微晶體雷射研究空間模態與極化奇異點特徵

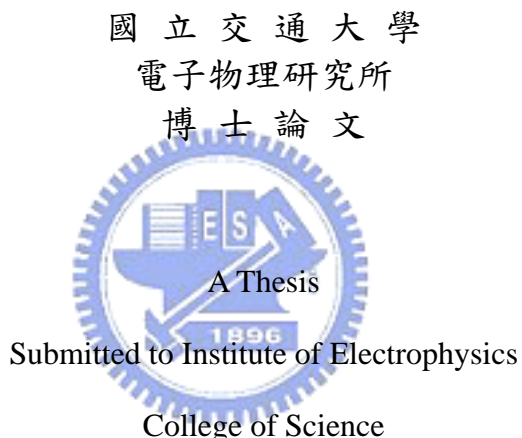
Study of Quantum and Optical Coherent Waves: Pattern Formation  
and Polarization Singularities Generated from Microchip Laser Cavity

研究 生：陸亭樺

Student : Ting-Hua Lu

指導 教授：陳永富

Advisor : Yung-Fu Chen



National Chiao Tung University  
in partial Fulfillment of the Requirements  
for the Degree of

PhD

in

Electrophysics

May 2008

Hsinchu, Taiwan, Republic of China

中華民國九十七年五月

# 量子與光學同調波之研究： 利用微晶體雷射研究空間模態與極化奇異點特徵

學生：陸亭樺

指導老師：陳永富教授

國立交通大學電子物理系博士班

## 摘要

本論文係用微晶體雷射的空間模態研究同調光波的量子與古典對應關係以及極化向量場中奇異點的特徵。由於雷射共振腔在近軸近似下的波函數解與量子簡諧運動有異曲同工的數學形式，因此深入研究量子簡諧運動為本論文中相當重要的基石。首先我們以一維 Schrödinger 同調態出發並推廣至二維系統。經由縝密的分析與思考得到符合共振腔條件的廣義同調態，藉此與實驗中所見之有趣的光學物理現象做一番連接。進一步研究發現共振腔中縱向與橫向的頻率耦合與模態鎖定的結果所顯示的”魔梯”現象。這一類的空間模態不僅帶領我們進入鮮少被探討的雷射領域更提供了介於微觀與宏觀之間的綜觀領域一些相關研究方向。再者，針對實驗結果的理論分析更顯示了這些空間模態擁有很大的角動量，這對於未來的雷射技術提供了一些前瞻性的想法。

本文另一個重點是探討極化向量場中奇異點的特徵。極化奇異點的形態與光場本身的模態密不可分且相依相生。文中利用半球形共振腔產生光與增益介質之交互作用使得空間模態衍生出極化糾纏的實驗結果。透過嚴謹的理論分析不僅完整地重建出光波之間模態，且各種極化奇異點特徵的有趣面貌亦被清楚地呈現。對於極化奇異點的深入研究除了能夠更了解光波的特性也對光波的應用層面提供了值得思考的方向。

# **Study of Quantum and Optical Coherent Waves: Pattern Formation and Polarization Singularities Generated from Microchip Laser Cavity**

Student: Ting-Hua Lu

Advisor: Prof. Yung-Fu Chen

Institute and Department of Electrophysics  
National Chiao Tung University

## **ABSTRACT**

This thesis presents several novel optical experiments which provide fresh insights for quantum-classical correspondence with pattern formation and polarization characteristics of light by use of microchip laser cavity. Quantum physics was developed substantially after Schrödinger proposed his important coherent states of quantum harmonic oscillator. Harmonic oscillator is the analogue of spherical laser cavity in our system. We start from one-dimensional Schrödinger coherent states and broaden the theory to two-dimensional problem to be related to our laser system under paraxial approximation.

We not only develop a general form to elucidate various kinds of states completely in the laser system which is slightly disturbed by coupling with environment but also extract the coherent states in the degenerate cavity of longitudinal-transverse coupling. In addition to the eigenstates in laser cavity, the three-dimensional coherent waves exhibit the classical-like feature on the transverse patterns in virtue of nonlinear optical effects. We verify that the specific phenomenon leads to “Devil’s staircase” which is demonstrated in other physical regime but firstly found in laser cavity. Furthermore, the analytic results have good agreement with experimental patterns and provide efficient approach to understand the nature of coherent waves in the cavity. With the theoretical results, the coherent waves are found to carry large angular momentum and may provide some applications in laser technique.

Another topic in this thesis is polarization singularity in laser cavity. Besides phase singularity in complex scalar waves which provide some unique applications, polarization singularities also play a vital role such as the skeleton in vector waves for the study of optical fields. We employ the hemispherical cavity to generate vector fields. After precise measurement and deliberate analysis, the variation of polarization singularities embedded in high-order vector laser waves can be realized. Interestingly, the polarization singularities are discovered as fascinating patterns accompany with vector fields. Studying the structures of the polarization singularities in coherent vector fields may help us to understand the nature of the waves and provide insights in application.

## 誌 謝

是我們選擇了生活，還是生活選擇了我？離開家鄉北上求學的我總不時地想到小時候頂著大熱天在市場幫忙工作的情境，當時只覺得媽媽工作很辛苦，生活卻過得不算輕鬆。小小年紀就想著在未來的日子我一定要有機會選擇讓自己快樂的生活方式。然而父母親告訴我，對於處在貧窮中的小孩，只有讀書才有機會讓自己的生活改變。在那些為聯考奮戰的日子裡，這句話始終在我心頭迴盪。如願考上交大也順利畢業，畢業後跟著大多數人的腳步踏入研究所，心想再充實兩年就可以去園區工作，完成小時候的夢想。天知道命運的安排卻是如此微妙，就差那麼一點，我就與美麗的物理世界擦身而過。

從四年前陳永富教授答應收我為碩士生的那天開始，原來我的人生已經開始了另一段自己從未預期的旅程。大四的下學期是我大學生活中最充實的一段時光，因為每個禮拜陳教授都願意教導我做研究的方法與知識。我在陳教授身上看到了教學的熱誠與研究的態度，這的確深深地感動了我，同時也潛移默化著我的想法。真正進入研究所後，除了陳教授以外還有與陳教授合作的黃凱風教授一起參與。黃教授是個很有風範的學者，對學術認真地投入，經常與我討論實驗的結果幫助我釐清許多研究上的困惑。在兩位教授的帶領之下，漸漸地我也能感受到物理的魅力與它帶給我的感動。我終於明白為什麼他們會不停地討論所看到的實驗現象、不斷地指導我讓我了解事物的真理，這是沒有用心投入過的人所不會了解的。從一個陌生的實驗結果要走到完全了解它背後所隱藏的意義是一條很漫長的路，路上總有些崎嶇與阻礙，我很幸運地有兩位良師的指導讓我能克服種種困難。不管是面臨研究上或是生活上的挫折，我都很感謝他們一再地鼓勵我、一再地給我機會，扮演我生命中的貴人。畢業只是一個轉折點，我會帶著在兩位老師身上所學到的精神與態度繼續探索這美麗的世界，期盼未來能不負他們的期望。

這四年來我得到許多人的幫助：從剛進入實驗室建勳學長、意鑫學長和怡君學姊的指導，到真正動手做實驗時蘇老大和 01 學姊的協助讓我學到許多寶貴知識。有寶妹、歐大戶、廖ㄟ、王胖、哲彥、小黃、國欽學長、思武學長和春蘋學姊的陪伴更充實了研究生活。還有實驗室裡的依萍、雅婷、恩毓、建誠、興弛、紀暉、彥廷、漢龍學長、柏祥學長、毓捷、建至、郁仁，能與他們共度實驗室的珍貴時光令我感到非常開心。更要感謝口試委員給我的指導讓我獲益良多。

在即將結束學生生涯之際，我特別要感謝我的家人無怨無悔地支持我。外公外婆和奶奶的疼愛、父親的鼓勵、妹妹的幫忙、尤其是母親從小到大給我的身教讓我學會感恩和惜福，母親一直是我努力向前的動力與典範。更要感謝七年來一直在我身邊給我無限包容和體貼的東賢，能一起分享生活中的點滴是我最大的幸福。最後，感謝上天讓我有機會選擇最適合自己的方式來成就我年輕歲月中最美好的時光。

# CONTENTS

|                 |     |
|-----------------|-----|
| 摘要              | i   |
| Abstract        | ii  |
| 誌謝              | iii |
| Contents        | iv  |
| List of Figures | vii |

## Chapter 0 . . . . . 1

### Introduction: Guide to the Main Text

## Chapter 1 . . . . . 3

### Classical and Quantum Harmonic Oscillators

|   |    |
|---|----|
| 1.1 One-dimensional Harmonic Oscillator                                     | 3  |
| 1.2 Two-dimensional Harmonic Oscillator                                     | 7  |
| 1.3 Schrödinger Coherent States of the 1D Harmonic Oscillator               | 10 |
| 1.4 Stationary Coherent States of 2D Harmonic Oscillator                    | 14 |
| 1.5 Unitary Transformation between Stationary States and wave packet states | 23 |
| REFERENCES  | 28 |

## Chapter 2 . . . . . 29

### Eigenstates of Harmonic Oscillator and Spherical Laser Cavity: Generalized Coherent States and Polarization-entangled Patterns

|  |    |
|--|----|
| 2.1 Paraxial Approximation of Maxwell's Equations                                | 29 |
| 2.2 The Generalized Coherent States:   |    |
| Between Hermite-Gaussian and Laguerre-Gaussian modes                             | 38 |
| 2.3 Generation of Polarization-entangled Optical Coherent Waves                  | 48 |
| 2.3.1 Experimental Setup and Results   | 50 |
| 2.3.2 Analytical Wave Functions for Experimental Polarization-entangled Patterns | 59 |
| 2.3.3 Summary  | 73 |
| REFERENCES   | 74 |

## **Chapter 3 . . . . .** 76

### **Three-dimensional Optical Coherent Waves with Longitudinal-transverse Coupling**

|  |     |
|--|-----|
| 3.1 Frequency Locking, Mode Locking, and Resonance . . . . .   | 77  |
| 3.2 Devil's Staircase with Two Competing Frequencies . . . . .   | 77  |
| 3.3 Three-dimensional Coherent Waves Demonstrated from Laser Cavity . . . . .                                  | 80  |
| 3.3.1 Theoretical Analysis for the Resonator . . . . .   | 80  |
| 3.3.2 Experimental Setup and Results . . . . .   | 86  |
| 3.3.3 Summary . . . . .  | 91  |
| 3.4 Spatially Localized Patterns Generated from Macroscopic Superposition of 3D Coherent Laser Waves . . . . . | 97  |
| 3.4.1 Experimental Setup and Results . . . . .   | 98  |
| 3.4.2 Analysis and Theoretical Results . . . . .   | 102 |
| 3.4.3 Summary . . . . .  | 107 |
| REFERENCES . . . . .   | 108 |

## **Chapter 4 . . . . .** 111

### **Polarization Singularities in Hemispherical Cavity**

|  |     |
|--|-----|
| 4.1 Polarization and Stokes Parameter . . . . .  | 111 |
| 4.2 Polarization Singularities . . . . .   | 121 |
| 4.3 Generalized Structures of Polarization Singularities in Laguerre- Gaussian Vector fields . . . . . | 122 |
| 4.3.1 Experimental setup and results . . . . .   | 122 |
| 4.3.2 Analytical Wave Functions for Experimental Patterns and Polarization Singularities . . . . .     | 128 |
| 4.3.3 Summary . . . . .  | 144 |
| REFERENCES . . . . .   | 145 |

## **Chapter 5 . . . . .** 148

### **Optical Waves Carrying Large Angular Momentum in Degenerate Cavity**

|   |     |
|---|-----|
| 5.1 Angular Momentum of Electromagnetic Fields . . . . .                          | 148 |
| 5.2 Linked and Knotted Coherent Laser Waves with Large Angular Momentum . . . . . | 151 |
| 5.2.1 Experimental Setup and Results . . . . .                                    | 151 |
| 5.2.2 Analyses of Angular Momentum for Two Degenerate Coherent States . . . . .   | 163 |

|               |     |
|---------------|-----|
| 5.2.3 Summary | 166 |
| REFERENCES    | 167 |

## **Chapter 6** . . . . . **Summary and Future Work** . . . . . 170

**Curriculum Vitae** . . . . . 172

**Publication List** . . . . . 173



## List of Figures

|            |  |    |
|------------|--|----|
| Fig. 1.1.1 | (a) 1D classical harmonic oscillator. (b) 1D quantum harmonic oscillator. (The probability density of several states)  | 6  |
| Fig. 1.2.1 | (a) The description of the potential of 2D harmonic oscillator. (b) Lissajous figures with different frequency ratio and phase. (c) The eigenstates of 2D quantum harmonic oscillator with different orders.   | 9  |
| Fig. 1.3.1 | (a) Sixtieth excited state of 1D harmonic oscillator (b) 1D coherent state moving with time  | 13 |
| Fig. 1.4.1 | Comparison between the quantum stationary state $ \Phi_{N,u_x,u_y}^{p,q}(\xi_x, \xi_y; A, \phi) ^2$ [(a)-(c)] and the classical Lissajous orbits [(a')-(c')] for the system of $p:q = 2:1$ with $N = 40$ , $A = 5.2$ and (a) $\phi = 0$ , (b) $\phi = 0.3\pi$ , and (c) $\phi = 0.6\pi$ .  | 19 |
| Fig. 1.4.2 | The same as Fig. 1.4.1 for the system of $p:q = 3:2$ with $N = 22$ , $A = 5.2$ and (a) $\phi = 0$ , (b) $\phi = 0.3\pi$ , and (c) $\phi = 0.6\pi$ .  | 20 |
| Fig. 1.4.3 | The same as Fig. 1.4.1 for the system of $p:q = 4:3$ with $N = 15$ , $A = 5.2$ and (a) $\phi = 0$ , (b) $\phi = 0.3\pi$ , and (c) $\phi = 0.6\pi$ .  | 21 |
| Fig. 1.4.4 | (a) Upper: wave patterns of stationary coherent states for $N=20$ with different values of the parameters $\phi$ . Lower: standing wave patterns corresponding to upper figures. (b) Upper: wave patterns of stationary coherent states for $N=20$ with different values of the parameters $A$ . Lower: standing wave patterns corresponding to upper figures. | 22 |
| Fig. 1.5.1 | (a) The 1D wave packet states with $M = 5$ and $n = 0 \sim 4$ respectively. (b) The 1D stationary states with $M = 5$ and $m = 0 \sim 4$ respectively.   | 25 |
| Fig. 1.5.2 | The 2D time-independent stationary states with $M = 7$ and $n = 0 \sim 6$ respectively.  | 26 |
| Fig. 1.5.3 | The 2D eigenstates with $M = 7$ and $m = 0 \sim 6$ respectively.   | 27 |
| Fig. 2.1.1 | (a) Hermite-Gaussian modes with different index $(m, n)$ . (b) Standing waves of Laguerre-Gaussian modes with different index $(l, p)$   | 37 |
| Fig. 2.2.1 | The wave functions with different $(n_1, n_2)$ of a charged particle in a harmonic oscillator with uniform magnetic field.   | 46 |
| Fig. 2.2.2 | Numerical patterns of the GCSs with different phase factor and different order.  | 47 |
| Fig. 2.3.1 | Experimental setup for the generation of polarization-entangled transverse modes with off-axis pumping scheme in a highly isotropic diode-pumped microchip laser.  | 51 |

|             |   |    |
|-------------|---|----|
| Fig. 2.3.2  | Experimental polarization-entangled patterns (a) square pattern, (b) hyperbolic pattern, (c) elliptic pattern, (d) circular pattern.  | 54 |
| Fig. 2.3.3  | Upper: Square experimental polarization-resolved patterns (a) $45^0$ polarization (b) $90^0$ polarization (c) $135^0$ polarization, (d) $180^0$ polarization  | 55 |
| Fig. 2.3.4  | Upper: Hyperbolic experimental polarization-resolved patterns (a) $45^0$ polarization (b) $90^0$ polarization (c) $135^0$ polarization, (d) $180^0$ polarization  | 56 |
| Fig. 2.3.5  | Upper: Elliptical experimental polarization-resolved patterns (a) $45^0$ polarization (b) $90^0$ polarization (c) $135^0$ polarization, (d) $180^0$ polarization  | 57 |
| Fig. 2.3.6  | Upper: Circular experimental polarization-resolved patterns (a) $45^0$ polarization (b) $90^0$ polarization (c) $135^0$ polarization, (d) $180^0$ polarization  | 58 |
| Fig. 2.3.7  | Numerically reconstructed patterns for the experimental results shown in Fig. 2.3.2.  | 62 |
| Fig. 2.3.8  | (a) The overlap functional $I(\varphi)$ as a function of $\varphi$ for the state $\bar{E}_x(x, y, z)$ in Eq. (2.3.6). (b) The overlap functional $I(\varphi)$ as a function of $\varphi$ for the state $\bar{E}_x(x, y, z)$ in Eq. (2.3.8).                         | 65 |
| Fig. 2.3.9  | Numerically reconstructed patterns for the experimental results shown in Fig. 2.3.3.  | 66 |
| Fig. 2.3.10 | Numerically reconstructed patterns for the experimental results shown in Fig. 2.3.4.  | 67 |
| Fig. 2.3.11 | Numerically reconstructed patterns for the experimental results shown in Fig. 2.3.5.  | 68 |
| Fig. 2.3.12 | Numerically reconstructed patterns for the experimental results shown in Fig. 2.3.6.  | 69 |
| Fig. 2.3.13 | Contour plot of angle field $\Theta(x, y)$ according to the reconstructed patterns in Fig. 2.3.7.   | 71 |
| Fig. 2.3.14 | Contour plot of angle field $\Theta(x, y)$ for the boxed regions shown in Fig. 2.4.13.  | 72 |
| Fig. 3.2.1  | Two oscillators of different frequencies with some coupling strength  | 79 |
| Fig. 3.2.2  | Results of circle map with different coupling strength.   | 79 |
| Fig. 3.3.1  | A portion of the spectrum $f(l, n, m)$ as a function of the bare mode-spacing ratio $\Omega$ for the range of $10 \leq l \leq 30$ and $0 \leq (m + n) \leq 20$ .  | 82 |
| Fig. 3.3.2  | Upper: an example for the <i>Lissajous</i> parametric surface described in equation (3.3.6) for the range from $z = -L/2$ to $z = L/2$ with $(p, q) = (3, 2)$ , $P = 2$ and $\phi_0 = 0$ . Bottom: the tomographic transverse patterns along the longitudinal axis. | 85 |

|            |  |     |
|------------|--|-----|
| Fig. 3.3.3 | Experimental setup for the generation of 3D coherent waves in a diode-pumped microchip laser with off axis pumping scheme in a symmetric spherical resonator.                                      | 88  |
| Fig. 3.3.4 | Experimental tomographic transverse patterns inside the cavity observed at $\Omega \approx 0.422$ .  | 90  |
| Fig. 3.3.5 | Bottom: Experimental mode-locked ratio $P/Q$ as a function of the bare 5ode-spacing ratio $\Omega$ . Upper: experimental far-field patterns observed in the mode-locked plateau with $P/Q = 2/5$ . | 92  |
| Fig. 3.3.6 | Experimental tomographic transverse patterns inside the cavity observed at $\Omega \approx 0.573$ .  | 93  |
| Fig. 3.3.7 | Bottom: Experimental mode-locked ratio $P/Q$ as a function of the bare 5ode-spacing ratio $\Omega$ . Upper: experimental far-field patterns observed in the mode-locked plateau with $P/Q = 1/3$ . | 94  |
| Fig. 3.3.8 | Bottom: Experimental mode-locked ratio $P/Q$ as a function of the bare 5ode-spacing ratio $\Omega$ . Upper: experimental far-field patterns observed in the mode-locked plateau with $P/Q = 1/4$ . | 95  |
| Fig. 3.3.9 | Bottom: Experimental mode-locked ratio $P/Q$ as a function of the bare 5ode-spacing ratio $\Omega$ . Upper: experimental far-field patterns observed in the mode-locked plateau with $P/Q = 2/7$ . | 96  |
| Fig. 3.4.1 | Photograph of the experimental laser cavity.   | 99  |
| Fig. 3.4.2 | Typical experimental far-field patterns observed in different cavity lengths for different indices $(p, q; P/Q)$ .   | 101 |
| Fig. 3.4.3 | Upper: Numerical results of 3D coherent modes according to different transverse orders. Bottom: Numerical results of the superposition from the coherent modes with different orders.              | 103 |
| Fig. 3.4.4 | (a) Experimental tomographic transverse patterns inside the cavity observed at $\Omega \approx 0.84$ . (b) Numerical results corresponding to (a).   | 105 |
| Fig. 3.4.5 | Experimental strong spatially localized patterns with different $(p, q; P/Q)$ .  | 106 |
| Fig. 4.1.1 | The evolution of the electric field vector leads to different kinds of polarization states: (a) Linear, (b) Circular, (c) Elliptical.  | 114 |
| Fig. 4.1.2 | Three kinds of polarization states of high-order transverse modes: (a) Azimuthally polarized, (b) Circularly polarized, (c) Radially polarized.  | 115 |
| Fig. 4.1.3 | The Poincaré representation of polarized light on a sphere.  | 120 |
| Fig. 4.3.1 | Experimental setup for the generation of propagation-dependent polarization  | 124 |

vector fields in a diode-pumped microchip laser in a hemi-spherical resonator.

Fig. 4.3.2 Experimental far-field transverse patterns with different radial index  $p$  and azimuthal index  $l$ : (a) (0, 9), (b) (0, 23), (c) (1, 39), (d) (1, 66), (e) (2, 41), (f) (7, 100). 125

Fig. 4.3.3 Polarization-resolved transverse patterns for the experimental result at three different propagation positions:  $z = 0$ ,  $z = z_R$ , and  $z \gg z_R$ : (a) corresponding to Fig. 4.3.2 (b) where  $z_R = 1.26$  mm. (b) corresponding to Fig. 4.3.2 (c) where  $z_R = 1.28$  mm. The arrows indicate the transmission axis of the polarizer.  $z = z_R$ , and  $z \gg z_R$ , where  $z_R = 1.28$  mm. 127

Fig. 4.3.4 (a) Numerically reconstructed patterns for the experimental results shown in Fig. 4.3.3 (a), (b) Numerically reconstructed patterns for the experimental results shown in Fig. 4.3.3 (b). 130

Fig. 4.3.5 Structure of the  $C$  line singularities of the theoretical vector field from the view of propagation direction to the beam waist with the same radial index  $p=0$  and different azimuthal index  $l$ : (a)  $(p, l)=(0, 1)$ ; (b)  $(p, l)=(0, 2)$ ; (c)  $(p, l)=(0, 3)$ ; (d)  $(p, l)=(0, 4)$ ; (e)  $(p, l)=(0, 5)$ ; (e)  $(p, l)=(0, 6)$ . 133

Fig. 4.3.6 Structure of the  $C$  line singularities of the theoretical vector field from the view of propagation direction to the beam waist with the same radial index  $p=0$  and different azimuthal index  $l$ : (a)  $(p, l)=(1, 1)$ ; (b)  $(p, l)=(1, 2)$ ; (c)  $(p, l)=(1, 3)$ ; (d)  $(p, l)=(1, 4)$ ; (e)  $(p, l)=(1, 5)$ ; (e)  $(p, l)=(1, 6)$ . 134

Fig. 4.3.7 Structure of the  $C$  line singularities of the theoretical vector field from the view of propagation direction to the beam waist with the same radial index  $p=0$  and different azimuthal index  $l$ : (a)  $(p, l)=(2, 1)$ ; (b)  $(p, l)=(2, 2)$ ; (c)  $(p, l)=(2, 3)$ ; (d)  $(p, l)=(2, 4)$ ; (e)  $(p, l)=(2, 5)$ ; (e)  $(p, l)=(2, 6)$ . 135

Fig. 4.3.8 Numerical patterns of the angle function at the far field of the same radial index  $p=0$  and different azimuthal index  $l$ : (a)  $(p, l)=(0, 1)$ ; (b)  $(p, l)=(0, 2)$ ; (c)  $(p, l)=(0, 3)$ ; (d)  $(p, l)=(0, 4)$ ; (e)  $(p, l)=(0, 5)$ ; (e)  $(p, l)=(0, 6)$ . 137

Fig. 4.3.9 Numerical patterns of the angle function at the far field of the same radial index  $p=0$  and different azimuthal index  $l$ : (a)  $(p, l)=(1, 1)$ ; (b)  $(p, l)=(1, 2)$ ; (c)  $(p, l)=(1, 3)$ ; (d)  $(p, l)=(1, 4)$ ; (e)  $(p, l)=(1, 5)$ ; (e)  $(p, l)=(1, 6)$ . 138

Fig. 4.3.10 Numerical patterns of the angle function at the far field of the same radial index  $p=0$  and different azimuthal index  $l$ : (a)  $(p, l)=(2, 1)$ ; (b)  $(p, l)=(2, 2)$ ; (c)  $(p, l)=(2, 3)$ ; (d)  $(p, l)=(2, 4)$ ; (e)  $(p, l)=(2, 5)$ ; (e)  $(p, l)=(2, 6)$ . 139

Fig. 4.3.11 (a) Experimental far-field pattern with radial and azimuthal index  $(p, l)=(1, 12)$ . (b) Structure of  $C$  line singularities of the correspondent 3D vector field. (c) Structure of the  $C$  line singularities from the view of propagation direction to the beam waist. (d) Numerical pattern of the angle function at the far field. 141

Fig. 4.3.12 Diagram of the representation of the polarization state under propagation corresponding to the singularities of  $C$  lines (blue line),  $V$  points (white points at far field and pink points at beam waist), and  $L$  surfaces (yellow dashed lines). 143

Fig. 5.2.1 Experimental setup for the generation of 3D coherent waves.

154

Fig. 5.2.2 (a) Experimental tomographic transverse patterns for the range from beam waist to far field with  $\Omega = 1/4$ ,  $(p, q) = (2, 2)$ . The pump position is at (0.29 mm, 0.30 mm); (b) Experimental tomographic transverse patterns for the range from beam waist to  $z = 2.75L$  with  $\Omega = 1/3$ ,  $(p, q) = (3, 3)$ . The pump position is at (0.23 mm, 0.30 mm).

155

Fig. 5.2.3 Experimental tomographic transverse patterns for the range from beam waist to far field with  $\Omega = 2/7$ ,  $(p, q) = (2, 5)$ . The pump position is at (0.22 mm, 0.32 mm).

156

Fig. 5.2.4 (a) Numerical tomographic transverse patterns corresponding to Fig. 5.2.2 (a) with Eq. (5.2.1) and the parameters of  $(m_o, n_o) = (110, 110)$ ,  $(p, q) = (2, 2)$ ,  $P/Q = 1/4$ ,  $\phi_o = 0$  and  $M = 13$ . (b) (a) Numerical tomographic transverse patterns corresponding to Fig. 5.2.2 (b) with Eq. (5.2.1) and the parameters of  $(m_o, n_o) = (60, 140)$ ,  $(p, q) = (3, 3)$ ,  $P/Q = 1/3$ ,  $\phi_o = 0$  and  $M = 8$ .

157

Fig. 5.2.5 Numerical tomographic transverse patterns corresponding to Fig. 5.2.3 with Eq. (5.2.1) and the parameters of  $(m_o, n_o) = (60, 130)$ ,  $(p, q) = (2, 5)$ ,  $P/Q = 2/7$ ,  $\phi_o = 0$  and  $M = 5$ .

158

Fig. 5.2.6 (a) Numerical tomographic transverse patterns corresponding to Fig. 5.2.2 (a) with Eq. (5.2.3) and the parameters of  $(m_o, n_o) = (110, 110)$ ,  $(p, q) = (2, 2)$ ,  $P/Q = 1/4$ ,  $\varphi = \pi/2$  and  $M = 13$ . (b) (a) Numerical tomographic transverse patterns corresponding to Fig. 5.2.2 (b) with Eq. (5.2.3) and the parameters of  $(m_o, n_o) = (60, 140)$ ,  $(p, q) = (3, 3)$ ,  $P/Q = 1/3$ ,  $\varphi = \pi/2$  and  $M = 8$ .

161

Fig. 5.2.7 Numerical tomographic transverse patterns corresponding to Fig. 5.2.3 with Eq. (5.2.3) and the parameters of  $(m_o, n_o) = (60, 130)$ ,  $(p, q) = (2, 5)$ ,  $P/Q = 2/7$ ,  $\varphi = \pi/2$  and  $M = 5$ .

162

Fig. 5.2.8 Numerical results for the orbital AM densities obtained with Eq. (4) and the parameters of  $(m_o, n_o) = (110, 110)$ ,  $(p, q) = (2, 2)$ ,  $P/Q = 1/4$ , and  $M = 13$  corresponding to experimental wave patterns shown in Fig. 5.2.2(a)

165

# Chapter 0

## Introduction:

### Guide to the Main Text

In recent years, pattern formation has become a famous topic in various fields of modern physics such as nonlinear optics, quantum chaos, and quantum billiard. At the same time coherent superposition is of significance for exploring the boundary between the microscopic (quantum; wave) and macroscopic (classical; ray) worlds. As demonstrated in diverse experiment, coherent superposition not only leads to understand the mesoscopic physics but also results in rich pattern formation in the transition from classical to quantum regime. Here I will introduce several interesting experimental results to reveal the importance of coherent superposition.



Firstly, we start from harmonic oscillator model to one-dimensional Schrödinger coherent states and broaden the theory to two-dimensional problem to be related to our laser system under paraxial approximation. Furthermore, the fundamental theory and the eigenmode of laser cavity will be mentioned in chapter 2. The generalized coherent state (GCS) has been found as the complete basis to form the various kinds of patterns which are the continuous transitions from Hermite-Gaussian to Laguerre-Gaussian modes. Furthermore, when the polarization entanglement is involved, the situation becomes more complicated. The GCSs can be properly employed to reconstruct the experimental results which are entangled with polarization. With the theoretical analysis of GCSs the polarization singularities can be revealed clearly.

Coherent superposition leads to complex pattern formation. In chapter 3 we will find another kind of fascinating patterns which induced form the longitudinal-transverse coupling

phenomenon. With the longitudinal-transverse coupling of frequencies, the degenerate states of the cavity can be coherent superposed to form the three-dimensional coherent states with Lissajous parametric surfaces which lead to constitute the nearly complete Devil's staircase. Moreover, when the experimental setup is slightly modified, there is not only one 3D coherent state to be excited. The superposition of 3D coherent modes which are caused by the longitudinal-transverse coupling and the mode-locking has been verified to lead to the formation of spatially localized patterns on the Lissajous parametric surface in the mesoscopic regime. The studies may provide some useful insights into the coherent superposition problems with optical coherent waves in mesoscopic regime.

When the polarization and longitudinal-transverse coupling are involved with the coherent superposition, the patterns become the most complicated to analyze. We have used an isotropic microchip laser with the longitudinal-transverse coupling and the entanglement of the polarization states to generate the propagation-dependent polarization vector fields in chapter 4. The phase singularity in complex scalar fields leads to orbital angular momentum and the polarization singularity in complex vector fields leads to spin angular momentum. It is why singular optics is so important in optical fields. We employed the analytical representation to perform comprehensive analysis for the singularities of the  $C$  lines,  $L$  surfaces, and  $V$  points, which play important roles in singular optics.

Angular momentum of optical waves can be decomposed into orbital angular momentum and spin angular momentum. Both of orbital and spin parts have extensive applications in biological and physical fields such as optical tweezers and optical spanner. A typical class of paraxial beams possess angular momentum, Laguerre-Gaussian beams, is studied for recent decades. In addition to typical paraxial Laguerre-Gaussian beams, we demonstrate the optical waves carrying large angular momentum in degenerate cavity in chapter 5. We look forward to useful applications of the specific coherent optical waves in other field in the future.

# Chapter 1

## Classical and Quantum Harmonic Oscillators

Harmonic oscillator is a general and useful model in either classical or quantum physics.

The quantum harmonic oscillator is the quantum analogue of the classical harmonic oscillator.

It is one of the most important systems in quantum mechanics because an arbitrary potential can be approximated as a harmonic potential at the vicinity of a stable equilibrium point. Moreover, it is one of the few quantum mechanical systems for which a simple exact solution is known. In this chapter we introduce the characteristics of classical and quantum harmonic oscillators for the basic preparation of following chapters.



### 1.1 One-dimensional Harmonic Oscillator

In classical dynamics, a particle of mass  $m$  subjects to the potential  $V(x) = \frac{1}{2}m\omega^2x^2$  is the so-called one-dimensional (1D) harmonic oscillator problem, where  $m\omega^2 = k$  is the force constant and  $\omega$  is the angular frequency. On the other hand, harmonic oscillator is a system according to Hooke's law:  $F(x) = -kx$ . If  $F$  is the only force acting on the system, the system is called a simple harmonic oscillator and moving as sinusoidal oscillations about the equilibrium point. Using Newton's second law of motion

$$F = ma = m \frac{d^2x}{dt^2} = -kx \quad (1.1.1)$$

and define  $\omega^2 = k/m$ , the differential equation can be written as  $\ddot{x} + \omega^2 x = 0$ . Solving the

differential equation, the general solution of the simple harmonic oscillator is

$$x(t) = A \cos(\omega t - \phi) \text{ or } x(t) = A \sin(\omega t - \phi), \quad (1.1.2)$$

where the amplitude  $A$  and the phase  $\phi$  are determined by the initial condition. From another view, we can put a particle into a parabolic potential and the projection of particle moves as the general solution, such as shown is Fig. 1.1.1 (a).

In quantum mechanics, the quantum harmonic oscillator is the analogue of the classical harmonic oscillator. Furthermore, it is one of the most important systems in quantum mechanics because an arbitrary potential can be approximated as a harmonic potential at the vicinity of a stable equilibrium point. Fortunately, the exact solution of the quantum harmonic oscillator can be solved analytically. The Hamiltonian can be written as

$$H = \frac{p^2}{2m} + \frac{m\omega^2}{2} x^2, \quad (1.1.3)$$



where  $x$  is the position operator and  $p$  is the momentum operator ( $p = -i\hbar \frac{\partial}{\partial x}$ ). In order to solve the differential equation, we have to solve the time-independent Schrödinger equation. Using the power series method, the energy eigenstates can be depicted as [1-2]

$$\psi_n = \frac{1}{\sqrt{2^n n! \sqrt{\pi}}} \left( \frac{m\omega}{\hbar} \right)^{\frac{1}{4}} \cdot \exp \left( -\frac{m\omega}{2\hbar} x^2 \right) \cdot H_n \left( \sqrt{\frac{m\omega}{\hbar}} x \right), \quad (1.1.4)$$

where  $n = 0, 1, 2, \dots$  and  $H_n(x) = (-1)^n e^{x^2} \frac{d^n}{dx^n} e^{-x^2}$  is the Hermite polynomial. The corresponding energy levels are  $E_n = \left( n + \frac{1}{2} \right) \hbar\omega$ . Figure 1.1.1 (b) shows the probability density  $|\psi_n|^2$  of the ground state and several excited states. The characteristics of the classical

and quantum harmonic system are quite different. The fact is well-known that when the quantum number of the excited state becomes large enough, the behavior of the quantum harmonic oscillator exhibits the classical-like feature of the classical harmonic oscillator. In order to connect the behavior of the particle and the wave in harmonic potential, we have to introduce the Schrödinger's coherent states. It plays an important role in the classical-quantum correspondence and will be discussed in section three of this chapter.



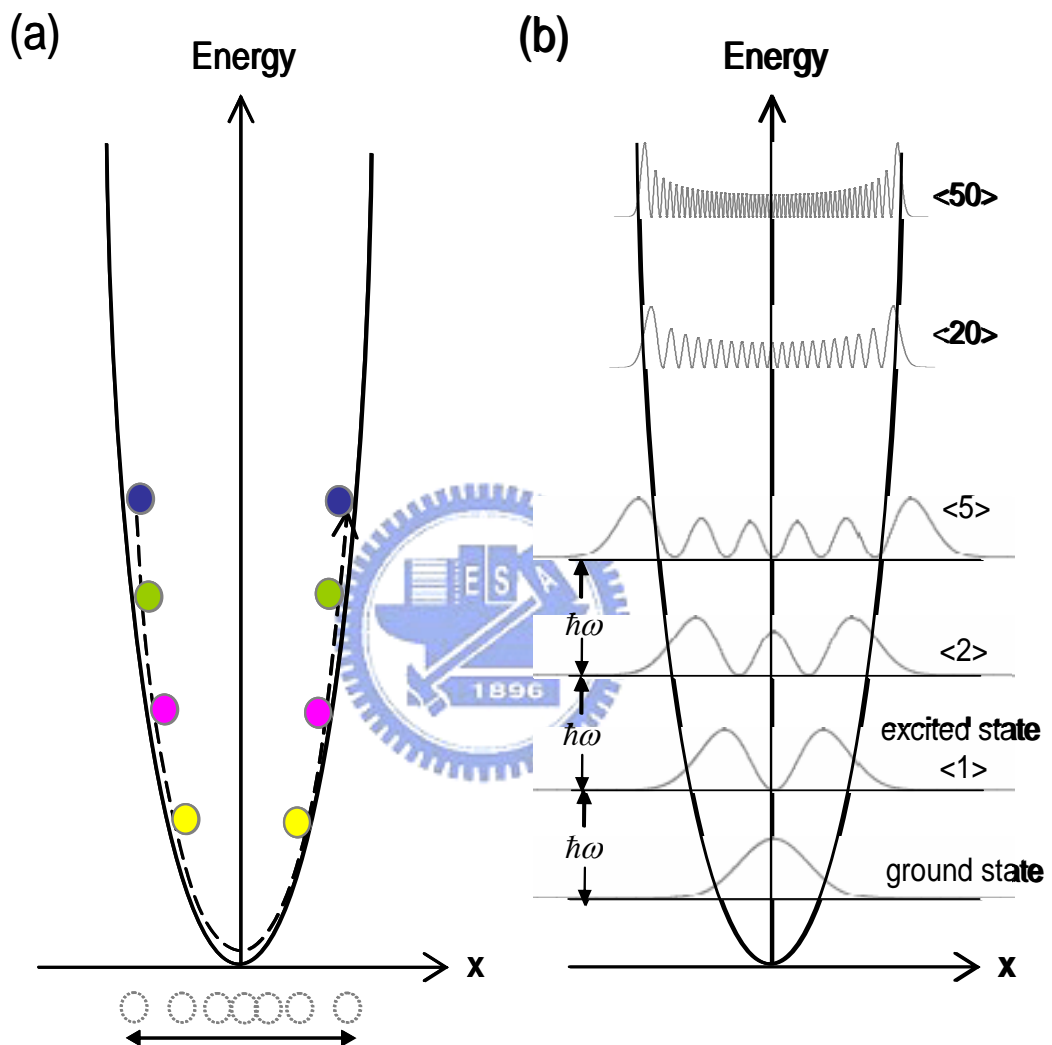


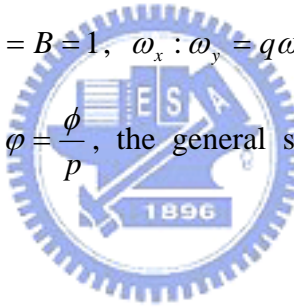
Fig. 1.1.1 (a) 1D classical harmonic oscillator. (b) 1D quantum harmonic oscillator. (The probability density of several states)

## 1.2 Two-dimensional Harmonic Oscillator

It is very important to extend the 1D harmonic oscillator problem to two-dimensional (2D), because 2D figure is more impressive than 1D figure for human's eye and the 2D problems are more general existing in many physics phenomenon. For the rectangular coordinate, which  $x$  and  $y$  is orthogonal, the general solution of the classical harmonic oscillator can be expressed as

$$x(t) = A \cos(\omega_x t - \varphi) \text{ and } y(t) = B \cos(\omega_y t), \quad (1.2.1)$$

where  $A$  and  $B$  are the amplitudes,  $\omega_x$  and  $\omega_y$  are the angular frequencies of  $x$  and  $y$ ,  $\varphi$  is the phase. If we assume that  $A = B = 1$ ,  $\omega_x : \omega_y = q\omega : p\omega$ , where  $q$  and  $p$  are integers and have no common factor and  $\varphi = \frac{\phi}{p}$ , the general solution of the 2D classical harmonic oscillator is



$$x(t) = \cos\left(q\omega t - \frac{\phi}{p}\right) \text{ and } y(t) = \cos(p\omega t). \quad (1.2.2)$$

The several examples of the solutions shown in Fig. 1.2.1 (b) are famous Lissajous figures. Lissajous figures can describe the trajectory of a particle which moves inside a parabolic-like bowl such as shown in Fig. 1.2.1 (a). This kind of curves was investigated by Nathaniel Bowditch in 1815, and later in more detail by Jules Antoine Lissajous in 1857. Jules Antoine Lissajous (1822-1880) was a French mathematician, who invented the Lissajous apparatus to create the figures that bear his name [3]. In the experiment, a light was shone off a mirror which attached to a vibrating tuning fork then the light was reflected off another mirror attached to another perpendicular vibrating tuning fork with different pitch, then on the wall

resulted in a Lissajous figure.

From 1D quantum harmonic oscillator, the general solution of 2D quantum harmonic oscillator can be easily demonstrated as the form which comprises two orthogonal parts:

$$\psi_{m,n} = \frac{1}{\sqrt{2^{m+n} m! n!}} \left( \frac{m_p \omega}{\pi \hbar} \right)^{\frac{1}{2}} \cdot \exp \left( -\frac{m_p \omega}{2\hbar} (x^2 + y^2) \right) \cdot H_m \left( \sqrt{\frac{m_p \omega}{\hbar}} x \right) \cdot H_n \left( \sqrt{\frac{m_p \omega}{\hbar}} y \right), \quad (1.2.3)$$

where  $m, n = 0, 1, 2, \dots$ ,  $H_m(x)$  and  $H_n(y)$  are the Hermite polynomials. The corresponding energy levels are  $E_{m,n} = \left( m + n + \frac{1}{2} \right) \hbar \omega$ . In order to distinguish the quantum number  $m$  and the mass of particle, we use  $m_p$  to represent the mass of particle. Figure 1.2.1

(c) shows the density of the wave function with different quantum number. Obviously, the quantum harmonic oscillator and classical harmonic oscillator lead to totally different results which are shown in Fig. 1.2.1. Therefore we have to connect the two ends of the classical and quantum harmonic oscillator problem from studying wave packet states and coherent states in quantum mechanics.

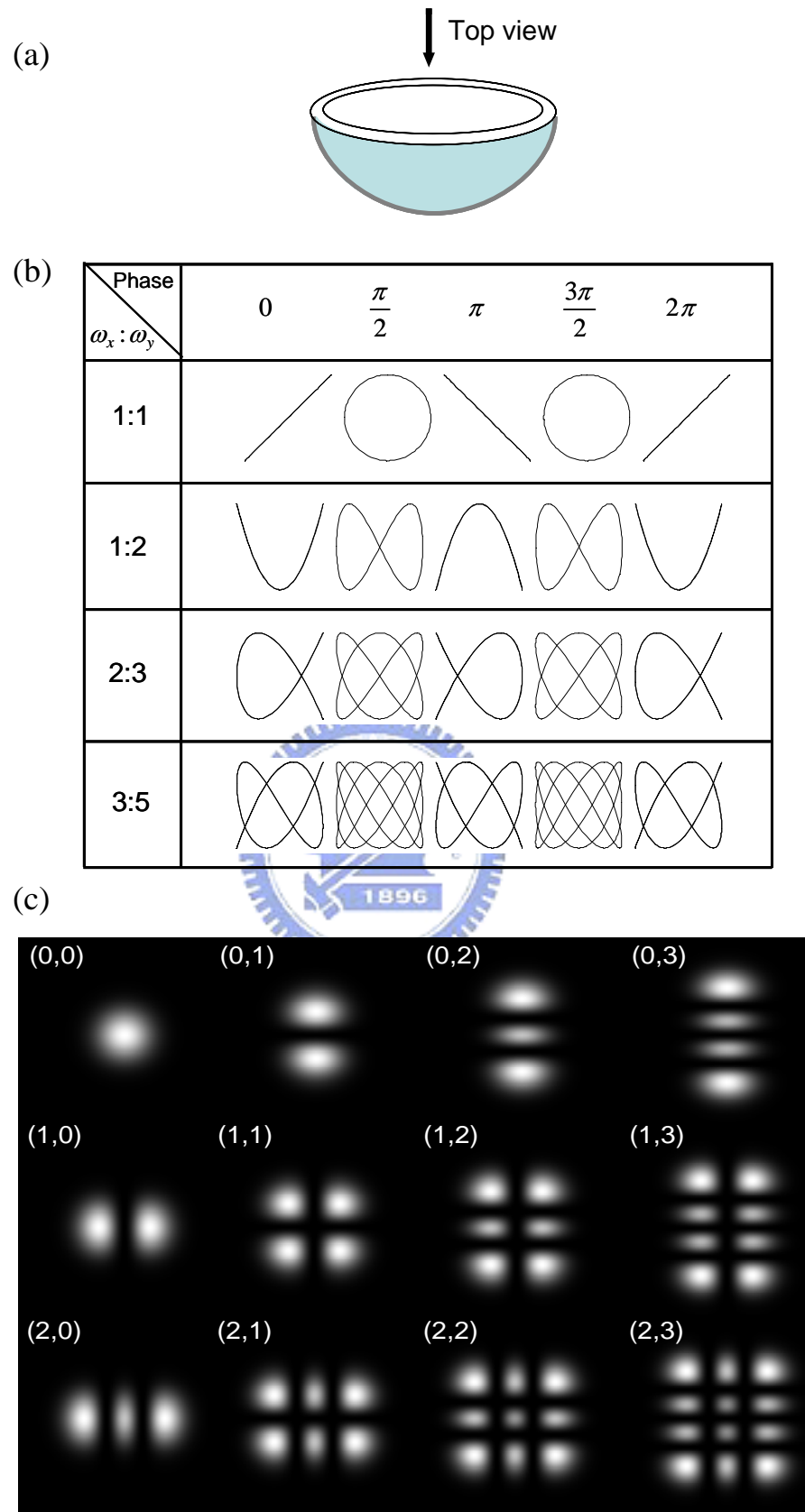
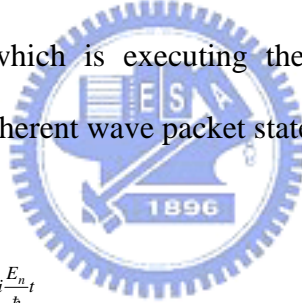


Fig. 1.2.1 (a) The description of the potential of 2D harmonic oscillator. (b) Lissajous figures with different frequency ratio and phase. (c) The eigenstates of 2D quantum harmonic oscillator with different orders.

### 1.3 Schrödinger Coherent States of the 1D Harmonic Oscillator

In recent years, there has been growing attention to quantum manifestations of classical periodic orbits in mesoscopic systems [4–14]. Therefore, the connection between the quantum wave functions and the classical trajectories in mesoscopic systems with internal nonlinear resonances is important for understanding the quantum features of nonlinear classical dynamics, which is also a central issue in modern physics. It is well known that Schrödinger in 1926 [15] originally constructed a coherent state of a 1D harmonic oscillator to describe a classical particle with a wave packet whose center in the time evolution follows the corresponding classical motion. Schrödinger demonstrated a coherent state to explore the continuous transition from micro- to macro-mechanics by showing that a group of proper vibrations of high-order quantum number and of relatively small quantum number differences may represent a “particle”, which is executing the “motion”, expected from the usual mechanics. The Schrödinger coherent wave packet state can be generalized as



$$\Psi(\xi, t; \alpha) = \sum_{n=0}^{\infty} c_n \tilde{\psi}_n(\xi) e^{-i \frac{E_n}{\hbar} t} , \quad (1.3.1)$$

with

$$c_n = \frac{\alpha^n}{\sqrt{n!}} e^{-|\alpha|^2/2} , \quad (1.3.2)$$

$$\tilde{\psi}_n(\xi) = \left( 2^n n! \sqrt{\pi} \right)^{-1/2} e^{-\xi^2/2} H_n(\xi) , \quad (1.3.3)$$

$$E_n = \left( n + \frac{1}{2} \right) \hbar \omega , \quad (1.3.4)$$

where the parameter  $\alpha$  can be generalized as

$$\alpha = |\alpha| e^{i\phi} , \quad (1.3.5)$$

where  $\phi$  is a real number and represents the phase factor. Note that the normalized eigenfunction for the variable  $x$  is given by  $\psi(x) = (m\omega/\hbar)^{1/4} \tilde{\psi}_n(\xi)$ ,  $\xi = \sqrt{\frac{m\omega}{\hbar}}x$ . It can be found that the norm square of the coefficient  $|c_n|^2$  is exactly the same as the Poisson distribution with the mean of  $|\alpha|^2$ . Substituting (1.3.3) and (1.3.4) into (1.3.1) and rearranging the result, we can obtain

$$\begin{aligned} \Psi(\xi, t; \alpha) &= \sum_{n=0}^{\infty} \frac{(|\alpha| e^{i\phi})^n}{\sqrt{n!}} e^{-|\alpha|^2/2} \frac{1}{\sqrt{2^n n! \sqrt{\pi}}} H_n(\xi) e^{-\xi^2/2} e^{-i(n+1/2)\omega t} \\ &= \frac{1}{\pi^{1/4}} e^{-(|\alpha|^2 + \xi^2)/2} e^{-i\omega t/2} \sum_{n=0}^{\infty} \frac{[\alpha |e^{-i(\omega t - \phi)} / \sqrt{2}]^n}{n!} H_n(\xi) \end{aligned} \quad (1.3.6)$$

Using the generating function, equation (1.3.6) can be rewritten as

$$\begin{aligned} \Psi(\xi, t; \alpha) &= \frac{1}{\pi^{1/4}} e^{-(|\alpha|^2 + \xi^2)/2} e^{-i\omega t/2} \exp \left\{ -[\alpha |e^{-i(\omega t - \phi)} / \sqrt{2}]^2 + \sqrt{2} |\alpha| |e^{-i(\omega t - \phi)} \xi \right\} \\ &= \frac{1}{\pi^{1/4}} e^{-(|\alpha|^2 + \xi^2)/2} e^{-i\omega t/2} \exp \left\{ -|\alpha|^2 e^{-i2(\omega t - \phi)}/2 + \sqrt{2} |\alpha| |e^{-i(\omega t - \phi)} \xi \right\} \end{aligned} \quad (1.3.7)$$

As a result, the probability distribution of the coherent state is given by

$$\begin{aligned}
P(\xi, t; \alpha) &= \Psi^*(\xi, t; \alpha) \Psi(\xi, t; \alpha) \\
&= \frac{1}{\sqrt{\pi}} e^{-(|\alpha|^2 + \xi^2)} \exp \left\{ -|\alpha|^2 \cos[2(\omega t - \phi)] + 2\sqrt{2} |\alpha| \xi \cos(\omega t - \phi) \right\} \\
&\quad , \\
&= \frac{1}{\sqrt{\pi}} \exp \left\{ -\xi^2 - 2|\alpha|^2 \cos^2(\omega t - \phi) + 2\sqrt{2} |\alpha| \xi \cos(\omega t - \phi) \right\} \\
&= \frac{1}{\sqrt{\pi}} \exp \left\{ -[\xi - \sqrt{2} |\alpha| \cos(\omega t - \phi)]^2 \right\}
\end{aligned} \tag{1.3.8}$$

It can be clearly seen that the center of the wave packet moves in the path of the classical motion

$$\xi = \sqrt{2} \alpha \cos(\omega t - \phi) \tag{1.3.9}$$

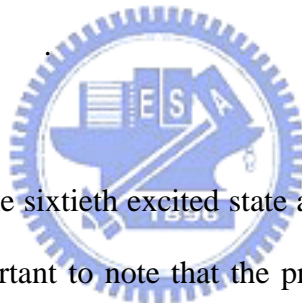


Figure 1.3.1(a) and (b) show the sixtieth excited state and 1D coherent state moving around a period, respectively. It is important to note that the probability density of 1D coherent state can represent the behavior of particle which was confined in a potential of 1D harmonic oscillator. As a result, Schrödinger coherent state of 1D harmonic oscillator plays a vital role to connect the relation between classical and quantum regime and makes a significant contribution to understand the mesoscopic physics between microscopic and macroscopic regime.

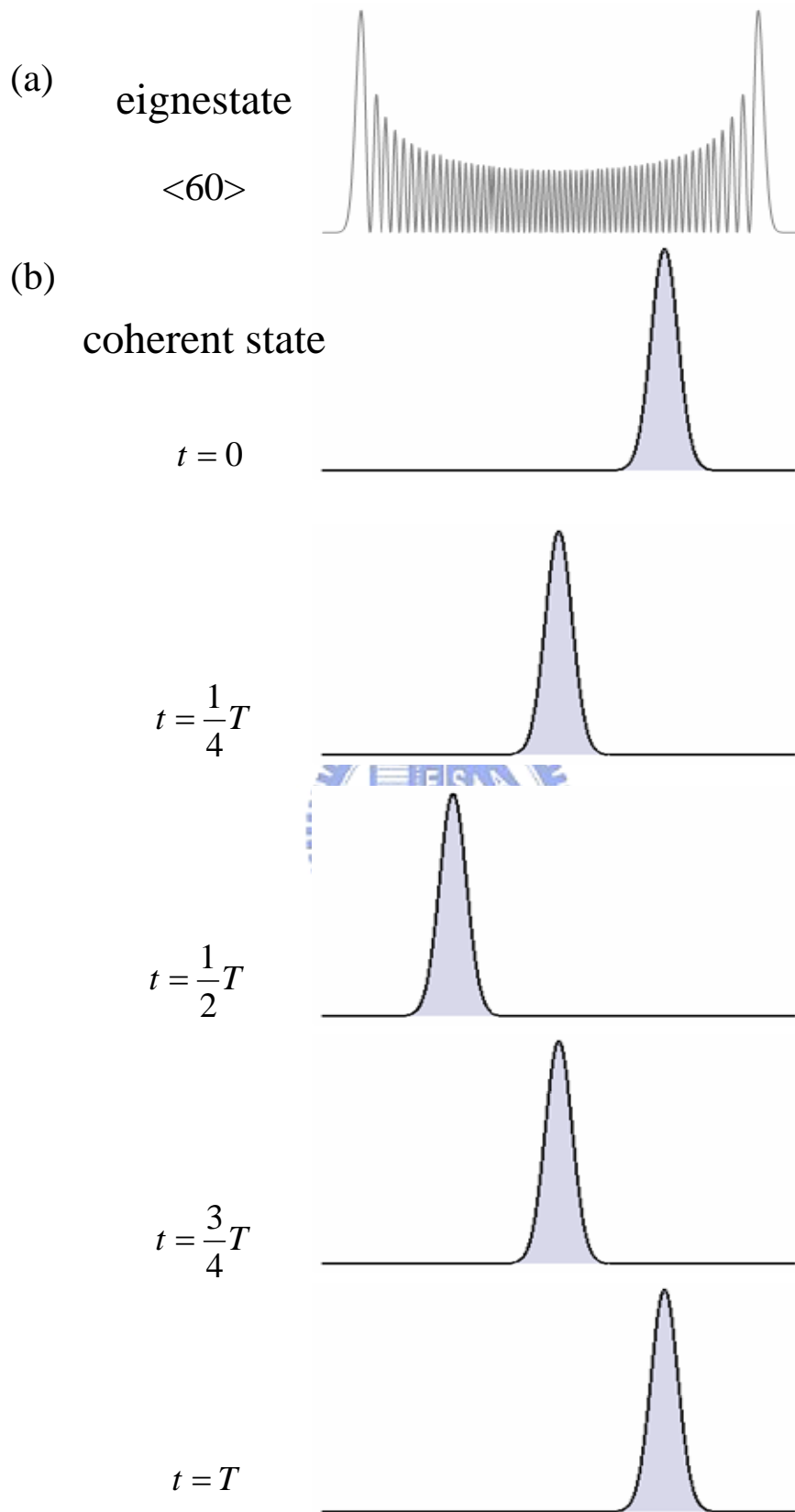


Fig. 1.3.1 (a) Sixtieth excited state of 1D harmonic oscillator (b) 1D coherent state moving with time

## 1.4 Stationary Coherent States of 2D Harmonic Oscillator

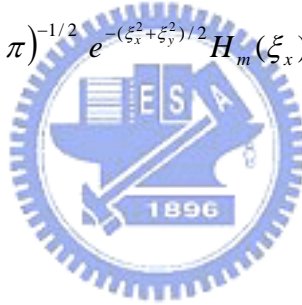
The time-independent Schrödinger equation for a 2D harmonic oscillator with commensurate frequencies can generally be given by

$$\left[ -\frac{\hbar^2}{2m} \left( \frac{\partial^2}{\partial x^2} + \frac{\partial^2}{\partial y^2} \right) + \frac{1}{2} m(\omega_x^2 x^2 + \omega_y^2 y^2) \right] \psi(x, y) = E \psi(x, y) , \quad (1.4.1)$$

where  $\omega_x = q\omega$  and  $\omega_y = p\omega$ ,  $\omega$  is the common factor of the frequencies by  $\omega_x$  and  $\omega_y$ , and  $p$  and  $q$  are relative prime integers. With the results in the preceding section, the eigenfunction and the eigenvalue of the 2D harmonic oscillator with commensurate frequencies are given by

$$\tilde{\psi}_{m,n}(\xi_x, \xi_y) = (2^{n+m} m! n! \pi)^{-1/2} e^{-(\xi_x^2 + \xi_y^2)/2} H_m(\xi_x) H_n(\xi_y) . \quad (1.4.2)$$

and



$$E_{m,n} = \left( m + \frac{1}{2} \right) \hbar \omega_x + \left( n + \frac{1}{2} \right) \hbar \omega_y , \quad (1.4.3)$$

where  $\xi_x = \sqrt{m\omega_x/\hbar}x$  and  $\xi_y = \sqrt{m\omega_y/\hbar}y$ . However the conventional eigenstates of a 2D harmonic oscillator with commensurate frequencies do not reveal the characteristics of classical Lissajous figures even in the correspondence limit of large quantum number.

Since the eigenfunction is separable, the corresponding Schrödinger coherent state can be extended to 2D system as the product of two 1D coherent states. The Schrödinger coherent state of 2D system is expected to correspond to a wave packet with its center generally moving along a classical trajectory. This exact correspondence enables us to construct the quantum stationary states localized on the classical Lissajous orbits from the

time-independent Schrödinger coherent state.

Since the Hamiltonian is separable, the Schrödinger coherent state for 2D harmonic oscillator can be expressed as:

$$\begin{aligned}
 \Psi(\xi_x, \xi_y, t) &= \left( \sum_{m=0}^{\infty} \frac{(\alpha_x e^{i\phi_x})^m}{\sqrt{m!}} e^{-\alpha_x^2/2} \frac{1}{\sqrt{2^m m! \sqrt{\pi}}} H_m(\xi_x) e^{-\xi_x^2/2} e^{-i(m+1/2)q\omega t} \right) \\
 &\quad \times \left( \sum_{n=0}^{\infty} \frac{(\alpha_y e^{i\phi_y})^n}{\sqrt{n!}} e^{-\alpha_y^2/2} \frac{1}{\sqrt{2^n n! \sqrt{\pi}}} H_n(\xi_y) e^{-\xi_y^2/2} e^{-i(n+1/2)p\omega t} \right) \\
 &= \sum_{n=0}^{\infty} \sum_{m=0}^{\infty} \frac{(\alpha_x e^{i\phi_x})^m (\alpha_y e^{i\phi_y})^n}{\sqrt{m!} \sqrt{n!}} e^{-(\alpha_x^2 + \alpha_y^2)/2} \tilde{\psi}_{m,n}(\xi_x, \xi_y) e^{-i(qm + pn + q/2 + p/2)\omega t}
 \end{aligned} \tag{1.4.4}$$

It is clear that the center of the wave packet follows the motion of a classical 2D isotropic harmonic oscillator, i.e.,



$$\xi_x = \sqrt{2}\alpha_x \cos(q\omega t - \phi_x); \quad \xi_y = \sqrt{2}\alpha_y \cos(p\omega t - \phi_y) \quad . \tag{1.4.5}$$

The set of states with indices  $(m, n)$  in (1.4.4) can be divided into subsets characterized by a pair of indices  $(u_x, u_y)$  given by  $m \equiv u_x \pmod{p}$  and  $n \equiv u_y \pmod{q}$ . In terms of these subsets, the Schrödinger coherent state in (1.4.4) can be rewritten as

$$\begin{aligned}
 \Psi(\xi_x, \xi_y, t) &= \left( \sum_{u_y=0}^{q-1} \sum_{u_x=0}^{p-1} \sum_{N_x=0}^{\infty} \sum_{N_y=0}^{\infty} \frac{(\alpha_x e^{i\phi_x})^{pN_x+u_x} (\alpha_y e^{i\phi_y})^{qN_y+u_y}}{\sqrt{(pN_x + u_x)!} \sqrt{(qN_y + u_y)!}} e^{-(\alpha_x^2 + \alpha_y^2)/2} \right. \\
 &\quad \times \left. \tilde{\psi}_{pN_x+u_x, qN_y+u_y}(\xi_x, \xi_y) e^{-i[pq(N_x + N_y) + q(u_x + 1/2) + p(u_y + 1/2)]\omega t} \right)
 \end{aligned} \tag{1.4.6}$$

As seen in (1.4.6), the 2D Schrödinger coherent state is divided into a product of two infinite

series and two finite series. The method of the triangular partial sums is used to make precise sense out of the product of two infinite series in (1.4.6). With the representation of the Cauchy product, the terms  $\tilde{\psi}_{pN_x+u_x, qN_y+u_y}(\xi_x, \xi_y)$  in (1.4.6) can be arranged diagonally by grouping together those terms for which  $N_x + N_y = N$ :

$$\begin{aligned}
 \Psi(\xi_x, \xi_y, t) &= \left( \sum_{u_y=0}^{q-1} \sum_{u_x=0}^{p-1} \sum_{N=0}^{\infty} \sum_{K=0}^N \frac{(\alpha_x e^{i\phi_x})^{pK+u_x} (\alpha_y e^{i\phi_y})^{q(N-K)+u_y}}{\sqrt{(pK+u_x)!} \sqrt{[q(N-K)+u_y]!}} e^{-(\alpha_x^2 + \alpha_y^2)/2} \right. \\
 &\quad \left. \times \tilde{\psi}_{pK+u_x, q(N-K)+u_y}(\xi_x, \xi_y) e^{-i[pqN+q(u_x+1/2)+p(u_y+1/2)]\omega t} \right), \\
 &= \sum_{u_y=0}^{q-1} \sum_{u_x=0}^{p-1} \sum_{N=0}^{\infty} e^{-(\alpha_x^2 + \alpha_y^2)/2} (\alpha_x e^{i\phi_x})^{u_x} (\alpha_y e^{i\phi_y})^{qN+u_y} e^{-i[pqN+q(u_x+1/2)+p(u_y+1/2)]\omega t} \\
 &\quad \times \left\{ \sum_{K=0}^N \frac{(\alpha_x^p / \alpha_y^q)^K [e^{i(p\phi_x - q\phi_y)}]^K}{\sqrt{(pK+u_x)!} \sqrt{[q(N-K)+u_y]!}} \tilde{\psi}_{pK+u_x, q(N-K)+u_y}(\xi_x, \xi_y) \right\} \tag{1.4.7}
 \end{aligned}$$

The expression in the curly bracket of Eq. (1.4.7) represents the stationary coherent states labeled with one major index  $N$  and two minor indices  $u_x$  and  $u_y$ . These stationary coherent states are physically expected to be associated with the Lissajous trajectories. Note that the minor indices  $u_x$  and  $u_y$  essentially do not affect the characteristics of the stationary states. Including the normalization condition, the stationary coherent states in Cartesian coordinates are given by

$$\begin{aligned}
 \Phi_{N, u_x, u_y}^{p, q}(\xi_x, \xi_y; A, \phi) &= \left( \sum_{K=0}^N \frac{A^{2K}}{(pK)! \cdot [q(N-K)+u_y]!} \right)^{-1/2} \\
 &\quad \times \sum_{K=0}^N \frac{[A e^{i\phi}]^K}{\sqrt{(pK)!} \sqrt{[q(N-K)+u_y]!}} \tilde{\psi}_{pK+u_x, q(N-K)+u_y}(\xi_x, \xi_y) \tag{1.4.8}
 \end{aligned}$$

where

$$A = \frac{(\alpha_x)^p}{(\alpha_y)^q}, \quad \phi = p\phi_x - q\phi_y \quad . \quad (1.4.9)$$

The equation (1.4.8) reveals that the stationary coherent states associated with the Lissajous trajectories are the superposition of degenerate eigenstates with the relative amplitude factor  $A$  and phase factor  $\phi$  [16]. Furthermore, the expression (1.4.9) indicates that the relative amplitude factor  $A$  and phase factor  $\phi$  in the stationary coherent states  $\Phi_{N,u_x,u_y}(\xi_x, \xi_y; A, \phi)$  are explicitly related to the classical variables  $(\alpha_x, \alpha_y, \phi_x, \phi_y)$  in (1.4.6).

From (1.4.7), the eigenenergies of the stationary coherent states  $\Phi_{N,u_x,u_y}^{p,q}(\xi_x, \xi_y; A, \phi)$  are found to be

$$E_{N,u_x,u_y} = [pqN + q(u_x + 1/2) + p(u_y + 1/2)]\hbar\omega \xrightarrow{N \gg 1} (Npq)\hbar\omega, \quad (1.4.10)$$

Figures 1.4.1-1.4.3 depicts the comparison between the quantum wave patterns  $|\Phi_{N,u_x,u_y}^{p,q}(\xi_x, \xi_y; A, \phi)|^2$  and the corresponding classical periodic orbits for  $p:q$  to be  $2:1$ ,  $3:2$ , and  $4:3$ , respectively. Here three different phase factors,  $\phi = 0$ ,  $\phi = 0.3\pi$ , and  $\phi = 0.6\pi$ , are displayed in each figure for the purpose of clear comparison. The behavior of the quantum wave patterns in all cases can be found to be in precise agreement with the classical Lissajous figures.

It is worthwhile to mention that the stationary coherent states for the 2D isotropic harmonic oscillator  $p:q = 1:1$  can be simplified to give rise to the expression of elliptic states [17]. After some algebra and setting  $u_x = u_y = 0$ , equation (1.4.7) can be rewritten as

$$\Psi(\xi_x, \xi_y, t) = \sum_{N=0}^{\infty} C_N \Phi_{N,u_x,u_y}^{1,1}(\xi_x, \xi_y; A, \phi) e^{-i(N+1)\omega t}, \quad (1.4.11)$$

where

$$C_N = e^{-(\alpha_x^2 + \alpha_y^2)/2} \frac{(\sqrt{1+A^2} \alpha_y e^{i\phi_y})^N}{\sqrt{N!}} , \quad (1.4.12)$$

$$\Phi_{N,u_x,u_y}^{1,1}(\xi_x, \xi_y; A, \phi) = \frac{1}{(\sqrt{1+A^2})^N} \sum_{K=0}^N \binom{N}{K}^{1/2} (A e^{i\phi})^K \tilde{\psi}_{K, N-K}(\xi_x, \xi_y) , \quad (1.4.13)$$

$$A = \frac{\alpha_x}{\alpha_y}, \quad \phi = \phi_x - \phi_y . \quad (1.4.14)$$

The wave function in (1.4.13) represents a type of normalized elliptic stationary coherent state.

Figure 1.4.4 shows the dependence of the wave pattern of the stationary coherent states

$\Phi_{N,0,0}^{1,1}(\xi_x, \xi_y; A, \phi)^2$  on the factors  $A$  and  $\phi$  for  $N=20$ . It can be seen that the coherent states

$\Phi_{N,0,0}^{1,1}(\xi_x, \xi_y; A, \phi)$  correspond to the elliptic stationary states. The superposition of two

elliptic states with a phase factor  $\phi$  in the opposite sign can form a standing wave pattern:

$\Phi_{N,0,0}^{1,1}(\xi_x, \xi_y; A, \phi) \pm \Phi_{N,0,0}^{1,1}(\xi_x, \xi_y; A, -\phi)$ . Figure 1.4.4 also shows the standing wave

patterns corresponding to the elliptic states.

Equation (1.4.11) manifestly reveals the relationship between the Schrödinger coherent state and the stationary coherent state. As is known from quantum mechanics,  $|C_N|^2$  represents the probability of finding the system in the elliptic stationary state with order  $N$ . With equation (1.4.12), it can be found that

$$|C_N|^2 = \frac{(\alpha_x^2 + \alpha_y^2)^N}{\sqrt{N!}} e^{-(\alpha_x^2 + \alpha_y^2)} , \quad (1.4.15)$$

As the result of the Schrödinger coherent state in the 1D harmonic oscillator, the probability distribution  $|C_N|^2$  is identical to the Poisson distribution with the mean value of  $\langle N \rangle = \alpha_x^2 + \alpha_y^2$ .

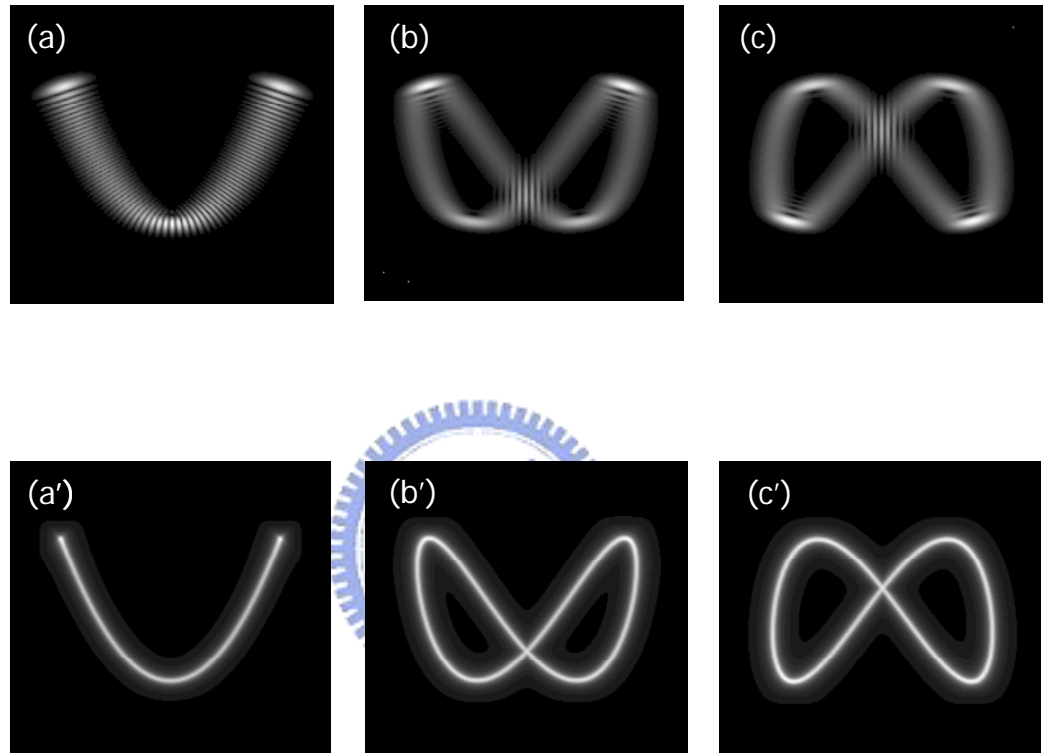


Fig. 1.4.1 Comparison between the quantum stationary state  $\left| \Phi_{N,u_x,u_y}^{p,q}(\xi_x, \xi_y; A, \phi) \right|^2$  [(a)-(c)] and the classical Lissajous orbits [(a')-(c')] for the system of  $p:q = 2:1$  with  $N = 40$ ,  $A = 5.2$  and (a)  $\phi = 0$ , (b)  $\phi = 0.3\pi$ , and (c)  $\phi = 0.6\pi$ .

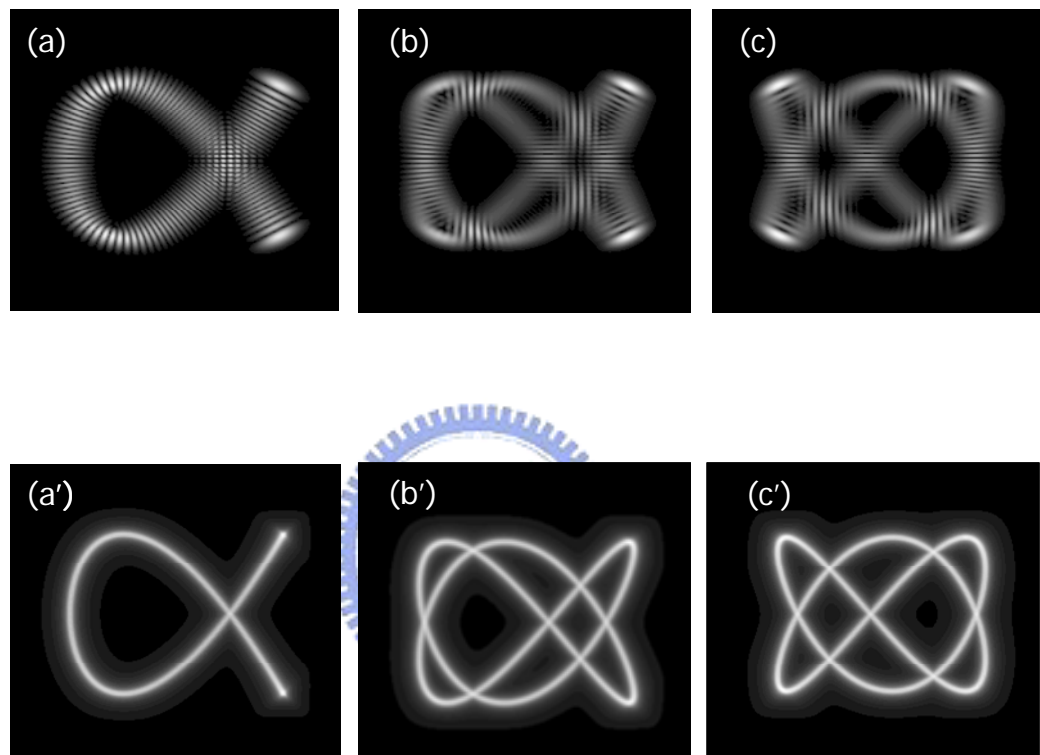


Fig. 1.4.2 The same as Fig. 1.4.1 for the system of  $p:q = 3:2$  with  $N = 22$ ,  $A = 5.2$  and (a)  $\phi = 0$ , (b)  $\phi = 0.3\pi$ , and (c)  $\phi = 0.6\pi$ .

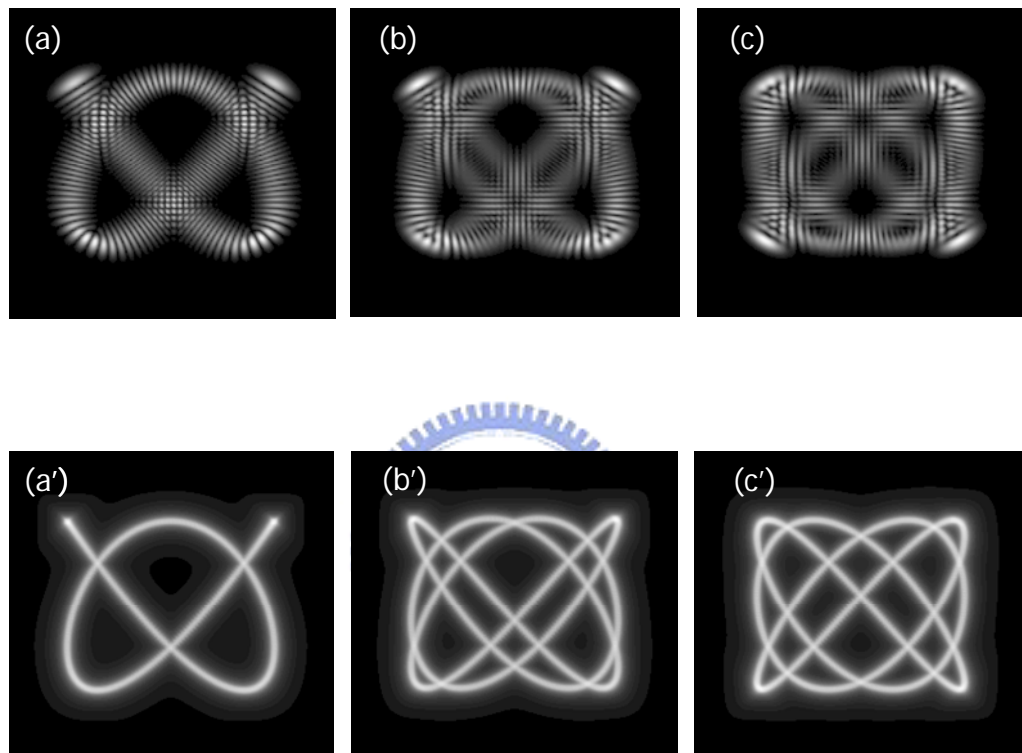


Fig. 1.4.3 The same as Fig. 1.4.1 for the system of  $p : q = 4 : 3$  with  $N = 15$ ,  $A = 5.2$  and (a)  $\phi = 0$ , (b)  $\phi = 0.3\pi$ , and (c)  $\phi = 0.6\pi$ .

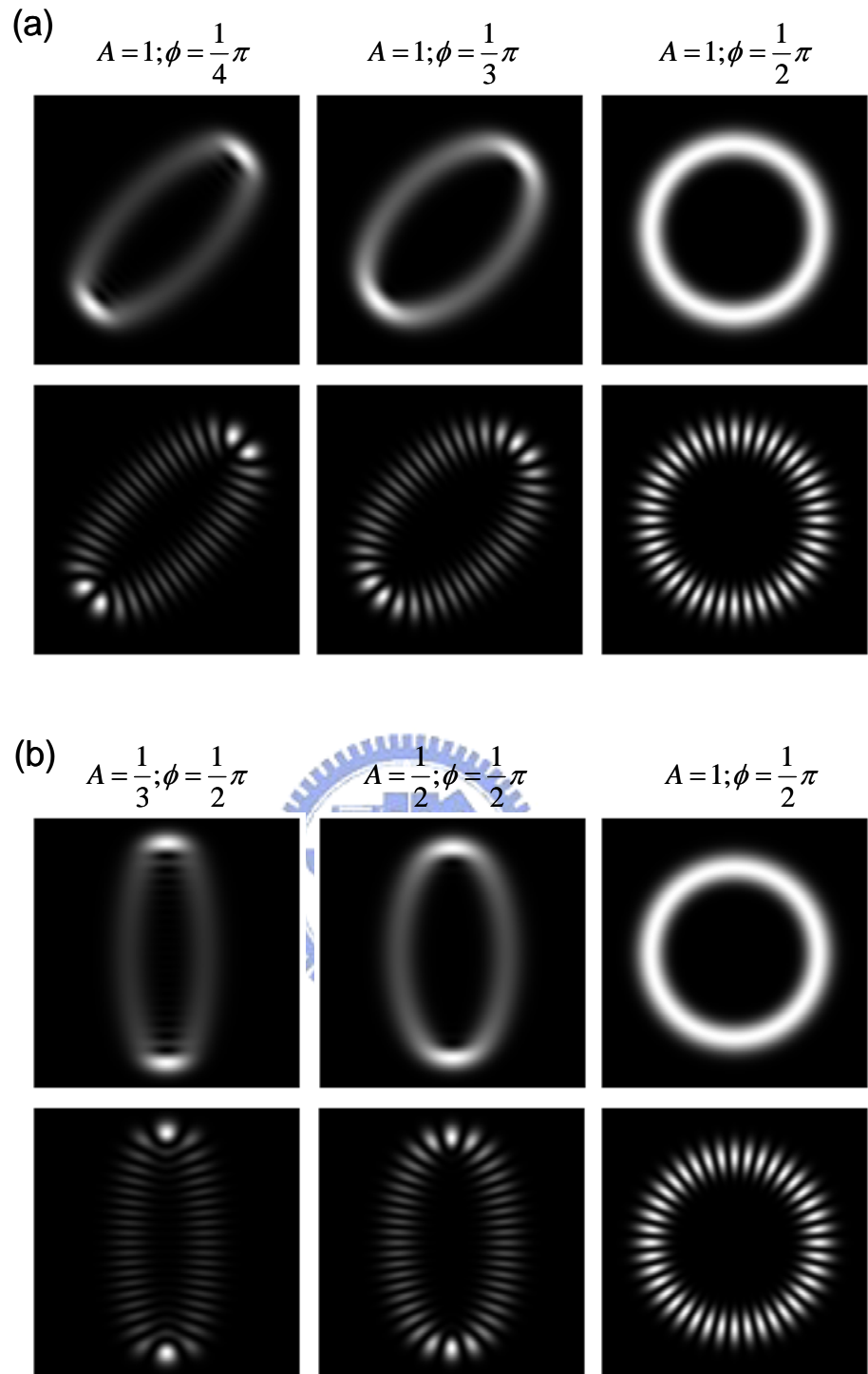


Fig. 1.4.4 (a) Upper: wave patterns of stationary coherent states for  $N=20$  with different values of the parameters  $\phi$ . Lower: standing wave patterns corresponding to upper figures. (b) Upper: wave patterns of stationary coherent states for  $N=20$  with different values of the parameters  $A$ . Lower: standing wave patterns corresponding to upper figures.

## 1.5 Unitary Transformation between Stationary States and wave packet states

Even though the Schrödinger coherent state is an analytic and elegant representation for the wave packet state, another important representation is given by

$$\Psi(\xi, t; \phi) = \frac{1}{\sqrt{M}} \sum_{m=0}^{M-1} e^{im\phi} \tilde{\psi}_{N+m}(\xi) e^{-i\frac{E_{N+m}}{\hbar}t} \quad (M \ll N) . \quad (1.5.1)$$

The representation in equation (1.5.1) resembles the definition of the phase state. Unlike the Schrödinger coherent state, the coherent state in equation (1.5.1) is expanded by a finite-dimensional basis. In order to simplify the representation of the wave function, here I use

$$|\Psi_n\rangle = \frac{1}{\sqrt{M}} \sum_{m=0}^{M-1} e^{im\phi_n} |\Phi_m\rangle \quad (1.5.2)$$

to replace (1.5.1). The phase  $\phi_n$  must be properly chosen to make the wave function to maintain the characteristic of orthonormal. Then we can get

$$\langle \Psi_n | \Psi_s \rangle = \frac{1}{M} \sum_{m=0}^{M-1} e^{im(\phi_s - \phi_n)} = \delta_{n,s} \quad \Rightarrow \phi_n = \frac{2\pi}{M} \cdot n, \phi_s = \frac{2\pi}{M} \cdot s . \quad (1.5.3)$$

Continuously, the relation between wave packet states and stationary states can be shown as following:

$$\begin{aligned} \langle \Phi_m | \Psi_n \rangle &= \frac{1}{\sqrt{M}} e^{i\frac{2\pi}{M}mn} \\ \langle \Psi_n | \Phi_m \rangle &= \frac{1}{\sqrt{M}} e^{-i\frac{2\pi}{M}mn} \\ |\Phi_m\rangle = \sum_{n=0}^{M-1} C_{mn} |\Psi_n\rangle \quad \Rightarrow \quad C_{mn} &= \langle \Psi_n | \Phi_m \rangle = \frac{1}{\sqrt{M}} \cdot e^{-i\frac{2\pi}{M}mn} . \end{aligned} \quad (1.5.4)$$

Finally, (1.5.5) shows that the stationary states can be represented as the superposition of wave packet states and vice versa.

$$\begin{aligned} |\Psi_n\rangle &= \frac{1}{\sqrt{M}} \sum_{m=0}^{M-1} e^{i \frac{2\pi}{M} mn} |\Phi_m\rangle \\ |\Phi_m\rangle &= \frac{1}{\sqrt{M}} \sum_{n=0}^{M-1} e^{-i \frac{2\pi}{M} mn} |\Psi_n\rangle = \frac{1}{\sqrt{M}} \sum_{n=0}^{M-1} e^{-i \frac{2\pi}{M} mn} \left( \frac{1}{\sqrt{M}} \sum_{m=0}^{M-1} e^{i \frac{2\pi}{M} mn} |\Phi_m\rangle \right). \end{aligned} \quad (1.5.5)$$

It is worthy to notice that  $\hat{U}_{mn} = \frac{1}{\sqrt{M}} e^{i \frac{2\pi}{M} mn}$  is the unitary operator which represents the

transition matrix from the wave packet states and stationary states. Figure 1.5.1 shows the 1D wave packet states (1D Schrödinger coherent states) and stationary states (eigenstates). Figure 1.5.1(a) represents the wave packet states  $|\Psi_n\rangle$  as  $M = 5$  and  $n = 0 \sim 4$  respectively. On the other, Fig. 1.5.1(b) reconstructs the stationary states from the superposition of wave packet states as  $M = 5$  and  $m = 0 \sim 4$  respectively.

In 1D harmonic oscillator, the unitary transform not only connect the wave packet states and stationary coherent states but also play an important role in the quantum-classical correspondence. To expand the method, the unitary transform of equation (1.5.5) can also express the relation between the time-independent stationary coherent states and eigenstates of 2D harmonic oscillator. Figure 1.5.2 depicts time-independent elliptical stationary coherent states as  $M = 7$  and  $n = 0 \sim 6$  respectively. On the other, Fig. 1.5.3 reconstructs the eigenstates from the superposition of stationary coherent states as  $M = 7$  and  $m = 0 \sim 6$  respectively.

In summary, the wave packet states and stationary states can be constructed by each other with unitary transformation in 1D harmonic oscillator. Therefore, the time-independent stationary coherent states and eigenstates can also be constructed by each other with unitary transformation in 2D harmonic oscillator.

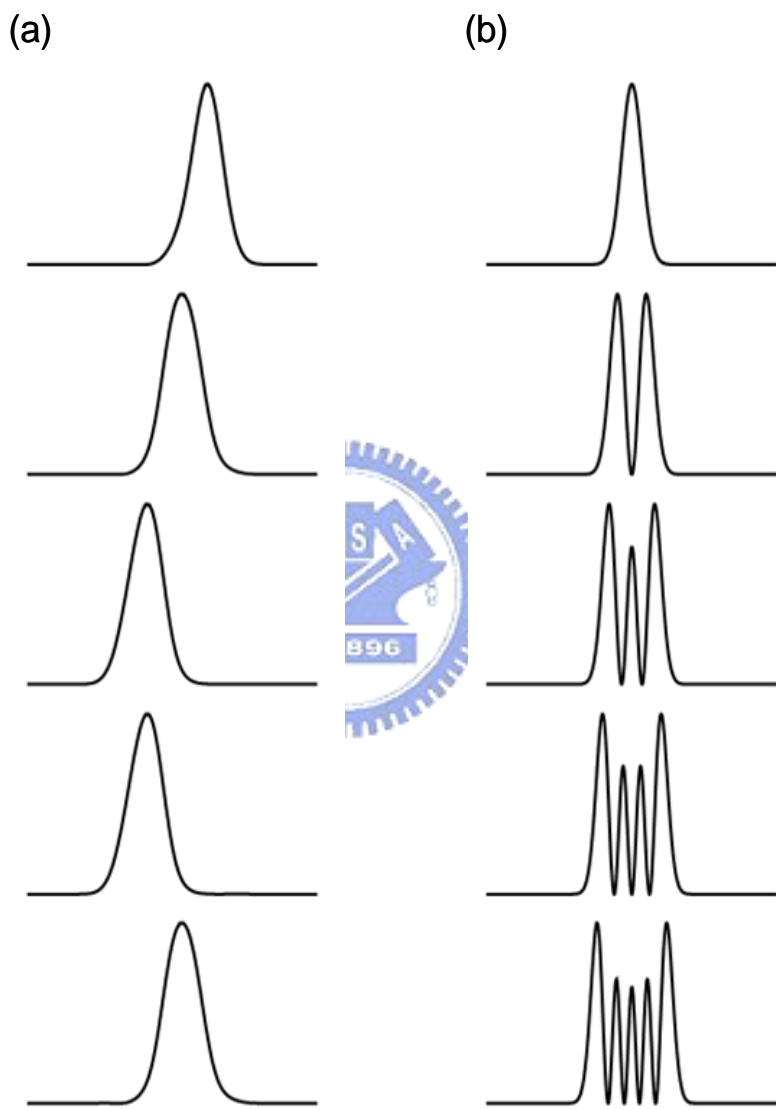


Fig. 1.5.1 (a) The 1D wave packet states with  $M = 5$  and  $n = 0 \sim 4$  respectively. (b) The 1D stationary states with  $M = 5$  and  $m = 0 \sim 4$  respectively.

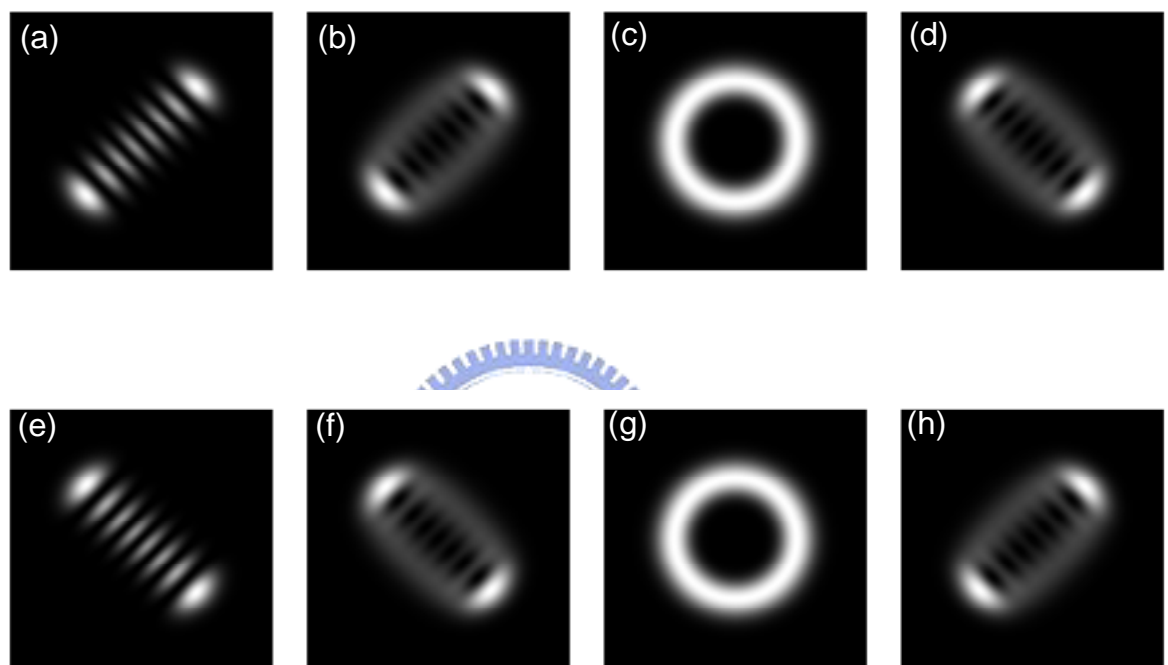


Fig. 1.5.2 The 2D time-independent stationary states with  $M = 7$  and  $n = 0 \sim 6$  respectively.

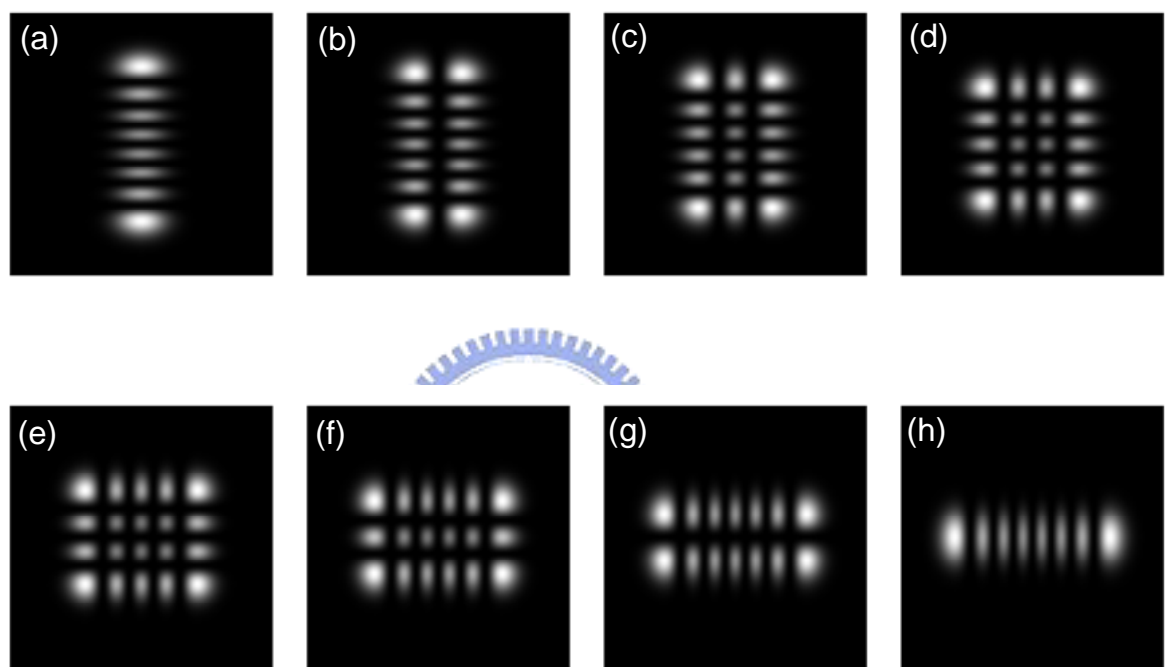


Fig. 1.5.3 The 2D eigenstates with  $M = 7$  and  $m = 0 \sim 6$  respectively.

## REFERENCES

- [1] Stephen Gasiorowicz, *Quantum physics* (third ed.), 2003.
- [2] David J. Griffiths, *Introduction to Quantum Mechanics*, 1994.
- [3] [http://en.wikipedia.org/wiki/Lissajous\\_curve](http://en.wikipedia.org/wiki/Lissajous_curve)
- [4] W. Li, L. E. Reichl, and B. Wu, Phys. Rev. E **65**, 056220 (2002).
- [5] R. Narevich, R. E. Prange, and O. Zaitsev, Phys. Rev. E **62**, 2046 (2000).
- [6] J. Wiersig, Phys. Rev. E **64**, 026212 (2001).
- [7] J. A. de Sales and J. Florencio, Physica A **290**, 101 (2001).
- [8] M. Brack and R. K. Bhaduri, *Semiclassical Physics* (Addison-Wesley, Reading, MA, 1997), Sec. 2.7.
- [9] F. von Oppen, Phys. Rev. B **50**, 17151 (1994).
- [10] R. W. Robinett, Am. J. Phys. **65**, 1167 (1997).
- [11] Y. F. Chen, K. F. Huang, and Y. P. Lan, Phys. Rev. E **66**, 046215 (2002).
- [12] Y. F. Chen, K. F. Huang, and Y. P. Lan, Phys. Rev. E **66**, 066210 (2002).
- [13] Y. F. Chen and K. F. Huang, Phys. Rev. E **68**, 066207 (2003).
- [14] Y. F. Chen and K. F. Huang, J. Phys. A **36**, 7751 (2003).
- [15] E. Schrödinger, Naturwiss. **14**, 644 (1926).
- [16] Y. F. Chen and Y. P. Lan, PHYSICAL REVIEW A **67**, 043814 (2003).
- [17] Y. F. Chen, T. H. Lu, K. W. Su, and K. F. Huang, PHYSICAL REVIEW E **72**, 056210 (2005).

# Chapter 2

## Eigenstates of Harmonic Oscillator and Spherical Laser Cavity: Generalized Coherent States and Polarization-entangled Patterns

It is well known that the paraxial wave equation for the spherical resonator has the identical form with the Schrödinger equation for the two dimensional (2D) harmonic oscillator. In this chapter we derive the paraxial wave equation has the same form with the Schrödinger equation for the 2D harmonic oscillator. The wave function for the paraxial field in the spherical laser resonator can be expressed as Hermite-Gaussian (HG) function with Cartesian symmetry or Laguerre-Gaussian function with cylindrical symmetry which are the eigenfunctions of harmonic oscillator mentioned in chapter one. We introduce the generalized coherent states (GCSs) to be related to the transition form HG modes to various experimental modes which are high order polarization-entangled transverse modes. With the connection between theoretical analysis and experimental results, the formation of complicated singularities can be represented.

### 2.1 Paraxial Approximation of Maxwell's Equations

According to the Helmholtz wave equation, the wave propagation in a source-free medium follows the Maxwell's equations which can be represented as [1-2]

$$\begin{aligned}
 \nabla \times E &= -\mu \frac{\partial}{\partial t} H \\
 \nabla \times H &= \epsilon \frac{\partial}{\partial t} E \\
 \nabla \cdot E &= 0 \\
 \nabla \cdot H &= 0
 \end{aligned} \tag{2.1.1}.$$

Therefore, the electric field can be expressed as

$$\nabla^2 E - \mu\epsilon \frac{\partial^2}{\partial t^2} E = 0. \tag{2.1.2}$$

Assume the electric field to be monochromatic wave  $E = E(x, y, z) \cdot e^{i\omega t}$ , Eq. (2.1.2) can be written as

$$(\nabla^2 + k^2) E(x, y, z) = 0, \tag{2.1.3}$$

where  $k$  is the wave vector. For a wave which propagates primarily along the  $z$  direction,  $E = E(x, y, z)$  can be written as

$$E(x, y, z) = u(x, y, z) \cdot e^{-ik_z z}, \tag{2.1.4}$$

where  $u(x, y, z)$  is the transverse variation,  $k_z$  is the  $z$ -component of the wave vector.

Substituting Eq. (2.1.4) into Eq. (2.1.3), the Helmholtz equation is represented as

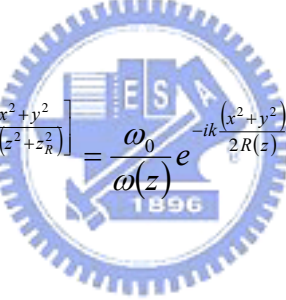
$$\left[ \frac{\partial^2}{\partial x^2} + \frac{\partial^2}{\partial y^2} + \frac{\partial^2}{\partial z^2} - 2ik_z \frac{\partial}{\partial z} + (k^2 - k_z^2) \right] u(x, y, z) = 0. \tag{2.1.5}$$

In the paraxial approximation, the term  $\frac{\partial^2}{\partial z^2}u(x,y,z)$  is quite small in comparison with remaining terms, therefore

$$\left[ \nabla_t^2 - 2ik_z \frac{\partial}{\partial z} + k_t^2 \right] u(x,y,z) = 0, \quad (2.1.6)$$

where  $\nabla_t^2 = \frac{\partial^2}{\partial x^2} + \frac{\partial^2}{\partial y^2}$  and  $k_t^2 = k^2 - k_z^2$ . We assume that  $u(x,y,z) = \Psi(x,y)G(x,y,z)$ ,

where  $\Psi(x,y)$  is a scalar wave function which describes the transverse variation of the beam,  $G(x,y,z)$  is a wave function which describes the wave as Gaussian spherical wave between plane wave and spherical wave. According to the cavity confinement, the Gaussian spherical wave can be written as



$$G(x,y,z) = \frac{z_R}{\sqrt{z^2 + z_R^2}} e^{-ikz \left[ \frac{x^2 + y^2}{2(z^2 + z_R^2)} \right]} = \frac{\omega_0}{\omega(z)} e^{-ik \frac{(x^2 + y^2)}{2R(z)}}, \quad (2.1.7)$$

where  $\omega_0$  is the minimum spot size at  $z = 0$ ,  $\omega(z)$  is the spot size at arbitrary position, and  $R(z)$  is the radius of curvature. The relation is given by  $\omega(z) = \omega_0 \sqrt{1 + \left( \frac{z}{z_R} \right)^2}$  and

$$R(z) = z \left[ 1 + \left( \frac{z_R}{z} \right)^2 \right]. \text{ Then Eq. (2.1.6) can be written as}$$

$$\left[ \nabla_t^2 - 2ik_z \frac{\partial}{\partial z} + k_t^2 \right] \Psi(x,y)G(x,y,z) = 0. \quad (2.1.8)$$

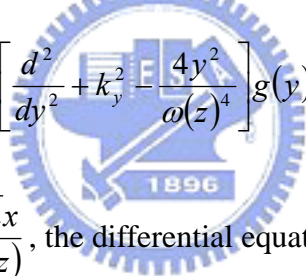
Using paraxial approximation and after some algebra, the paraxial wave equation can be analyzed as:

$$\begin{aligned}
 & G(x, y, z) \left( \nabla_t^2 + k_t^2 \right) \Psi(x, y) + \Psi(x, y) \left( \nabla_t^2 - 2ik_z \frac{\partial}{\partial z} \right) G(x, y, z) \\
 &= G(x, y, z) \left[ \nabla_t^2 + k_t^2 - \frac{(k_z z_R)^2 (x^2 + y^2)}{(z^2 + z_R^2)^2} \right] \Psi(x, y) = 0
 \end{aligned} \quad (2.1.9)$$

Let's replace the variation in Eq. (2.1.9), the general transverse wave equation is shown in rectangular coordinate as

$$\left[ \nabla_t^2 + k_t^2 - \frac{4(x^2 + y^2)}{\omega(z)^4} \right] \Psi(x, y) = 0. \quad (2.1.10)$$

We can divide the wave function into two independent parts as  $\Psi(x, y) = f(x)g(y)$ , then


 $\left[ \frac{d^2}{dx^2} + k_x^2 - \frac{4x^2}{\omega(z)^4} \right] f(x) = 0$  ;  $\left[ \frac{d^2}{dy^2} + k_y^2 - \frac{4y^2}{\omega(z)^4} \right] g(y) = 0$  and  $k_x^2 + k_y^2 = k_t^2$ . Assume that  $f(x) = v(x) e^{-\frac{x^2}{\omega(z)^2}}$  and  $\xi = \frac{\sqrt{2}x}{\omega(z)}$ , the differential equation can be written as

$$\frac{d^2 v}{d\xi^2} - 2\xi \frac{dv}{d\xi} + \left( \frac{k_x^2 \omega(z)^2}{2} - 1 \right) v = 0, \quad (2.1.11)$$

which has the same form with Hermite polynomial:  $y'' - 2xy' + 2my = 0$ . Therefore the normalized wave functions are

$$\Psi_{m,n}(x, y) = \frac{1}{\sqrt{2^{m+n-1} \pi m! n!}} H_m \left( \frac{\sqrt{2}x}{\omega(z)} \right) H_n \left( \frac{\sqrt{2}y}{\omega(z)} \right) e^{-\frac{(x^2+y^2)}{\omega(z)^2}}, \quad (2.1.12)$$

and the eigenvalues are  $k_x^2 = \frac{2}{\omega(z)^2} (2m+1)$  ;  $k_y^2 = \frac{2}{\omega(z)^2} (2n+1)$ , where  $m, n = 0, 1, 2, \dots$

Here  $H_m(\cdot)$  is the  $m$ th order Hermite polynomial. It is worthy to note that the differential equation is similar to the time-independent Schrödinger equation for the simple harmonic oscillator [3]. Combine the equations used before and the paraxial approximation, the longitudinal component of the wave vector can be given by

$$k_z = k - \frac{2}{k_z \omega(z)^2} (m + n + 1). \quad (2.1.13)$$

Using  $\int \frac{dx}{x^2 + a^2} = \frac{1}{a} \tan^{-1} \left( \frac{x}{a} \right)$  and integrate the phase term, then

$$k_z z = kz - (m + n + 1) \tan^{-1} \left( \frac{z}{z_R} \right), \quad (2.1.14)$$

where  $-(m + n + 1) \tan^{-1} \left( \frac{z}{z_R} \right)$  is the Gouy phase shift. In Summary, the wave function in rectangular coordinate can be expressed as

$$E(x, y, z) = \Psi_{m,n}(x, y) \cdot \frac{\omega_0}{\omega(z)} \cdot e^{-ik_z z \frac{x^2 + y^2}{2(z^2 + z_R^2)}} \cdot e^{-i[kz - (m + n + 1) \tan^{-1} \left( \frac{z}{z_R} \right)]}, \quad (2.1.15)$$

where

$$\Psi_{m,n}(x, y) = \frac{1}{\sqrt{2^{m+n-1} \pi m! n!}} H_m \left( \frac{\sqrt{2}x}{\omega(z)} \right) H_n \left( \frac{\sqrt{2}y}{\omega(z)} \right) e^{-\frac{(x^2 + y^2)}{\omega(z)^2}}, \quad (2.1.12)$$

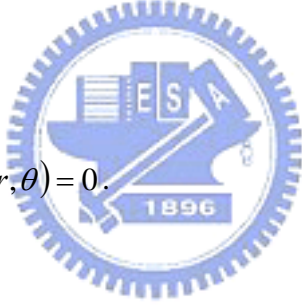
For a cylindrical symmetry system, the general wave equation shown in Eq. (2.1.6) can be represented as

$$\left[ \frac{1}{r} \frac{\partial}{\partial r} \left( r \frac{\partial}{\partial r} \right) + \frac{1}{r^2} \frac{\partial^2}{\partial \theta^2} - 2ik_z \frac{\partial}{\partial z} + k_t^2 \right] u(r, \theta, z) = 0, \quad (2.1.16)$$

where  $\nabla_t^2 = \frac{1}{r} \frac{\partial}{\partial r} \left( r \frac{\partial}{\partial r} \right) + \frac{1}{r^2} \frac{\partial^2}{\partial \theta^2}$  and  $u(r, \theta, z) = \Psi(r, \theta) \cdot G(r, \theta, z)$ . Then

$$u(r, \theta, z) = \Psi(r, \theta) \cdot \frac{\omega_0}{\omega(z)} \cdot e^{-i \frac{k_z r^2}{2R(z)}}, \quad (2.1.17)$$

where  $\Psi(r, \theta)$  is a scalar wave function describing the transverse profile of the wave. Using the paraxial approximation  $R(z) \gg r$ , the general transverse wave equation in cylindrical coordinate can be written as



$$\left[ \nabla_t^2 + k_t^2 - \frac{4(x^2 + y^2)}{\omega(z)^4} \right] \Psi(r, \theta) = 0. \quad (2.1.18)$$

Assume that  $\Psi(r, \theta)$  becomes two independent functions  $\Psi(r, \theta) = R(r) \cdot e^{il\theta}$ , then Eq.(2.1.18) can be expressed as

$$\left[ \frac{d^2}{dr^2} + \frac{1}{r} \frac{d}{dr} - \frac{l^2}{r^2} + k_t^2 - \frac{4r^2}{\omega(z)^4} \right] R(r) = 0. \quad (2.1.19)$$

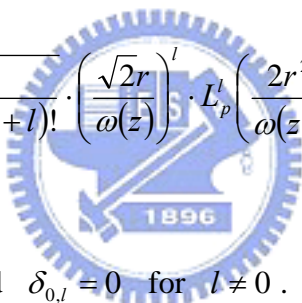
Continuously letting  $R(r) = r^{|l|} \cdot e^{-\frac{r^2}{\omega^2}} F(r)$ , then we can get

$$F'' + \left( \frac{2|l|+1}{r} - 4 \frac{r}{\omega^2} \right) F' + \left( k_t^2 - 4 \frac{|l|+1}{\omega^2} \right) F = 0. \quad (2.1.20)$$

Considering the condition  $t = \frac{2r^2}{\omega^2}$ , the differential equation can be varied as

$$t \cdot \frac{d^2 F}{dt^2} + (|l| + 1 - t) \frac{dF}{dt} + \frac{1}{2} \left[ \frac{\omega^2}{4} k_t^2 - (|l| + 1) \right] F = 0. \quad (2.1.21)$$

Eq. (2.1.21) is similar to the Laguerre polynomial:  $xy'' + (\alpha + 1 - x)y' + py = 0$ , then the eigenvalues are  $k_t^2 = \frac{4}{\omega(z)^2} (2p + |l| + 1)$ , where  $p = 0, 1, 2, \dots$  and  $l = 1, 2, \dots$ . Compare with the eigenvalues in rectangular coordinate, the relation is  $2p + |l| + 1 = m + n + 1$ . As a result, the normalized wave function can be represented as

$$\Psi_{p,l}(r, \theta) = \sqrt{\frac{2p!}{(1 + \delta_{0,l})\pi(p+l)!}} \cdot \left(\frac{\sqrt{2r}}{\omega(z)}\right)^l \cdot L_p^l\left(\frac{2r^2}{\omega(z)^2}\right) \cdot e^{-\frac{r^2}{\omega(z)^2}} \cdot e^{il\theta}, \quad (2.1.22)$$


where  $\delta_{0,l} = 1$  for  $l = 0$  and  $\delta_{0,l} = 0$  for  $l \neq 0$ . In summary, the wave function in cylindrical coordinate can be represented as

$$E(r, \theta, z) = \Psi_{p,l}(r, \theta) \cdot \frac{\omega_0}{\omega(z)} \cdot e^{-ik_z z \frac{r^2}{2(z^2 + z_R^2)}} \cdot e^{-i \left[ kz - (2p + |l| + 1) \tan^{-1} \left( \frac{z}{z_R} \right) \right]}. \quad (2.1.23)$$

Figure 2.1.1 shows HG modes with different index ( $m, n$ ) and standing waves of LG modes with different index ( $l, p$ ). Both of the two modes are the eigenstates of 2D harmonic oscillator in rectangular and cylindrical coordinates respectively. Besides the two special eigenmodes in spherical laser cavity, there should be a general wave function for the cavity in case of some perturbations existing in the system. We will discuss the “generalized coherent

states" in the spherical laser cavity in next section to explain the experimental results between HG and LG beams in some special condition.



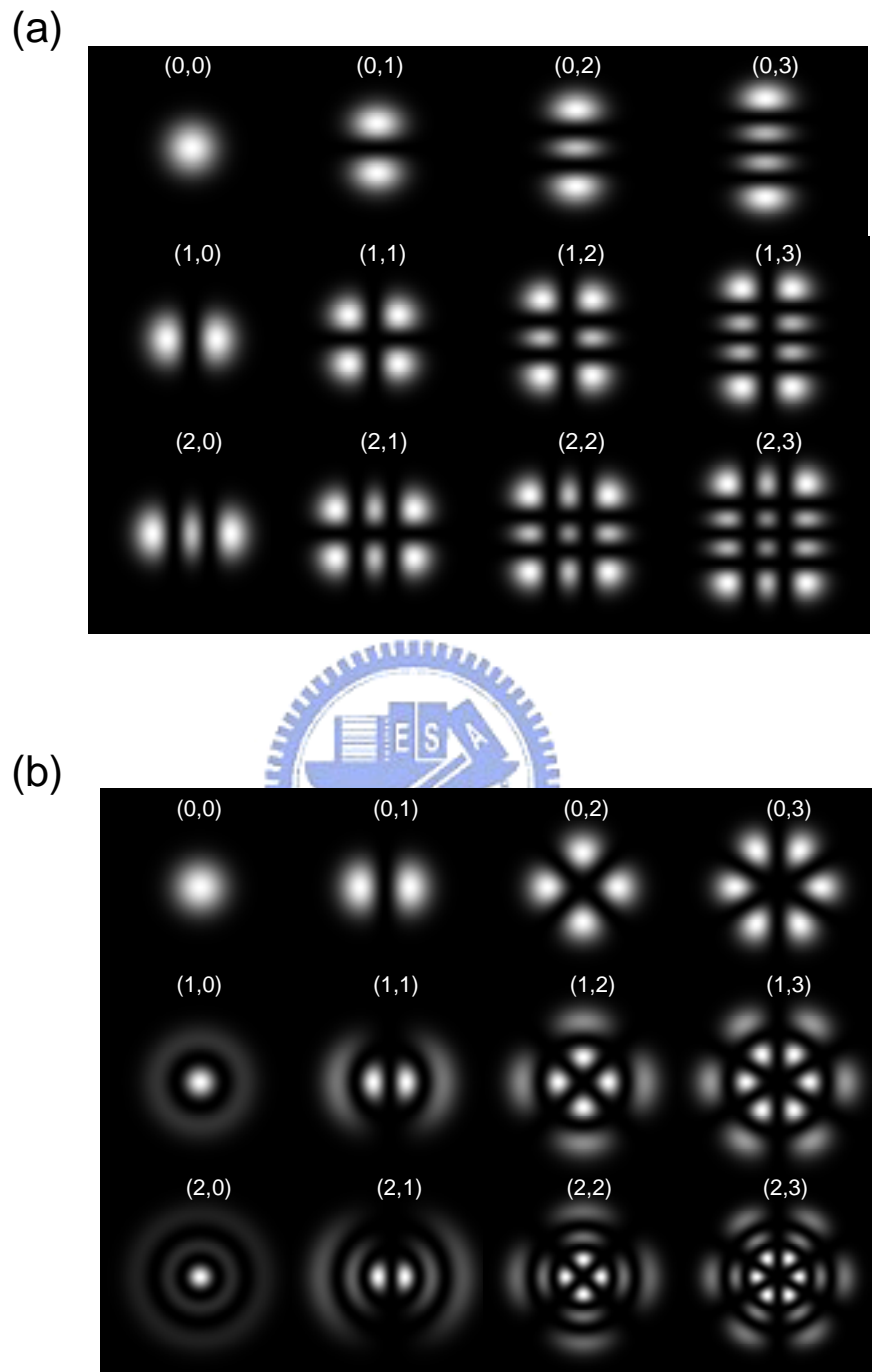


Fig. 2.1.1 (a) Hermite-Gaussian modes with different index  $(m, n)$ . (b) Standing waves of Laguerre-Gaussian modes with different index  $(l, p)$

## 2.2 The Generalized Coherent States:

### Between Hermite-Gaussian and Laguerre-Gaussian modes

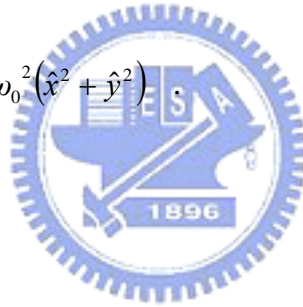
As mentioned above, HG and LG modes are the eigenmodes of the spherical laser cavity.

In this section we will discuss another complete basis, generalized coherent state, which is also the eigenmode between HG and LG modes in the laser cavity. To explain other experimental patterns which are different from HG and LG modes, we need to use the generalized coherent states to be related to the transition from HG modes  $\Phi_{m,n}^{HG}(x, y, z)$  into various experimental modes with different phase factor. Before demonstrating the generalized coherent states, we consider a related problem of harmonic oscillator with a perturbation.

The Hamiltonian of a 2D isotropic harmonic oscillator can be expressed as

$$\hat{H}_0 = \frac{1}{2m} \left( \hat{P}_x^2 + \hat{P}_y^2 \right) + \frac{1}{2} m \omega_0^2 (\hat{x}^2 + \hat{y}^2) \quad (2.2.1)$$

After some definitions,<sup>†</sup>



$$\begin{aligned} \hat{q}_1 &= \sqrt{\frac{m\omega_0}{\hbar}} \hat{x} , \quad \hat{q}_2 = \sqrt{\frac{m\omega_0}{\hbar}} \hat{y} \quad ; \quad \hat{P}_1 = \sqrt{\frac{1}{m\omega_0\hbar}} \hat{P}_x , \quad \hat{P}_2 = \sqrt{\frac{1}{m\omega_0\hbar}} \hat{P}_y \\ \hat{a}_1 &= \frac{1}{\sqrt{2}} (\hat{q}_1 + i\hat{P}_1) , \quad \hat{a}_1^\dagger = \frac{1}{\sqrt{2}} (\hat{q}_1 - i\hat{P}_1) \quad ; \quad \hat{a}_2 = \frac{1}{\sqrt{2}} (\hat{q}_2 + i\hat{P}_2) , \quad \hat{a}_2^\dagger = \frac{1}{\sqrt{2}} (\hat{q}_2 - i\hat{P}_2) \end{aligned} \quad (2.2.2)$$

The Hamiltonian can be written as

$$\hat{H}_0 = \frac{1}{2} \hbar \omega_0 \left( \hat{P}_1^2 + \hat{P}_2^2 + \hat{q}_1^2 + \hat{q}_2^2 \right) = \hbar \omega_0 \left( \hat{a}_1^\dagger \hat{a}_1 + \hat{a}_2^\dagger \hat{a}_2 + 1 \right) . \quad (2.2.3)$$

In order to simplify the complex mathematics, here we use some operators to make the

process smoothly:

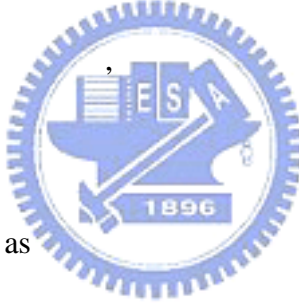
$$\hat{J}_x = \frac{1}{2}(\hat{a}_1^\dagger \hat{a}_2 + \hat{a}_2^\dagger \hat{a}_1), \quad \hat{J}_y = \frac{1}{2}(\hat{a}_1^\dagger \hat{a}_2 - \hat{a}_2^\dagger \hat{a}_1), \quad \hat{J}_z = \frac{1}{2}(\hat{a}_1^\dagger \hat{a}_1 - \hat{a}_2^\dagger \hat{a}_2). \quad (2.2.4)$$

Therefore, the operators have some characteristics as following:

$$\begin{aligned} \hat{J}_z |n_1, n_2\rangle &= \left( \frac{n_1 - n_2}{2} \right) |n_1, n_2\rangle \\ \hat{J}^2 &= \hat{J}_x^2 + \hat{J}_y^2 + \hat{J}_z^2 \\ \hat{J}^2 |n_1, n_2\rangle &= \left( \frac{n_1 + n_2}{2} \right) \left( \frac{n_1 + n_2}{2} + 1 \right) |n_1, n_2\rangle \end{aligned} \quad (2.2.5)$$

Replacing the index of the state  $|n_1, n_2\rangle$  with

$$\begin{aligned} j &= \frac{n_1 + n_2}{2}, \quad m = \frac{n_1 - n_2}{2} \\ n_1 &= j + m, \quad n_2 = j - m \end{aligned} \quad (2.2.6)$$



equation (2.2.5) can be reduced as

$$\begin{aligned} \hat{J}^2 |j, m\rangle &= j(j+1) |j, m\rangle \\ \hat{J}_z |j, m\rangle &= m |j, m\rangle \end{aligned} \quad (2.2.7)$$

Consider a charged particle in a harmonic oscillator potential and is applied a uniform magnetic field in the  $z$  direction. The Hamiltonian is expressed as

$$\begin{aligned} \hat{H} &= \frac{1}{2m}(\hat{P}_x^2 + \hat{P}_y^2) + \frac{1}{2}m(\omega_0^2 + \omega_L^2)(\hat{x}^2 + \hat{y}^2) + \omega_L(\hat{x}\hat{P}_y - \hat{y}\hat{P}_x) \\ &= \hbar\sqrt{\omega_0^2 + \omega_L^2}(\hat{a}_1^\dagger \hat{a}_1 + \hat{a}_2^\dagger \hat{a}_2 + 1) + 2\hbar\omega_L \hat{J}_y \end{aligned} \quad (2.2.8)$$

The operator  $\hat{J}_y$  in equation (2.2.8) share the same eigenstate of  $\hat{H}_0$ , so we should use

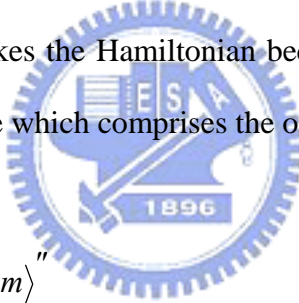
some techniques of unitary transformation to solve this problem. After the unitary transformation twice as

$$\begin{aligned}\hat{U} &= e^{-i\frac{\pi}{2}\hat{J}_z} \Rightarrow \hat{H}' = \hat{U}\hat{H}\hat{U}^\dagger & , \\ \hat{V} &= e^{\mp i\frac{\pi}{2}\hat{J}_y} \Rightarrow \hat{H}'' = \hat{V}\hat{H}'\hat{V}^\dagger = \hat{V}\hat{U}\hat{H}\hat{U}^\dagger\hat{V}^\dagger\end{aligned}\quad (2.2.9)$$

the new Hamiltonian can be written as

$$\begin{aligned}\hat{H}' &= \hbar\sqrt{\omega_0^2 + \omega_L^2}\left(\hat{a}_1^\dagger\hat{a}_1 + \hat{a}_2^\dagger\hat{a}_2 + 1\right) + 2\hbar\omega_L\hat{J}_x \\ \hat{H}'' &= \hbar\sqrt{\omega_0^2 + \omega_L^2}\left(\hat{a}_1^\dagger\hat{a}_1 + \hat{a}_2^\dagger\hat{a}_2 + 1\right) \pm 2\hbar\omega_L\hat{J}_z\end{aligned}\quad (2.2.10)$$

The unitary transformation makes the Hamiltonian become a new one, so the corresponding eigenstate become the new state which comprises the old eigenstate with degeneracy



$$\hat{H}''|j,m\rangle'' = \hat{V}\hat{U}\hat{H}\hat{U}^\dagger\hat{V}^\dagger|j,m\rangle''$$

$$\hat{U}^\dagger\hat{V}^\dagger|j,m\rangle'' = \sum_{m'=-j}^j e^{i\frac{\pi}{2}m'} \cdot d_{m',m}^j\left(\mp\frac{\pi}{2}\right)|j,m'\rangle\quad (2.2.11)$$

where  $d_{m',m}^j\left(\mp\frac{\pi}{2}\right)$  is the so-called Wigner  $d$ -coefficient [4-5]. If the  $d$ -coefficient can be known, the problem can be solved exactly. Therefore we want to extract the  $d$ -coefficient following. The  $d$ -coefficient can be expressed as  $d_{m',m}^j(\beta) = \langle j,m' | e^{-i\beta\hat{J}_y} | j,m \rangle$ , here we use the relations:

$$|n_1, n_2\rangle = \frac{(\hat{a}_1^\dagger)^{n_1}(\hat{a}_2^\dagger)^{n_2}}{\sqrt{n_1!n_2!}}|0,0\rangle\quad (2.2.12)$$

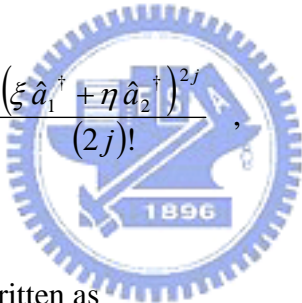
then

$$|j, m\rangle = \frac{(\hat{a}_1^\dagger)^{j+m}(\hat{a}_2^\dagger)^{j-m}}{\sqrt{(j+m)!(j-m)!}} |0,0\rangle \quad . \quad (2.2.13)$$

The generating function is applied to find out the  $d$ -coefficient:

$$\begin{aligned} G(\xi, \eta) &= \langle j, m' | e^{-i\beta \hat{J}_y} \sum_{m=-j}^j \frac{(\xi \hat{a}_1^\dagger)^{j+m}(\eta \hat{a}_2^\dagger)^{j-m}}{(j+m)!(j-m)!} |0,0\rangle \\ &= \sum_{m=-j}^j \frac{(\xi)^{j+m}(\eta)^{j-m}}{\sqrt{(j+m)!(j-m)!}} d_{m',m}^j(\beta) \end{aligned} \quad . \quad (2.2.14)$$

It is worthy to note the binomial term in equation (2.2.14)

$$\sum_{m=-j}^j \frac{(\xi \hat{a}_1^\dagger)^{j+m}(\eta \hat{a}_2^\dagger)^{j-m}}{(j+m)!(j-m)!} = \frac{(\xi \hat{a}_1^\dagger + \eta \hat{a}_2^\dagger)^{2j}}{(2j)!} \quad , \quad (2.2.15)$$


then equation (2.2.14) can be written as

$$\begin{aligned} G(\xi, \eta) &= \frac{1}{(2j)!} \langle j, m' | e^{-i\beta \hat{J}_y} (\xi \hat{a}_1^\dagger + \eta \hat{a}_2^\dagger)^{2j} |0,0\rangle \\ &= \frac{1}{(2j)!} \langle j, m' | \left[ e^{-i\beta \hat{J}_y} (\xi \hat{a}_1^\dagger + \eta \hat{a}_2^\dagger) e^{-i\beta \hat{J}_y} \right]^{2j} |0,0\rangle \end{aligned} \quad . \quad (2.2.16)$$

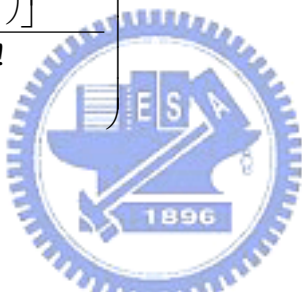
Using the important relations:

$$\begin{aligned} e^{-i\beta \hat{J}_y} \hat{a}_1^\dagger e^{i\beta \hat{J}_y} &= \cos\left(\frac{\beta}{2}\right) \hat{a}_1^\dagger + \sin\left(\frac{\beta}{2}\right) \hat{a}_2^\dagger \\ e^{-i\beta \hat{J}_y} \hat{a}_2^\dagger e^{i\beta \hat{J}_y} &= -\sin\left(\frac{\beta}{2}\right) \hat{a}_1^\dagger + \cos\left(\frac{\beta}{2}\right) \hat{a}_2^\dagger \end{aligned} \quad , \quad (2.2.17)$$

The generating function is simplified to

$$G(\xi, \eta) = \frac{\left[ \xi \cos\left(\frac{\beta}{2}\right) - \eta \sin\left(\frac{\beta}{2}\right) \right]^{j+m'} \left[ \xi \sin\left(\frac{\beta}{2}\right) + \eta \cos\left(\frac{\beta}{2}\right) \right]^{j-m'}}{\sqrt{(j+m')!(j-m')!}} \quad . \quad (2.2.18)$$

Again using the binomial expansion, equation (2.2.18) is written as

$$G(\xi, \eta) = \sqrt{(j+m')!(j-m')!} \left( \sum_{\nu=0}^{j+m'} \frac{\left[ \xi \cos\left(\frac{\beta}{2}\right) \right]^{j+m'-\nu} \left[ -\eta \sin\left(\frac{\beta}{2}\right) \right]^{-\nu}}{(j+m'-\nu)! \nu!} \times \left( \sum_{u=0}^{j-m'} \frac{\left[ \xi \sin\left(\frac{\beta}{2}\right) \right]^u \left[ \eta \cos\left(\frac{\beta}{2}\right) \right]^{j-m'-u}}{(j-m'-u)! u!} \right) \right) \quad (2.2.19)$$


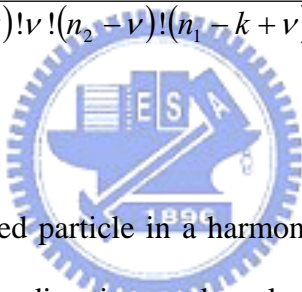
After some complicated algebra, equation (2.2.19) is shown as

$$G(\xi, \eta) = \sum_{m=-j}^j \sum_{\nu} \sqrt{(j+m')!(j-m')!} (-1)^{\nu} \frac{(\xi)^{j+m} (\eta)^{j-m} \left[ \cos\left(\frac{\beta}{2}\right) \right]^{2j-m+m'-2\nu} \left[ \sin\left(\frac{\beta}{2}\right) \right]^{m-m'+2\nu}}{(j+m'-\nu)! \nu! (j-m-\nu)! (m-m'+\nu)!} \quad . \quad (2.2.20)$$

Finally, the  $d$ -coefficient can be extracted by comparing equation (2.2.14) and (2.2.20):

$$d_{m',m}^j(\beta) = \sqrt{(j+m')!(j-m')!(j+m)!(j-m)!} \times \left( \sum_{\nu=\max[0,m'-m]}^{\min[j-m,j+m']} (-1)^\nu \times \frac{\left[\cos\left(\frac{\beta}{2}\right)\right]^{2j-(m-m'+2\nu)} \left[\sin\left(\frac{\beta}{2}\right)\right]^{(m-m'+2\nu)}}{(j+m'-\nu)!\nu!(j-m-\nu)!(m-m'+\nu)!} \right) \quad (2.2.21)$$

Replacing the  $|j, m\rangle$  state by  $|n_1, n_2\rangle$ , the  $d$ -coefficient becomes:

$$d_{k-\frac{(n_1+n_2)}{2}, \frac{n_1-n_2}{2}}^{\frac{n_1+n_2}{2}}(\beta) = \sqrt{(k)!(n_1+n_2-k)!(n_1)!(n_2)!} \times \left( \sum_{\nu=\max[0,k-n_1]}^{\min[n_2,k]} (-1)^\nu \times \frac{\left[\cos\left(\frac{\beta}{2}\right)\right]^{n_2+k-2\nu} \left[\sin\left(\frac{\beta}{2}\right)\right]^{n_1-k+2\nu}}{(k-\nu)!\nu!(n_2-\nu)!(n_1-k+\nu)!} \right) \quad (2.2.22)$$


Finally the problem of a charged particle in a harmonic oscillator potential and is applied a uniform magnetic field in the  $z$  direction can be solved exactly. The wave function is

$$\psi_{n_1, n_2}(x, y) = e^{-i\frac{(n_1+n_2)}{2}\alpha} \sum_{k=0}^{n_1+n_2} e^{ik\alpha} \times d_{k-\frac{(n_1+n_2)}{2}, \frac{n_1-n_2}{2}}^{\frac{n_1+n_2}{2}}(\beta) \times \Phi_{k, (n_1+n_2)-k}(x, y) \quad (2.2.23)$$

where

$$\Phi_{n_1, n_2}(x, y) = \langle x, y | n_1, n_2 \rangle = \left[ \frac{1}{\sqrt{2^{n_1} n_1! \sqrt{\pi}}} \left( \frac{m\omega}{\hbar} \right)^{\frac{1}{4}} \cdot \exp\left(-\frac{m\omega}{2\hbar} x^2\right) \cdot H_{n_1}\left(\sqrt{\frac{m\omega}{\hbar}} x\right) \right] \times \left[ \frac{1}{\sqrt{2^{n_2} n_2! \sqrt{\pi}}} \left( \frac{m\omega}{\hbar} \right)^{\frac{1}{4}} \cdot \exp\left(-\frac{m\omega}{2\hbar} y^2\right) \cdot H_{n_2}\left(\sqrt{\frac{m\omega}{\hbar}} y\right) \right] \quad (2.2.24)$$

and  $\alpha = \beta = \frac{\pi}{2}$ . Figure 2.2.1 depicts the wave function with different  $(n_1, n_2)$  of a charged particle in a harmonic oscillator with uniform magnetic field. It is obvious to understand that a charged particle in a harmonic oscillator with uniform magnetic field leads to the eigenmodes to be LG modes which comprise degenerate HG modes with special  $d$ -coefficients and other phase. In general, equation (2.2.23) and (2.2.24) demonstrate the connection between HG and LG modes of harmonic oscillator. With manipulating the parameters  $\alpha$  and  $\beta$ , various wave functions between HG and LG modes can be demonstrated arbitrarily.

The problem which is solved exactly by use of the unitary transformation and complicated algebra can be analogous to the eigenstates in the spherical laser cavity. Because it is well known that the paraxial wave equation for the spherical resonator has the identical form with the Schrödinger equation for the 2D harmonic oscillator. The wave function for the paraxial field in the spherical laser resonator can be expressed as HG function with Cartesian symmetry or LG function with cylindrical symmetry. The normalized wave function of the HG mode for a spherical cavity with longitudinal index  $l$  and transverse index  $m$  and  $n$  in Cartesian coordinates  $(x, y, z)$  is given by

$$\Phi_{m,n,l}^{(HG)}(x, y, z) = \Phi_{m,n}(x, y, z) e^{i(m+n+1) \tan^{-1}\left(\frac{z}{z_R}\right)} e^{-i\left(\frac{\pi z}{L}\right)[l+(m+n+1)\Omega]\left[\frac{x^2+y^2}{2(z^2+z_R^2)}+1\right]},$$

where

$$\Phi_{m,n}(x, y, z) = \frac{1}{\sqrt{2^{m+n+1} \pi m! n!}} \frac{1}{w(z)} H_m\left(\frac{\sqrt{2}x}{w(z)}\right) H_n\left(\frac{\sqrt{2}y}{w(z)}\right) \exp\left[-\frac{x^2+y^2}{w(z)^2}\right]. \quad (2.2.25)$$

The normalized wave function of LG mode with longitudinal index  $s$ , transverse radial index  $p$ , and transverse azimuthal index  $l$  in cylindrical coordinates  $(\rho, \phi, z)$  is given by

$$\Psi_{p,l,s}(\rho, \phi, z) = e^{il\phi} \Phi_{p,l,s}(\rho, z),$$

where

$$\begin{aligned} \Phi_{p,l,s}(\rho, z) = & \sqrt{\frac{2 p!}{\pi (p+|l|)!}} \frac{1}{w(z)} \left( \frac{\sqrt{2}\rho}{w(z)} \right)^{|l|} L_p^{|l|} \left( \frac{2\rho^2}{w(z)^2} \right) \exp \left[ -\frac{\rho^2}{w(z)^2} \right] \\ & \times \exp \left\{ -ik_{p,l,s} z \left[ 1 + \frac{\rho^2}{2(z^2 + z_R^2)} \right] \right\} \exp \left[ i(2p+|l|+1) \tan^{-1} \left( \frac{z}{z_R} \right) \right], \end{aligned} \quad (2.2.26)$$

$w(z) = w_o \sqrt{1 + (z/z_R)^2}$ ,  $w_o$  is the beam radius at the waist, and  $z_R$  is the Rayleigh range.

$H_{m,n}(\cdot)$  and  $L_p^l(\cdot)$  are the Hermite polynomials and associated Laguerre polynomials,

respectively. The factor  $\Omega = \Delta f_T / \Delta f_L$ ,  $\Delta f_L = c/2L$  is the longitudinal mode spacing and

$\Delta f_T$  is the transverse mode spacing. Therefore,  $k_{p,l,s}$  is the wave number and  $\tan^{-1}(z/z_R)$

is the Gouy phase. In terms of the effective length  $L$ , the wave number  $k_{p,l,s}$  is given by

$k_{p,l,s}L = \pi[s + (2p+|l|)\Omega]$ . Here we applied the same method which is mentioned above to

connect HG and LG in spherical cavity. Equation (2.2.23) represents the general wave

function, so we fix  $\beta = \frac{\pi}{2}$  and manipulate  $\alpha$  to get the various wave functions which are

defined as GCSs between HG and LG modes. Figure 2.2.2 shows the numerical patterns of the GCSs with different phase factor and different order. As shown in Fig. 2.2.2, it exhibits that the phase factor  $\alpha$  plays an important role for the GCSs to transform from the HG modes to the LG modes in different order. On the one hand the GCSs represent to the HG modes when the phase factor is equal to zero, and on the other the GCSs represent to the LG modes when the phase factor is equal to  $\pi/2$ . It can be seen distinctly that HG modes steadily convert to LG modes by controlling the phase factor precisely.

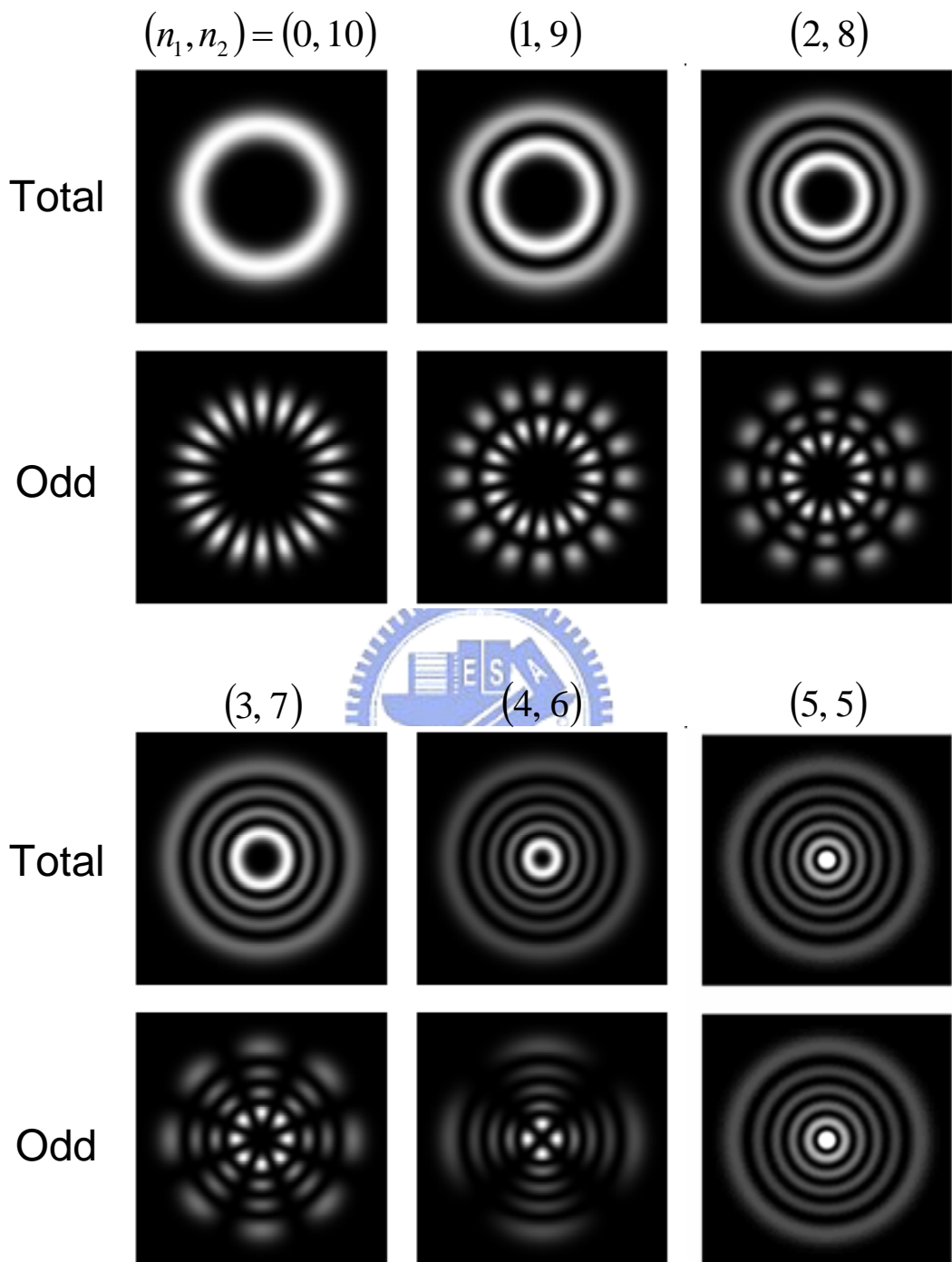


Fig. 2.2.1 The wave functions with different  $(n_1, n_2)$  of a charged particle in a harmonic oscillator with uniform magnetic field.

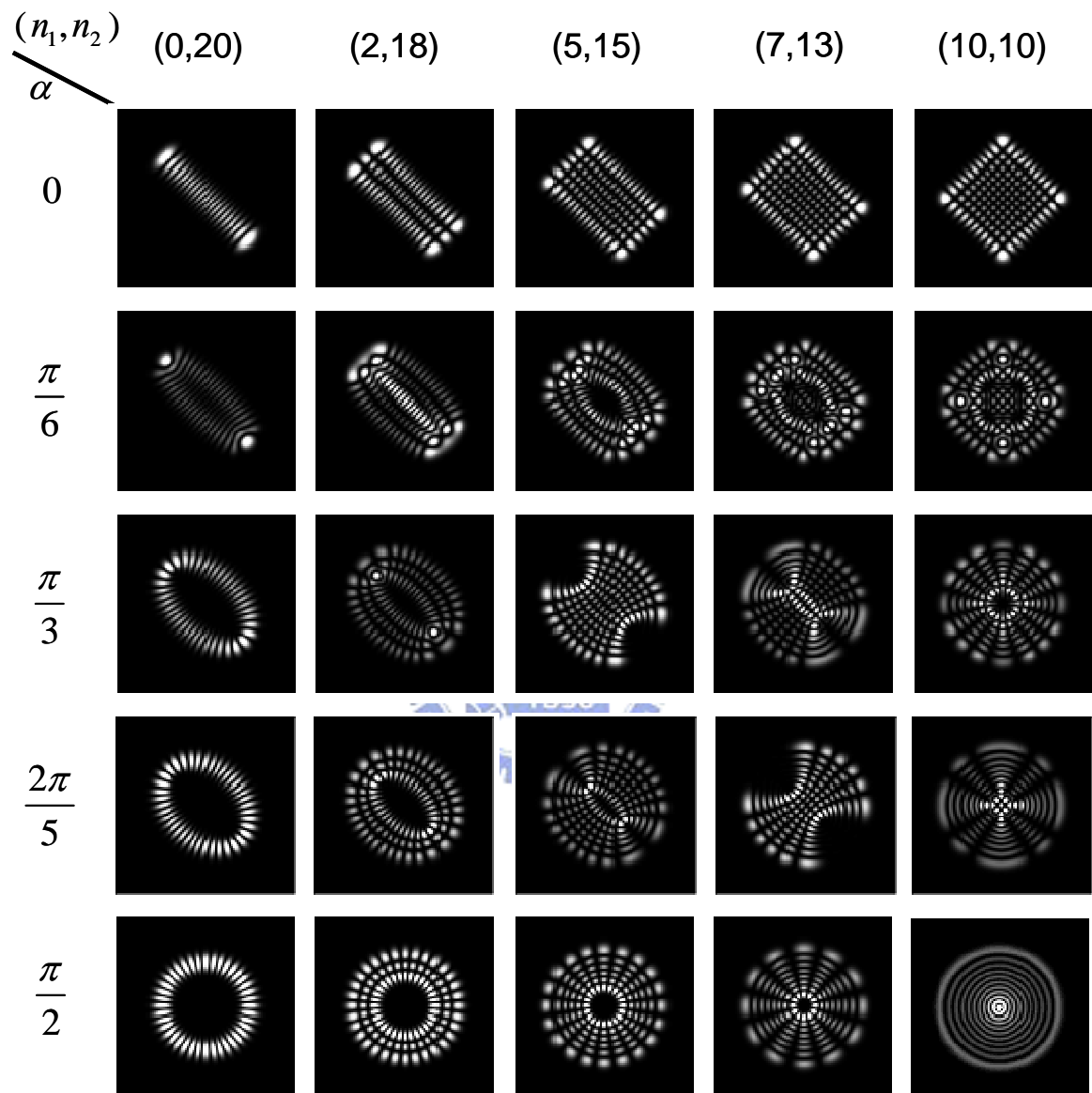


Fig. 2.2.2 Numerical patterns of the GCSs with different phase factor and different order.

## 2.3 Generation of Polarization-entangled Optical Coherent Waves

Over the past few years a considerable number of studies have been made on the coherent wave properties in mesoscopic physics. Many researches have been focused on phase singularities in scalar fields, known as wave front dislocations, such as quantum ballistic transport [6], vortex lattices in superconductors [7], quantum Hall effects [8], linear and nonlinear optics [9-10] and Bose-Einstein condensates [11-12]. In recent years, polarization singularities, known as wave front disclinations, are also noticed in modern physics [13-15]. As mentioned by Freund [16], there are two types of singularities of the polarization vectors of paraxial optical beams: vector singularities and Stokes singularities. Vector singularities are isolated, stationary points in a plane at which the orientation of the electric vector of a linearly polarized vector field becomes undefined. The nature of the vector singularities has been studied in coherent optical waves with the correlated behavior of spatial structures and polarization states [17-20]. The experimental results reveal the importance of vector singularities with the coherent polarization vector field from a highly isotropic microchip laser system [21].

Currently, a diode-pumped microchip laser has been employed to perform analogous studies of coherent phenomenon in scalar waves [22-23]. The experimental polarization vector field is found to be made up of two linearly polarized modes with different spatial structures that are phase synchronized to a single frequency. With the pump source of ring-shaped profile, the high order entangled transverse modes constructed by the polarization-resolved patterns are found to lack of variety and manipulation in microchip laser cavity. To overcome the weakness of operation, in this experiment we demonstrate the two important configurations instead of the doughnut pump profile to get various kinds of polarization-entangled patterns. One of the configurations is off-axis focused pumping profile, and the other is on-axis circular pumping. Consequently, the complex transverse modes can

be differentiated into four types: square pattern, hyperbolic pattern, elliptic pattern, and circular pattern. More noteworthy is that all types of the polarization-entangled patterns can be well analyzed with the generalized coherent states.

With the relation between pumping position and the phase factor in the overlap function of intensity distribution and pumping distribution, we can manipulate various kinds of polarization-entangled patterns in the highly isotropic resonator. For that reason, the formation of complex singularities can be clearly represented with the connection between theoretical analysis and experimental results.



### 2.3.1 Experimental Setup and Results

In this experiment, the laser system is a diode-pumped Nd:YVO<sub>4</sub> microchip laser and the resonator configuration is shown in Fig. 2.3.1. The laser gain medium was a c-cut 2.0-at. % Nd:YVO<sub>4</sub> crystal with a length of 2 mm. One side of the Nd:YVO<sub>4</sub> crystal was coated for partial reflection at 1064nm. The radius of curvature of the cavity mirror is R=10 mm and its reflectivity is 99.8% at 1064nm. The pump source was an 809 nm fiber-coupled laser diode with a core diameter of 100 $\mu$ m, a numerical aperture of 0.16, and a maximum output power of 1W. A focusing lens with 20 mm focal length and 90% coupling efficiency was used to reimaging the pump beam into the laser crystal. Since the YVO<sub>4</sub> crystal belongs to the group of oxide compounds crystallizing in a Zircon structure with tetragonal space group, the Nd-doped YVO<sub>4</sub> crystals show strong polarization dependent fluorescence emission due to the anisotropic crystal field. The fourfold symmetry axis of the YVO<sub>4</sub> crystal is the crystallographic c axis; perpendicular to this axis are the two indistinguishable a and b axes. Therefore, the Nd: YVO<sub>4</sub> crystal is precisely cut along the c axis for high-level transverse isotropy. It is practical to note that our gain medium is different from the conventional Nd: YVO<sub>4</sub> crystals that are cut along the a axis to use the largest stimulated emission cross section for lowering the lasing threshold. To measure the transverse far-field pattern, the output beam was directly projected into the CCD camera. Figure 1 shows the scheme of the highly isotropic laser system in this work. All of the experimental modes are preserved from the near-field to the far-field patterns because they are pure transverse modes which correspond to the same Gouy phase.

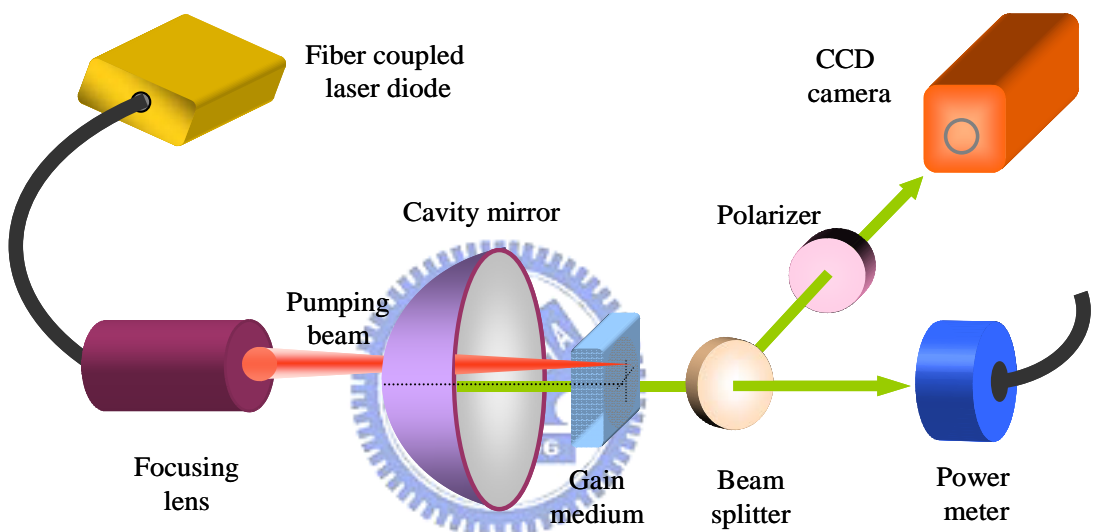


Fig. 2.3.1 Experimental setup for the generation of polarization-entangled transverse modes with off-axis pumping scheme in a highly isotropic diode-pumped microchip laser.

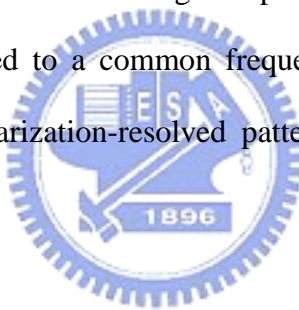
Experimental results demonstrate that the transverse patterns were localized on the elliptic orbits when we used an output coupler with the reflectivity of 98% in the laser cavity [17-18]. However, the transverse patterns were usually the extended structures restricted by the hyperbolic caustics when we used an output coupler with the reflectivity of 99%. Above-mentioned results were all manifested with the pump source of ring-shaped profile. In this experiment we demonstrate the off-axis focused configuration to get the first three kinds of polarization-entangled patterns: square pattern, hyperbolic pattern, and elliptic pattern which are shown in Fig. 2.3.2 (a)-(c). With controlling the pumping position  $(x_0, y_0)$ , the square, hyperbolic, and elliptic pattern can be generated according to the pumping positions which are equal to  $(-50\mu m, 63\mu m)$ ,  $(-140\mu m, 20\mu m)$ , and  $(-137\mu m, 61\mu m)$ , respectively.

The radial distance of the pumping beam  $r_0 = \sqrt{x_0^2 + y_0^2}$  determines the lasing mode size.

Here the radial distances of pumping beam of the square, hyperbolic, and elliptic pattern are 80, 140, and  $150\mu m$ , respectively. Consistently the mode sizes of the three experimental transverse modes are 95, 139, and  $131\mu m$ , respectively. By use of the ring-pump profile in the past, we can generate the hyperbolic pattern which is unstable due to the environmental disturbances. To our knowledge, this is the first time to employ the off-axis pumping to generate the polarization-entangled states which are respectably stable with highly isotropic laser system. Figure 2.3.2 (d) shows the circular pattern which can be generated with the on-axis defocused pumping scheme. The on-axis pumping provides a good symmetry to generate the stable circular modes. It can be seen that the formation of the stationary polarization-entangled mode is primarily dependent on the overlap between the pump intensity and the lasing mode distribution. This is consistent with the fact that the cavity mode with the biggest overlap of the gain region will dominate the lasing process. Accordingly, a significant finding is that controlling the pumping approach and pumping position can straightforwardly manipulate the generation of various stationary polarization-entangled

modes in the highly isotropic resonator.

For reasons mentioned above, adjusting the pumping beam delicately can generate the lasing modes to be made up of two distinct patterns with orthogonal linear polarization. That is to say, the transverse pattern is linearly polarized, but the polarization is spatially dependent. Although the structures of the polarization-entangled patterns are complex, the transverse modes are still stable and repeatable with the critical pumping approach in highly isotropic laser system. Figure 2.3.3-2.3.6 show the experimental polarization-resolved patterns in the  $45^0$ ,  $90^0$ ,  $135^0$ , and  $180^0$  direction according to the patterns in Fig. 2.3.2 (a)-(d). It is found that the entanglement of the spatial structures and polarization states forms an optical vector field and leads to the transverse patterns to be polarization dependent. The basic essentiality for a vector polarization pattern is that the orthogonal polarization modes with different spatial patterns are phase synchronized to a common frequency. The measurement of the optical spectrum verifies that the polarization-resolved pattern is phase synchronized to a single frequency at 1064 nm.



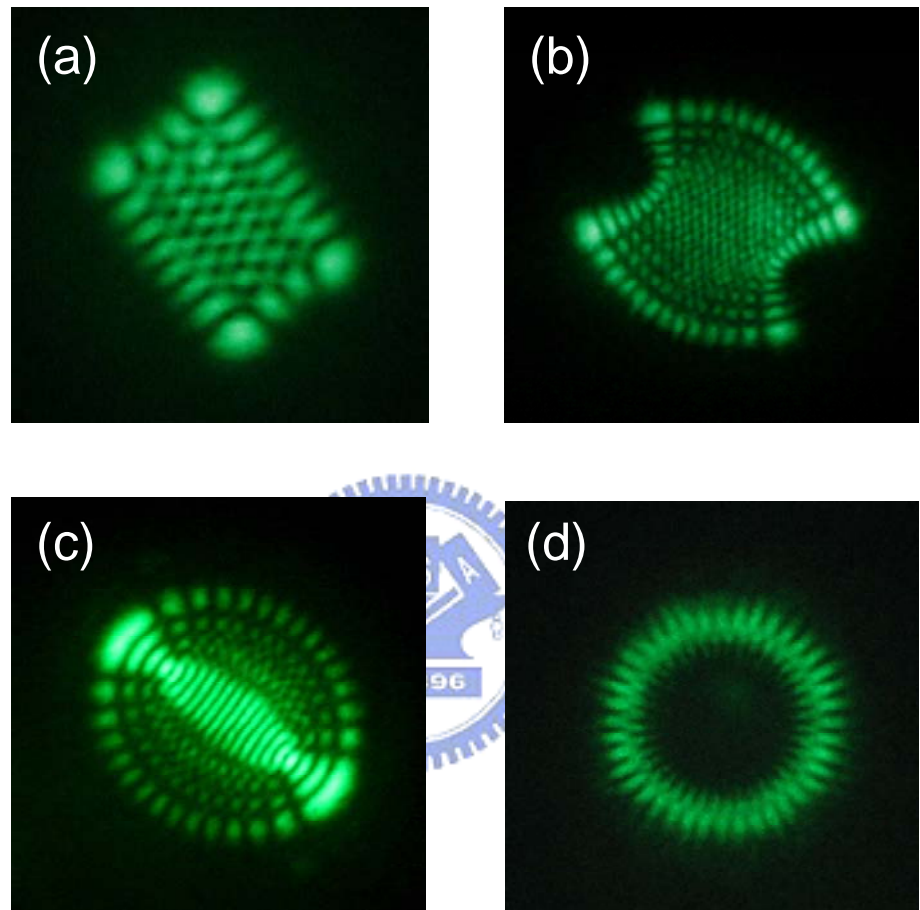


Fig. 2.3.2 Experimental polarization-entangled patterns (a) square pattern, (b) hyperbolic pattern, (c) elliptic pattern, (d) circular pattern.

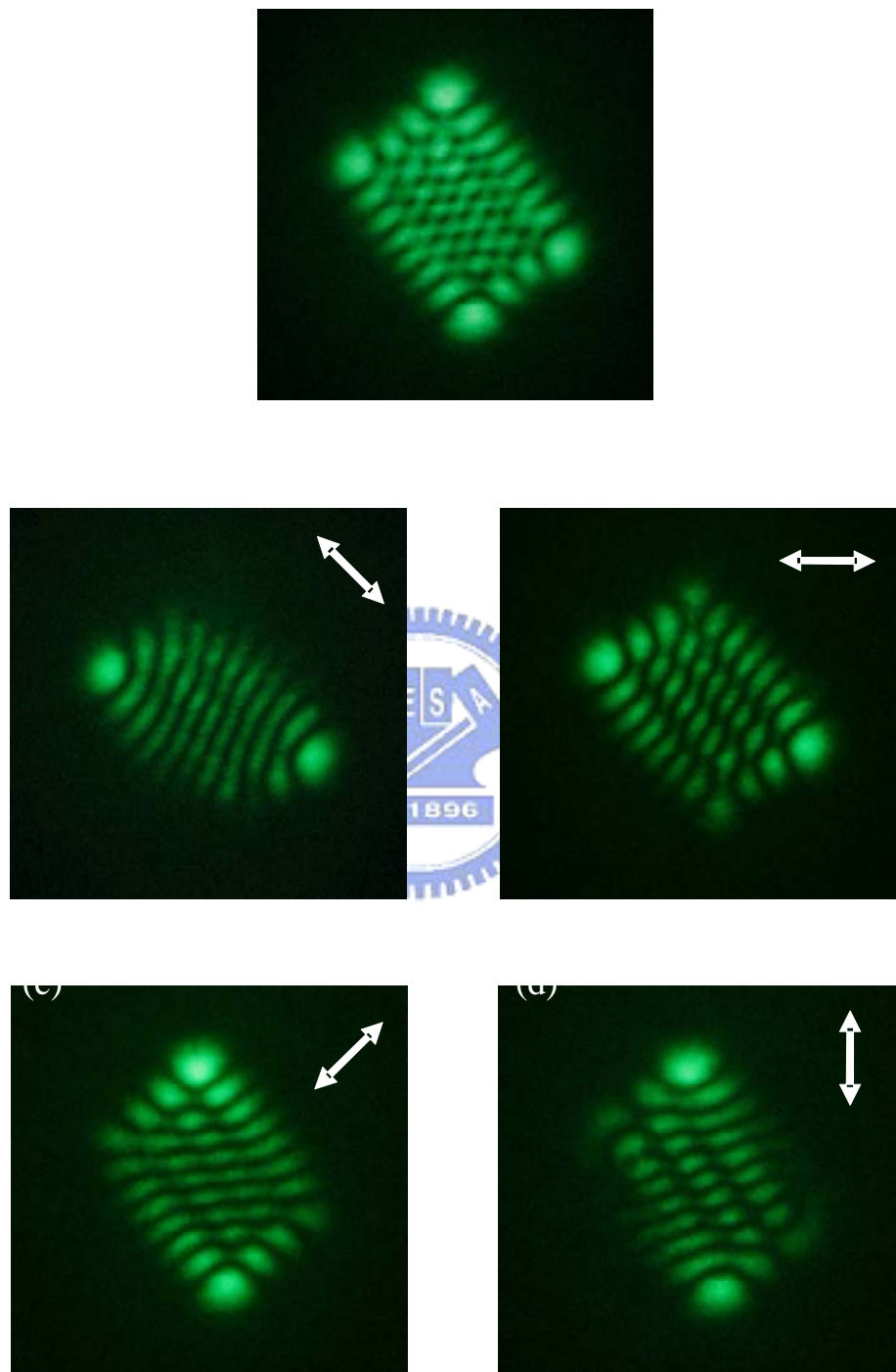


Fig. 2.3.3 Upper: Square experimental polarization-resolved patterns (a)  $45^0$  polarization (b)  $90^0$  polarization (c)  $135^0$  polarization, (d)  $180^0$ polarization

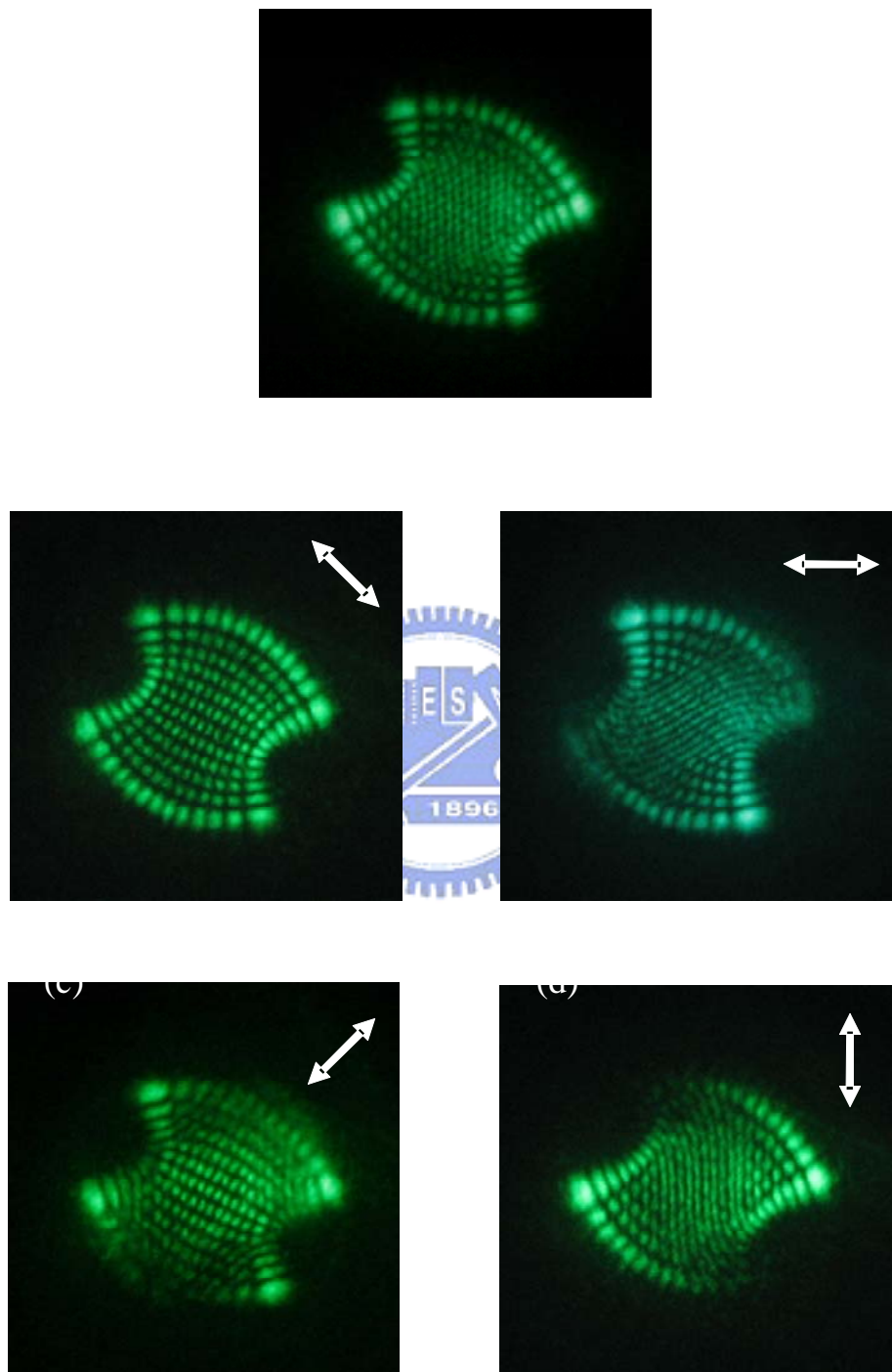


Fig. 2.3.4 Upper: Hyperbolic experimental polarization-resolved patterns (a)  $45^0$  polarization  
(b)  $90^0$  polarization (c)  $135^0$  polarization, (d)  $180^0$ polarization

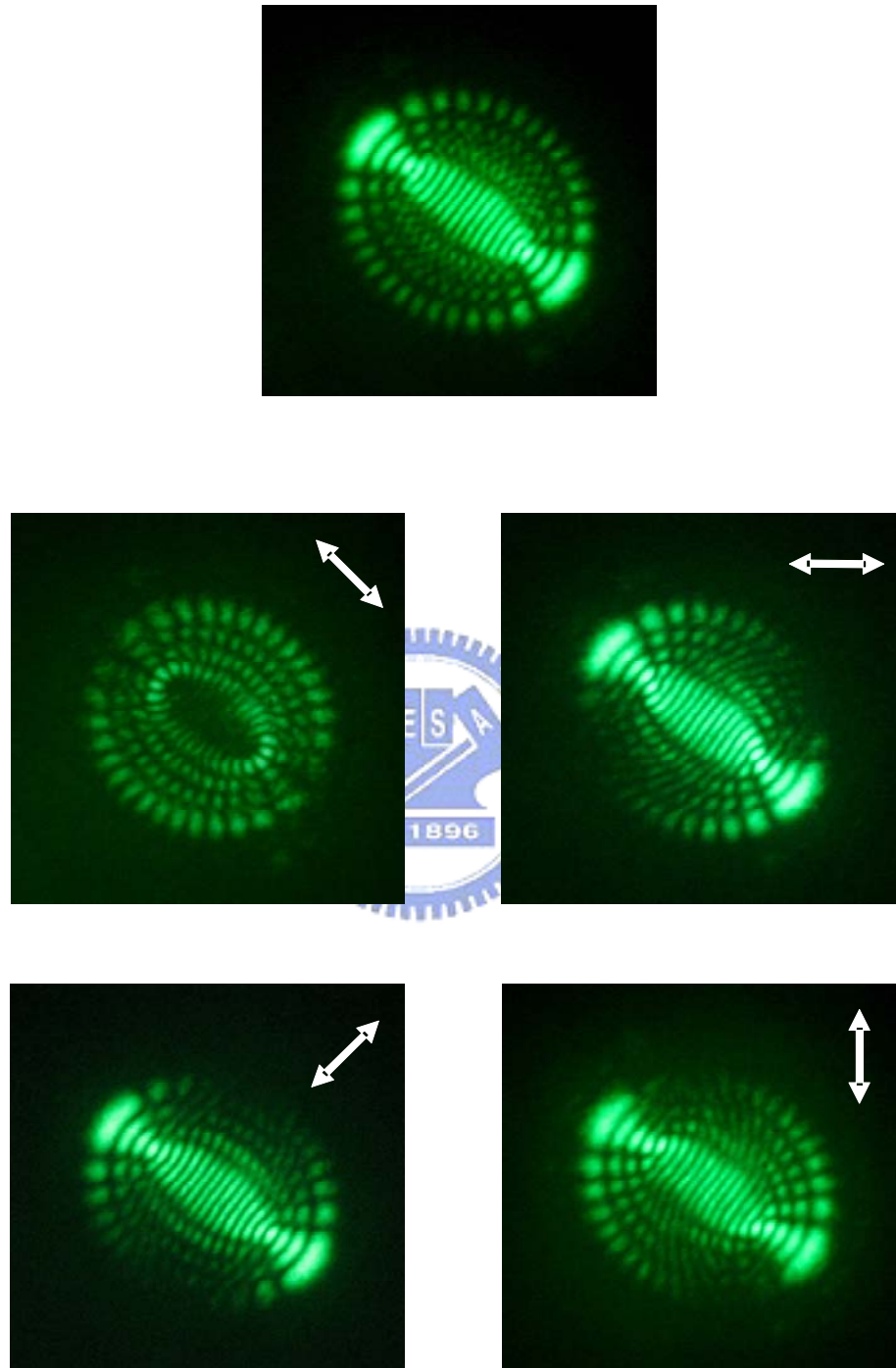


Fig. 2.3.5 Upper: Elliptical experimental polarization-resolved patterns (a)  $45^0$  polarization (b)  $90^0$  polarization (c)  $135^0$  polarization, (d)  $180^0$  polarization

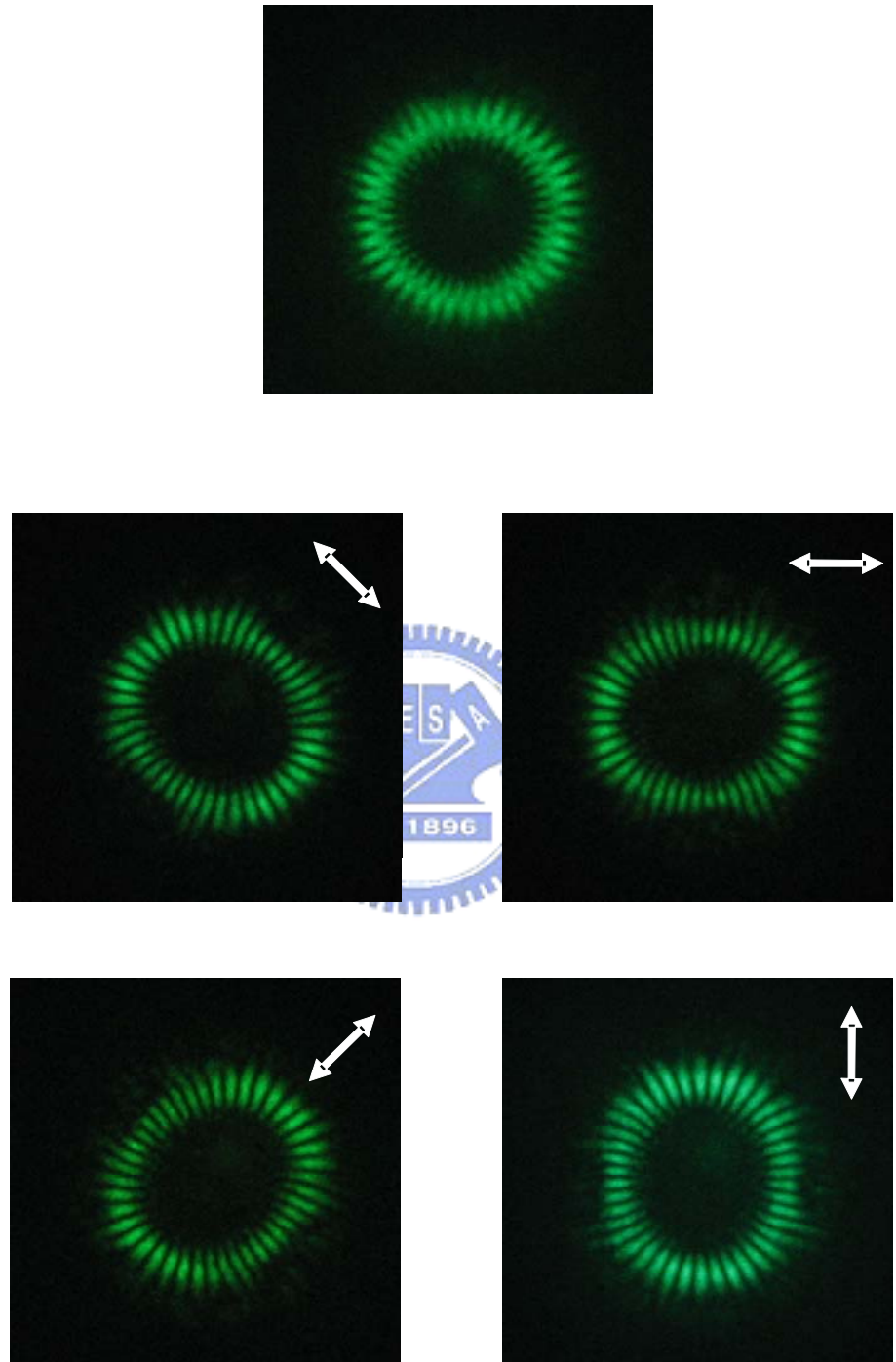


Fig. 2.3.6 Upper: Circular experimental polarization-resolved patterns (a)  $45^0$  polarization (b)  $90^0$  polarization (c)  $135^0$  polarization, (d)  $180^0$  polarization

### 2.3.2 Analytical Wave Functions for Experimental Polarization-entangled Patterns

In terms of the HG modes, the SU(2) coherent states for the elliptic modes are expressed as [24,25]

$$\Psi_N^{CS}(x, y, z; \varphi) = \frac{1}{\sqrt{2^N}} \sum_{K=0}^N \frac{\sqrt{N!}}{\sqrt{(N-K)!} \sqrt{K!}} e^{iK\varphi} \Phi_{N-K, K}^{HG}(x, y, z) \quad (2.3.1)$$

where the parameter  $\varphi$  is the relative phase between various HG modes and is related to the eccentricity of the elliptic trajectory. As shown in a variety of integrable 2D quantum billiard systems, the phase factor  $\varphi$  in the SU(2) coherent states plays a vital role in the quantum-classical correspondence [26,27]. It has been confirmed that the experimental elliptic patterns agree very well with the SU(2) elliptic states [28,29]. However the SU(2) coherent states can only be used to describe the elliptic patterns, we develop the GCSs to be related to the transition from a HG mode  $\Phi_{m,n}^{HG}(x, y, z)$  into various experimental modes with different phase factor. Any LG modes  $\Phi_{p,l}^{LG}(r, \phi, z)$  can be decomposed into a sum of HG modes  $\Phi_{k, n_1 + n_2 - k}^{HG}(x, y)$  with index relations  $n_1 = p$ ,  $n_2 = p + l$  and the Wigner  $d$ -coefficient and phase factor  $\alpha$  equal to  $\pi/2$ :

$$\Phi_{p,l}^{LG}(r, \phi, z) = e^{-\frac{i(n_1+n_2)}{2}\alpha} \sum_{k=0}^{n_1+n_2} e^{ik\alpha} \times d_{\frac{k-(n_1+n_2)}{2}, \frac{n_1-n_2}{2}}(\beta) \times \Phi_{k, (n_1+n_2)-k}^{HG}(x, y, z) \quad (2.3.2)$$

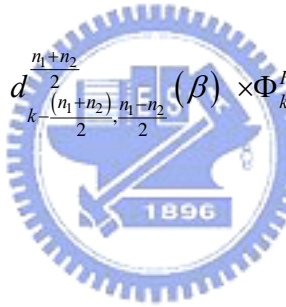
where

$$\Phi_{n_1, n_2}^{HG}(x, y, z) = \frac{1}{\sqrt{2^{n_1+n_2-1} \pi n_1! n_2!}} \frac{1}{w(z)} \cdot H_{n_1} \left[ \frac{\sqrt{2} x}{w(z)} \right] \cdot H_{n_2} \left[ \frac{\sqrt{2} y}{w(z)} \right] \cdot \exp \left[ -\frac{x^2 + y^2}{w(z)} \right] \quad (2.3.3)$$

As mentioned in last section, the GCSs can be written as

$$\psi_{n_1, n_2}(x, y, z) = e^{-i \frac{(n_1+n_2)}{2} \alpha} \sum_{k=0}^{n_1+n_2} e^{i k \alpha} \times d_{\frac{n_1+n_2}{2}, \frac{n_1-n_2}{2}}(\beta) \times \Phi_{k, (n_1+n_2)-k}^{HG}(x, y, z) . \quad (2.3.4)$$

The GCSs in Eq. (2.3.4) exhibit a traveling-wave property. The standing-wave representation of GCSs is given by

$$\begin{bmatrix} \Psi_{n_1, n_2}^{\cos} \\ \Psi_{n_1, n_2}^{\sin} \end{bmatrix} = \left[ \sum_{k=0}^{n_1+n_2} \begin{bmatrix} \cos(k\varphi) \\ \sin(k\varphi) \end{bmatrix} d_{\frac{n_1+n_2}{2}, \frac{n_1-n_2}{2}}(\beta) \times \Phi_{k, (n_1+n_2)-k}^{HG}(x, y, z) \right] ,$$


where the phase factor can be replaced by  $\varphi$ . The GCSs represent a general family to comprise the HG and LG mode families as special cases. More importantly, the superposition of the GCSs with the particular phase factor reveals the patterns of experimental results. It is worthwhile to mention that the present GCSs are intimately correlated to the Ince-Gaussian (IG) beams described by Miguel A. Bandres and Julio C. Gutierrez-Vega [30-33]. Ince-Gaussian beams not only constitute the exact and continuous transition modes between HG and LG beams but also constitute the third complete family of transverse eigenmodes of stable resonator. The transverse structures of IG modes are adjusted by the ellipticity factor, whereas the present GCSs are varied by the additional phase factor. It can be shown that the IG modes can be completely identical to the GCSs with some connection between the ellipticity factor of IG modes and the phase factor of GCSs. However the representation of

GCSs is more convenient and elegant to interpret the present experimental patterns.

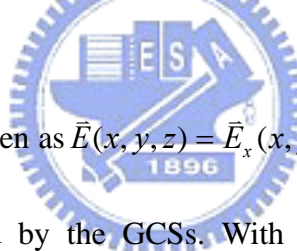
With the discussion of GCSs before, we applied the GCSs to explain the experimental results and found that the observed vector patterns shown in Figs. 2.3.3-2.3.6 can be fittingly described as following wave functions respectively:

$$\vec{E}(x, y, z) = \Psi_{4,7}^{\sin}(x, y, z; 0.048\pi)\hat{x} + \Psi_{4,7}^{\cos}(x, y, z; 0.048\pi)\hat{y} \quad (2.3.6)$$

$$\begin{aligned} \vec{E}(x, y, z) = & \Psi_{5,18}^{\sin}(x, y, z; 0.305\pi)\hat{x} \\ & + [\Psi_{5,18}^{\cos}(x, y, z; 0.305\pi) - \Psi_{5,18}^{\sin}(x, y, z; 0.35\pi)]\hat{y} \end{aligned} \quad (2.3.7)$$

$$\begin{aligned} \vec{E}(x, y, z) = & \Psi_{3,18}^{\sin}(x, y, z; 0.4\pi)\hat{x} \\ & + [\Psi_{3,18}^{\sin}(x, y, z; 0.295\pi) + \Psi_{2,19}^{\cos}(x, y, z; 0.295\pi)]\hat{y} \end{aligned} \quad (2.3.8)$$

$$\vec{E}(x, y, z) = \Psi_{0,21}^{\cos}(x, y, z; 0.48\pi)\hat{x} + \Psi_{0,21}^{\cos}(x, y, z; 0.45\pi)\hat{y} \quad (2.3.9)$$



The wave function can be written as  $\vec{E}(x, y, z) = \vec{E}_x(x, y, z)\hat{x} + \vec{E}_y(x, y, z)\hat{y}$ , where  $\vec{E}_x(x, y, z)$  and  $\vec{E}_y(x, y, z)$  are composed by the GCSs. With the analytical function given in Eqs. (2.3.6)-(2.3.9), Fig. 2.3.7 depicts the numerically reconstructed patterns for the four kinds of the experimental results shown in Fig. 2.3.2. The patterns in Fig. 2.3.7(a) and (d) which are found to be close to HG and LG mode arise from the phase factor slightly different from the phase factor of HG and LG mode. Moreover, the superposition of GCSs with the phase factor appreciably different from the phase factors of HG and LG modes reveals the hyperbolic and elliptic modes shown in Figs. 2.3.7(b) and (c). From this point of view, the phase factor indeed plays a vital role in the GCSs to construct the polarization-entangled modes different from pure HG and LG modes.

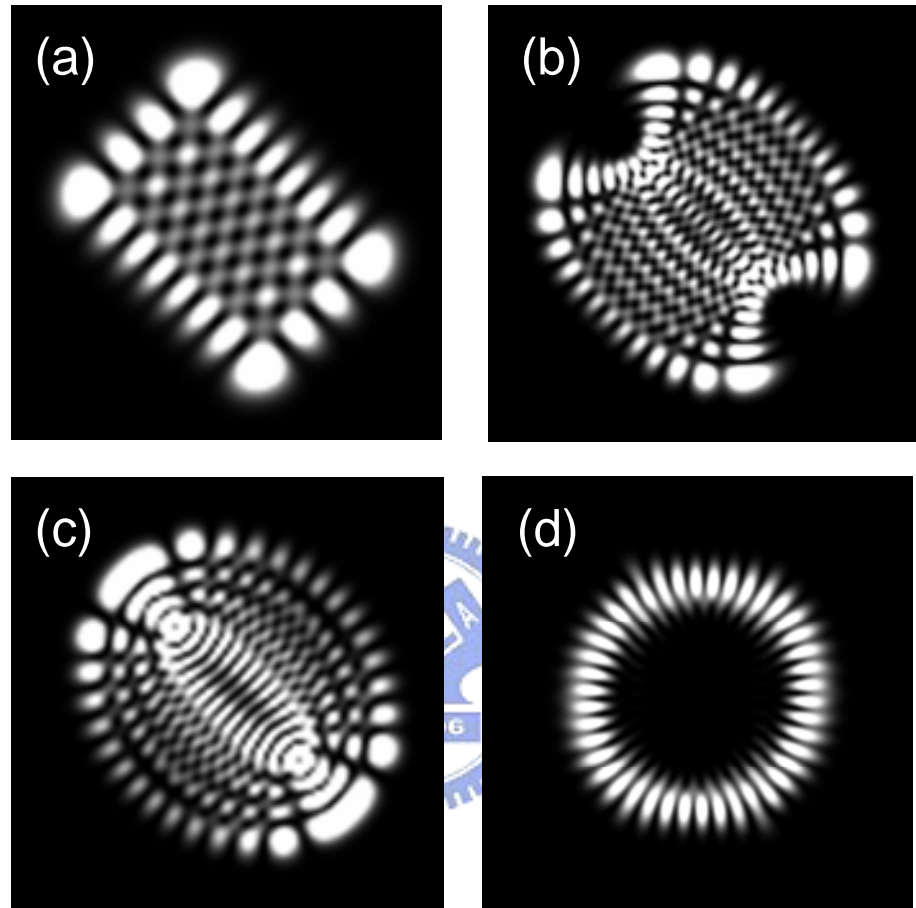


Fig. 2.3.7 Numerically reconstructed patterns for the experimental results shown in Fig. 2.3.2.

For stable stationary polarization-entangled wave patterns, the phase factor  $\varphi$  of the GCS is governed by the criterion of the maximum overlap between the cavity mode distribution and the pump distribution. Note that the maximum overlap integral corresponds to the minimum pump threshold. The overlap integral for the transverse mode  $\vec{E}_i(x, y, z)$  can be written as

$$I(\varphi) = \iint S(x, y, z; \varphi) R_p(x, y) dx dy \quad (2.3.10)$$

where the normalized intensity distribution  $S(x, y, z; \varphi)$  and the pumping distribution  $R_p(x, y)$  are given by

$$S(x, y, z; \varphi) = \frac{|\vec{E}_i(x, y, z)|^2}{\int_{-\infty}^{\infty} dx \int_{-\infty}^{\infty} dy \int_{-\infty}^{\infty} dz |\vec{E}_i(x, y, z)|^2}, \quad i = x, y \quad (2.3.11)$$

and

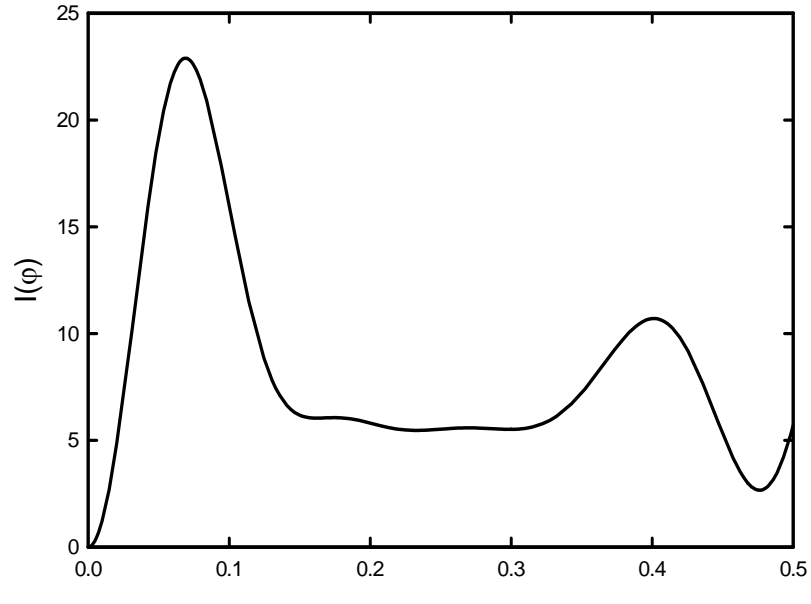
$$R_p(x, y) = \frac{2}{\pi} \frac{1}{\omega_p^2} \exp\left[-2 \frac{(x - x_0)^2 + (y - y_0)^2}{\omega_p^2}\right] \quad (2.3.12)$$

with the pumping radius  $\omega_p \approx 25 \mu m$  in the scheme. Figure 2.3.8 shows the overlap functional  $I(\varphi)$  as a function of  $\varphi$  for the state  $\vec{E}_x = \Psi_{4,7}^{\sin}(x, y, z; \varphi)$  and  $\vec{E}_x(x, y, z) = \Psi_{3,18}^{\sin}(x, y, z; \varphi)$  corresponding to the experimental patterns shown in Figs. 2.3.2 (a) and (c) with  $x_0 = -50 \mu m$ ,  $y_0 = 63 \mu m$ , and  $x_0 = -137 \mu m$ ,  $y_0 = 61 \mu m$ , respectively. The maximum of the overlap indicates the most possible phase factor to construct the experimental result with the specific off axis. As a result, we can control the phase factor in the vicinity of the peaks  $0.07\pi$  and  $0.4\pi$  in Figs. 2.3.8 (a) and (b) to simulate the patterns

which are in good agreement with the experimental patterns as shown in Figs. 2.3.2 (a) and (c). The diagram of the phase factor indicates the accurate direction to construct the experimental results. In other words, we can manipulate various patterns by use of the relation between the pumping position and the phase factor in the overlap function. Continuously, Fig. 2.3.9-2.3.12 display the numerical results of the polarization-resolved patterns according to the patterns in Fig. 2.3.3-2.3.6. From the analytical results of the polarization-resolved patterns, we can confirm that the polarization-entangled patterns are composed of two distinct patterns with orthogonal linear polarization. The important point to note is that the transverse pattern is linearly polarized, but the polarization is spatially dependent. The good agreement between the reconstructed and experimental patterns verifies that the GCSs provide a practical description for the polarization-entangled optical coherent waves.



(a)


 $\varphi(\pi)$ 

(b)

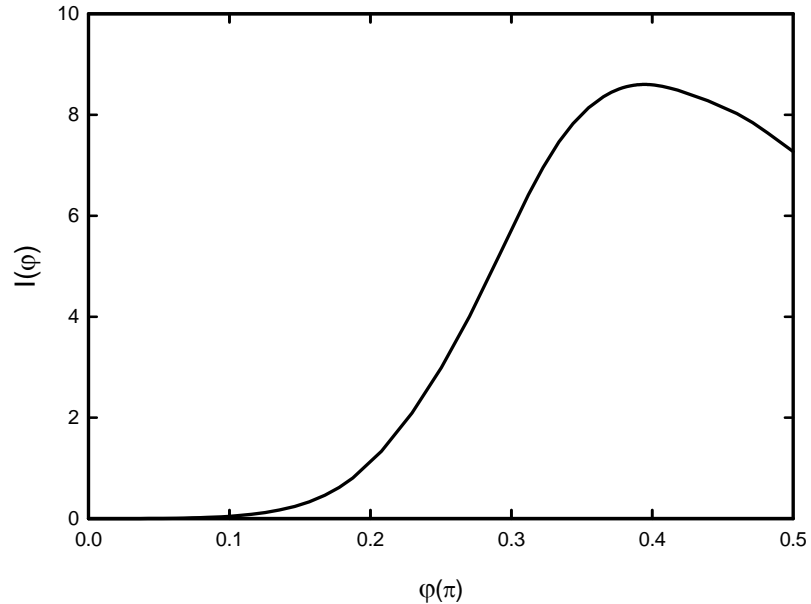

 $\varphi(\pi)$ 

Fig. 2.3.8 (a) The overlap functional  $I(\varphi)$  as a function of  $\varphi$  for the state  $\vec{E}_x(x, y, z)$  in Eq. (2.3.6). (b) The overlap functional  $I(\varphi)$  as a function of  $\varphi$  for the state  $\vec{E}_x(x, y, z)$  in Eq. (2.3.8).

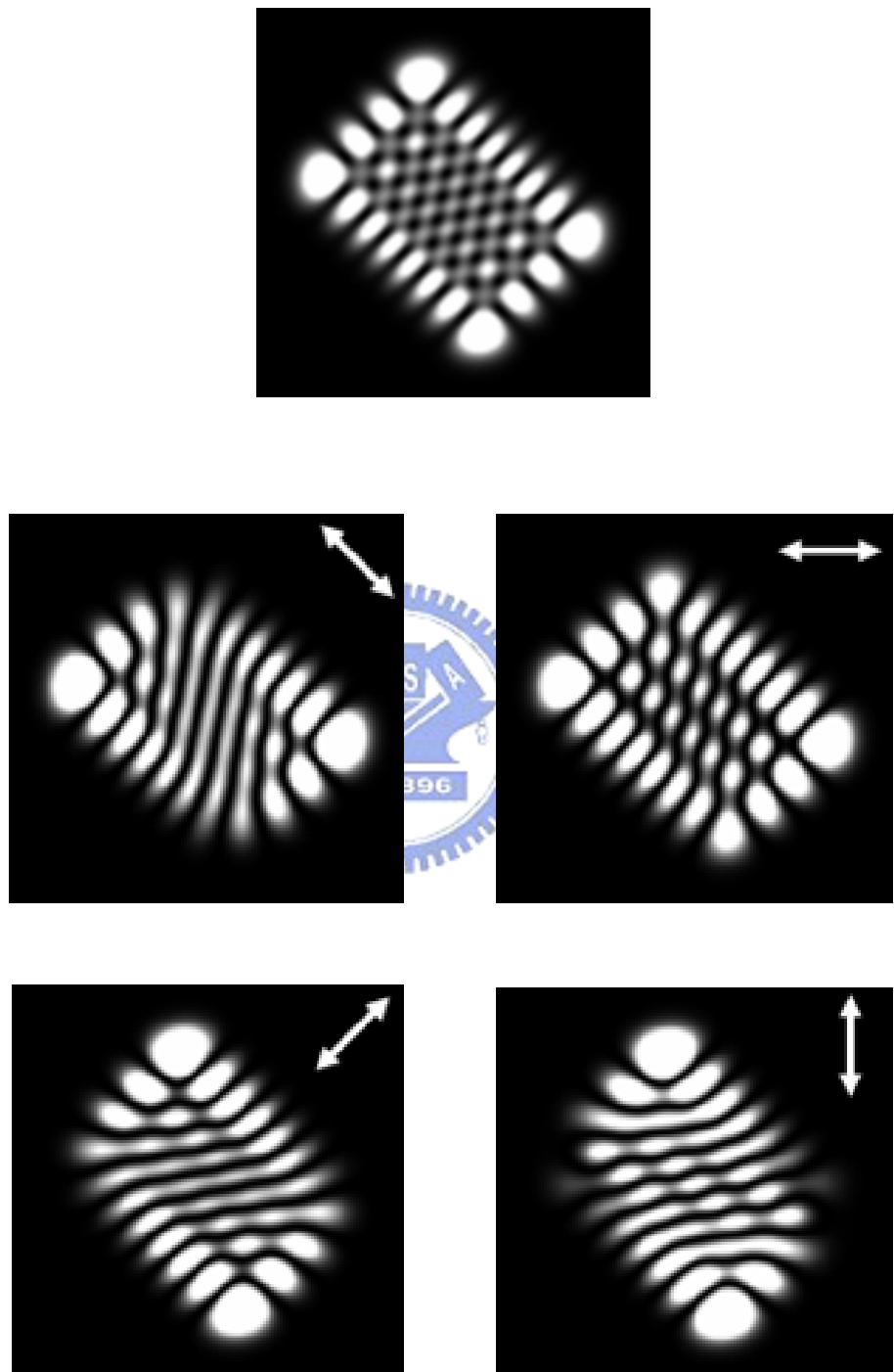


Fig. 2.3.9 Numerically reconstructed patterns for the experimental results shown in Fig. 2.3.3.

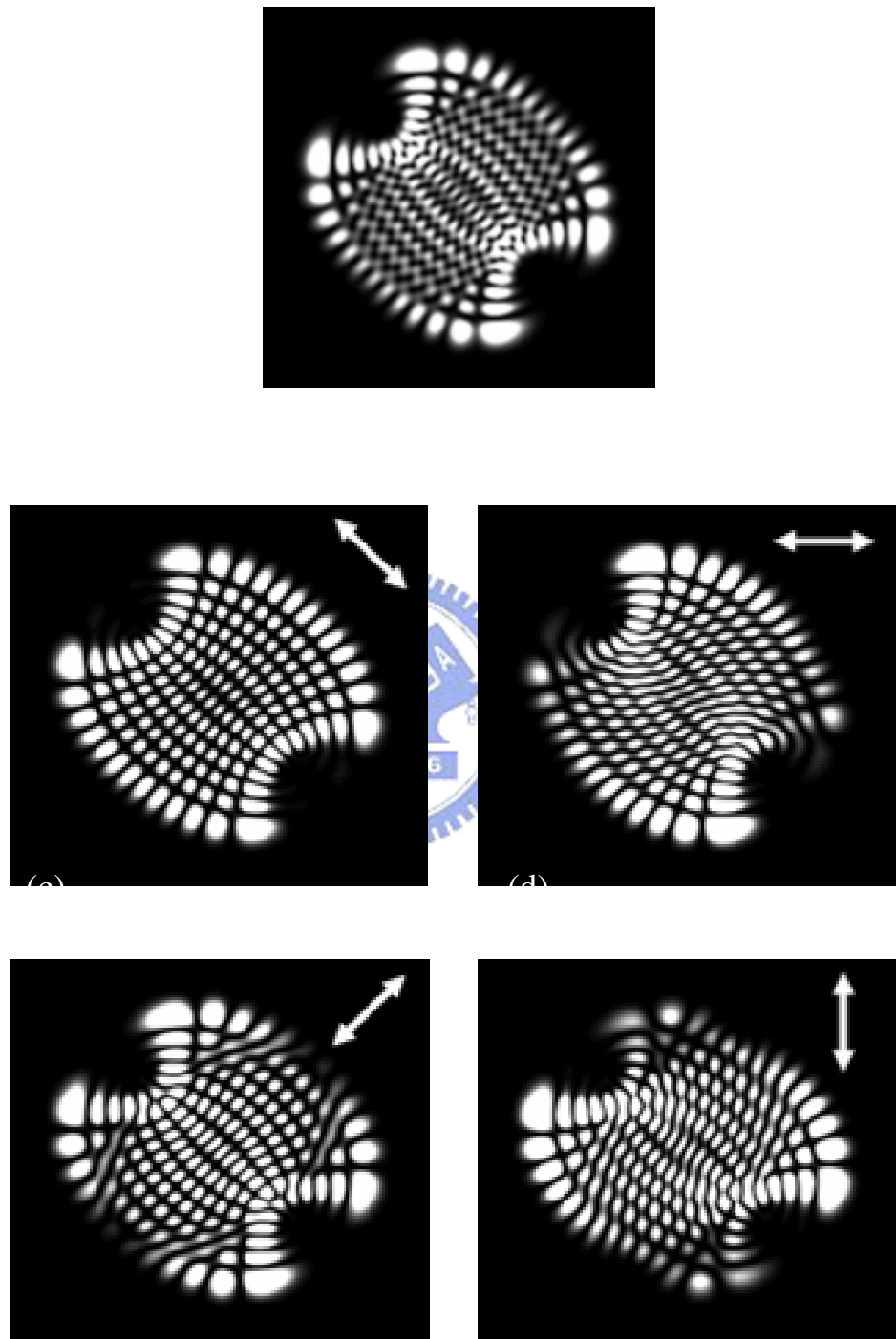


Fig. 2.3.10 Numerically reconstructed patterns for the experimental results shown in Fig. 2.3.4.

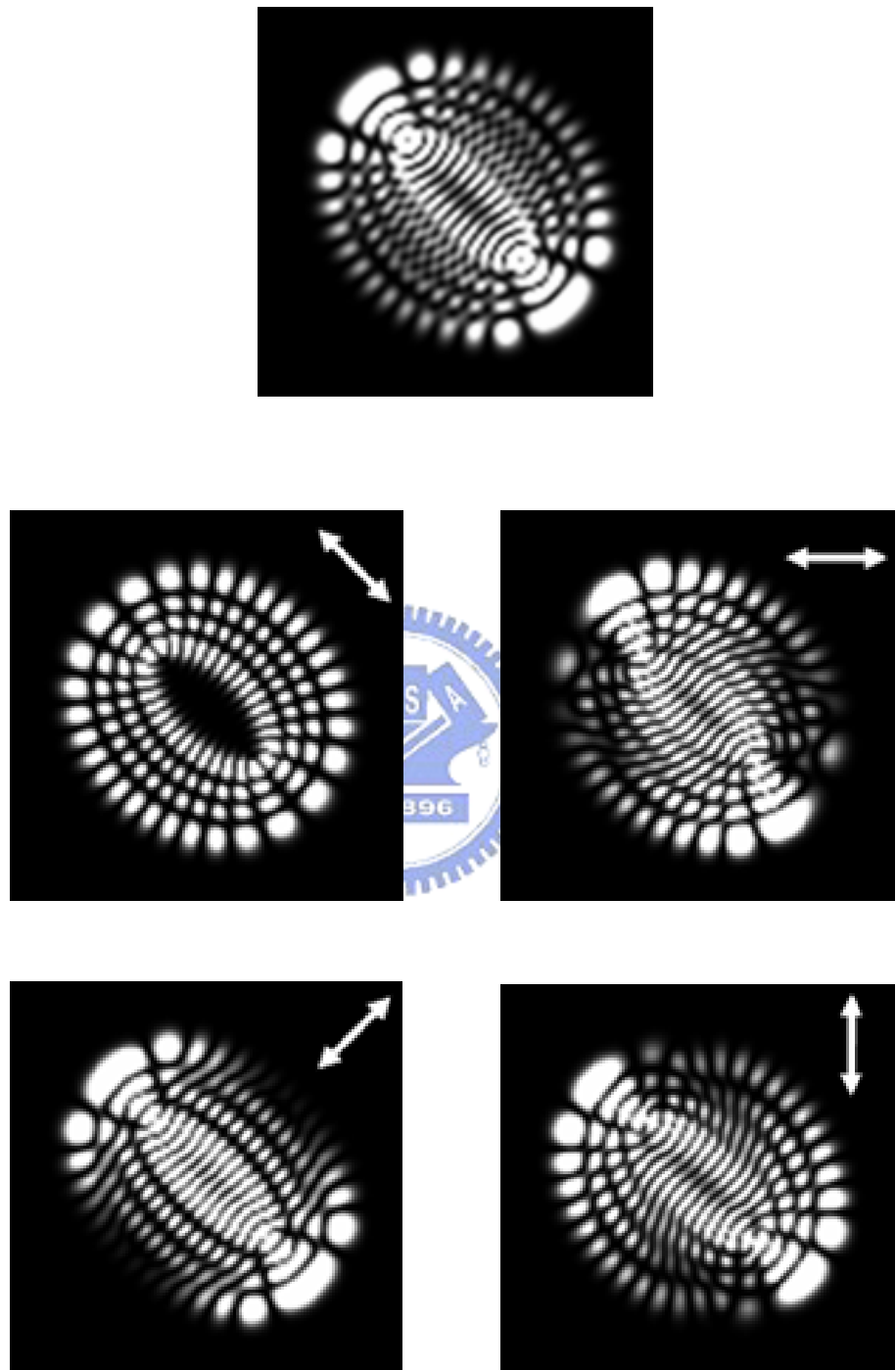


Fig. 2.3.11 Numerically reconstructed patterns for the experimental results shown in Fig. 2.3.5.

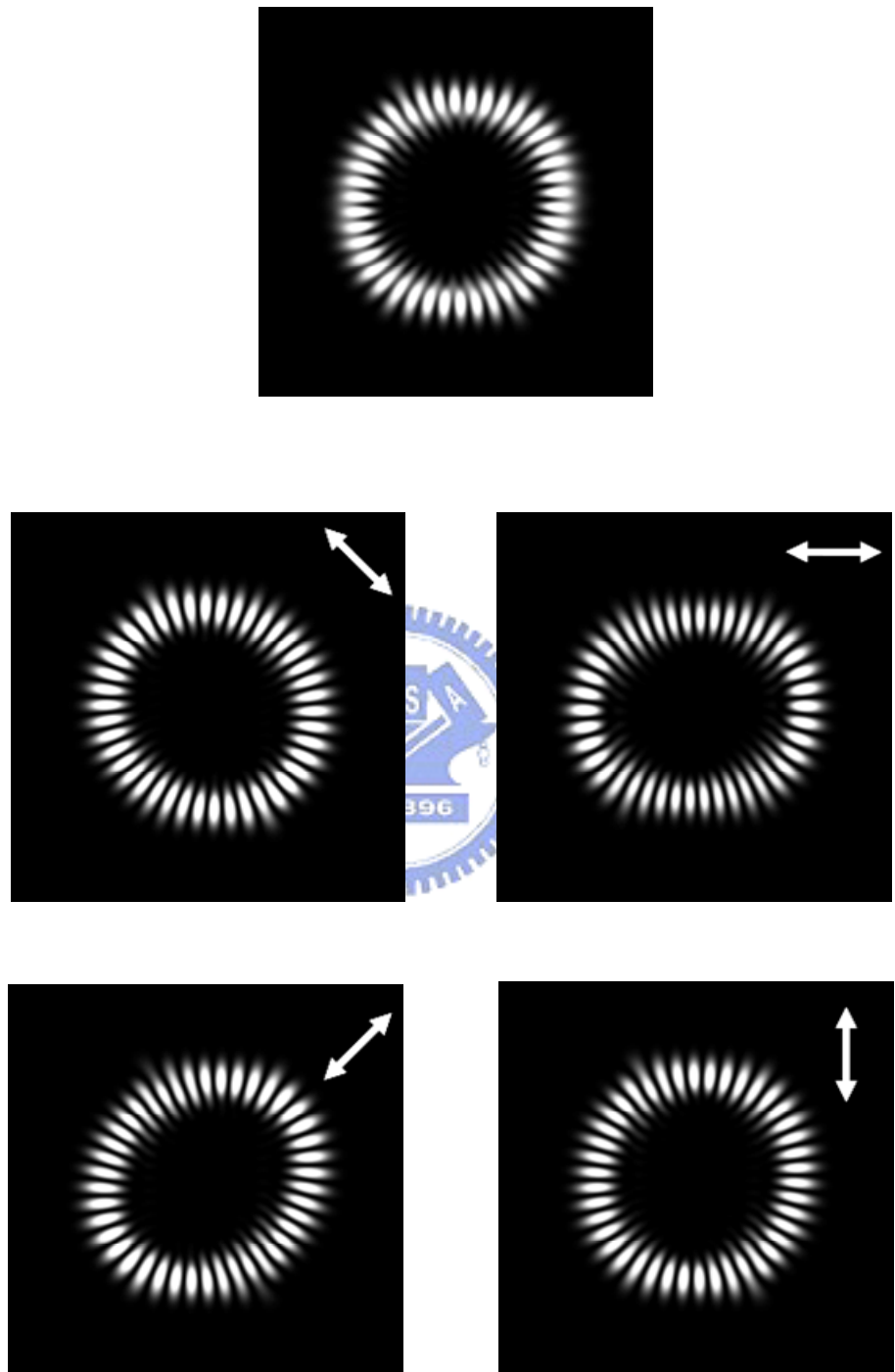


Fig. 2.3.12 Numerically reconstructed patterns for the experimental results shown in Fig. 2.3.6.

Two types of point singularities in the polarization of a paraxial Gaussian laser beam had been researched in recent years. Vector singularities are isolated, stationary points in a plane at which the orientation of the electric vector of a linearly polarized vector field becomes undefined. Therefore elliptic singularities are isolated, stationary points in a plane at which the orientation of the elliptically polarized fields becomes undefined. In this chapter, we investigate the elegant GCSs to reconstruct the polarization-entangled experimental results. For this reason, the V-points of the various experimental patterns which are the transitions between HG and LG modes can be revealed explicitly. Vector point singularities are conventionally described in terms of the angle field  $\Theta(x, y) = \arctan(E_y / E_x)$ , where  $E_x$  and  $E_y$  are the scalar components of the vector field  $\vec{E}$  along the x and y axes. The vortices of  $\Theta(x, y)$  are the vector singularities at which the orientation of the vector of  $\vec{E}$  is undefined. Figure 2.3.13 shows the contour plot of phase field  $\Theta(x, y)$  according to the patterns which are reconstructed by the GCSs in Fig. 2.3.7. The contour plots reveal that the singularities of different GCSs belong to extremely different kinds of singular patterns. Figures 2.3.13 (a), (b), and (d) display the grid, twist, and row patterns respectively. As well, Fig. 2.3.13 (c) shows that the singular pattern seems to be the transition between the twist and row patterns according to Fig. 2.3.13 (b) and (d). Figure 2.3.14 depicts the contour plot of angle field  $\Theta(x, y)$  for the boxed regions to show the details, and it can be found that all saddle points are to be open saddles with no joined arms. Since no closed saddles are found in the experimental vector field, no extrema are observed. The phase extrema are really rare because there is little room left in the phase field to accommodate them [34,35].

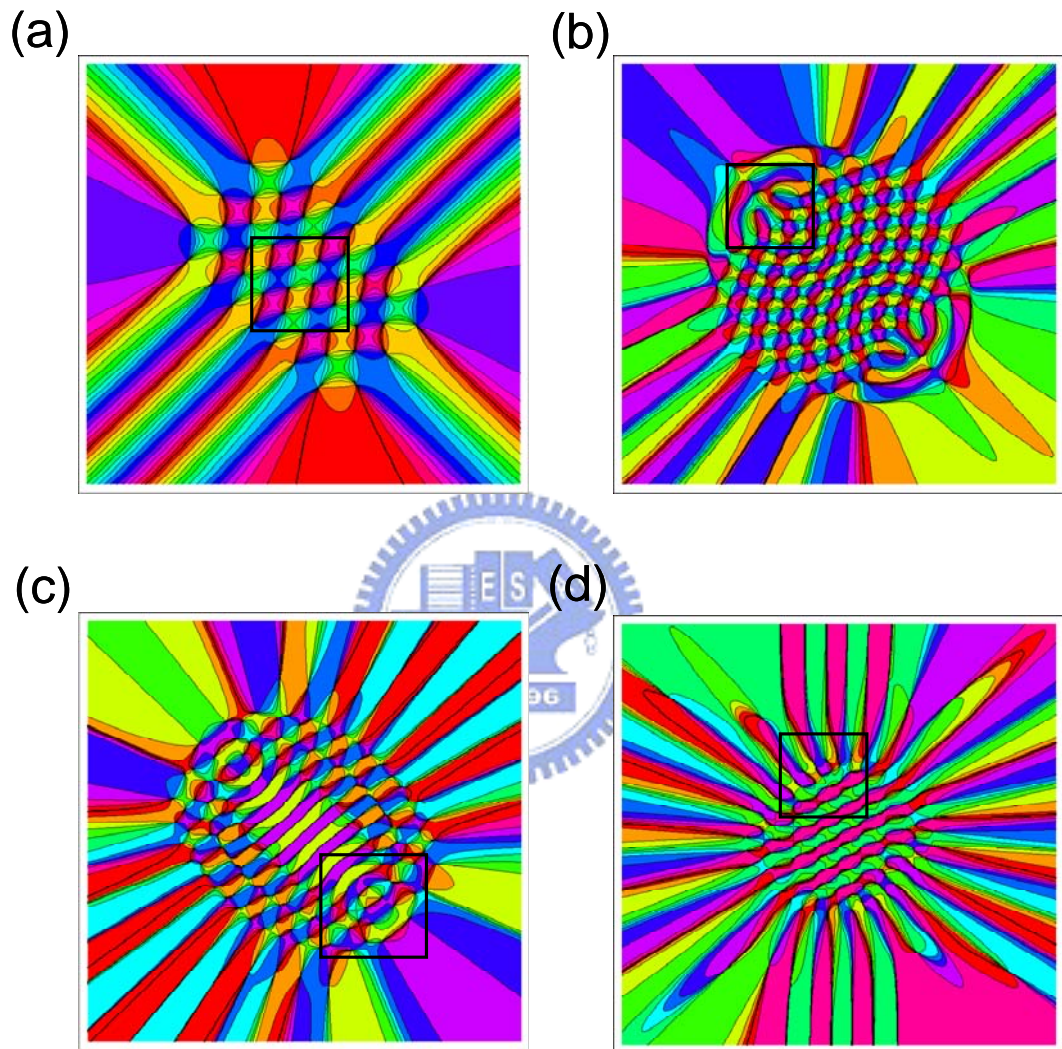


Fig. 2.3.13 Contour plot of angle field  $\Theta(x, y)$  according to the reconstructed patterns in Fig. 2.3.7.

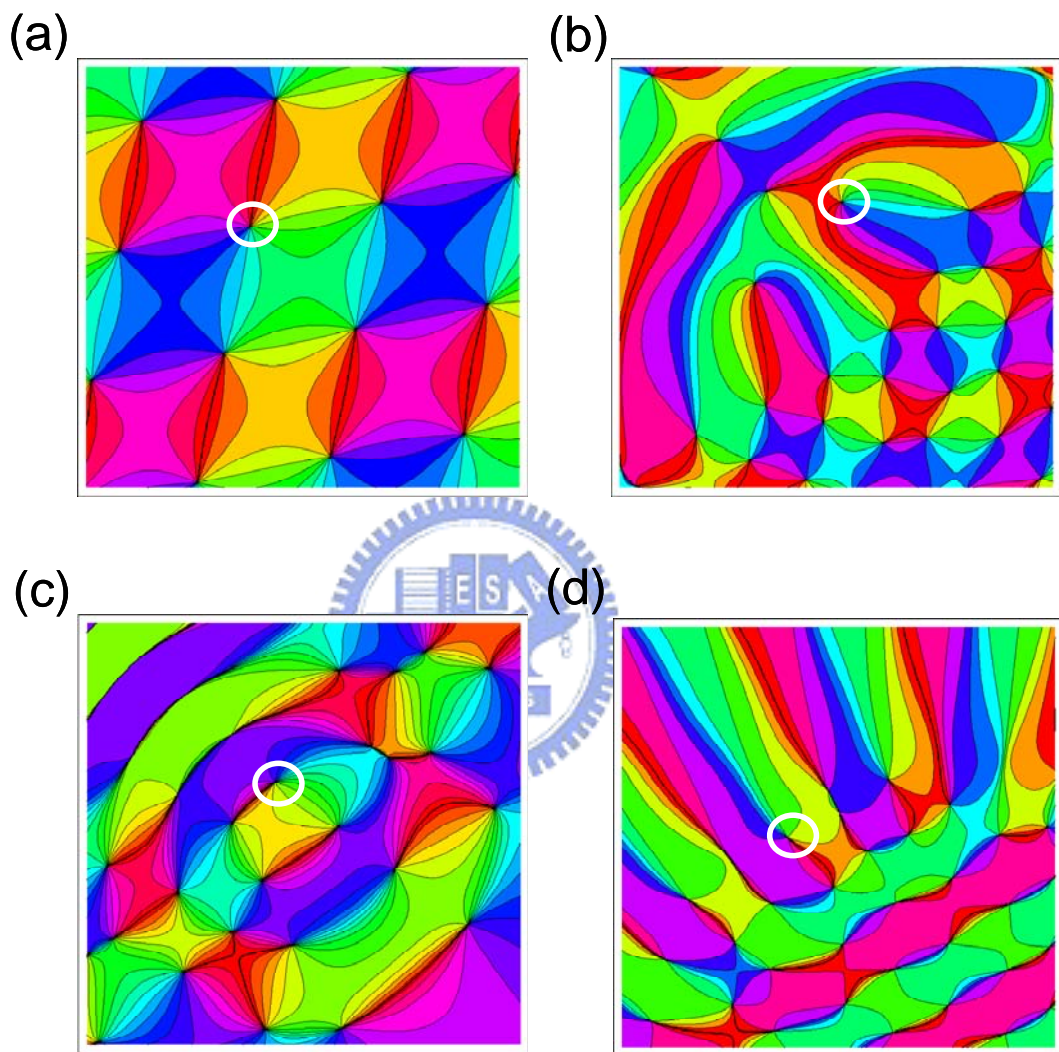
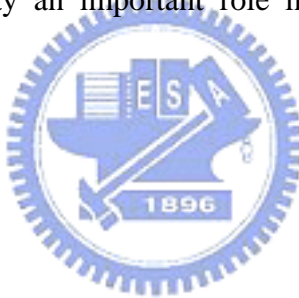


Fig. 2.3.14 Contour plot of angle field  $\Theta(x, y)$  for the boxed regions shown in Fig. 2.4.13.

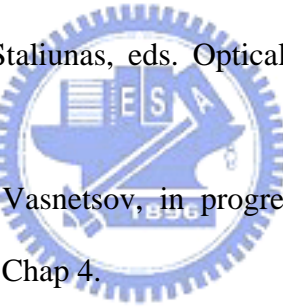
### 2.3.3 Summary

In summary, we have used a high-level isotropic laser with off-axis focused pumping and on-axis defocused pumping to generate various high-order polarization-entangled optical coherent patterns. The structures of the polarization-entangled patterns are highly stable and the experimental results are easily reproducible. All the experimental patterns have been well analyzed with the GCSs which constitute a useful family of quantum states for the 2D harmonic oscillator. Furthermore, various patterns can be manifestly explained by use of the relation between the pumping position and the phase factor of the GCSs in the overlap integral. With the connection between theoretical analysis and experimental results, the formation of vector singularities can be clearly represented. The perfect reconstructed results also reveal that the GCSs play an important role in the mesoscopic region with optical coherent waves.



## REFERENCES

- [1] David J. Griffiths, *Introduction to Electrodynamics* (3rd ed.), (1999).
- [2] John David Jackson, *Classical Electrodynamics* ( 3rd ed.), (1998).
- [3] A. E. Siegman, *Lasers* (1986).
- [4] J. J. Sakurai, *Modern Quantum Mechanics* (revised ed.), (1994).
- [5] *Quantum Theory of Angular Momentum: A Collection of Reprints and Original Papers*, Edited by L. C. Biedenharn and H. Van Dam (1967) p. 229-279.
- [6] K. F. Berggren, A. F. Sadreev, and A. A. Starikov, Phys. Rev. E **66**, 016218 (2002).
- [7] G. Blatter, M. V. Feigelman, and V. B. Geshkenbein, Rev. Mod. Phys. **66**, 1125 (1994).
- [8] R. E. Prange and M. Girvin, *The Quantum Hall Effect* 2nd ed. (Springer-Verlag, Berlin, 1990).
- [9] M. V. Vasnetsov and K. Staliunas, eds. *Optical Vortices* (Nova Science, New York, 1999).
- [10] M. S. Soskin and M. V. Vasnetsov, in *Progress in Optics*, E. Wolf, ed. (Elsevier, Amsterdam, 2001), vol. **42**, Chap 4.
- [11] E. L. Andronikashvili and Y.G. Mamaladze, Rev. Mod. Phys. **38**, 567 (1996).
- [12] K. W. Madison, F. Chevy, W. Wohlleben, and J. Dalibard, Phys. Rev. Lett. **84**, 806 (2000).
- [13] J. F. Nye, Proc. Roy. Soc. Lond. A **387**, 105 (1983).
- [14] M. Soskin, V. Denisenko, and R. Egorov, J. Opt. A: Pure Appl. Opt. 6, S281 (2004).
- [15] M. V. Berry, J. Opt. A: Pure Appl. Opt. 6, 475 (2004).
- [16] I. Freund, Opt. Commun. **199**, 47 (2001).
- [17] L. Gil, Phys. Rev. Lett. **70**, 162 (1993).
- [18] T. Erdogan, Appl. Phys. Lett. **60**, 1921 (1992).
- [19] Y. F. Chen, K. F. Huang, H. C. Lai, and Y. P. Lan, Phys. Rev. Lett. **90**, 053904 (2003).
- [20] I. V. Veshneva, A. I. Konukhov, L. A. Melnikov, and M. V. Ryabinina, J. Opt. B **3**, S209



(2001).

- [21] Y. F. Chen, T. H. Lu, and K. F. Huang, Phys. Rev. Lett. **96**, 033901 (2006).
- [22] Y. F. Chen, C. H. Jiang, Y.P. Lan, and K. F. Huang, Phys. Rev. A **69**, 053807 (2004).
- [23] Y. F. Chen, Y.P. Lan, and K. F. Huang, Phys. Rev. A **68**, 043803 (2003).
- [24] V. Buz'ek and T. Quang, J. Opt. Soc. Am. B **6**, 2447(1989).
- [25] J. Banerji and G. S. Agarwal, Opt. Express **5**, 220 (1999).
- [26] Y. F. Chen and K. F. Huang, Phys. Rev. E **68**, 066207(2003).
- [27] Y. F. Chen, Y. P. Lan, and K. F. Huang, Phys. Rev. E **66**, 066210 (2002).
- [28] Y. F. Chen and Y. P. Lan, Phys. Rev. A **66**, 053812 (2002).
- [29] Y. F. Chen and Y. P. Lan, Phys. Rev. A **67**, 043814 (2003).
- [30] Miguel A. Bandres and Julio C. Gutierrez-Vega, Opt. Lett. **29**, 2 (2004).
- [31] Ulrich T. Schwarz, Miguel A. Bandres and Julio C. Gutierrez-Vega, Opt. Lett. **29**, 16 (2004).
- [32] Miguel A. Bandres , Opt. Lett. **29**, 15 (2004).
- [33] Miguel A. Bandres and Julio C. Gutierrez-Vega, Opt. Lett. **29**, 19 (2004).
- [34] I. Freund, Phys. Rev. E **52**, 2348 (1995).
- [35] M. S. Soskin, V. Denisenko, and I. Freund, Opt. Lett. **28**, 1475(2003).

# Chapter 3

## Three-dimensional Optical Coherent Waves with Longitudinal-transverse Coupling

The bunch of energy levels in the quantum spectra has been found to lead to the shell structures in nuclei [1], metallic clusters [2], and quantum dots [3]. More intriguingly, the existence of bunch level has a deep and far-reaching relation with the emergence of classical features in a mesoscopic quantum system [4-5]. Recent experimental and theoretical studies have verified that the coherent superposition of degenerate or nearly degenerate quantum states can result in mesoscopic quantum wave functions localized on periodic orbits in the classical counterpart of the given system [6-7]. Furthermore, experimental results [8-10] indicated that the mode-locking effects lead to the stationary coherent waves associated with periodic orbits to be robust and structurally stable within a finite range of the perturbation or detuning. Devil's staircases, Arnold tongues, and Farey trees are the hallmark of mode locking and have been found to be ubiquitous in physical, chemical and biological systems [11-13]. The phenomenon of mode-locked staircases have been extensively studied in Rayleigh-Bénard experiments [14], charge-density-wave system [15-16], Josephson-junction arrays [17-18], reaction-diffusion systems [19], the modulated external-cavity semiconductor laser [20], the driven vortex lattices with periodic pinning [21], the motion of a charge particle in two waves [22], and the bimode CO<sub>2</sub> laser with a saturable absorber [23]. Nevertheless, experiments on the mode-locked staircase in high-order optical coherent waves have never been realized.

### 3.1 Frequency Locking, Mode Locking, and Resonance

In the 17<sup>th</sup> century the Dutch physicist Christian Huyghens observed that two clocks hanging back to back on the wall tend to synchronize their motion. This phenomenon is known as phase locking, frequency locking, or resonance, and is generally present in dynamical systems with two competing frequencies [24-25]. The phenomenon of these important effects has been extensively studied in current-driven Josephson junction [26], Belusov-Zabotinsky reaction [27], and ionic conductor barium sodium niobate [28]. Furthermore Mogens Jensen, Per Bak, and Tomas Bohr found that at the transition to chaos the motion is always locked. As one changes the frequency of either oscillator, the ratio between the two frequencies locks onto every single rational value  $p/q$ . To demonstrate the important and interesting results, we employ the high-Q laser system to realize the frequency locking with the coupling of longitudinal and transverse modes.



### 3.2 Devil's Staircase with Two Competing Frequencies

The phenomenon of devil's staircase comes from two competing frequencies. For two oscillators in Fig. 3.2.1, as one changes the frequency of either oscillator the ratio between the two frequencies locks onto every single rational value  $p/q$ . If a pendulum is employed to fix to a driving frequency and plots the actual frequency of the pendulum against the natural frequency, we will obtain a curve consisting of infinity of steps. The transition can be established by varying the ratio of two frequencies and may be studied by means of circle map,

$$f(\theta) = \theta + \Omega - (K/2\pi)\sin(2\pi\theta) \quad (3.2.1)$$

where  $\Omega$  represents the ratio of two frequencies and  $K$  is the coupling strength of the two

oscillator. The ratio between the frequencies with considering the coupling strength is given by the winding number

$$W(K, \Omega) = \lim_{n \rightarrow \infty} n^{-1} [f^n(\theta) - \theta]. \quad (3.2.2)$$

Figure 3.2.2 shows the variation when the coupling strength starts from 0 to 0.99. When the coupling strength is strong enough ( $K = 0.99$ ), the ratio of two frequencies always locks onto one of the infinity of resonant frequencies. If one slowly changes the driving frequency, the pendulum will lock onto each resonant frequency, jumping from one to the next, forming an infinite series of steps. There is infinity of steps between any two steps because between any two rational numbers there is infinity of rational numbers. It is the reason why the property of the curve shown in Fig. 3.2.2 (d) has been named “the Devil’s staircase”.



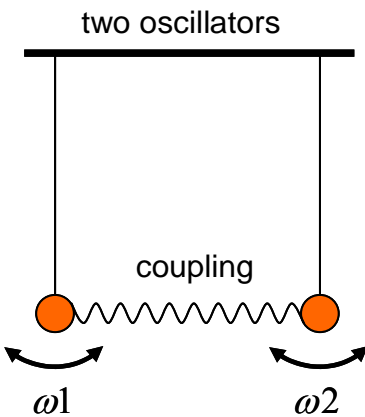


Fig. 3.2.1 Two oscillators of different frequencies with some coupling strength

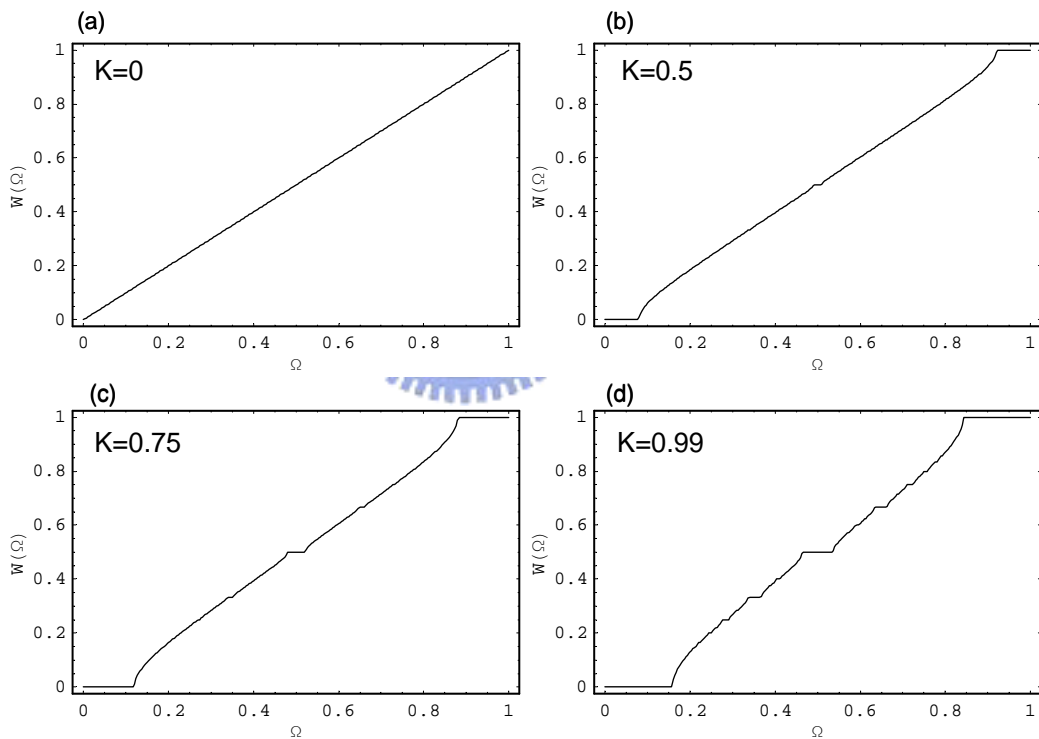
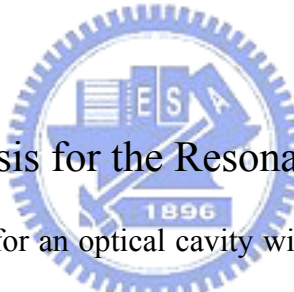


Fig. 3.2.2 Results of circle map with different coupling strength.

### 3.3 Three-dimensional Coherent Waves Demonstrated from Laser Cavity

In this section we originally show that the longitudinal-transverse coupling leads to the formation of three-dimensional coherent waves localized on Lissajous parametric surfaces which are formed by the Lissajous curves with the relative phase varying with the longitudinal direction. A high-Q symmetric laser cavity is experimentally employed to verify the existence and prevalence of 3D coherent waves in the mesoscopic regime. More importantly, the detailed experimental measurements indicate that the formation of plentiful 3D coherent waves constructs a nearly complete devil's staircase in the mesoscopic regime. Since the laser cavity may be used as an excellent analog system for the investigation of quantum systems, the present results will be useful for understanding the mesoscopic wave functions.



#### 3.3.1 Theoretical Analysis for the Resonator

The resonance frequency for an optical cavity with two spherical mirrors and the mirror distance  $L$  is generally expressed as  $f(n, m, l) = \Delta f_L [l + (m + n + 1)(\Delta f_T / \Delta f_L)]$ , where  $\Delta f_L = c/2L$  is the longitudinal mode spacing,  $\Delta f_T$  is the transverse mode spacing, and  $l$  is the longitudinal mode index, and  $m$  and  $n$  are the transverse mode indices. For an empty symmetric resonator consisting of two identical spherical mirrors with radius of curvature  $R$ , the bare ratio between the transverse and longitudinal mode spacing is given by  $\Omega = \Delta f_T / \Delta f_L = (1/\pi) \cos^{-1}(1 - L/R)$ , where  $z_R = \sqrt{L(2R - L)}/2$ . As a consequence, the bare mode-spacing ratio  $\Omega$  can be changed in the range between 0 and 1 by varying the cavity length  $L$  for a given  $R$ . Figure 3.3.1 shows a portion of the spectrum  $f(l, n, m)$  as a function of the bare mode-spacing ratio  $\Omega$  for the range of  $10 \leq l \leq 30$  and  $0 \leq (m + n) \leq 20$ . It can be seen that the degeneracies and gaps appear at the values of  $\Omega$  corresponding to the rational numbers  $P/Q$ , forming an interesting fractal structure. Degeneracies in the spectra of the

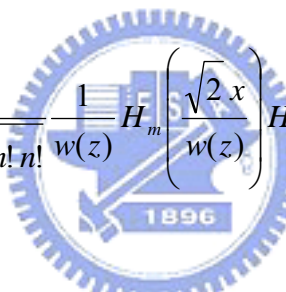
quantum systems have been found to play a vital role in the relationship between quantum shell structures and classical periodic orbits, especially in the mesoscopic regime. The following analysis will verify that the longitudinal-transverse coupling and the mode-locking effect can lead to the 3D coherent waves to be localized on the parametric surfaces with Lissajous transverse patterns.

The wave functions of the Hermite-Gaussian (HG) modes for a spherical cavity are given by

$$\Phi_{m,n,l}^{(HG)}(x, y, z) = \Phi_{m,n}(x, y, z) e^{i(m+n+1)\tan^{-1}\left(\frac{z}{z_R}\right)} e^{-i\left(\frac{\pi z}{L}\right)[l+(m+n+1)\Omega]\left[\frac{x^2+y^2}{2(z^2+z_R^2)}+1\right]}, \quad (3.3.1)$$

where

$$\Phi_{m,n}(x, y, z) = \frac{1}{\sqrt{2^{m+n+1} \pi m! n!}} \frac{1}{w(z)} H_m\left(\frac{\sqrt{2}x}{w(z)}\right) H_n\left(\frac{\sqrt{2}y}{w(z)}\right) \exp\left[-\frac{x^2+y^2}{w(z)^2}\right], \quad (3.3.2)$$



$w(z) = w_o \sqrt{1 + (z/z_R)^2}$ ,  $w_o$  is the beam radius at the waist, and  $z_R$  is the Rayleigh range. When the mode-spacing ratio  $\Omega$  is locked to a rational number  $P/Q$ , the group of the HG modes  $\Phi_{m_o+pk, n_o+qk, l_o+sk}^{(HG)}(x, y, z)$  with  $k=0,1,2,3,\dots$  can be found to constitute a family of frequency degenerate states, provided that the given integers  $(p, q, s)$  obey the equation  $s + (p + q)P/Q = 0$ . For convenience, the integer  $s$  is taken to be negative. The equation  $s + (p + q)P/Q = 0$  indicates that  $q + p$  needs to be an integral multiple of  $Q$ , i.e.  $q + p = K \times Q$ , where  $K=1, 2, 3, \dots$ . It has been verified that the coherent superposition of the mode-locked degenerate states manifestly leads to the wave functions to be associated with the classical periodic orbits in the 2D quantum systems [29-31].

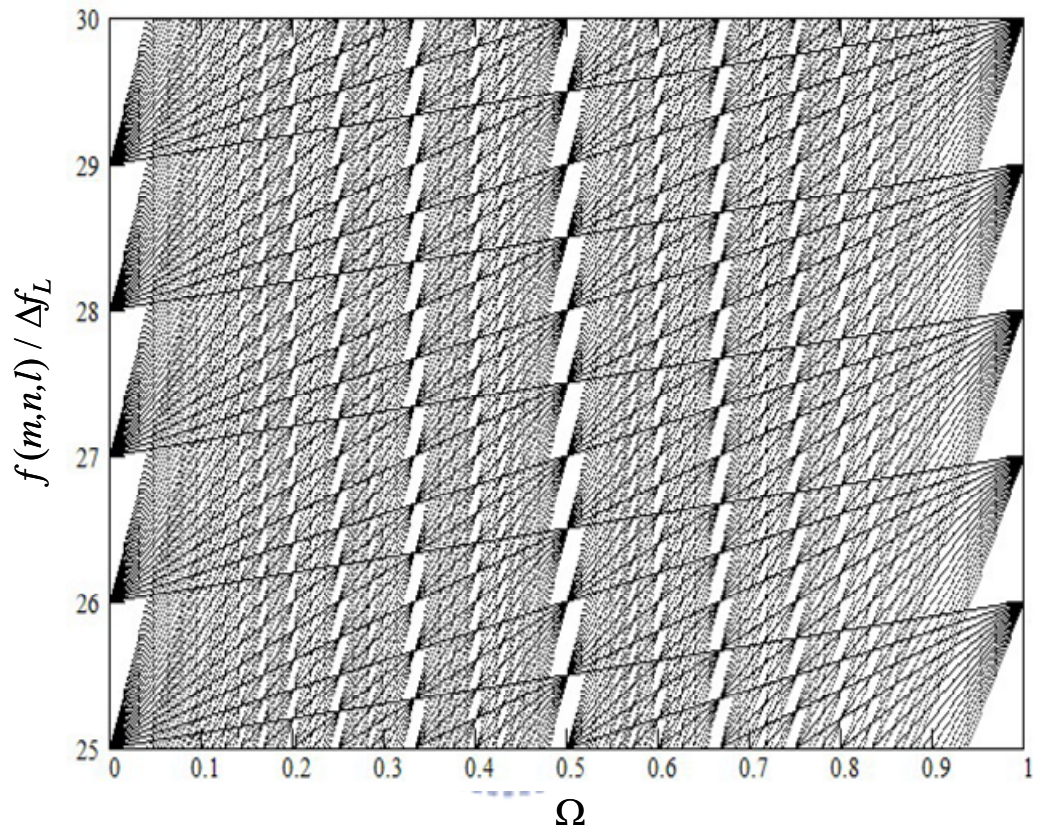


Fig. 3.3.1 A portion of the spectrum  $f(l, n, m)$  as a function of the bare mode-spacing ratio  $\Omega$  for the range of  $10 \leq l \leq 30$  and  $0 \leq (m + n) \leq 20$ .

In the present case, the 3D coherent states constructed by the family of  $\Phi_{m_o+pk, n_o+qk, l_o+sk}^{(HG)}(x, y, z)$  can be generally given by  $\Psi_{m_o, n_o, l_o}^{p, q, s}(x, y, z; \phi_o) = \sum_{k=0}^M e^{ik\phi_o} \Phi_{m_o+pk, n_o+qk, l_o+sk}^{(HG)}(x, y, z)$ , where the parameter  $\phi_o$  is the relative phase between various HG modes at  $z=0$ . The relative phase  $\phi_o$  has been verified to play an important role in the quantum-classical connection. With the expression of equation (3.3.1), the 3D coherent states can be rewritten as

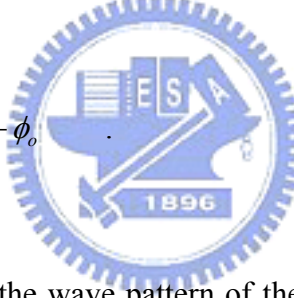
$$\Psi_{m_o, n_o, l_o}^{p, q, s}(x, y, z; \phi_o) = \Psi_{m_o, n_o}^{p, q}(x, y, z; \phi_o) e^{-i\left(\frac{\pi z}{L}\right)\left[l_o + (m_o + n_o + 1)\right]\left[\frac{P}{Q}\right]\left[\frac{x^2 + y^2}{2(z^2 + z_R^2)} + 1\right]}, \quad (3.3.3)$$

where

$$\Psi_{m_o, n_o}^{p, q}(x, y, z; \phi_o) = \sum_{k=0}^M e^{ik\phi(z)} \Phi_{m_o+pk, n_o+qk}(x, y, z), \quad (3.3.4)$$

and

$$\phi(z) = (q + p) \tan^{-1}(z/z_R) + \phi_o \quad (3.3.5)$$



Equation (3.3.3) indicates that the wave pattern of the 3D coherent state  $\Psi_{m_o, n_o, l_o}^{p, q, s}(x, y, z; \phi_o)$  is utterly determined by the wave function  $\Psi_{m_o, n_o}^{p, q}(x, y, z; \phi_o)$ . As seen in equation (3.3.4), the wave function  $\Psi_{m_o, n_o}^{p, q}(x, y, z; \phi_o)$  is a coherent superposition of the modes  $\Phi_{m_o+pk, n_o+qk}(x, y, z; \phi_o)$  with the phase factor  $\phi(z)$ . It is worth while to mention that the  $z$ -dependence of the phase factor  $\phi(z)$  arises from the Gouy-phase difference between the HG modes with distinct transverse orders. With the results obtained in the 2D quantum harmonic oscillator [32], the wave function  $\Psi_{m_o, n_o}^{p, q}(x, y, z; \phi_o)$  can be manifestly deduced to have the intensity distribution concentrated on the parametric surface:

$$x(\vartheta, z) = \sqrt{m_o + \frac{M}{2}} w(z) \cos \left[ q\vartheta - \frac{\phi(z)}{p} \right]; \quad y(\vartheta, z) = \sqrt{n_o + \frac{M}{2}} w(z) \cos(p\vartheta), \quad (3.3.6)$$

where  $0 \leq \vartheta \leq 2\pi$  and  $-\infty \leq z \leq \infty$ . Equation (3.3.6) reveals that the parametric surface related to the 3D coherent waves is formed by the Lissajous curves with the relative phase varying with the position  $z$ . In other words, the longitudinal-transverse coupling leads to the 3D coherent states to be localized on the Lissajous parametric surfaces. With  $q + p = K \times Q$  and equation (3.3.5), the total change of the relative phase of the 3D coherent wave from  $z = -\infty$  to  $z = \infty$  is given by  $\phi(\infty) - \phi(-\infty) = (K \times Q)\pi$ . On the other hand, the total change of the relative phase of the 3D coherent wave from one cavity mirror at  $z = -L/2$  to another one at  $z = L/2$  is given by  $\phi(L/2) - \phi(-L/2) = (K \times P)\pi$ , where the mode-locking condition  $\tan^{-1}(L/2R) = (P/Q)(\pi/2)$  is used. Figure 3.3.2 depicts an example for the Lissajous parametric surface described in equation (3.3.6) for the range from  $z = -L/2$  to  $z = L/2$  with  $(p, q) = (3, 2)$ ,  $P = 2$ , and  $\phi_o = 0$ . The tomographic transverse patterns are also plotted in the same figure to display the Lissajous feature of the 3D coherent state. Even though the relationship between the 2D quantum coherent states and the Lissajous curves has been previously developed [29-31], this is the first time that the 3D coherent states are derived to be related to the Lissajous parametric surfaces.

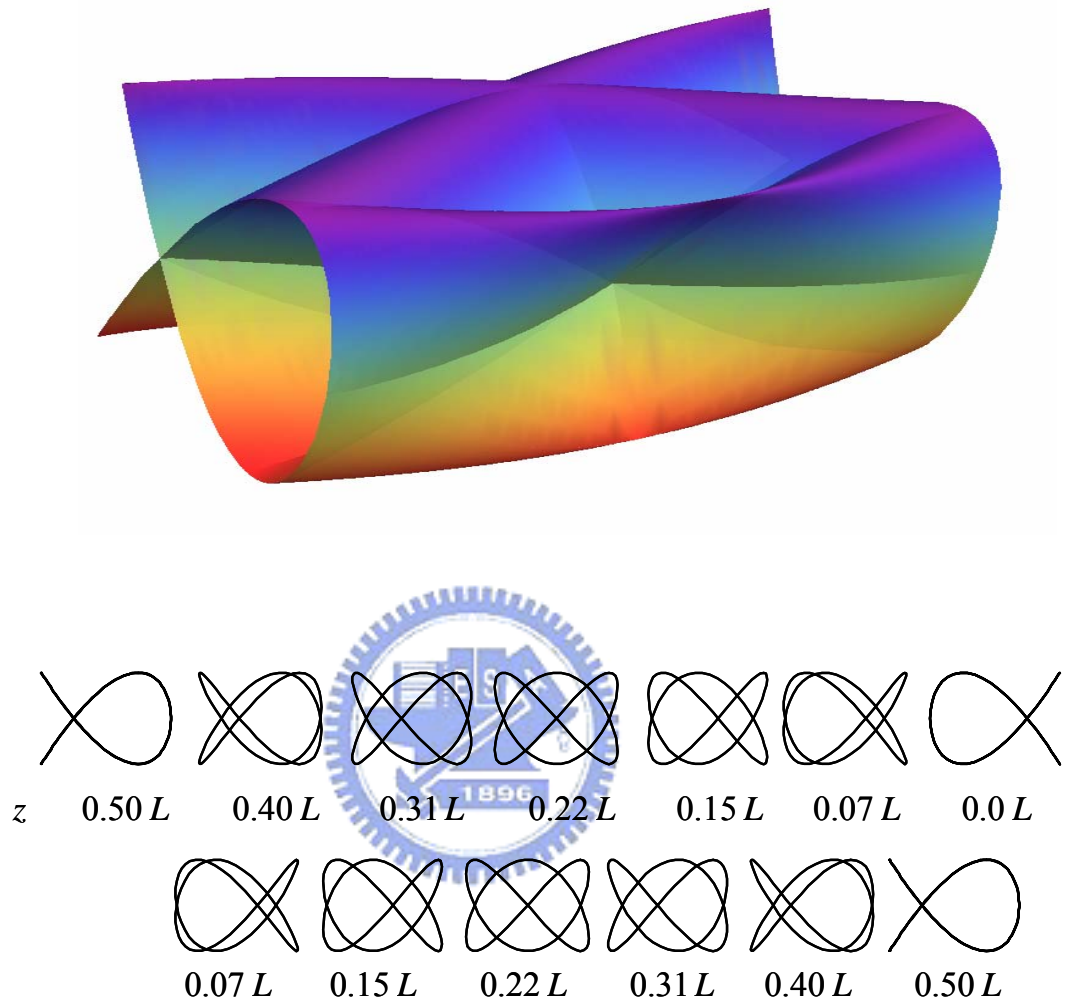


Fig. 3.3.2 Upper: an example for the Lissajous parametric surface described in equation (3.3.6) for the range from  $z = -L/2$  to  $z = L/2$  with  $(p,q) = (3,2)$ ,  $P = 2$  and  $\phi_o = 0$ . Bottom: the tomographic transverse patterns along the longitudinal axis.

### 3.3.2 Experimental Setup and Results

The wave patterns localized on the classical orbits have been realized in the degenerate laser resonator with the ring-shaped pump profile [33]. However, the index order of the laser modes is not high enough to explore the complete devil's staircase phenomenon in the wave-ray correspondence or quantum-classical correspondence. To generate super high-order laser modes, here we use the off-axis focused pumping scheme to excite a very high-gain crystal in a symmetric cavity with extremely low losses (<0.5%), as depicted in Fig. 3.3.3. The laser medium was a *a*-cut 2.0-at.% Nd<sup>3+</sup>:YVO<sub>4</sub> crystal with a length of 1 mm. Both sides of the Nd:YVO<sub>4</sub> crystal was coated for antireflection at 1064 nm (reflection < 0.1%). The radius of curvature of the cavity mirrors are  $R=10$  mm and their reflectivity is 99.8% at 1064 nm. The pump source was an 809 nm fiber-coupled laser diode with a core diameter of 100  $\mu\text{m}$  of core diameter, a numerical aperture of 0.16, and a maximum output power of 1 W. A focusing lens with 20 mm focal length and 90% coupling efficiency was used to reimaging the pump beam into the laser crystal. The pump radius was estimated to be 25  $\mu\text{m}$ . A microscope objective lens mounted on a translation stage was used to reimaging the tomographic transverse patterns inside the cavity onto a CCD camera. To measure the far-field pattern, the output beam was directly projected on a paper screen at a distance of  $\sim 50$  cm from the rear cavity mirror and the scattered light was captured by a digital camera.

At a pump power of 1 W, the emission powers were generally found to be on the order of 0.5 mW. The low emission powers indicate the cavity Q value to be rather high. The pump positions on the gain medium were controlled to excite the laser modes with the transverse orders  $n$  and  $m$  in the range of 100 to 500. Experimental results revealed that the far-field transverse patterns were not the familiar HG modes but were almost the coherent waves concentrated on various Lissajous figures for all cavity lengths. Furthermore, the tomographic transverse patterns inside the cavity evidently displayed the revolution of the Lissajous curve

along the longitudinal axis to form a Lissajous parametric surface. Figure 3.3.4 shows the experimental tomographic transverse patterns observed at  $\Omega \approx 0.422$ . The experimental tomographic transverse patterns are found to be in good agreement with the



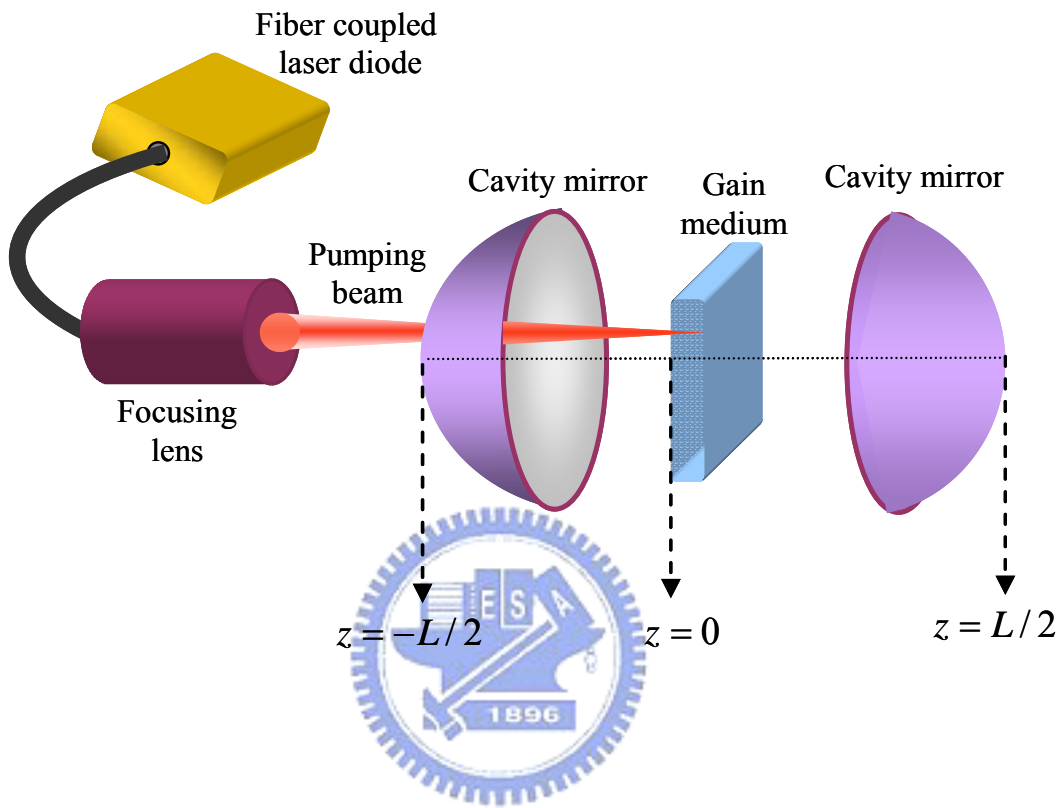


Fig. 3.3.3 Experimental setup for the generation of 3D coherent waves in a diode-pumped microchip laser with off axis pumping scheme in a symmetric spherical resonator.

feature that the 3D coherent states are well localized on the Lissajous parametric surfaces. Furthermore, the experimental patterns shown in Fig. 3.3.4 for  $-0.15L \leq z \leq 0.15L$  have a noticeable bright spot that represents the location of the pump beam. It can be seen that the pump intensity has a great overlap with the lasing mode distribution. Since the cavity mode possessing the biggest overlap with the gain region will dominate the laser emission, distinct 3D coherent waves can be precisely generated by manipulating the pump position. Figure 3.3.6 shows another set of experimental tomographic transverse patterns observed at  $\Omega \approx 0.573$  for  $0.0L \leq z \leq 0.5L$ . Here we use a filter to reflect the pumping light to make the patterns clearly demonstrated.

Continuously adjusting the bare mode-spacing ratio  $\Omega$ , the far-field transverse patterns were found to change from one mode-locked Lissajous wave to another in discrete steps. According to the above-mentioned analysis, the appearance of the Lissajous waves signifies the mode-spacing ratios to be locked to rational numbers  $P/Q$ . The analytical representation of the 3D coherent states enables us to identify the mode-locked ratios  $P/Q$  precisely from the information of the revolution numbers of the Lissajous wave patterns inside and outside the cavity. Based on thorough experiments, we found that each mode-locked ratio  $P/Q$  is composed of numerous 3D coherent waves localized on various Lissajous parametric surfaces with indices  $q+p$  to be an integral multiple of  $Q$ . On the whole, more than 560 different 3D coherent states have been obtained. The locking range of each coherent state was found to be  $\Delta\Omega \approx (1.5 \pm 0.2) \times 10^{-3}$  on average. More noticeably, the experimental mode-locked ratios  $P/Q$  were found to form a fairly complete devil staircase, as shown in Fig. 3.3.5. Figure 3.3.5 also demonstrates the experimental far-field patterns observed in the mode-locked plateau with  $P/Q = 2/5$ . The 3D optical waves which localize on the Lissajous parametric surface are not special cases in the laser cavity. With longitudinal-transverse coupling and mode-locking effect, the localized 3D optical coherent waves are general phenomenon of the laser system. Figure 3.3.7-3.3.9 depict the experimental far-field patterns observed in the

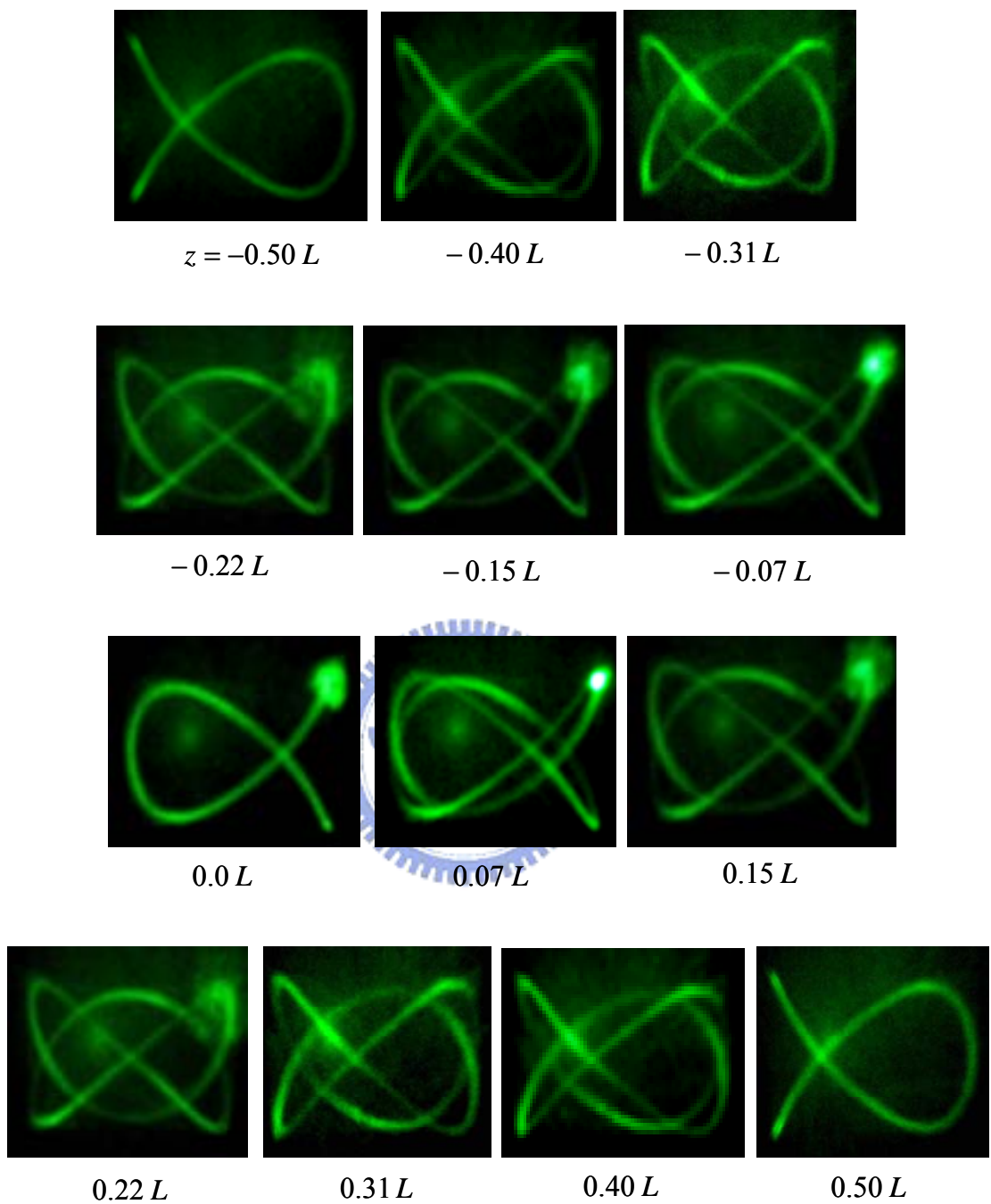


Fig. 3.3.4 Experimental tomographic transverse patterns inside the cavity observed at  $\Omega \approx 0.422$ .

mode-locked plateau with  $P/Q = 1/3$ ,  $1/4$ , and  $2/7$  respectively. The absolute values of the indices  $p$  and  $q$  were firstly determined from the feature of the Lissajous transverse pattern and their signs were determined from the equation of  $q + p = K \times Q$ , where the factor  $K$  could be found from the total change of the relative phase of the Lissajous transverse pattern inside the cavity and the indices  $Q$  and  $P$  were confirmed with the cavity length. The indices  $(p, q)$  of blue color in Fig. 3.3.5 and 3.3.7-3.3.9 represent that the factor  $K$  is not equal to one. It is worth while to mention that  $p$  and  $q$  can have the opposite sign, as long as  $q + p$  is an integral multiple of  $Q$ . On the other hand, the locking regimes for the coherent states with the indices  $(p, q)$  and  $(q, p)$  are split due to the anisotropic properties of the gain medium. As the transverse order  $(m_o, n_o)$  of the coherent mode is increased, the number of mode-locked plateaus increases, suggesting that all rational steps will be seen in an infinite order system.



### 3.3.3 Summary

In summary, the longitudinal-transverse coupling has been verified to cause the formation of 3D coherent waves with localization on parametric surfaces in the mesoscopic regime. The theoretical analysis reveals that the tomographic transverse patterns of the 3D coherent waves exhibit to be well localized on the Lissajous parametric surfaces. A high-Q symmetric laser cavity with the off-axis pumping scheme has been utilized to realize the experiment. Experimental results reveal that the mode locking of the 3D coherent states forms a nearly complete Devil's staircase with the hierarchical ordering. Our studies may provide some useful insights into the nature of the mesoscopic wave functions.

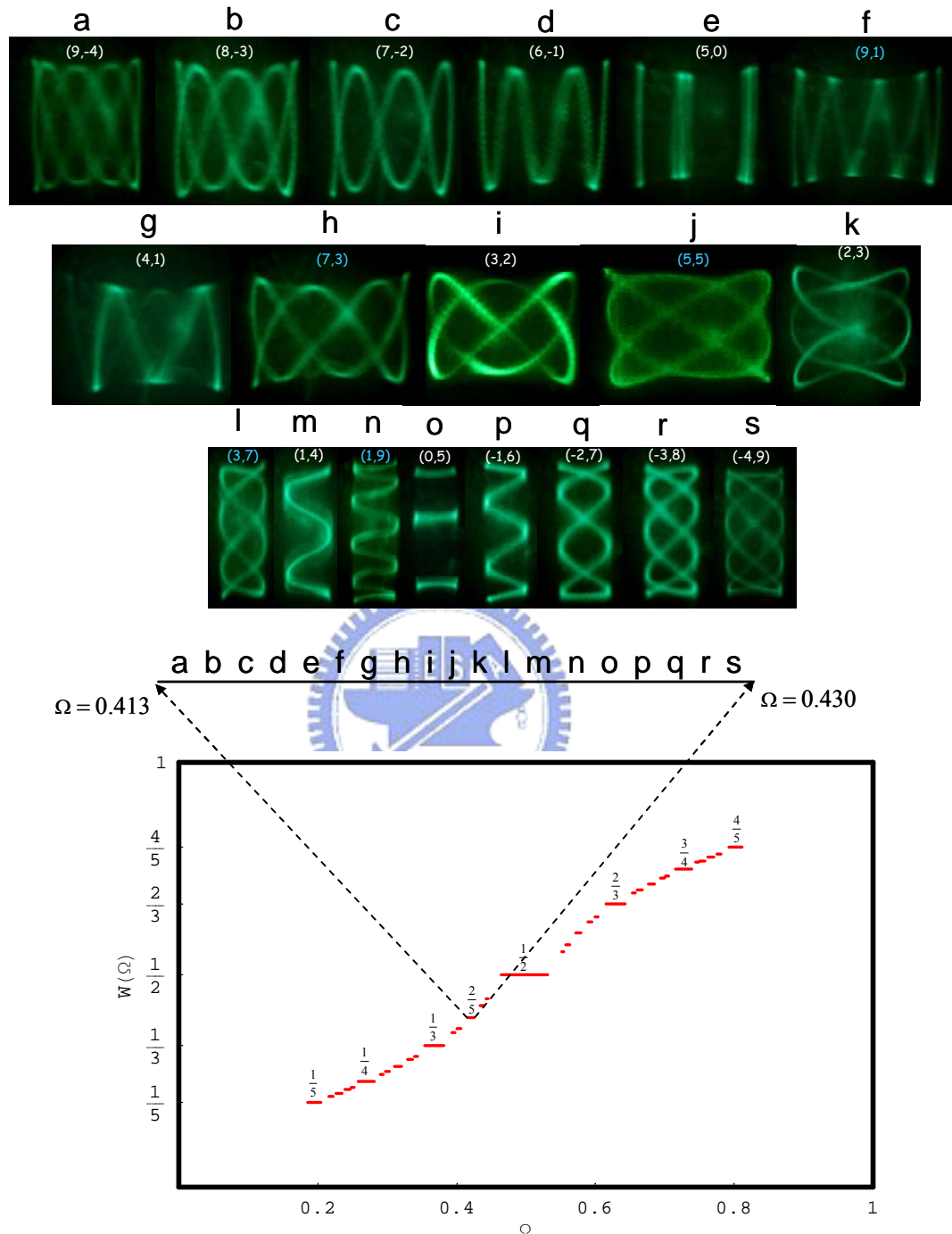


Fig. 3.3.5 Bottom: Experimental mode-locked ratio  $P/Q$  as a function of the bare mode-spacing ratio  $\Omega$ . Upper: experimental far-field patterns observed in the mode-locked plateau with  $P/Q = 2/5$ .

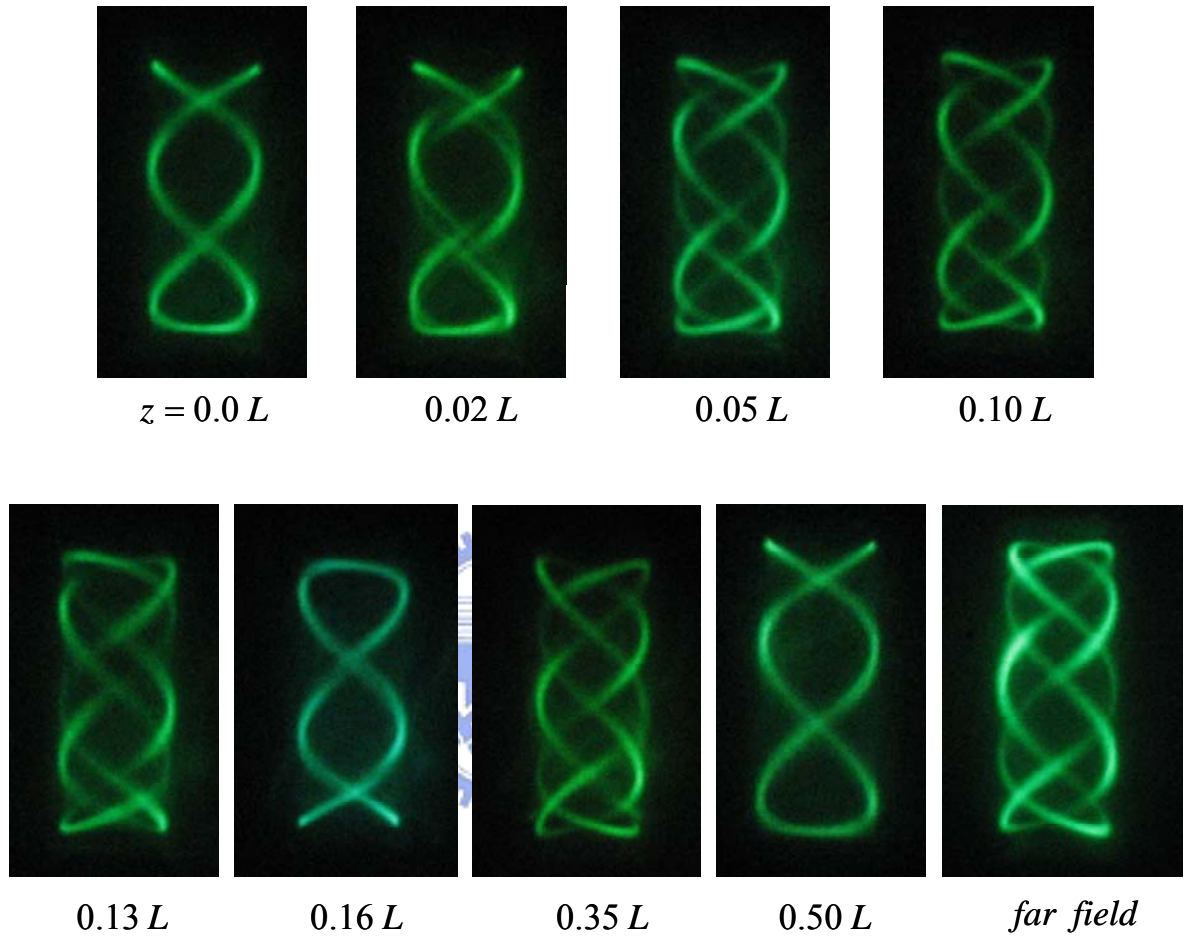


Fig. 3.3.6 Experimental tomographic transverse patterns inside the cavity observed at  $\Omega \approx 0.573$ .

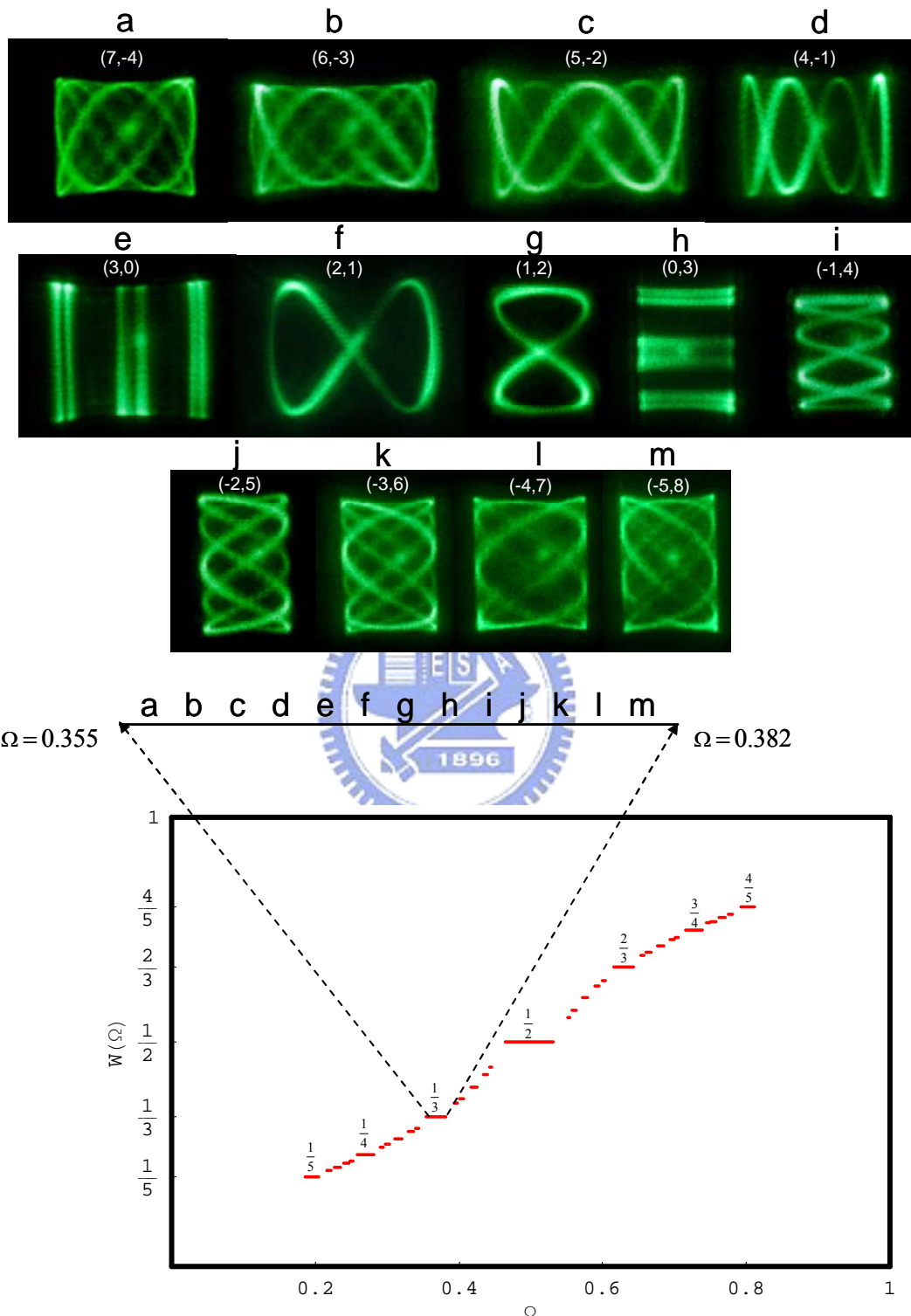


Fig. 3.3.7 Bottom: Experimental mode-locked ratio  $P/Q$  as a function of the bare mode spacing ratio  $\Omega$ . Upper: experimental far-field patterns observed in the mode-locked plateau with  $P/Q = 1/3$ .

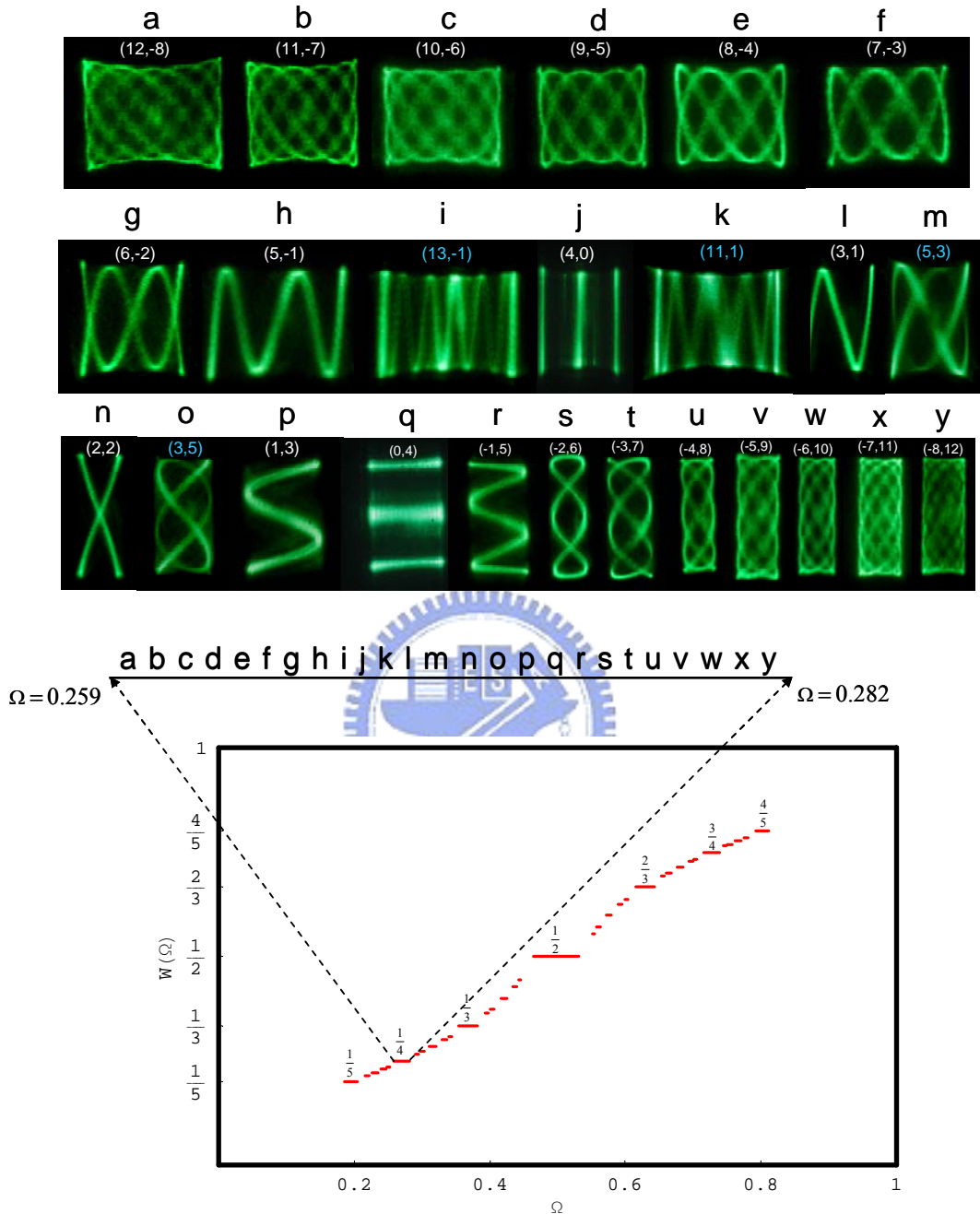


Fig. 3.3.8 Bottom: Experimental mode-locked ratio  $P/Q$  as a function of the bare mode spacing ratio  $\Omega$ . Upper: experimental far-field patterns observed in the mode-locked plateau with  $P/Q = 1/4$ .

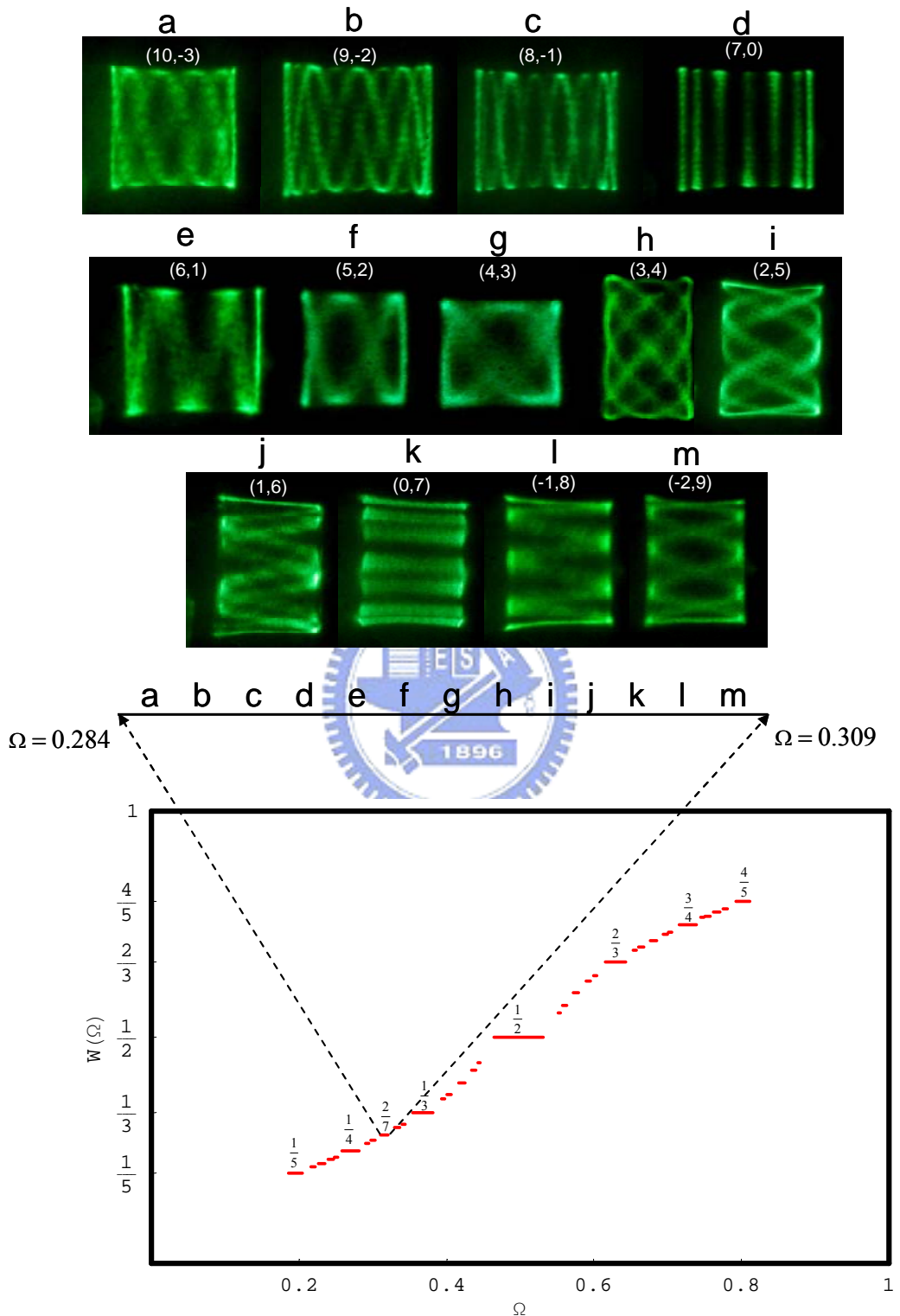


Fig. 3.3.9 Bottom: Experimental mode-locked ratio  $P/Q$  as a function of the bare mode-spacing ratio  $\Omega$ . Upper: experimental far-field patterns observed in the mode-locked plateau with  $P/Q = 2/7$ .

### 3.4 Spatially Localized Patterns Generated from Macroscopic Superposition of 3D Coherent Laser Waves

In recent years coherent wave properties of mesoscopic physics have been studied for understanding the pattern formations of laser modes such as honeycomb patterns [34], whispering gallery modes [35-36], and high-order transverse patterns [37-38]. Coherence plays an important role not only in optical waves such as pattern formation of nonlinear optical fields [39-41] but also in matter waves such as spatial interference patterns of Bose-Einstein condensates [42-44] for connecting the relation between quantum-classical correspondences. The coherence of Bose-Einstein condensates represents that the system should be characterized by a well-controlled phase to form the spatial interference patterns, however it is the most difficult point to control the Bose-Einstein condensates. Frequency beating and transverse-mode locking of coherent waves in nonlinear optical resonators have been focused in mesoscopic regime of modern physics [45-47]. Furthermore, recent experimental and theoretical studies have verified that the coherent superposition of degenerate or nearly degenerate quantum state can result in mesoscopic quantum wave functions localized on periodic orbits in the classical counterpart of the given system [48-49]. Perceivably, coherent wave properties are critical in a considerable number of physical systems to connect the quantum-classical correspondence in mesoscopic regime [50-53].

While the issue of quantum superposition of macroscopic states has been discussed by Schrödinger in 1935 [54], there has been growing attention to the generation and manipulation of the superposition states [55-56]. In this experiment we investigate the spatially localized patterns from superposition of 3D coherent optical modes localized on Lissajous parametric surface. The spatially localized patterns from the superposition of 3D coherent modes provide analogous evidences for the existence of macroscopic quantum superposition states. Experimental results [57] show that in a high-Q symmetric laser cavity the longitudinal-transverse coupling leads to the formation of 3D coherent waves localized on

Lissajous parametric surfaces which are formed by the Lissajous curves with the relative phase varying with the longitudinal direction. By the superposition of two coherent optical modes with different close Fresnel number, the spatial interference patterns become structure-localized on Lissajous parametric surface which represent the spatial beating of the two coherent optical modes in the resonator. Theoretical analysis reveals that the superposition of optical coherent modes with different order leads to different kinds of structured-localized patterns which can be related to the beating phenomenon of different but close frequencies in time domain. With the good agreement of theoretical analysis and experimental results, the formation of spatially interfered structure-localized patterns can provide a useful aspect for the coherent wave properties in mesoscopic physics.

### 3.4.1 Experimental Setup and Results

The formation of the nearly complete devil's staircase from the wave patterns localized on the Lissajous parametric surface has been realized in the degenerate laser resonator. However, the index order of the laser modes is not high enough to explore the super-high-order 3D coherent optical modes to generate the interference pattern from the superposition of coherent modes with different orders. The resonator configuration is basically similar to that used in section 3.3 but with different size of gain medium with sides of 10 mm and length of 2 mm shown in Fig. 3.4.1. In this section we investigate the spatially localized patterns from interference of 3D coherent optical waves localized on Lissajous parametric surface. The modification of the cavity medium size makes the generation of super-high-order coherent optical waves to be flexibly controlled. In other words, the large area of gain medium provides an improvement to generate the super-high-order 3D coherent optical waves. To generate the super-high-order laser modes, we control the off-axis pump positions on the gain medium with the transverse orders  $n$  and  $m$  in the range of 500 to 1000.

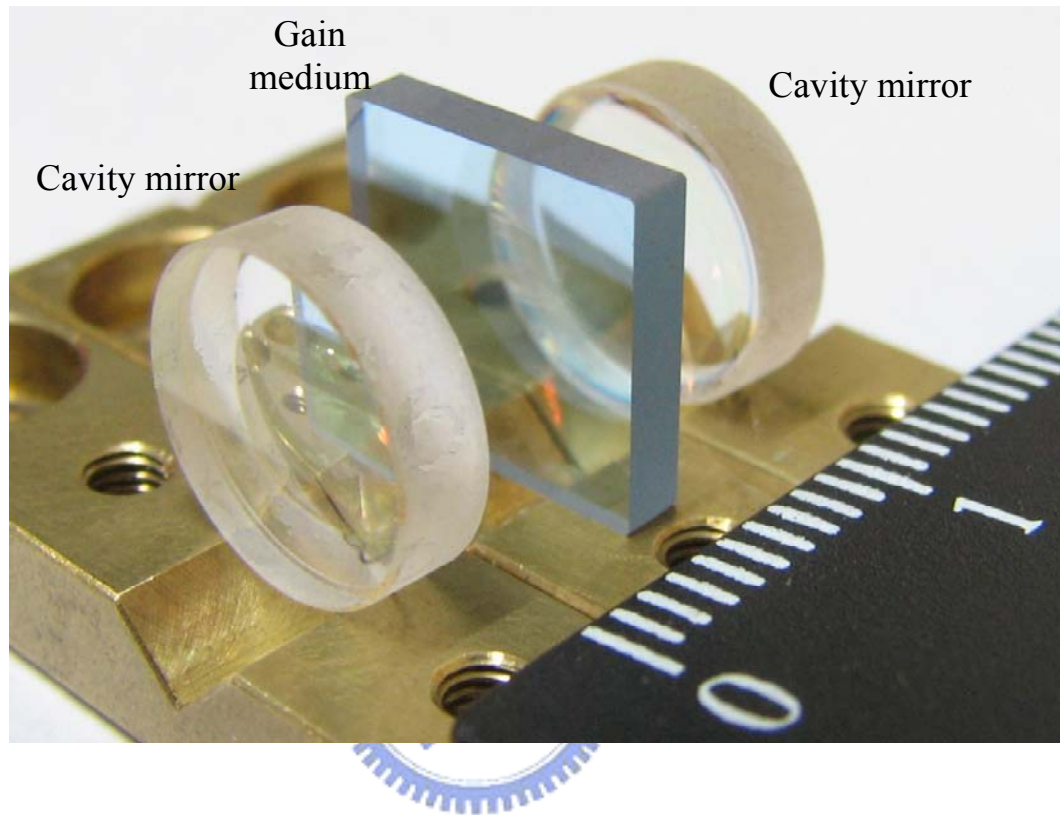


Fig. 3.4.1 Photograph of the experimental laser cavity.

Experimental results revealed that the far-field transverse patterns become spatially structure localized on the classical Lissajous trajectory from the interference of the super-high-order coherent optical waves. Here we select several spatially localized patterns with Lissajous transverse patterns of different cavity length in Fig. 3.4.2. The figure shows the two kinds of structure localized patterns which the top two rows indicate the dot-like patterns localized on the Lissajous trajectory and the third row indicates the line-like patterns localized on the Lissajous trajectory with different cavity length. The pump positions on the gain medium were controlled to excite the 3D coherent optical waves with the vicinity of transverse orders. With adjusting the cavity length to manipulate the mode size inside the resonator, the super-high-order coherent modes can be generated to achieve the superposition condition. The following analysis will verify that the interference patterns of super-high-order 3D coherent optical modes which are localized on the Lissajous parametric surface can lead to be further spatially localized to form the dot-like or line-like patterns with Lissajous transverse trajectory.



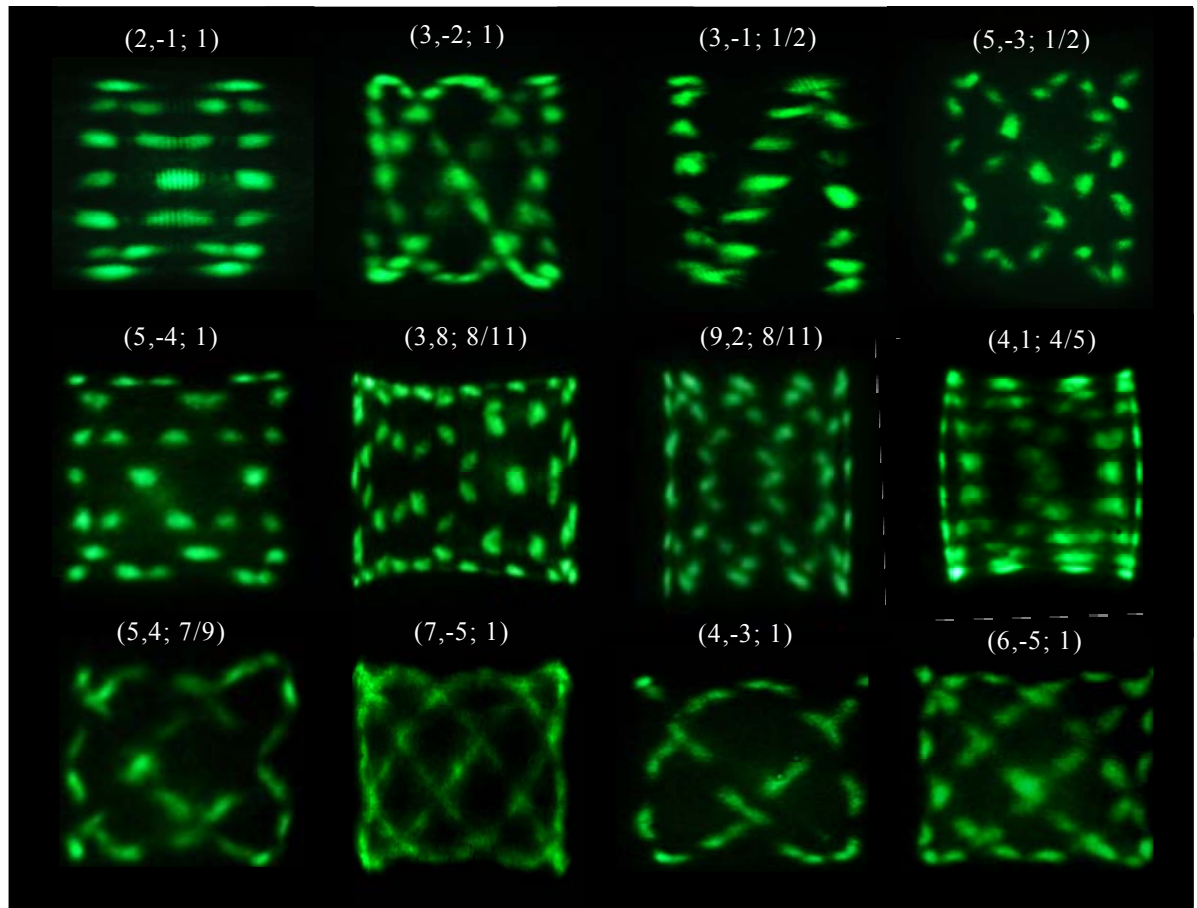


Fig. 3.4.2 Typical experimental far-field patterns observed in different cavity lengths for different indices  $(p, q; P/Q)$ .

### 3.4.2 Analysis and Theoretical Results

It follows from what has been said that the wave function  $\Psi_{m_o, n_o}^{p, q}(x, y, z; \phi_o)$  represents the 3D coherent optical mode with Lissajous transverse pattern from the coherent superposition of the modes  $\Phi_{m_o + pk, n_o + qk}(x, y, z; \phi_o)$  with the phase factor  $\phi(z)$ . By the superposition of the 3D coherent optical modes localized on the Lissajous parametric surface with different transverse mode indices  $n$  and  $m$ , the spatially localized patterns from the interference of 3D coherent optical waves can be realized. Nevertheless, the relative phase  $\phi_o$  has been verified to play a vital role in the quantum-classical connection. Here we choose  $\phi_o = 0$  and  $M=6$  to construct the spatially localized far-field patterns of the experimental results. Figure 3.4.3 reveals the spatially localized patterns which are the superposition of 3D coherent optical modes with different transverse mode indices such as  $\Psi_{70,70}^{5,4} + \Psi_{73,73}^{5,4}$  and  $\Psi_{70,70}^{5,4} + \Psi_{80,80}^{5,4}$ . Apparently, the spatially localized patterns become line-like modes from the interference of two coherent optical waves with close transverse orders. Moreover, the spatially localized patterns become dot-like modes from the interference of two coherent optical waves with far transverse orders. As a result of the calculation limit of mathematical software, the theoretical patterns with the transverse orders in the range of 140 to 160 are not localized completely as the experimental results with the transverse orders in the range of 500 to 1000. However the tendency of the theoretical appearance is found to be in good agreement with the experimental patterns. It is worthwhile to mention that the interference patterns which are the superposition of the 3D coherent optical modes with different transverse indices can be analog to the beating phenomenon of different but close frequencies in time domain. Until now there has been no experimental evidence of the spatially localized patterns from interference of super-high-order 3D coherent optical waves in mesoscopic regime.

The phase factor  $\phi(z)$  which arises from the Gouy phase difference between the HG

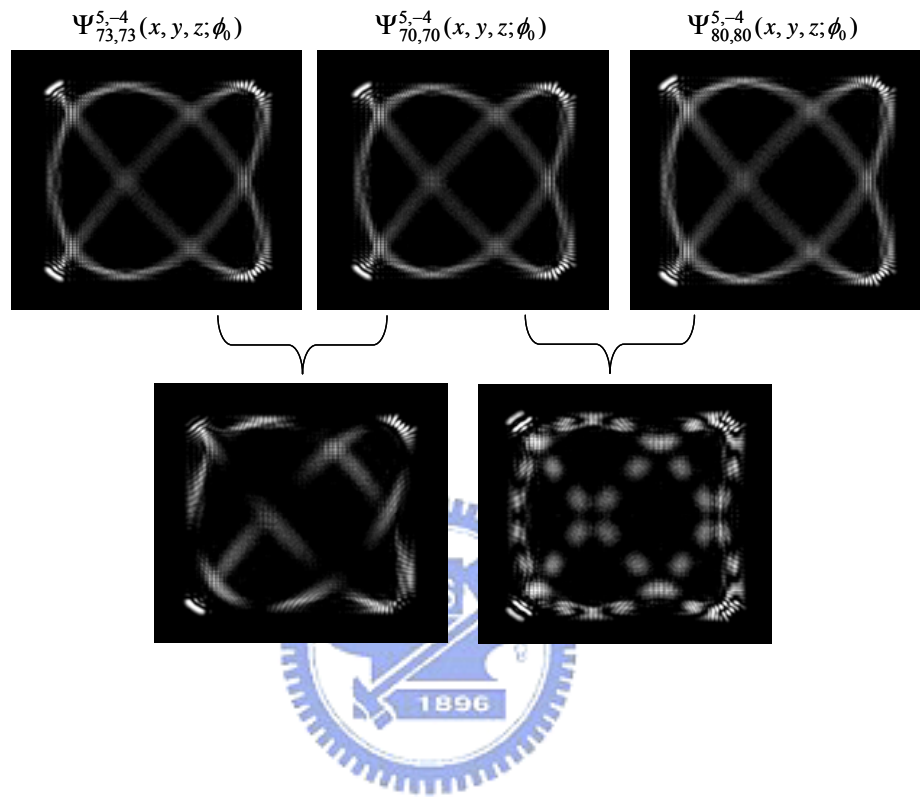


Fig. 3.4.3 Upper: Numerical results of 3D coherent modes according to different transverse orders. Bottom: Numerical results of the superposition from the coherent modes with different orders.

modes with distinct transverse orders is verified to play an important role in the 3D coherent waves localized on Lissajous parametric surfaces. Furthermore, the tomographic transverse patterns inside the cavity displayed the revolution of the spatially localized patterns along the longitudinal axis to form a complete 3D interference patterns from the superposition of 3D coherent optical waves. Figure 3.4.4 (a) shows the experimental tomographic transverse patterns observed at  $\Omega \approx 0.84$ . The experimental patterns are found to be in good agreement with the feature of the theoretical results shown in Fig. 3.4.4 (b). Furthermore, the spatially interfered patterns which were found to be structure localized on the Lissajous parametric surface are clearly visualized. It is worthwhile to emphasize that the Gouy phase of the coherent modes with different transverse orders is predominant in the degenerate laser cavity to induce the phase difference of the spatially localized patterns in the different positions of z-axis. According to the analysis mentioned in last section, the appearance of the Lissajous waves signifies the mode-spacing ratios to be locked to rational numbers  $P/Q$ . Continuously controlling the pump position of the off-axis corresponding to the mode size in proper cavity length, the super-high-order coherent modes can be generated flexibly and the superposition of the coherent modes can be achieved in the laser cavity. Figure 3.4.5 shows the interference patterns of the superposition of the super-high-order coherent modes with strongly localized dot-like Lissajous patterns. The structure of the spatially localized patterns is highly stable because of the mode-locked effect in the nonlinear resonator.

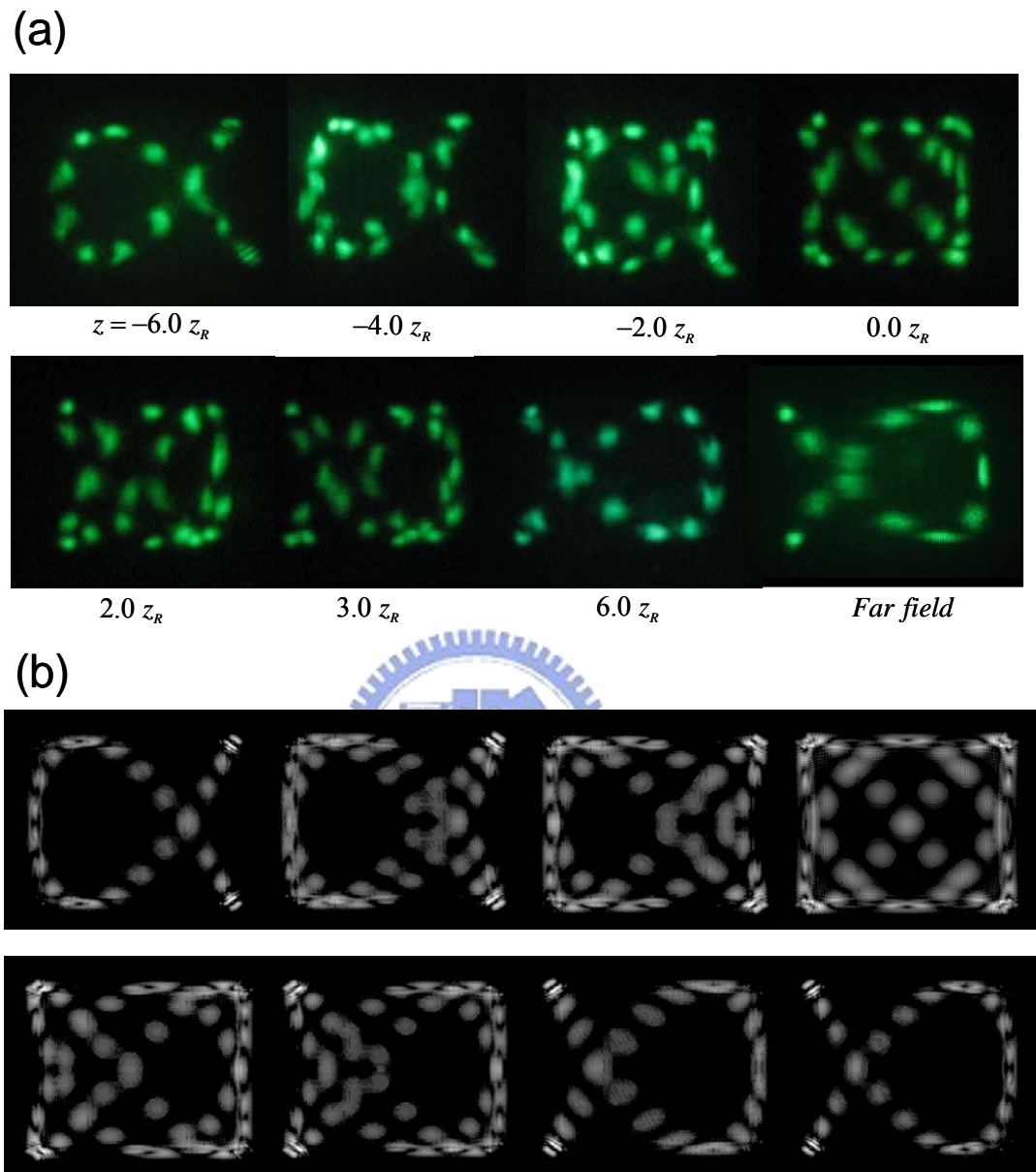


Fig. 3.4.4 (a) Experimental tomographic transverse patterns inside the cavity observed at  $\Omega \approx 0.84$ . (b) Numerical results corresponding to (a).

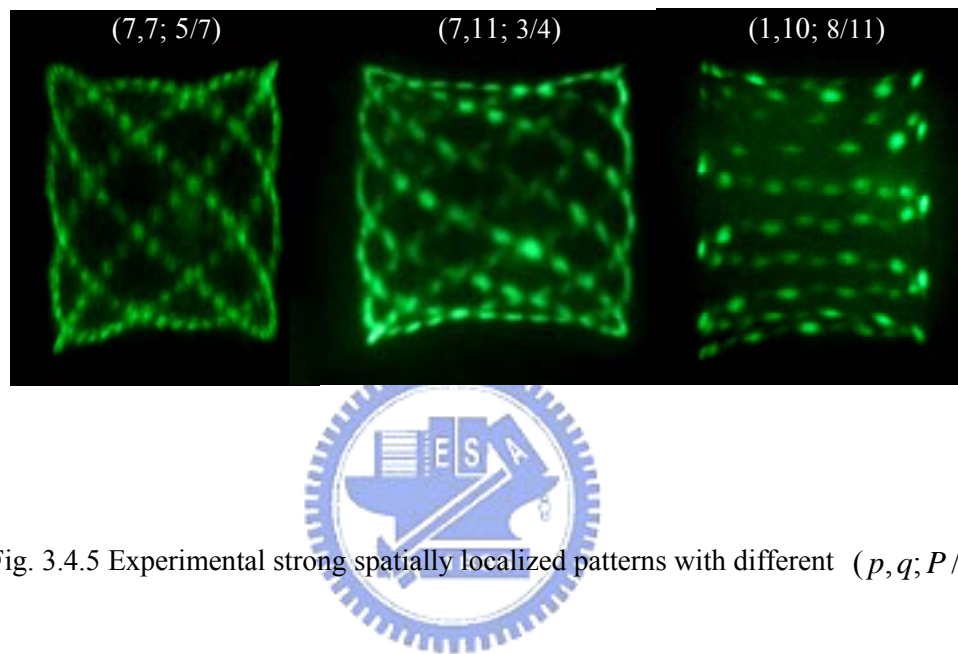


Fig. 3.4.5 Experimental strong spatially localized patterns with different  $(p, q; P / Q)$ .

### 3.4.3 Summary

In summary, we have used an off-axis focused pumping laser system with a large-size gain medium to generate various super-high-order coherent modes. The superposition of 3D coherent modes which are caused by the longitudinal-transverse coupling and the mode-locking has been verified to lead to the formation of spatially localized patterns on the Lissajous parametric surface in the mesoscopic regime. The theoretical analysis has revealed that the superposition of the coherent modes with different transverse orders leads to dot-like or line-like transverse patterns which are corresponding to the difference of transverse orders of the coherent modes. Furthermore, the structures of the interference patterns are highly stable and the experimental results are easily reproducible in the degenerate laser cavity. Our studies may provide some useful insights into the coherent superposition problems with optical coherent waves in mesoscopic regime.



## REFERENCES

- [1] A. Bohr and B. R. Mottelson, *Nuclear Structure* (Benjamin, New York, 1975), Vol. 2.
- [2] M. Brack, Rev. Mod. Phys. **65**, 677 (1993).
- [3] S. M. Reimann and M. Manninen, Rev. Mod. Phys. **74**, 1283 (2002).
- [4] R. K. Bhaduri, S. Li, K. Tanaka, and J. C. Waddington, J. Phys. A **27**, L553 (1994).
- [5] B. L. Johnson and G. Kirczenow, Europhys. Lett. **51**, 367 (2000).
- [6] I.V. Zozoulenko and K. F. Berggren, Phys. Rev. B **56**, 6931 (1997).
- [7] R. Narevich, R. E. Prange, and O. Zaitsev, Phys. Rev. E **62**, 2046 (2000).
- [8] K. F. Huang, Y. F. Chen, H. C. Lai, and Y. P. Lan, Phys. Rev. Lett. **89**, 224102 (2002).
- [9] Y. F. Chen and Y. P. Lan, Phys. Rev. A **66**, 053812 (2002).
- [10] Y. F. Chen, K. F. Huang, H. C. Lai, and Y. P. Lan, Phys. Rev. E **68**, 026210 (2003).
- [11] H. G. Shuster, *Deterministic Chaos* (VCH Verlag, Weinheim, 1988).
- [12] E. Ott, *Chaos in Dynamic System* (Cambridge University Press, Cambridge, 1993).
- [13] A. Pikovsky, M. Rosenblum, and J. Kurths, *Synchronization* (Cambridge University Press, Cambridge, 2001).
- [14] J. Stavans, F. Heslot, and A. Libchaber, Phys. Rev. Lett. **55**, 596 (1985).
- [15] S. E. Brown, G. Mozurkewich, and G. Gruenner, Phys. Rev. Lett. **52**, 2277 (1984).
- [16] A. A. Middleton, O. Biham, P. B. Littlewood, and P. Sibani, Phys. Rev. Lett. **68**, 1586 (1992).
- [17] P. Alstrøm and M. T. Levinsen, Phys. Rev. B **31**, 2753 (1985).
- [18] E. Orignac and T. Giamarchi, Phys. Rev. B **64**, 144515 (2001).
- [19] A. L. Lin, M. Bertram, K. Martinez, and H. L. Swinney, Phys. Rev. Lett. **84**, 4240 (2000).
- [20] D. Baums, W. Elsaesser, and E. O. Goebel, Phys. Rev. Lett. **63**, 155 (1989).
- [21] C. Reichhardt and F. Nori, Phys. Rev. Lett. **82**, 414 (1999).
- [22] A. Macor, F. Doveil, and Y. Elskens, Phys. Rev. Lett. **95**, 264102 (2005).

- [23] D. Hennequin, D. Dangoisse, and P. Glorieux, Phys. Rev. A **42**, 6966 (1990).
- [24] Statics and Dynamics of Nonlinear Systems, Sprinnger-Verlag, Berlin(1983).
- [25] P. Bak, Phys. Today **39**, No. 12, 38 (1986).
- [26] V. N. Belykh, N. F. Pedersen, O. H. Sorensen, Phys. Rev. B 16, 4860 (1977).
- [27] J. Maselko, H. L. Swinney, Phys. Scr. T9, 35 (1985).
- [28] S. Martin, W. Martienssen, Phys. Rev. Lett. 56, 1522 (1986).
- [29] Y. F. Chen, K. F. Huang, and Y. P. Lan, Phys. Rev. E **66**, 046215 (2002).
- [30] Y. F. Chen, K. F. Huang, and Y. P. Lan, Phys. Rev. E **66**, 066210 (2002).
- [31] Y. F. Chen and K. F. Huang, Phys. Rev. E **68**, 066207 (2003).
- [32] Y. F. Chen and K. F. Huang, J. Phys. A **36**, 7751 (2003).
- [33] Y. F. Chen, Y. P. Lan, and K. F. Huang, Phys. Rev. A **68**, 043803 (2003).
- [34] Ryan S. Bennink, Vincent Wong, Alberto M. Marino, David L. Aronstein, Robert W. Boyd, C. R. Stroud, Jr., and Svetlana Lukishova, Phys. Rev. Lett. **88**, 113901 (2002).
- [35] F. Sugihwo, M.C. Larson and J.S. Harris, Jr, Electronics Lett. **33**, 17 (1997).
- [36] S. L. McCall, A. F. J. Levi, R. E. Slusher, S. J. Pearton, and R. A. Logan, Appt. Phys. Lett. **60** , 3 (1992).
- [37] Y. F. Chen, Y. P. Lan, Phys. Rev. A. **66**, 053812 (2002).
- [38] Y. F. Chen, T. H. Lu, and K. F. Huang, Phys. Rev. Lett. **96**, 033901 (2006).
- [39] Y. F. Chen, K. F. Huang, and Y. P. Lan, Phys. Rev. E. **66**, 046215 (2002).
- [40] Y. F. Chen, K. F. Huang, and Y. P. Lan, Phys. Rev. E. **66**, 066210 (2002).
- [41] Y. F. Chen, K. F. Huang, Phys. Rev. E. **68**, 066207 (2003).
- [42] Shujuan Liu, Hongwei Xiong, Zhijun Xu, and Guoxiang Huang, J. Phys. B: At. Mol. Opt. Phys. **36** 2083 (2003).
- [43] Jan Chwedenczuk, Paweł Zieliński, Kazimierz Rzaewski, and Marek Trippenbach, Phys. Rev. Lett. **97**, 170404 (2006).
- [44] P. Zieliński, J. Chwedenczuk, A. Veitia, K. Rzazewski, and M. Trippenbach, Phys. Rev. Lett.

**94**, 200401 (2005).

[45] L. A. Lugiato, C. Oldano, and L. M. Narducci, *J. Opt. Soc. Am. B* **5**, 879 (1988).

[46] E. Louvergneaux, G. Slekys, D. Dangoisse, and P. Glorieux, *Phys. Rev. A* **57**, 4899 (1998).

[47] R. Gordon, A. P. Heberle, and J. R. A. Cleaver, *Appl. Phys. Lett.* **81**, 4523 (2002).

[48] I. V. Zozoulenko and K. F. Berggren, *Phys. Rev. B* **56**, 6931 (1997).

[49] R. Narevich, R. E. Prange, and O. Zaitsev, *Phys. Rev. E* **62**, 2046 (2000).

[50] Luz V. Vela-Arevalo and Ronald F. Fox, *Phys. Rev. A* **71**, 063403 (2005).

[51] Ronald F. Fox and Mee Hyang Choi, *Phys. Rev. A* **61**, 032107 (2000).

[52] J. I. Cirac, M. Lewenstein, K. Molmer, and P. Zoller, *Rev. A* **57**, 1208 (1998).

[53] V. V. Dodonov, *J. Opt. B: Quantum Semiclass. Opt.* **4**, R1 (2002).

[54] E. Schrödinger, *Naturwissenschaften* **23**, 807 (1935).

[55] X. B. Zou, Y. L. Dong, and G. C. Guo, *Phys. Rev. A* **74**, 045601 (2006).

[56] Moorad Alexanian and Subir K. Bose, *Phys. Rev. A* **65**, 033819 (2002).

[57] Y. F. Chen, T. H. Lu, K. W. Su, and K. F. Huang, *Phys. Rev. Lett.* **96**, 213902 (2006).

# Chapter 4

## Polarization Singularities in Hemispherical Cavity

Recently, singular optics has become an important topic in modern physics. In 1974, J. F. Nye and M. V. Berry proposed the notion about phase singularities (optical vortices) which are points in the plane and lines in space where the phase of an optical field becomes undefined [1]. The phase singularities in complex scalar waves have been discussed extensively in lasers [2-5], and other optical beams [6-7]. Furthermore, the phase singularity also provides some unique applications [8-9].

In addition to phase singularities of the scalar field, there are two types of singularities of the polarization vector field should be mentioned: Vector singularities and Stokes singularities [10-12]. The importance of the vector singularities has been explored in the optical coherent waves with the representation of spatial structures and polarization states [13-16]. However, the more general state of the optical field with two orthogonal components is elliptically polarized state which leads to two special conditions of Stokes singularities: *C* lines and *L* surfaces [17]. In this chapter we will introduce the polarization characteristics of light and verify the importance in the specific laser cavity.

### 4.1 Polarization and Stokes Parameter

Christian Huygens was the first to suggest that light was not a scalar quantity based on his work on the propagation of light through crystals. It appeared that light had “sides” in the

words of Newton. This nature of light is called polarization. The polarization light is one of its important and fundamental properties, the others being its intensity, frequency, and coherence [18-19]. Polarization is a property of transverse waves which describes the orientation of the oscillations in the plane perpendicular to the direction of traveling waves. In electrodynamics, polarization characterizes electromagnetic waves, such as light, by specifying the direction of the electric field of waves. Longitudinal waves such as sound waves in air or liquids do not exhibit polarization, because for the direction of oscillation of these waves is along the direction of wave's travel. The simplest manifestation of polarization to visualize is a plane wave, which is a good approximation of most light waves. All electromagnetic waves propagating in free space or in a uniform material have electric and magnetic fields perpendicular to the direction of propagation. However, when considering polarization, the electric field vector is described and the magnetic field is ignored since it is perpendicular to the electric field and proportional to it. Figure 4.1.1 shows some examples of the evolution of the electric field vector with time (the vertical axes), along with its  $x$  and  $y$  components, and the path traced by the tip of the vector in the plane. In Fig. 4.1.1 (a), the two orthogonal components are in phase. In this case the ratio of the strengths of the two components is constant, so the direction of the electric vector is constant. Since the tip of the vector traces out a single line in the plane, this special case is called linear polarization. The direction of this line depends on the relative amplitudes of the two components. In Fig. 4.1.1 (b), the two orthogonal components have exactly the same amplitude and are exactly ninety degrees out of phase. In this case one component is zero when the other component is at maximum or minimum amplitude. There are two possible phase relationships that satisfy this requirement: the  $x$  component can be ninety degrees ahead of the  $y$  component or it can be ninety degrees behind the  $y$  component. In this special case the electric vector traces out a circle in the plane, so this special case is called circular polarization. The direction the field rotates in depends on which of the two phase relationships exists. These cases are called right-hand circular

polarization and left-hand circular polarization, depending on which way the electric vector rotates. In all other cases, where the two components are not in phase and either do not have the same amplitude or are not ninety degrees out of phase, the polarization is called elliptical polarization because the electric vector traces out an ellipse in the plane. This is shown in Fig. 4.1.1 (c). For high-order transverse patterns, there are three kinds of polarization states embedded in the light beams such as shown in Fig. 4.1.2 which represents azimuthally polarized, circularly polarized, and radially polarized respectively.



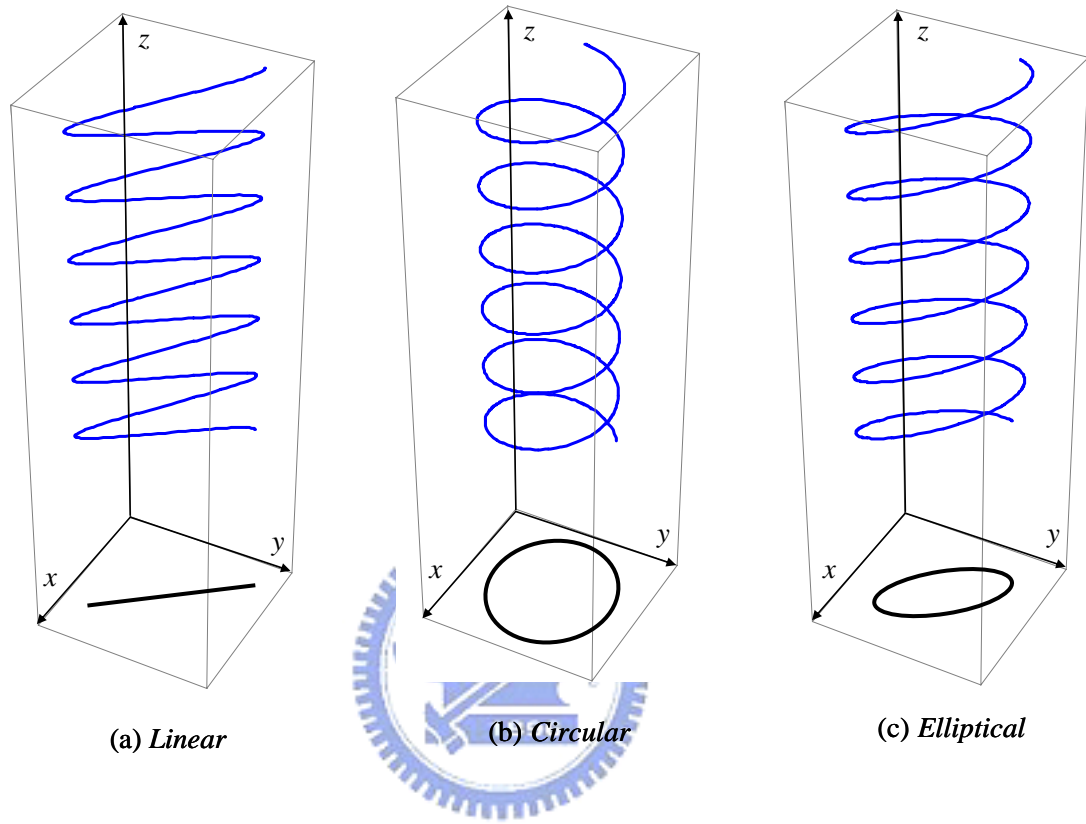


Fig. 4.1.1 The evolution of the electric field vector leads to different kinds of polarization states: (a) Linear, (b) Circular, (c) Elliptical.

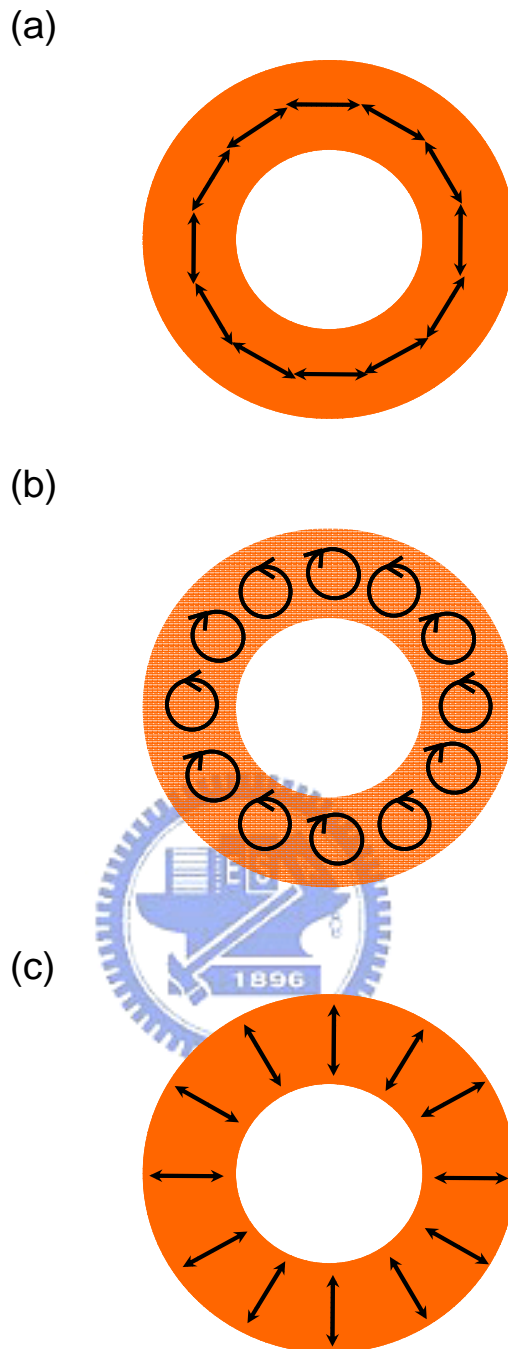


Fig. 4.1.2 Three kinds of polarization states of high-order transverse modes: (a) Azimuthally polarized, (b) Circularly polarized, (c) Radially polarized.

In order to understand the Stokes parameter we have to consider a pair of plane waves that are orthogonal to each other in space and take to be  $z = 0$ :

$$\begin{aligned} E_x(t) &= E_{0x}(t) \cos[\omega t + \delta_x] = \operatorname{Re}[E_{0x}(t) e^{i(\omega t + \delta_x)}] \\ E_y(t) &= E_{0y}(t) \cos[\omega t + \delta_y] = \operatorname{Re}[E_{0y}(t) e^{i(\omega t + \delta_y)}] \end{aligned} \quad (4.1.1)$$

where  $E_{0x}(t)$  and  $E_{0y}(t)$  are the instantaneous amplitudes,  $\omega$  is the instantaneous angular frequency, and  $\delta_x$  and  $\delta_y$  are the instantaneous phase factors. Equation (4.1.1) can be written as

$$\begin{aligned} \frac{E_x(t)}{E_{0x}(t)} &= \cos[\omega t] \cos[\delta_x] - \sin[\omega t] \sin[\delta_x] \\ \frac{E_y(t)}{E_{0y}(t)} &= \cos[\omega t] \cos[\delta_y] - \sin[\omega t] \sin[\delta_y] \end{aligned} \quad (4.1.2)$$

Hence,

$$\begin{aligned} \frac{E_x(t)}{E_{0x}(t)} \sin[\delta_y] - \frac{E_y(t)}{E_{0y}(t)} \sin[\delta_x] &= \cos[\omega t] \sin[\delta_y - \delta_x] \\ \frac{E_x(t)}{E_{0x}(t)} \cos[\delta_y] - \frac{E_y(t)}{E_{0y}(t)} \cos[\delta_x] &= \sin[\omega t] \sin[\delta_y - \delta_x] \end{aligned} \quad (4.1.3)$$

Squaring (4.1.3) and adding gives

$$\frac{E_x^2(t)}{E_{0x}^2(t)} + \frac{E_y^2(t)}{E_{0y}^2(t)} - 2 \frac{E_x(t) E_y(t)}{E_{0x}(t) E_{0y}(t)} \cos[\delta] = \sin^2[\delta] \quad (4.1.4)$$

where  $\delta = \delta_y - \delta_x$ . For monochromatic radiation, the amplitudes and phases are constant for all time, so Eq. (4.1.4) reduces to

$$\frac{E_x^2(t)}{E_{0x}^2} + \frac{E_y^2(t)}{E_{0y}^2} - 2 \frac{E_x(t)E_y(t)}{E_{0x}E_{0y}} \cos[\delta] = \sin^2[\delta] \quad . \quad (4.1.5)$$

While  $E_{0x}$ ,  $E_{0y}$ , and  $\delta$  are constants,  $E_x$  and  $E_y$  continue to be implicitly dependent on time. In order to represent Eq. (4.1.5) in terms of the observables of the optical field, we must take an average over the time of observation. However, in view of the periodicity of  $E_x(t)$  and  $E_y(t)$ , we have to average Eq. (4.1.5) only over a single period of oscillation. The time average is represented by the symbol  $\langle \dots \rangle$ . So we write Eq. (4.1.5) as

$$\frac{\langle E_x^2(t) \rangle}{E_{0x}^2} + \frac{\langle E_y^2(t) \rangle}{E_{0y}^2} - 2 \frac{\langle E_x(t)E_y(t) \rangle}{E_{0x}E_{0y}} \cos[\delta] = \sin^2[\delta] \quad , \quad (4.1.6)$$

where

$$\langle E_i(t)E_j(t) \rangle = \lim_{T \rightarrow \infty} \frac{1}{T} \int_0^T E_i(t)E_j(t)dt \quad , \quad i, j = x, y \quad . \quad (4.1.7)$$

Multiplying Eq. (4.1.6) by  $4E_{0x}^2E_{0y}^2$ , we can get that

$$4E_{0y}^2 \langle E_x^2(t) \rangle + 4E_{0x}^2 \langle E_y^2(t) \rangle - 8E_{0x}E_{0y} \langle E_x(t)E_y(t) \rangle \cos[\delta] = (2E_{0x}E_{0y} \sin[\delta])^2 \quad . \quad (4.1.8)$$

Using Eq. (4.1.7) and (4.1.1), we find that the average values are

$$\begin{aligned}
 \langle E_x^2(t) \rangle &= \frac{1}{2} E_{0x}^2 \\
 \langle E_y^2(t) \rangle &= \frac{1}{2} E_{0y}^2 \\
 \langle E_x(t)E_y(t) \rangle &= \frac{1}{2} E_{0x}E_{0y} \cos[\delta]
 \end{aligned} \quad . \quad (4.1.9)$$

Substituting Eq. (4.1.9) into (4.1.8) yields

$$2E_{0x}^2E_{0y}^2 + 2E_{0x}^2E_{0y}^2 - (2E_{0x}E_{0y} \cos[\delta])^2 = (2E_{0x}E_{0y} \sin[\delta])^2 \quad . \quad (4.1.10)$$

After some algebra, Eq. (4.1.10) can be represented as

$$(E_{0x}^2 + E_{0y}^2)^2 - (E_{0x}^2 - E_{0y}^2)^2 - (2E_{0x}E_{0y} \cos[\delta])^2 = (2E_{0x}E_{0y} \sin[\delta])^2 \quad . \quad (4.1.11)$$

We write the quantities above as

$$\begin{aligned}
 S_0 &= E_{0x}^2 + E_{0y}^2 \\
 S_1 &= E_{0x}^2 - E_{0y}^2 \\
 S_2 &= 2E_{0x}E_{0y} \cos[\delta] \\
 S_3 &= 2E_{0x}E_{0y} \sin[\delta]
 \end{aligned} \quad , \quad (4.1.12)$$

and then

$$S_0 = S_1^2 + S_2^2 + S_3^2. \quad (4.1.13)$$

The four quantities given in Eq. (4.1.12) are the Stokes polarization parameters for a plane wave. They were introduced by George Gabriel Stokes in 1852, as a mathematically convenient alternative to the more common description of incoherent or partially polarized radiation light. It is important to note that the Stokes parameters are real quantities. The first

Stokes parameter  $S_0$  is the total intensity of the light. The  $S_1$  describes the amount of linear horizontal or vertical polarization, the  $S_2$  describes the amount of linear  $+45^\circ$  or  $-45^\circ$  polarization, and the parameter  $S_3$  describes the amount of right or left circular polarization contained within the beam. Combining polarization ellipse and Stokes parameter, Eq. (4.1.12) can be represented as another mathematical form which can be related to a polarization state easily:

$$\begin{aligned}\frac{S_1}{S_0} &= \cos[2\chi]\cos[2\psi] \\ \frac{S_2}{S_0} &= \cos[2\chi]\sin[2\psi] \quad . \\ \frac{S_3}{S_0} &= \sin[2\chi]\end{aligned}\tag{4.1.14}$$

The Stokes parameters are almost identical to the equations relating Cartesian coordinates to Spherical coordinates where

$$\begin{aligned}x &= r \sin[\theta]\cos[\phi] \\ y &= r \sin[\theta]\sin[\phi] \\ z &= r \cos[\theta]\end{aligned}\tag{4.1.15}$$

and  $\theta = 90^\circ - 2\chi, \phi = 2\psi$ . In Fig. 4.1.3 we have drawn a sphere which is called Poincaré sphere expressing the polarization state of an optical beam in terms of  $\chi$  and  $\psi$  and allows us to describe its ellipticity and orientation on a sphere. The radius of the sphere is taken to be unity. The representation of the polarization state on a sphere was first introduced by Henri Poincaré in 1892. It is useful for describing the change in polarized light when it interacts with polarizing elements and some nonlinear phenomenon.

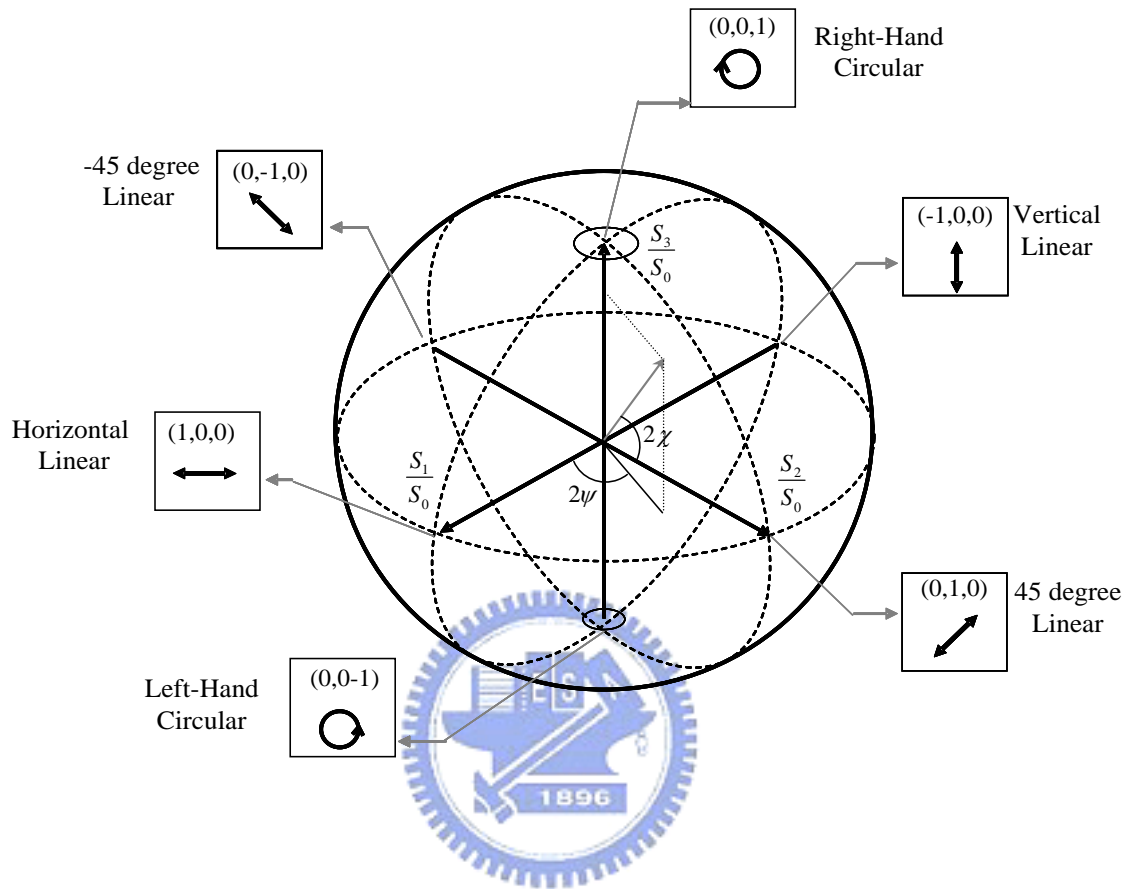


Fig. 4.1.3 The Poincaré representation of polarized light on a sphere.

## 4.2 Polarization Singularities

Singular optics which includes phase and polarization singularities has become an important topic in modern physics to understand the physics of light [20-21]. Recently, a considerable number of studies have been focused on experimental and theoretical results of phase singularities in scalar fields, known as wave front dislocations, such as optical vortices [22], vortex lattices in superconductors [23], quantum and microwave billiards [24], quantum Hall effects [25], and linear and nonlinear optics [26-28]. In addition to phase singularities in scalar fields, there are two types of polarization singularities in vector fields of paraxial optical beams, known as wave front disclinations, to be discussed: vector singularities and Stokes singularities [29]. Vector singularities (*V* points) are stationary points at which the orientation of the electric vector of a linearly polarized vector field becomes undefined. The importance of the vector singularities has been explored in the optical coherent waves with the representation of spatial structures and polarization states [30-33]. Recently, the complicated *V* point structure has been studied from the low-order [34] and high-order [35] space-dependent linearly polarized fields in transversely isotropic laser systems. However, the mapping of vector field singularities onto the scalar field vortices leads to many new consequences [29].

The more general state of optical field with two orthogonal components is elliptically polarized state which leads to two special conditions of Stokes singularities. *C* lines on which the field is circularly polarized and the orientations of the major and minor axes of the ellipse are undefined indicate the North and South Pole of the Poincaré sphere. *L* surfaces on which the field is linearly polarized and the handedness of the ellipse is undefined [36] indicate the equator of the Poincaré sphere. In paraxial optics, *C* lines present as isolated points in the observation plane and *L* surfaces present as continuous lines, *L* lines, which separate regions of right-handed and left-handed polarization [37-39]. With the experimental results of

microwaves [29] and optical waves [40-43], the importance of polarization singularities of elliptically polarized fields has been revealed.

## 4.3 Generalized Structures of Polarization Singularities in Laguerre-Gaussian Vector fields

Recently, a diode-pumped microchip laser has been employed to generate the propagation-dependent polarization vector fields with the longitudinal-transverse coupling and the entanglement of the polarization states [44]. However, the characteristics of polarization singularities are revealed with the theoretical wave representation only in the condition of single-ring wave pattern. In next section we demonstrate the general expression of the multiple structures of polarization singularities embedded in the multi-ring vector wave patterns. With the coherent superposition of orthogonal circularly polarized vortex modes composed of two Laguerre-Gaussian (LG) modes with different order, the general structures of the polarization singularities are systematically analyzed. The theoretical analyses reveal that the projection of the  $C$  lines on the transverse plane displays the intriguing petal structures. From the analytical results of the singularities, the polarization states of the experimental LG vector fields under propagation can be clearly demonstrated.

### 4.3.1 Experimental setup and results

In this experiment, the laser system was a diode-pumped Nd:YVO<sub>4</sub> microchip laser and the resonator was formed by a spherical mirror and a gain medium such as shown in Fig. 4.3.1. The spherical mirror was a 10-mm radius-of-curvature concave mirror with antireflection coating at the pumping wavelength on the entrance face ( $R<0.2\%$ ), high-reflection coating at lasing wavelength ( $R>99.8\%$ ), and high-transmission coating at the pumping wavelength on the other surface ( $T>95\%$ ). The gain medium was a 2.0 at.% Nd:YVO<sub>4</sub> crystal with the length of 2 mm. The laser crystal was precisely cut along the c-axis for high-level transverse isotropy

[45]. One planar surface of the laser crystal was coated for antireflection at the pumping and lasing wavelengths; the other surface was coated to be an output coupler with the reflectivity of 99%. The pump source was a 1-W 808-nm fiber-coupled laser diode with a core diameter of 100  $\mu\text{m}$  and a numerical aperture of 0.2. A focusing lens was used to re-image the pump beam into the laser crystal. The pump spot radius was controlled to be in the range of 50~200  $\mu\text{m}$ . The effective cavity length was set in the range of 9.6~9.9 mm to form a nearly hemispherical resonator, in which the fundamental cavity mode size was approximately 20  $\mu\text{m}$ . Since the pump-to-mode size ratio was significantly greater than unity, a variety of high-order transverse modes could be generated. The pump power was controlled to be near lasing threshold to maintain the single mode in the cavity to explore the characteristic of polarization. To measure the far-field pattern, the output beam was directly projected on a paper screen at a distance of  $\sim 50$  cm from the rear cavity mirror and the scattered light was captured by a digital camera.

Figures 4.3.2(a)-1(c) show experimental far-field transverse patterns with different radial index  $p$  and azimuthal index  $l$  which are represented as flower modes. Not only the single-ring but also the multi-ring is the general transverse mode formed by the propagation-dependent polarization states to prevail in the laser cavity. The fundamental mode is not excited because the pump-to-mode size ratio is significantly greater than unity and then the lasing threshold of fundamental mode is higher than that of high-order transverse modes. A microscope objective lens mounted on a translation stage was used to reimaging the tomographic transverse patterns at different propagation position onto a CCD camera. Figure 4.3.3 display the polarization-resolved transverse patterns at three different propagation positions:  $z = 0$ ,  $z = z_R$ , and  $z \gg z_R$ , where the  $Z_R$  is the Rayleigh range and  $Z_R = 1.26$  and 1.28 mm. It can be found that the polarization-resolved pattern represent as an azimuthally polarized flower mode at the beam waist ( $z = 0$ ), whereas it turns to be like a radially polarized flower mode at the far field ( $z \gg z_R$ ). Moreover, the polarization state at  $z = z_R$  was confirmed

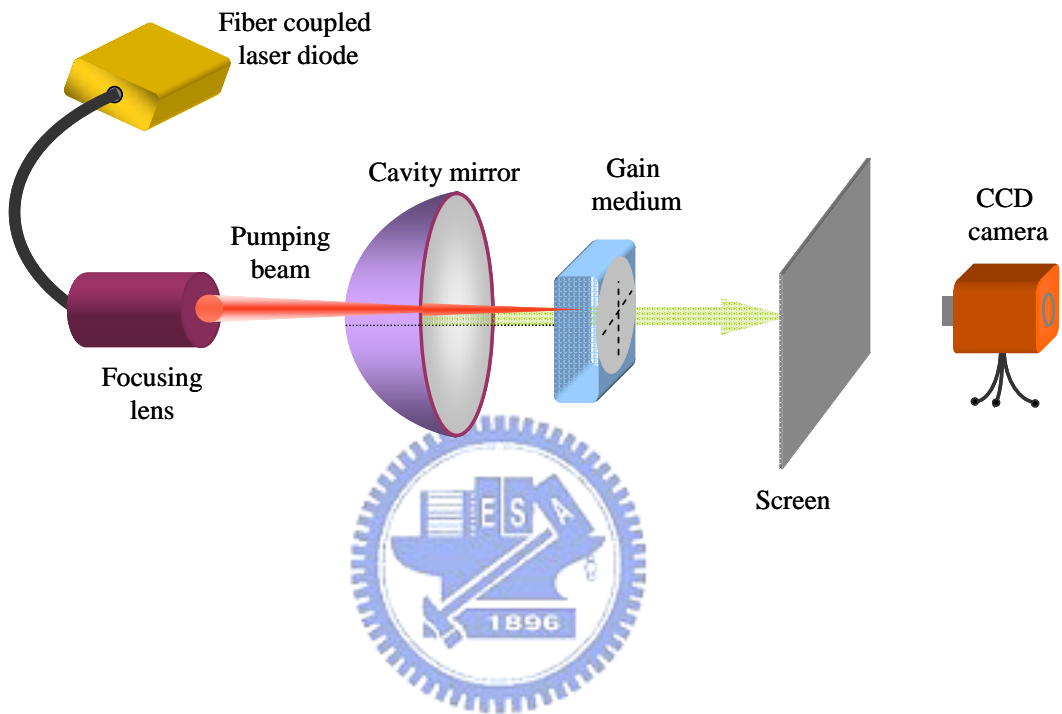


Fig. 4.3.1 Experimental setup for the generation of propagation-dependent polarization vector fields in a diode-pumped microchip laser in a hemi-spherical resonator.

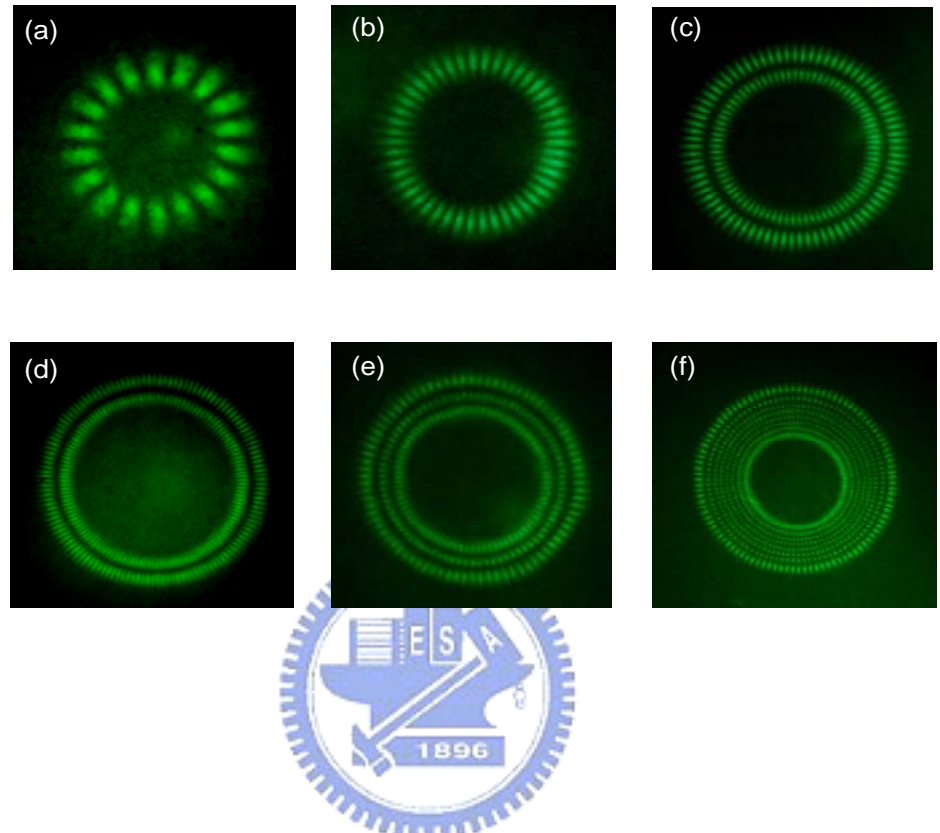


Fig. 4.3.2 Experimental far-field transverse patterns with different radial index  $p$  and azimuthal index  $l$ : (a) (0, 9), (b) (0, 23), (c) (1, 39), (d) (1, 66), (e) (2, 41), (f) (7, 100).

to behave as a circularly polarized flower mode by use of a quarter-wave plate. The polarization-resolved transverse modes formed by the three-dimensional (3D) coherent vector field provide an important aspect to explore the physics of polarization singularities. It is worthwhile to mention that the lasing modes are propagation-dependent polarization vector fields which are generated from the nearly hemispherical cavity. The following analysis will substantiate that the longitudinal-transverse coupling with the entanglement of the polarization states leads to the formation of 3D coherent vector fields in the isotropic laser cavity. Therefore, the generalized structures of polarization singularities in coherent vector fields with longitudinal-transverse coupling can be clearly revealed with the theoretical analysis.



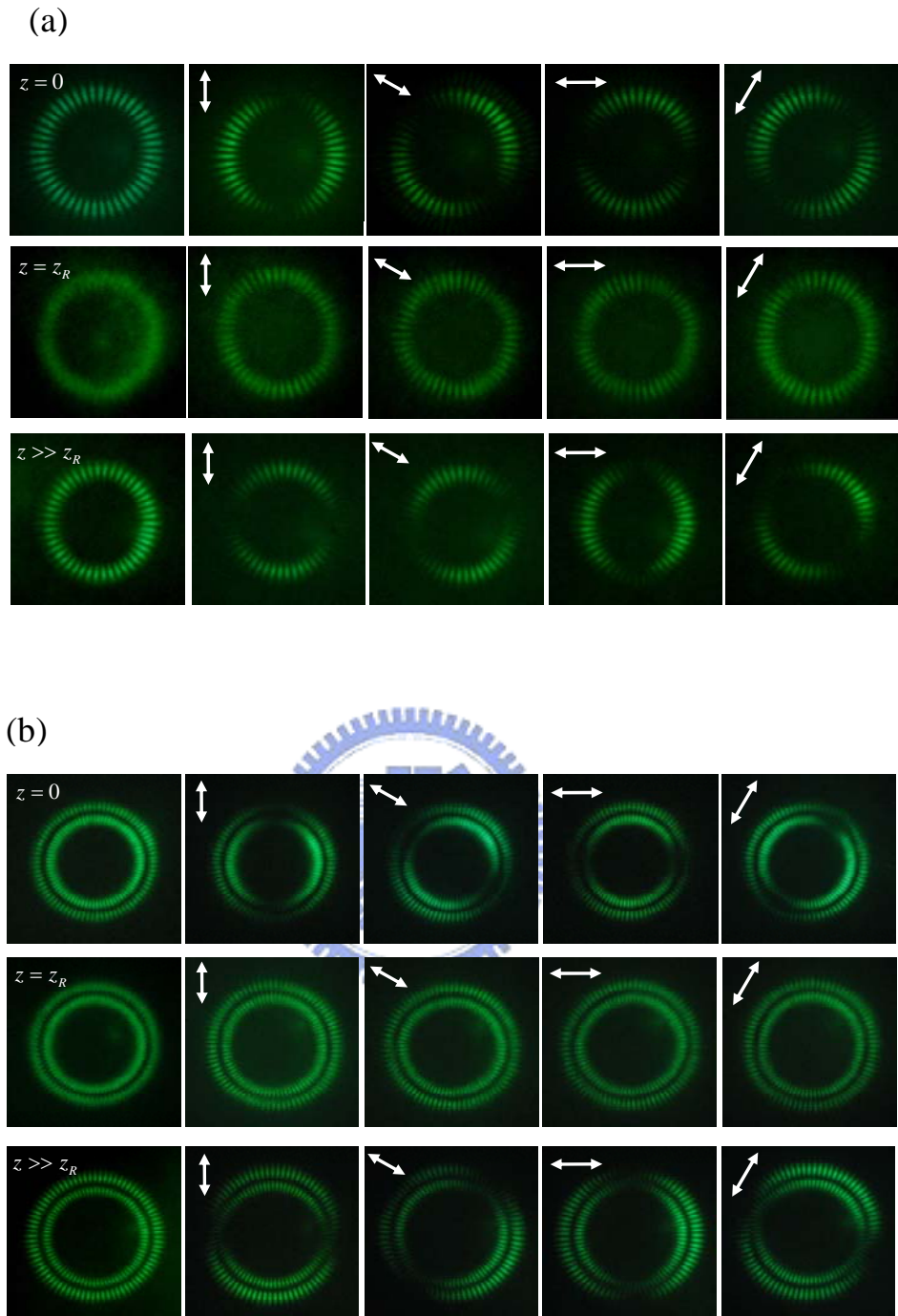


Fig. 4.3.3 Polarization-resolved transverse patterns for the experimental result at three different propagation positions:  $z = 0$ ,  $z = z_R$ , and  $z \gg z_R$ : (a) corresponding to Fig. 4.3.2 (b) where  $z_R = 1.26$  mm. (b) corresponding to Fig. 4.3.2 (c) where  $z_R = 1.28$  mm. The arrows indicate the transmission axis of the polarizer.  $z = z_R$ , and  $z \gg z_R$ , where  $z_R = 1.28$  mm.

### 4.3.2 Analytical Wave Functions for Experimental Patterns and Polarization Singularities

According to the lasing modes represented as flower modes in the transverse patterns, we start from the LG mode to be the basis of the experimental results. The wave function of LG mode with longitudinal index  $s$ , transverse radial index  $p$ , and transverse azimuthal index  $l$  in cylindrical coordinates  $(\rho, \phi, z)$  is given by  $\Psi_{p,l,s}(\rho, \phi, z) = e^{il\phi} \Phi_{p,l,s}(\rho, z)$ , where

$$\Phi_{p,l,s}(\rho, z) = \sqrt{\frac{2 p!}{\pi (p+|l|)!}} \frac{1}{w(z)} \left( \frac{\sqrt{2} \rho}{w(z)} \right)^{|l|} L_p^{|l|} \left( \frac{2 \rho^2}{w(z)^2} \right) \exp \left[ -\frac{\rho^2}{w(z)^2} \right] \times \exp \left\{ -ik_{p,l,s} z \left[ 1 + \frac{\rho^2}{2(z^2 + z_R^2)} \right] \right\} \exp [i(2p + |l| + 1)\theta_G(z)], \quad (4.3.1)$$

where  $w(z) = w_0 \sqrt{1 + (z/z_R)^2}$ ,  $w_0$  is the beam radius at the waist, and  $z_R = \pi w_0^2 / \lambda$  is the

Rayleigh range,  $L_p^l(\cdot)$  are the associated Laguerre polynomials,  $k_{p,l,s}$  is the wave number,

and  $\theta_G(z) = \tan^{-1}(z/z_R)$  is the Gouy phase. In the resonator with the effective length  $L$ , the

wave number  $k_{p,l,s}$  is given by  $k_{p,l,s}L = \pi [s + (2p + |l|)(\Delta f_T / \Delta f_L)]$ , where  $\Delta f_L = c/2L$

is the longitudinal mode spacing and  $\Delta f_T$  is the transverse mode spacing. It has been

verified [46] that the longitudinal-transverse coupling and mode-locking effect can lead to the

frequency locking among different transverse modes with the help of different longitudinal

orders when the ratio  $\Delta f_T / \Delta f_L$  is close to a simple fractional. As a result, the

configuration of the nearly hemispherical cavity refers to be  $\Delta f_T / \Delta f_L \approx 1/2$ , and the group

of LG modes  $\Psi_{p,l+2k,s-k}(\rho, \phi, z)$ , with  $k = 0, 1, 2, 3, \dots$ , forms an important family of frequency

degenerate states. With LG modes as the basis, the experimental vector fields can be

decomposed into a coherent superposition of orthogonal circularly polarized helical modes

$\bar{E} = E_R(\rho, \phi, z) \hat{a}_R + E_L(\rho, \phi, z) \hat{a}_L$ , where

$$E_R(\rho, \phi, z) = \left[ \Psi_{p, -(l+1), s-1}(\rho, \phi, z) - \Psi_{p, l-1, s}(\rho, \phi, z) \right] / \sqrt{2} \quad , \quad (4.3.2)$$

$$E_L(\rho, \phi, z) = \left[ \Psi_{p, l+1, s-1}(\rho, \phi, z) - \Psi_{p, -(l-1), s}(\rho, \phi, z) \right] / \sqrt{2} \quad , \quad (4.3.3)$$

and  $\hat{a}_R = (\hat{a}_x - i \hat{a}_y) / \sqrt{2}$  and  $\hat{a}_L = (\hat{a}_x + i \hat{a}_y) / \sqrt{2}$  are the helical basis unit vectors for the right- and left-handed circulation polarizations, respectively. Figure 4.3.4 displays the numerically reconstructed patterns for the experimental results shown in Fig. 4.3.3. There is a good agreement between the reconstructed and experimental patterns. From this point of view, the circularly polarized vortex modes indeed play an important role to form the propagation-dependent polarization vector fields. Equations (4.3.2) and (4.3.3) indicate that each circularly polarized component of the vector fields is composed of two LG modes with different order. It is worthwhile to mention that the frequency locking of two LG modes with different azimuthal orders arises from the longitudinal-transverse coupling in a nearly hemispherical cavity.

After some algebra, Eq. (4.3.2) and (4.3.3) for the general condition can be simplified as

$$E_R(\rho, \phi, z) = \left[ \tilde{\rho}_l^2 e^{-i2l\phi} e^{i2\theta_G(z)} - 1 \right] e^{i(l-1)\phi} \Phi_{p, l-1, s}(\rho, z) / \sqrt{2} \quad , \quad (4.3.4)$$

$$E_L(\rho, \phi, z) = \left[ \tilde{\rho}_l^2 e^{i2l\phi} e^{i2\theta_G(z)} - 1 \right] e^{-i(l-1)\phi} \Phi_{p, l-1, s}(\rho, z) / \sqrt{2} \quad , \quad (4.3.5)$$

where

$$\tilde{\rho}_l^2 = \left[ \sqrt{2} \rho / w(z) \right]^2 \left[ 1 / \sqrt{(l+p)(l+p+1)} \right] \left[ L_p^{l+1} \left( \frac{2\rho^2}{w(z)^2} \right) / L_p^{l-1} \left( \frac{2\rho^2}{w(z)^2} \right) \right]. \quad (4.3.6)$$

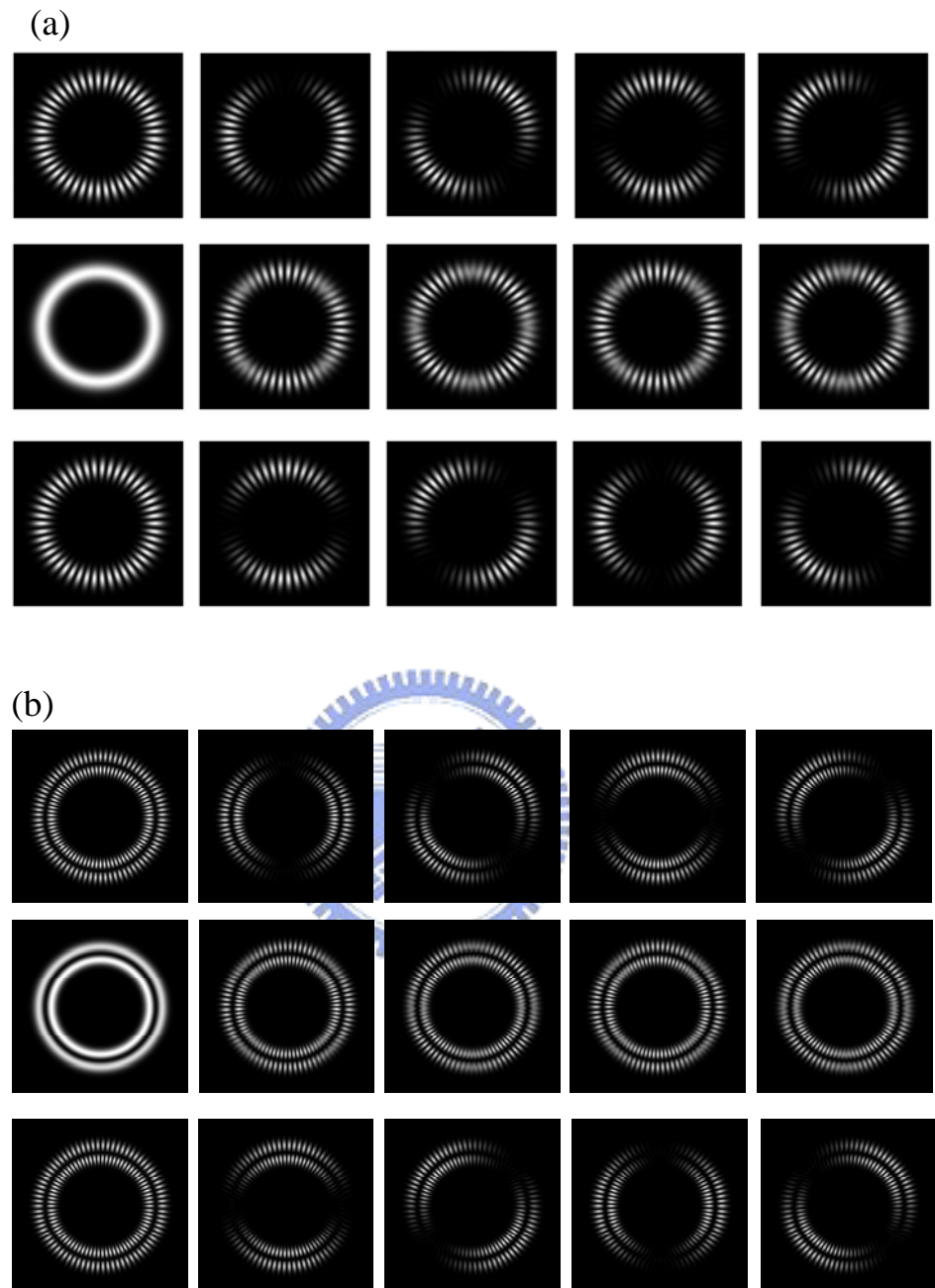
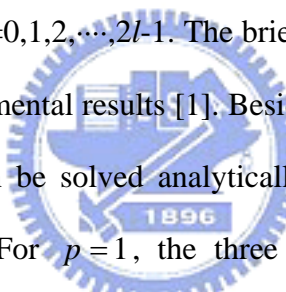


Fig. 4.3.4: (a) Numerically reconstructed patterns for the experimental results shown in Fig. 4.3.3 (a), (b) Numerically reconstructed patterns for the experimental results shown in Fig. 4.3.3 (b).

In the basis of circular polarizations, the condition for left-handed and right-handed  $C$  point loci can be given by  $E_R(\rho, \phi, z) = 0$  and  $E_L(\rho, \phi, z) = 0$ , respectively. For the paraxial 3D vector fields, the trajectories of  $C$  singularities can be expressed as the parametric curves with  $z$  as a variable. In addition to the central singularity at the origin, the expression in the bracket of Eq. (4.3.4) indicates the left-handed  $C$  point trajectories are determined by the two conditions: (1)  $\tilde{\rho}_l^2 = 1$  and  $e^{-i2l\phi} e^{i2\theta_G(z)} = 1$ , (2)  $\tilde{\rho}_l^2 = -1$  and  $e^{-i2l\phi} e^{i2\theta_G(z)} = -1$ . In general, there are  $2p+1$  solutions of the exact radius which the  $C$  points are symmetrically embedded in. Note that for  $p=0$  there are  $2l$  peripheral left-handed  $C$  points symmetrically arrayed on a circle of radius  $\rho_0 = \sqrt{\sqrt{l(l+1)} w(z)}/\sqrt{2}$  at angles  $\phi_m = (\theta_G(z) + m\pi)/l$  with  $m=0, 1, 2, \dots, 2l-1$  and  $2l$  peripheral right-handed  $C$  points on the same circle of radius at angles  $\phi_m = (-\theta_G(z) + m\pi)/l$  with  $m=0, 1, 2, \dots, 2l-1$ . The brief case of  $p=0$  has been verified to be in good agreement with experimental results [1]. Besides of  $p=0$ , the theoretical solution of radius with radial index  $p$  can be solved analytically for the cases  $p=1 \sim 3$ . Further, we analyzed the case of  $p \geq 1$ . For  $p=1$ , the three solutions of radius can be expressed analytically:



$$\rho_1 = \frac{1}{2} \sqrt{2 + l + \sqrt{(l+1)(l+2)} - \sqrt{6 + 7l + 2l^2 + 4\sqrt{(l+1)(l+2)} - 2l\sqrt{(l+1)(l+2)}}} w(z) \quad (4.3.7)$$

$$\rho_2 = \frac{1}{2} \sqrt{2 + l + \sqrt{(l+1)(l+2)} + \sqrt{6 + 7l + 2l^2 + 4\sqrt{(l+1)(l+2)} - 2l\sqrt{(l+1)(l+2)}}} w(z) \quad (4.3.8)$$

$$\rho_3 = \frac{1}{2} \sqrt{2 + l - \sqrt{(l+1)(l+2)} + \sqrt{6 + 7l + 2l^2 - 4\sqrt{(l+1)(l+2)} + 2l\sqrt{(l+1)(l+2)}}} w(z). \quad (4.3.9)$$

On the one hand there are  $2l$  peripheral left-handed and  $2l$  peripheral right-handed  $C$  points symmetrically arrayed at angles  $\phi_m = (\theta_G(z) + m\pi)/l$  and  $\phi_m = (-\theta_G(z) + m\pi)/l$  respectively with  $m=0,1,2,\dots,2l-1$  according to the circle radius in the situation of  $\tilde{\rho}_l^2 = 1$ , and on the other there are  $2l$  peripheral left-handed and  $2l$  peripheral right-handed  $C$  points symmetrically arrayed at angles  $\phi_m = (2\theta_G(z) + (2m+1)\pi)/2l$  and  $\phi_m = (-2\theta_G(z) + (2m+1)\pi)/2l$  respectively with  $m=0,1,2,\dots,2l-1$  according to the circle radius in the situation of  $\tilde{\rho}_l^2 = -1$ . As a result, there are  $2l(2p+1)$  left-handed  $C$  points and  $2l(2p+1)$  right-handed  $C$  points embedded in the polarization-dependent vector field. Therefore,  $C$  lines singularities embedded in the propagation-dependent polarization vector field with  $p=0$  form the hyperboloid structure. The theoretical results of the view from the propagation direction to the beam waist of the general structures of the  $C$  lines singularities with  $p=0 \sim 2$  and  $l=1 \sim 6$  are represented in Fig. 4.3.5-4.3.7. The different color of  $C$  line singularities represents the different allowable circle of radius according to the radial index  $p$  of the transverse modes. Therefore, the different radial position of the  $C$  line singularity with the same color implies the different propagation position of the propagation-dependent polarization vector field. The minimum of the radial position represents the beam waist and the maximum of the radial position represents the far field.

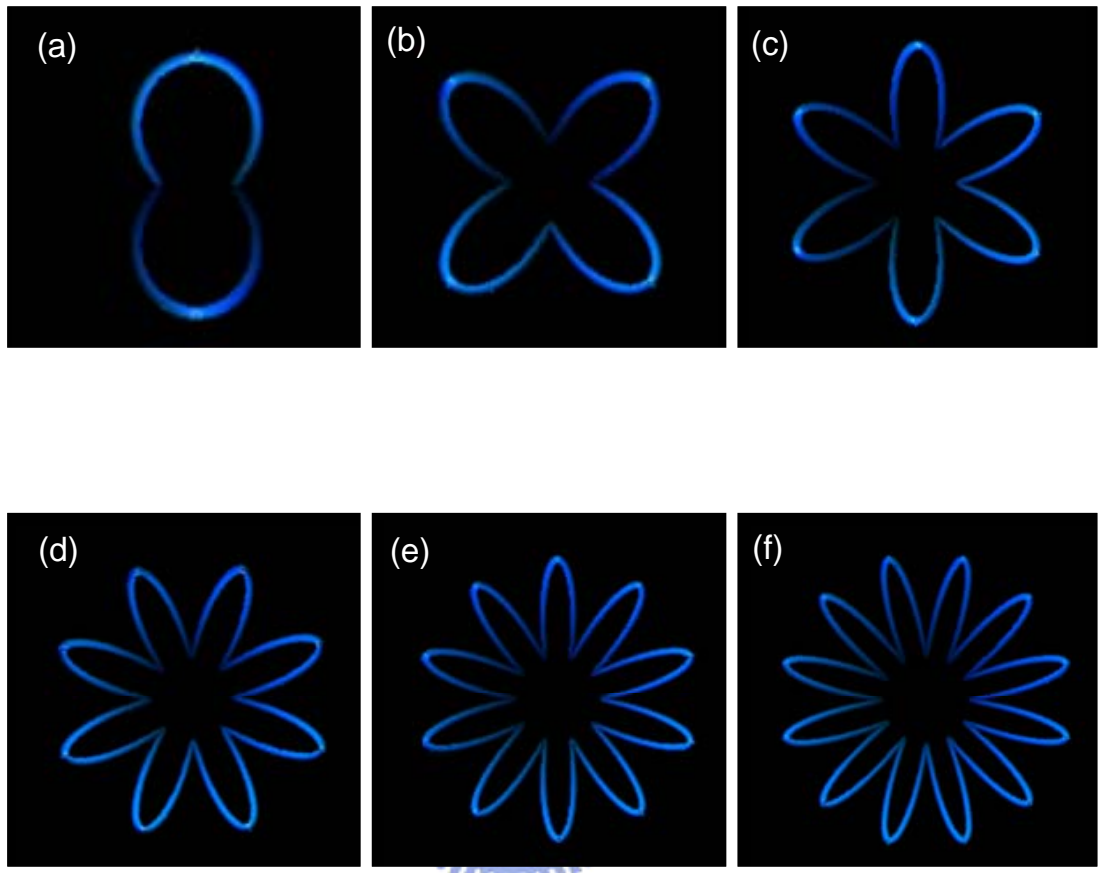


Fig. 4.3.5 Structure of the  $C$  line singularities of the theoretical vector field from the view of propagation direction to the beam waist with the same radial index  $p=0$  and different azimuthal index  $l$ : (a)  $(p, l)=(0, 1)$ ; (b)  $(p, l)=(0, 2)$ ; (c)  $(p, l)=(0, 3)$ ; (d)  $(p, l)=(0, 4)$ ; (e)  $(p, l)=(0, 5)$ ; (e)  $(p, l)=(0, 6)$ .

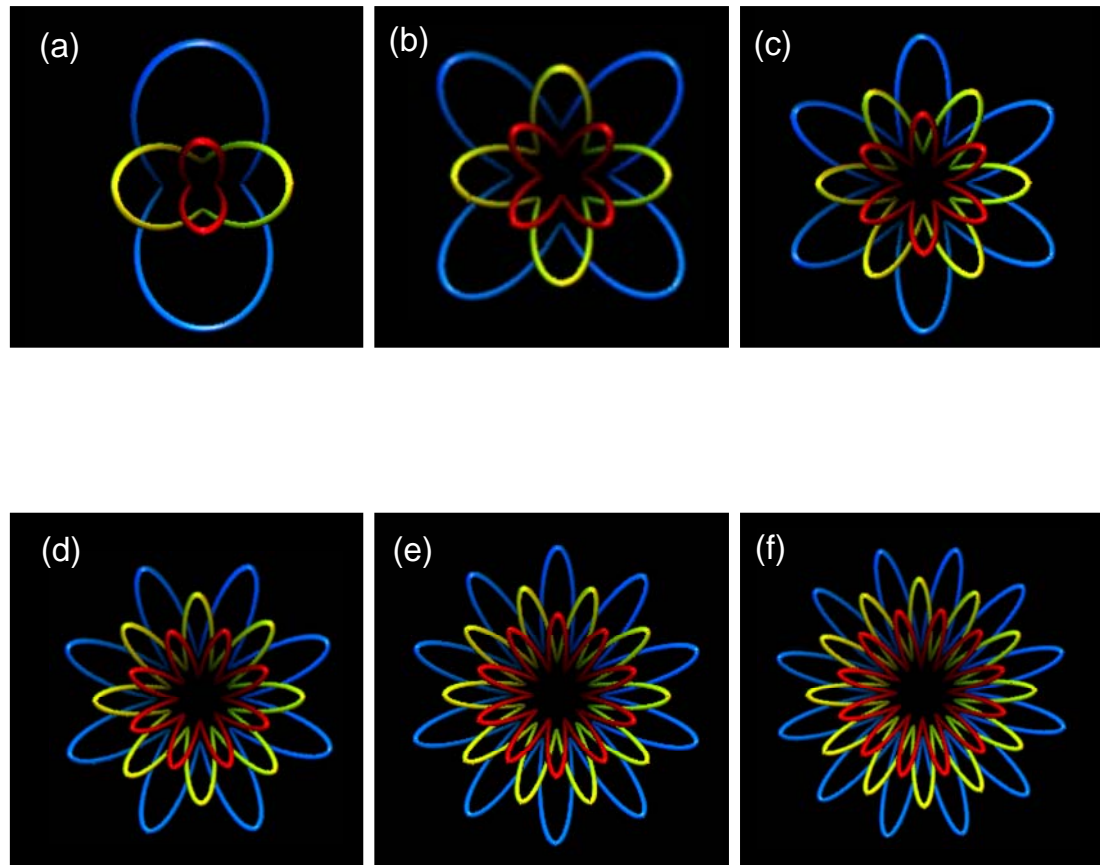


Fig. 4.3.6 Structure of the  $C$  line singularities of the theoretical vector field from the view of propagation direction to the beam waist with the same radial index  $p=0$  and different azimuthal index  $l$ : (a)  $(p, l)=(1, 1)$ ; (b)  $(p, l)=(1, 2)$ ; (c)  $(p, l)=(1, 3)$ ; (d)  $(p, l)=(1, 4)$ ; (e)  $(p, l)=(1, 5)$ ; (e)  $(p, l)=(1, 6)$ .

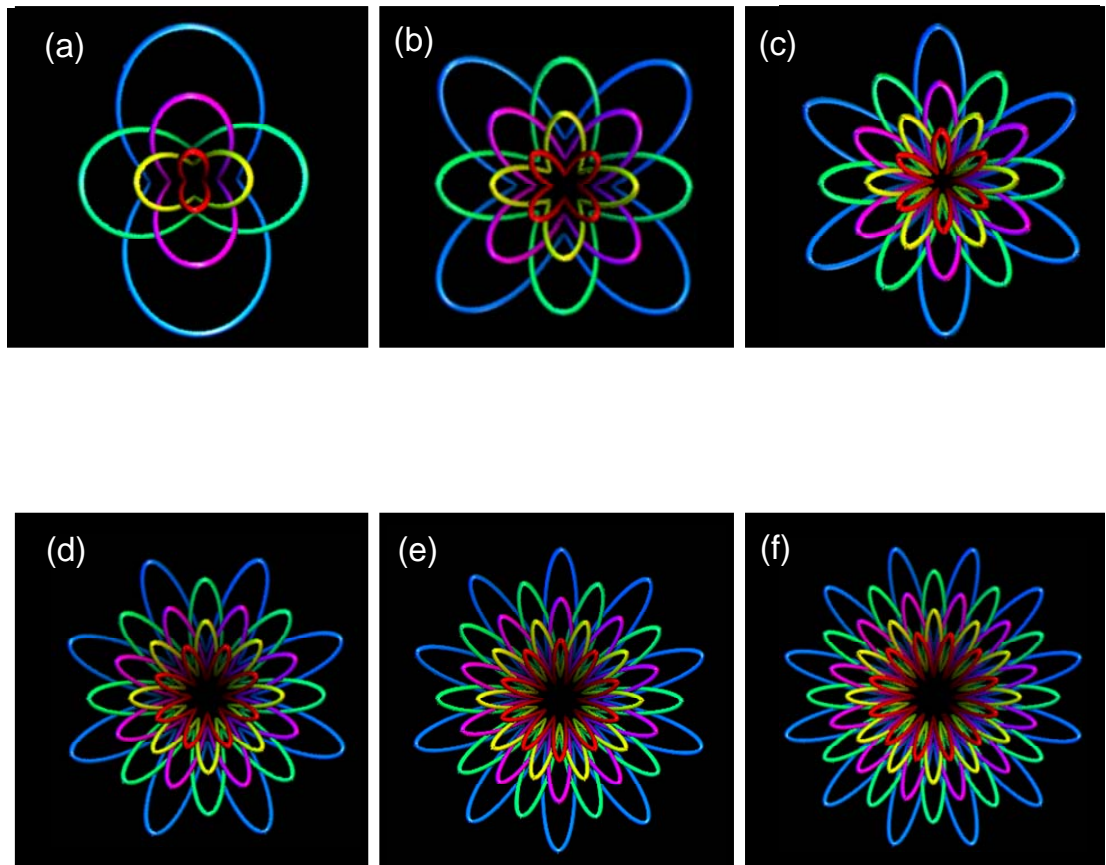


Fig. 4.3.7 Structure of the C line singularities of the theoretical vector field from the view of propagation direction to the beam waist with the same radial index  $p=0$  and different azimuthal index  $l$ : (a)  $(p, l)=(2, 1)$ ; (b)  $(p, l)=(2, 2)$ ; (c)  $(p, l)=(2, 3)$ ; (d)  $(p, l)=(2, 4)$ ; (e)  $(p, l)=(2, 5)$ ; (e)  $(p, l)=(2, 6)$ .

Another important and interesting feature is that the experimental 3D polarization vector fields at the beam waist and far field which are made up of two linearly polarized modes with different spatial structures. For the general condition, the experimental vector field can be given by  $\bar{E} = E_x(\rho, \phi, p) \hat{x} + E_y(\rho, \phi, p) \hat{y}$ , where

$$E_x(\rho, \phi, z) = \Phi_{p, l-1, s}(\rho, 0) \left\{ \tilde{\rho}_l^2 e^{i2\theta_G(z)} \cos[(l+1)\phi] - \cos[(l-1)\phi] \right\} / \sqrt{2} , \quad (4.3.10)$$

and

$$E_y(\rho, \phi, z) = \Phi_{p, l-1, s}(\rho, 0) \left\{ \tilde{\rho}_l^2 e^{i2\theta_G(z)} \sin[(l+1)\phi] + \sin[(l-1)\phi] \right\} / \sqrt{2} . \quad (4.3.11)$$

The transverse vector field at beam waist and far field can be verified to possess the *V* point singularities that are generally described in terms of the field of the angle function  $\Theta(x, y) = \arctan(E_y / E_x)$  [47], where  $E_x$  and  $E_y$  are the scalar components of the vector field along the  $x$  and  $y$  axes. The vortices of  $\Theta(x, y)$  are the vector singularities at which the orientation of the electric vector is undefined. Figures 4.3.8-4.3.10 show the angle pattern  $\Theta(x, y)$  of the numerical vector field at the far field. Consistently, the *V* point singularities are right at the intersections of the right-handed and left-handed *C* lines shown in Fig. 4.3.5-4.3.7.

With Eqs. (4.3.10) and (4.3.11) and some algebra, there are  $2l$  peripheral *V* points symmetrically arrayed at angles  $\phi_m = m\pi/l$  on a circle of radius  $\rho$  of the condition  $\tilde{\rho}_l^2 = 1$  and  $2l$  peripheral *V* points symmetrically arrayed at angles  $\phi_m = (2m+1)\pi/2l$  on a circle of radius  $\rho$  of the condition  $\tilde{\rho}_l^2 = -1$  with  $m=0,1,2,\dots,2l-1$  at the beam waist in addition to the central singularity at the origin. The Gouy phase plays a vital role to transform the singularities between *V* points and *C* points under propagation of the 3D vector field.

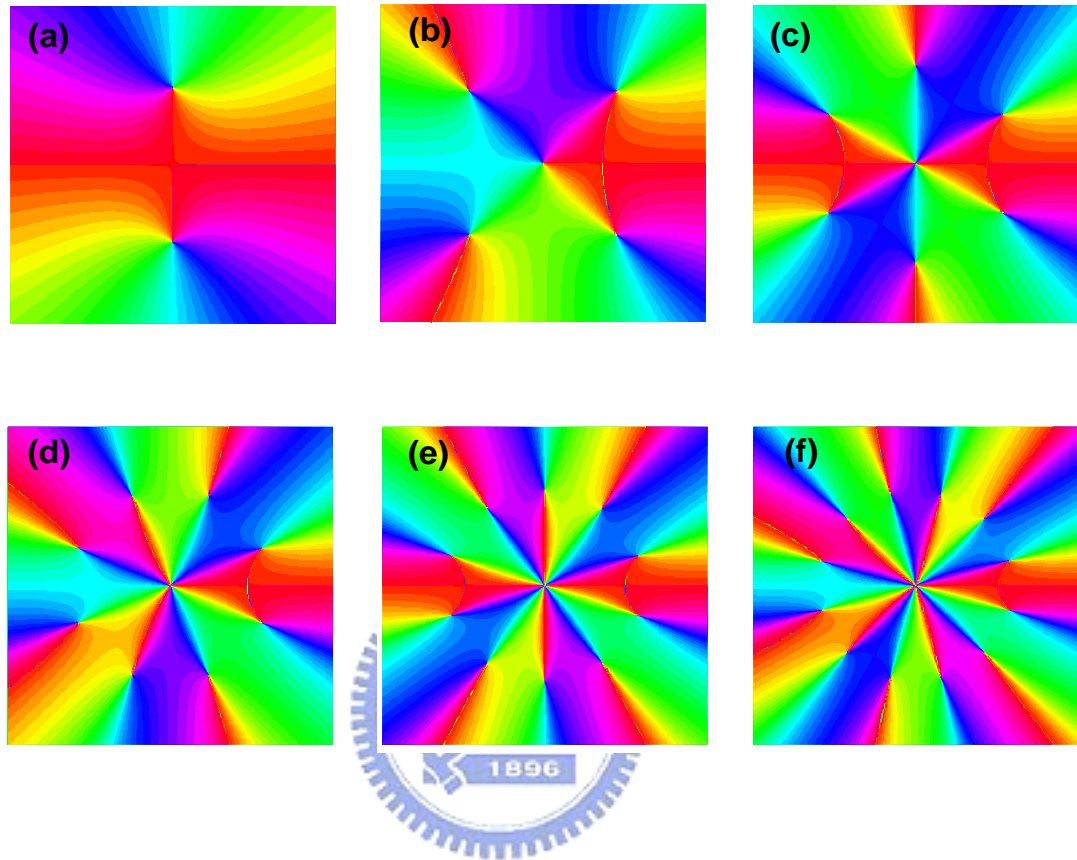


Fig. 4.3.8 Numerical patterns of the angle function at the far field of the same radial index  $p=0$  and different azimuthal index  $l$ : (a)  $(p, l)=(0, 1)$ ; (b)  $(p, l)=(0, 2)$ ; (c)  $(p, l)=(0, 3)$ ; (d)  $(p, l)=(0, 4)$ ; (e)  $(p, l)=(0, 5)$ ; (e)  $(p, l)=(0, 6)$ .

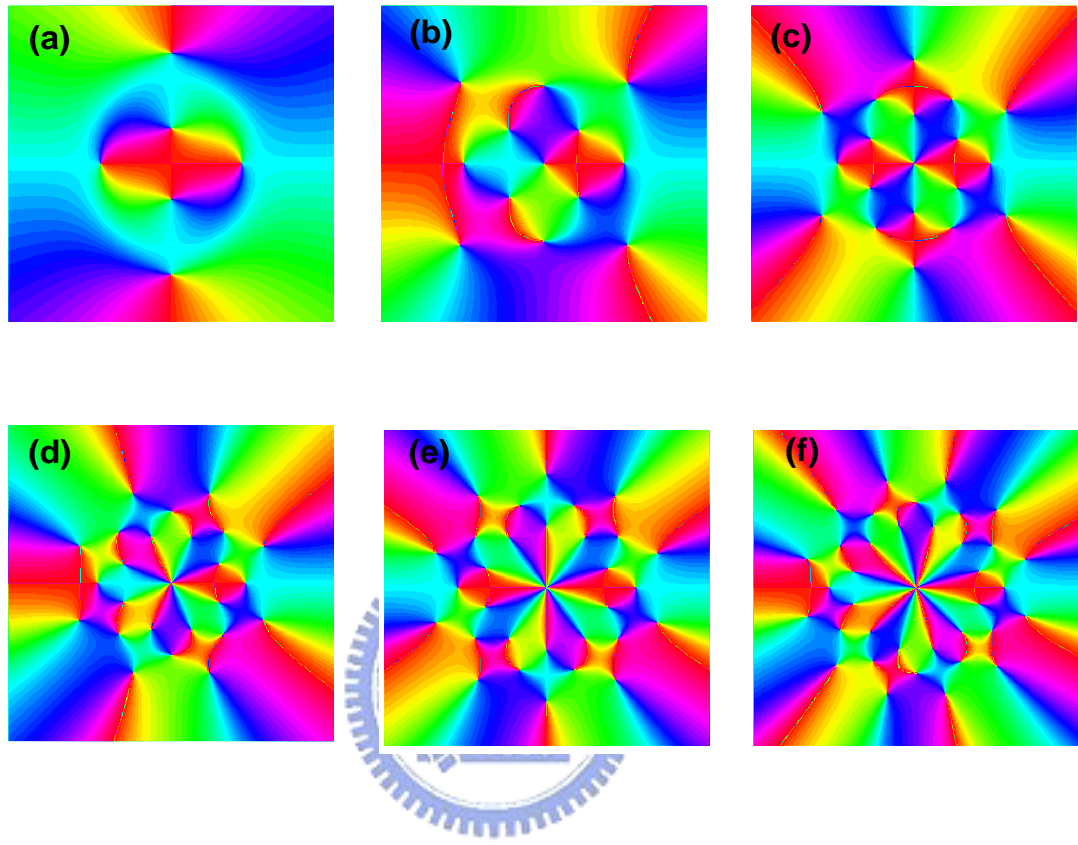


Fig. 4.3.9 Numerical patterns of the angle function at the far field of the same radial index  $p=0$  and different azimuthal index  $l$ : (a)  $(p, l)=(1, 1)$ ; (b)  $(p, l)=(1, 2)$ ; (c)  $(p, l)=(1, 3)$ ; (d)  $(p, l)=(1, 4)$ ; (e)  $(p, l)=(1, 5)$ ; (e)  $(p, l)=(1, 6)$ .

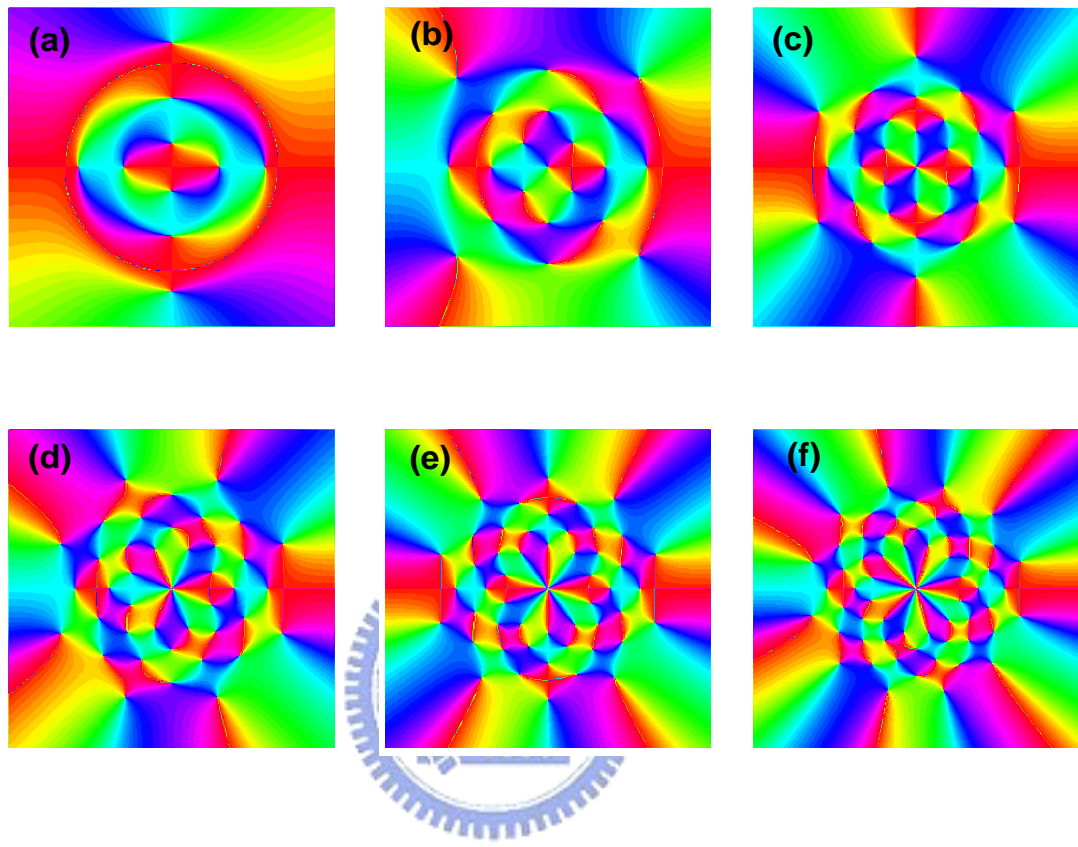


Fig. 4.3.10 Numerical patterns of the angle function at the far field of the same radial index  $p=0$  and different azimuthal index  $l$ : (a)  $(p, l)=(2, 1)$ ; (b)  $(p, l)=(2, 2)$ ; (c)  $(p, l)=(2, 3)$ ; (d)  $(p, l)=(2, 4)$ ; (e)  $(p, l)=(2, 5)$ ; (e)  $(p, l)=(2, 6)$ .

Consequently, there are  $2l$  peripheral  $V$  points symmetrically arrayed at angles  $\phi_m = (2m+1)\pi/2l$  on a circle of radius  $\rho$  of the condition  $\tilde{\rho}_l^2 = 1$  and  $2l$  peripheral  $V$  points symmetrically arrayed at angles  $\phi_m = m\pi/l$  on a circle of radius  $\rho$  of the condition  $\tilde{\rho}_l^2 = -1$  with  $m=0,1,2,\dots,2l-1$  at the far field in addition to the central singularity at the origin. Intriguingly, each peripheral  $V$  point with the winding number of 1 is transformed to two different handed  $C$  points with the winding number of  $1/2$ . Apparently, the winding numbers are conserved during the singularity transformation and under the vector field propagation [48]. Figure 4.3.11 depicts the characteristics of the  $C$  line and  $V$  point singularities of an experimental result. It can be found that the structure of  $C$  lines shown in Fig. 4.3.11 (b) forms the hyperboloid with multi-layer in the radial direction. The theoretical pattern of the view from the propagation direction to the beam waist of the structures of the  $C$  lines singularities forms a kind of fascinating petal pattern corresponding to the experimental transverse pattern shown in Fig. 4.3.11 (a).

Besides  $C$  line and  $V$  point singularities, there is  $L$  surface singularity embedded in the propagation-dependent polarization vector fields with the longitudinal-transverse coupling and the entanglement of the polarization states. The  $L$  singularities can be determined by the conditions  $|E_R|^2 = |E_L|^2$ . With Eqs. (4.3.4) and (4.3.5), it can be found that there are  $4l$   $L$  surfaces on the  $\rho$ - $z$  plane with the azimuthal angles at  $\phi_n = n\pi/(2l)$ , where  $n=0,1,2,\dots,4l-1$ .

Figure 4.3.12 displays the vector and polarization singularities with the analytical representation of the transverse pattern with the radial and azimuthal index  $(p,l)$  to be  $(0,4)$  from the view of the propagation direction to the beam waist. The different radial position of the figure implies the different propagation position of the 3D polarization vector field. The minimum of the radial position represents the beam waist and the maximum of the radial position represents the far field.

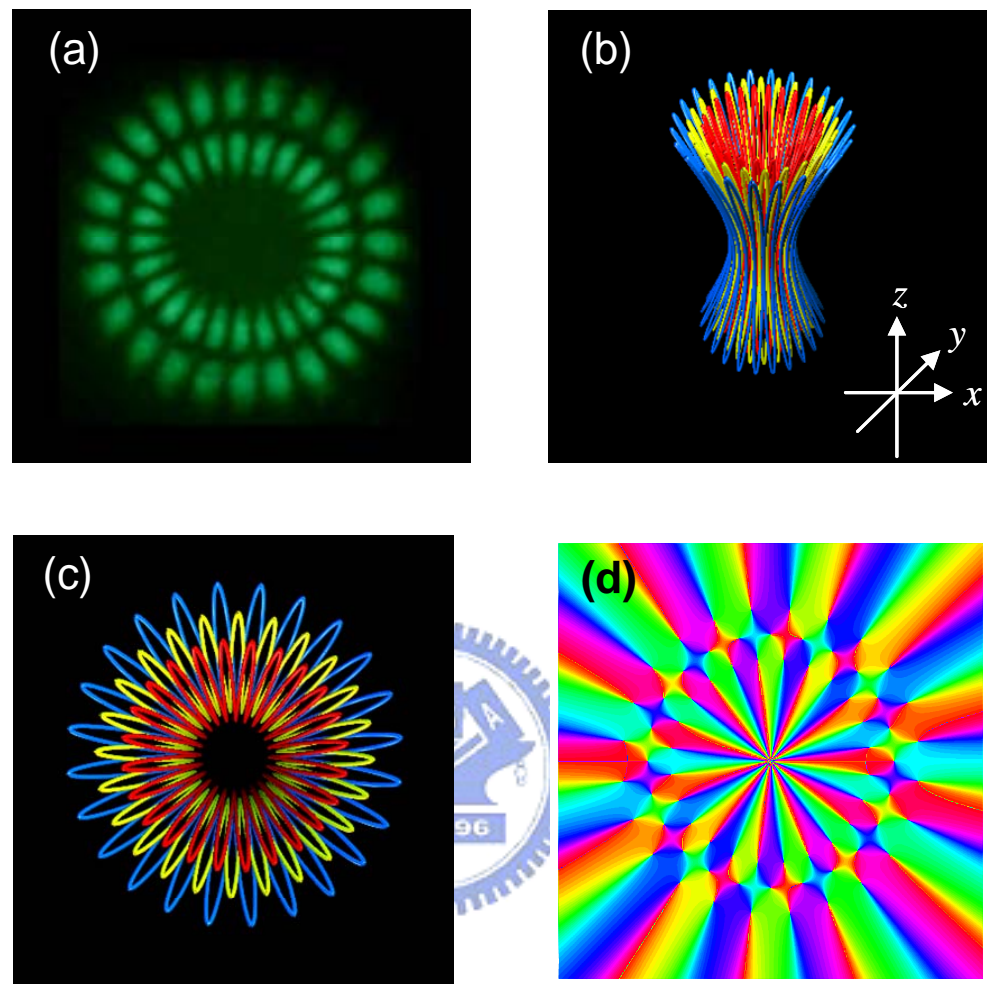


Fig. 4.3.11 (a) Experimental far-field pattern with radial and azimuthal index  $(p, l) = (1, 12)$ . (b) Structure of  $C$  line singularities of the correspondent 3D vector field. (c) Structure of the  $C$  line singularities from the view of propagation direction to the beam waist. (d) Numerical pattern of the angle function at the far field.

From the analytical structures of the singularities, the polarization state of the experimental 3D vector field under propagation can be clearly revealed. From the loci of *C* lines, it can be confirmed that *L* surfaces separate regions of right-handed and left-handed polarization and *V* points locate on the intersection of right-handed and left-handed polarization.

It is worthwhile to give a more detailed comparison between theory and experimental results. The present hyperboloid structures of polarization singularities are directly derived from Eq. (4.3.2) and (4.3.3) in which the two different LG modes are superposed with equal amplitude. For general cases of experimental results, however, the amplitude of the two LG modes can be somewhat different. Nevertheless, with the same theoretical analysis, the distributions of the polarization singularities can be certainly found to be topologically invariant. In other words, the hyperboloid structure of polarization singularities represents a characteristic feature of resonant laser modes emitted from degenerate cavities. On the other hand, a more complicated phase singularities, such as link and knot structures, can be produced by using a Gaussian laser beam illuminating a hologram or a phase modulator [49-50]. However, these complex structures are not at all related to the fundamental aspects of laser resonators.

The present polarization singularities are explored based on the paraxial approximation in which the longitudinal electric field is neglected. For a rigorous point of view, it is more appropriate to analyze the experimental polarization singularities with the full 3D electric field. Recently, Berry [51] has confirmed that the separations between two singularities obtained with the paraxial approximation and the full 3D fields are generally much smaller than the wavelength. Therefore, the present findings are almost not affected by neglecting the longitudinal field.

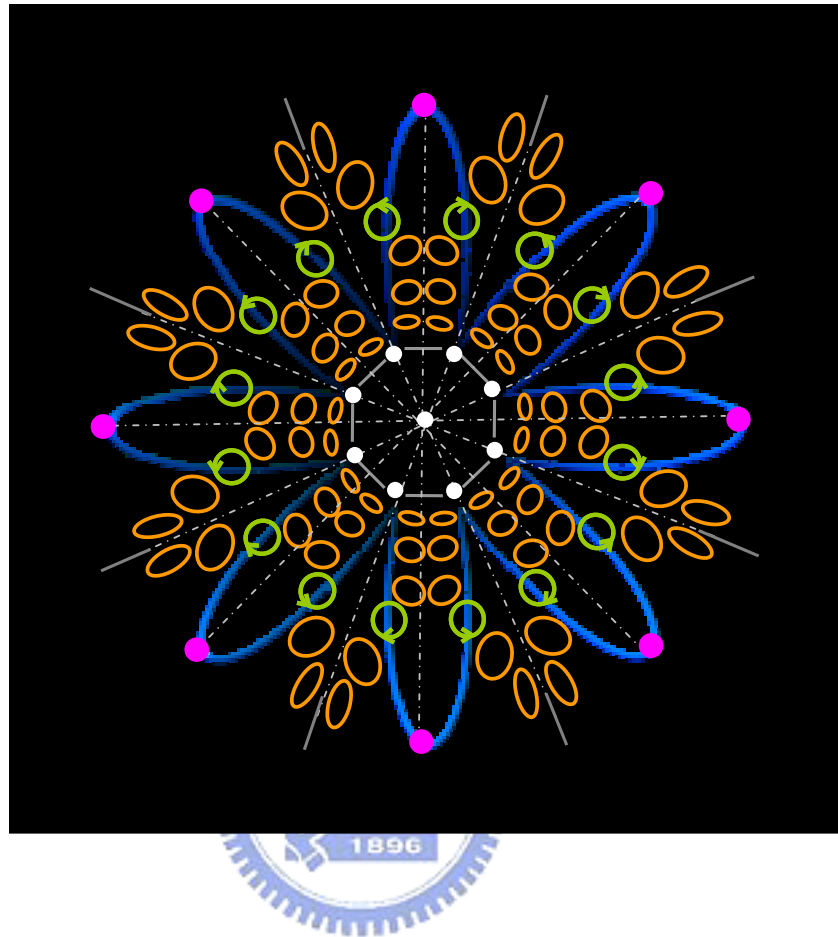
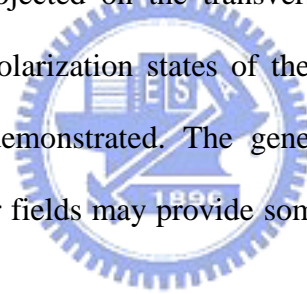


Fig. 4.3.12 Diagram of the representation of the polarization state under propagation corresponding to the singularities of  $C$  lines (blue line),  $V$  points (white points at far field and pink points at beam waist), and  $L$  surfaces (yellow dashed lines).

### 4.3.3 Summary

In summary, we have used an isotropic microchip laser to generate the propagation-dependent polarization vector fields with the longitudinal-transverse coupling and the entanglement of the polarization states. It is found that the experimental 3D coherent vector fields can be reconstructed by the orthogonal circularly polarized vortex mode which is made up of two LG modes with different order. With the analytical representation, the general structures for the singularities of the *C* lines, *V* points, and *L* surfaces can be systematically analyzed. In general, there are  $2p+1$  solutions of the radius which the *C* lines and *V* points are symmetrically embedded in and the theoretical solutions of the radius can be represented analytically for the cases  $p = 0 \sim 3$ . Importantly, the theoretical analyses reveal that the trajectories of the *C* lines projected on the transverse plane displays the intriguing petal structures. Furthermore, the polarization states of the experimental LG vector fields under propagation can be clearly demonstrated. The generalized structures of the polarization singularities in coherent vector fields may provide some useful insights into the nature of the waves.



## REFERENCES

- [1] J. F. Nye and M. V. Berry, Proc. R. Soc. A **336**, 165 (1974).
- [2] V. Y. Bazhenov, M. V. Vasnetsov, and M. S. Soskin, JETP Lett. **52**, 429 (1990).
- [3] L. Allen, M. W. Beijersbergen, R. J. C. Spreeuw, and J. P. Woerdman, Phys. Rev. A **45**, 8185 (1992).
- [4] N. R. Heckenberg, R. McDuff, C. P. Smith, and A. G. White, Opt. Lett. **17**, 221 (1992).
- [5] K. Dholakia, N. B. Simpson, M. J. Padgett, and L. Allen, Phys. Rev. A **54**, R3742 (1996).
- [6] M. V. Berry and M. R. Dennis, Proc. Roy. Soc. A **456**, 2059 (2000).
- [7] M. V. Berry and M. R. Dennis, Proc. Roy. Soc. A **457**, 2251 (2001).
- [8] Y. S. Kivshar, B. Luther-Davies, Phys. Rep. **298**, 81 (1998).
- [9] M. S. Soskin and M. V. Vasnetsov, Photonic Science News **4**, 21 (1999).
- [10] J. F. Nye, Proc. R. Soc. A **387**, 105 (1983).
- [11] M. Soskin, V. Denisenko, and R. Egorov, J. Opt. A Prue Appl. Opt. **6**, S281 (2004).
- [12] M. V. Berry, J. Opt. A Prue Appl. Opt. **6**, 475 (2004).
- [13] L. Gil, Phys. Rev. Lett. **70**, 162 (1993).
- [14] T. Erdogan, Appl. Phys. Lett. **60**, 1921 (1992).
- [15] Y. F. Chen, K. F. Huang, H. C. Lai, and Y. P. Lan, Phys. Rev. Lett. **90**, 053904 (2003).
- [16] I. V. Veshneva, A. I. Konukhov, L. A. Melnikov, and M. V. Byabina, J. Opt. B: Quantum Semiclassical Opt. **3**, S209 (2001).
- [17] J. F. Nye, *Natural Focusing and Fine Structure of Light: Caustics and Wave Dislocations* (Institute of Physics Publishing Bristol, 1999).
- [18] Dennis Goldstein, *Polarized Light* ( 2nd ed.), Revised and Expanded, (2003).
- [19] David S. Kliger, James W. Lewis, and Cora Einterz Randall, *Polarized Light in Optics and Spectroscopy*, (1990).
- [20] M S Soskin and M V Vasnetsov, Pure Appl. Opt. **7**, 301–311 (1998).
- [21] Michael Berry, SPIE Vol. 4403, p. 1-12 (2001).

- [22] J. F. Nye, M. V. Berry, Proc. Roy. Soc. Lond. A **366**, 165-190 (1974).
- [23] G. Blatter, M. V. Feigelman, and V. B. Geshkenbein, Rev. Mod. Phys. **66**, 1125 (1994).
- [24] P. Seba, U. Kuhl, M. Barth, and H. J. Stockmann, J. Phys. A **32**, 8225 (1999).
- [25] *The Quantum Hall Effect*, (2nd ed. edited by R.E. Prange and S.M. Girvin) (Springer-Verlag, Berlin, 1990).
- [26] M. V. Berry, J. Mod. Opt. **45**, 1845-1858 (1998).
- [27] *Optical Vortices*, edited by M. V. Vasnetsov and K. Staliunas (Nova Science, New York, 1999).
- [28] M. S. Soskin and M. V. Vasnetsov, in *Progress in Optics*, edited by E. Wolf (Elsevier, New York, 2001), Vol. 42, Chap. 4.
- [29] I. Freund, Opt. Commun. **199**, 47 (2001).
- [30] L. Gil, Phys. Rev. Lett. **70**, 162 (1993).
- [31] T. Erdogan, Appl. Phys. Lett. **60**, 1921 (1992).
- [32] Y. F. Chen, K. F. Huang, H. C. Lai, and Y. P. Lan, Phys. Rev. Lett. **90**, 053904 (2003).
- [33] I. V. Veshneva, A. I. Konukhov, L. A. Melnikov, and M. V. Ryabinina, J. Opt. B: Quantum Semiclassical Opt. **3**, S209 (2001).
- [34] F. Prati, G. Tissoni, M. S. Miguel, and N. B. Abraham, Opt. Commun. **143**, 133 (1997).
- [35] T. H. Lu, Y. F. Chen, and K. F. Huang, Phys. Rev. E. **75**, 026614 (2007).
- [36] J. F. Nye, *Natural Focusing and Fine Structure of Light: Caustics and Wave Dislocations* (Institute of Physics Publishing, Bristol, 1999).
- [37] M. V. Berry, J. Opt. A: Pure Appl. Opt. **6**, 475 (2004).
- [38] J. F. Nye and J. V. Hajnal, Proc. R. Soc. London Ser. A **409**, 21 (1987).
- [39] I. Freund, Opt. Lett. **29**, 15 (2004).
- [40] M. S. Soskin, V. Denisenko, and I. Freund, Opt. Lett. **28**, 1475 (2003).
- [41] F. Flossmann, U. T. Schwartz, M. Maier, and M. R. Dennis, Phys. Rev. Lett. **95**, 253901 (2005).

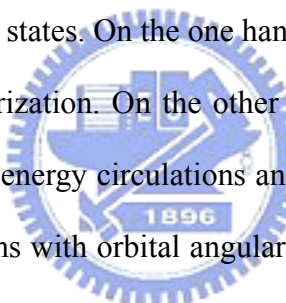
- [42] A. Volyar, V. Shvedov, T. Fadeyeva, A. S. Desyatnikov, D. N. Neshev, W. Krolikowski, and Y. S. Kivshar, Opt. Express **14**, 3724 (2006).
- [43] M V Berry and M R Dennis, Journal of Physics A Mathematical and Theoretical **40**, 65 (2007).
- [44] Y. F. Chen, T. H. Lu, and K. F. Huang, Phys. Rev. Lett. **97**, 233903 (2006).
- [45] Y. F. Chen, T. H. Lu, and K. F. Huang, Phys. Rev. Lett. **96**, 033901 (2006).
- [46] Y. F. Chen, T. H. Lu, K. W. Su, and K. F. Huang, Phys. Rev. Lett. **96**, 213902 (2006).
- [47] I. Freund, Opt. Commun. **201**, 251 (2002).
- [48] G. Indebetouw, J. Mod. Opt. **40**, 73 (1993).
- [49] M. V. Berry and M. R. Dennis, Proc. R. Soc. London Ser. A **457**, 2251 (2001).
- [50] J. Leach, M. R. Dennis, J. Courtial, and M. J. Padgett, Nature **432**, 165 (2004).
- [51] M. V. Berry, J. Opt. A: Pure Appl. Opt. **6**, 475 (2004).



# Chapter 5

## Optical Waves Carrying Large Angular Momentum in Degenerate Cavity

A general study of paraxial light beans' spatial structures such as transverse energy flows is presented in recent years. The transverse spatial energy can be divided into the spin and orbital contributions which lead to the spin and orbital angular momentum, correspondingly [1]. Characteristics of these elements are studied in relation with the optical field of linear and circular orthogonal polarization states. On the one hand, the spin angular momentum is related to the photons of circular polarization. On the other hand, the orbital angular momentum is related to the macro transverse energy circulations and independent of the polarization states. A typical class of paraxial beams with orbital angular momentum is Laguerre-Gaussian beam which possesses angular momentum with  $l\hbar$  per photon. The applications include the transmission of the beam's angular momentum to other bodies such as optical elements and to suspend micro particles. In this chapter we introduce the angular momentum of electromagnetic fields firstly and then demonstrate the optical coherent waves which are different from Laguerre-Gaussian beams carrying large angular momentum in degenerate cavity.



### 5.1 Angular Momentum of Electromagnetic Fields

For electromagnetism the electric and magnetic fields can be represented as

$$\vec{E} = 1/2 \left[ (E_x e^{i\phi} + E_x^* e^{-i\phi}) \hat{x} + (E_y e^{i\phi} + E_y^* e^{-i\phi}) \hat{y} + (E_z e^{i\phi} + E_z^* e^{-i\phi}) \hat{z} \right] \quad (5.1.1)$$

and

$$\vec{B} = 1/2 \left[ (B_x e^{i\phi} + B_x^* e^{-i\phi}) \hat{x} + (B_y e^{i\phi} + B_y^* e^{-i\phi}) \hat{y} + (B_z e^{i\phi} + B_z^* e^{-i\phi}) \hat{z} \right] \quad (5.1.2)$$

respectively. The parameter  $\phi$  is  $kz - \omega t$  where  $k$  is the wave vector and  $\omega$  is the angular frequency. The linear momentum density  $\vec{p}$  and angular momentum density  $\vec{j}$  of a light beam can be calculated from the electric,  $\vec{E}$ , and magnetic,  $\vec{B}$ , fields, such as  $\vec{p} = \epsilon_0 \langle \vec{E} \times \vec{B} \rangle$  and  $\vec{j} = \vec{r} \times \vec{p}$  [2-3], where  $\epsilon_0$  is the permittivity of vacuum. From Maxwell's equations  $\vec{\nabla} \cdot \vec{E} = 0$  and  $\vec{\nabla} \times \vec{E} = -\partial \vec{B} / \partial t$ , the  $z$  component of the electric and magnetic fields can be determined under the paraxial approximation. After some algebra, the linear momentum density  $\vec{p} = p_x \hat{x} + p_y \hat{y} + p_z \hat{z}$  can be written in detail:

$$p_x = \frac{\epsilon_0}{2\omega} \text{Im} \left[ E_x^* \frac{\partial}{\partial x} E_x + E_y^* \frac{\partial}{\partial x} E_y - \frac{\partial}{\partial y} (E_x E_y^*) \right] \quad (5.1.3)$$

$$p_y = \frac{\epsilon_0}{2\omega} \text{Im} \left[ E_x^* \frac{\partial}{\partial y} E_x + E_y^* \frac{\partial}{\partial y} E_y + \frac{\partial}{\partial x} (E_x E_y^*) \right] \quad (5.1.4)$$

$$p_z = \frac{\epsilon_0 k}{2\omega} \left( |E_x|^2 + |E_y|^2 \right) = \frac{\epsilon_0}{2c} \left( |E_x|^2 + |E_y|^2 \right) \quad (5.1.5)$$

where  $\text{Im}$  denotes the imaginary part of the expression. Following, the angular momentum density of  $z$  component,  $\vec{j}_z$ , which contributes to the orbital angular momentum can be written as

$$\vec{j}_z = \frac{\epsilon_0}{2\omega} \text{Im} \left[ \vec{r} \times (E_x^* \nabla E_x + E_y^* \nabla E_y) \right] . \quad (5.1.6)$$

When the cylindrical coordinate is used to replace the Cartesian coordinate, the orbital angular momentum density  $\vec{j}_z$  can be represented in a concise form such as

$$\vec{j}_z = \frac{\epsilon_0}{2\omega} \text{Im} \left[ E_x^* \frac{\partial}{\partial \phi} E_x + E_y^* \frac{\partial}{\partial \phi} E_y \right] . \quad (5.1.7)$$

As a consequence, the z-component of the orbital AM density for a linearly polarized light beam is given by

$$\ell_z = \frac{\epsilon_0}{2\omega} \text{Im} \left[ \Psi^* \left( x \frac{\partial}{\partial y} - y \frac{\partial}{\partial x} \right) \Psi \right] . \quad (5.1.8)$$

The optical AM contains spin and orbital AM densities that are related to the circular polarization and the spatial distribution of the optical beam, respectively. The spin angular momentum density  $\vec{S}_z$  can be written as

$$\vec{S}_z = \frac{\epsilon_0}{2\omega} \text{Im} \left[ \vec{r} \times \nabla \times (E_x E_y^*) \right] . \quad (5.1.9)$$

After some algebra, the spin angular momentum density can be represented as

$$\vec{S}_z = \frac{\epsilon_0}{\omega} \text{Im} [E_x^* E_y] . \quad (5.1.10)$$

Through the electromagnetism and the classical concept, the linear and angular momentum of electromagnetic waves can be understood more clearly. Besides, the representation of angular momentum of natural light helps us to study and analyze the wave properties in the laser cavity.

## 5.2 Linked and Knotted Coherent Laser Waves with Large Angular Momentum

Pattern formation has been the subject of interest in many physical, chemical, and biological problems such as, nonlinear optics [4-5], BZ interaction [6], structures inside living cells [7], Turing patterns in reaction-diffusion systems [8-10], and the DNA structures [11-12]. Naturally, pattern formation possesses some common features that make it possible to understand the analogies in different fields. In recent years, various laser systems are widely employed to realize optical transverse pattern formation including the high order Laguerre-Gaussian (LG) modes, Hermite-Gaussian (HG) modes, and the generalized coherent states that form a general family to comprise the HG and LG mode families as special cases [13-16].

In the optical pattern formation, the phase singularities or the optical vortices which have been studied by Nye and Berry [17] not only reveal the interesting phase structures but also signify the existence of the local angular momentum (AM) [18-20]. The AM of optical waves can be divided into an orbital part associated with spatial distribution of the fields and a spin part associated with polarization in electromagnetic radiation [21-23]. So far, LG laser modes have been confirmed to have a well-defined orbital AM [24-25] and applied to the fields of fundamental researches and practical applications such as optical tweezers, optical traps, and wireless and optical communications [26-29]. Motivated by these applications, there are noticeably a rapidly increasing number of researches exploring the orbital AM of coherent optical waves.

In this section, we originally demonstrate a fascinating discovery of linked and knotted optical waves that are experimentally found to be the prevailing resonant modes in large-Fresnel-number laser cavities with longitudinal-transverse coupling. Although we had found that longitudinal-transverse coupling and mode-locking effect lead to the localization of 3D coherent waves on the Lissajous parametric surface. We neglect the fine structures of the

linked and knotted characteristics and demonstrate the optical wave as only one 3D coherent state. Based on the thorough experiments and established theory, it is confirmed that linked and knotted laser waves can be analytically expressed as a superposition of two degenerate 3D coherent states with a relative phase of  $\pi/2$ . With the analytical representation, the AM densities of linked and knotted lasing modes are manifestly visualized and the average AM per photon is derived to be proportional to the Fresnel numbers of the laser cavities. The exploration of linked and knotted optical waves can provide a fresh insight into pattern formation and the large AM can be quite beneficial to many scientific applications.

### 5.2.1 Experimental Setup and Results

As mentioned before, a diode-pumped microchip laser has been employed to perform the analogous investigation of quantum-classical correspondence and pattern formation [30-32]. For an empty plane-concave resonator consisting of spherical mirror with radius of curvature  $R$  and cavity length  $L$ , the bare ratio between the transverse and longitudinal mode spacing is given by  $\Omega = \Delta\nu_T / \Delta\nu_L = (1/\pi) \cos^{-1}(1 - L/R)^{1/2}$ . The bare ratio can be changed in the range between 0 to 1/2 by varying the cavity length  $L$  for a given  $R$  in the half-spherical cavity. As shown in Fig. 5.2.1, the experimental setup in this section is only the half of the setup in chapter three. The experimental results are almost the same but it is easier to observe the variation from the near-field to far-field patterns. It has been experimentally observed [30-32] in chapter three that the longitudinal-transverse coupling and the mode-locking effect generally force the bare ratio,  $\Omega$ , to be locked to a rational number  $P/Q$ , forming an interesting fractal structure in a high- $Q$  laser cavity with a large Fresnel number. The experimental lasing modes were found to form 3D coherent waves that are localized on the parametric surfaces with Lissajous transverse patterns. Figure 5.2.2 displays two typical experimental results for the tomographic transverse patterns of the 3D coherent waves for

$P/Q = 1/4$  with  $(p, q) = (2, 2)$  and  $P/Q = 1/3$  with  $(p, q) = (3, 3)$ . It can be seen that the experimental transverse patterns are not only localized on the Lissajous figures but also exhibit linked features. Figure 5.2.3 displays another experimental result for the tomographic transverse patterns of the 3D coherent waves for  $P/Q = 2/7$  with  $(p, q) = (2, 5)$  and exhibits knotted features. In our previous work in chapter three, we have employed the representation of quantum coherent states to derive the analytical wave functions well concentrated on Lissajous parametric surfaces. Figures 5.2.4-5.2.5 depicts the numerical result corresponding to the experimental transverse patterns shown in Fig. 5.2.2 and 5.2.3. Although the 3D coherent states are confirmed to display the coarse morphology of the experimental transverse patterns, they can not manifest the stereographic features. Reconstructing the stereographic patterns is indispensable for extracting the all-encompassing information in linked or knotted coherent laser waves.



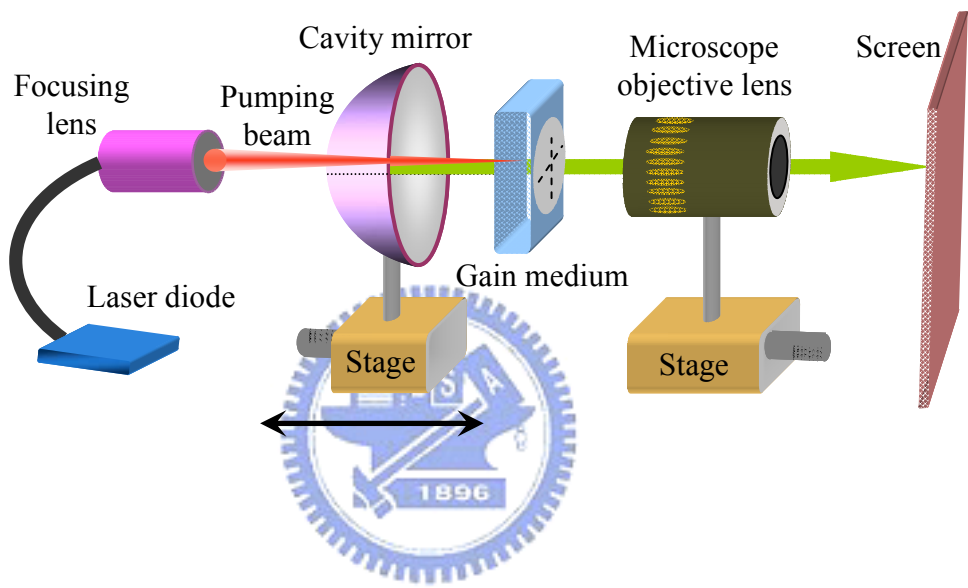
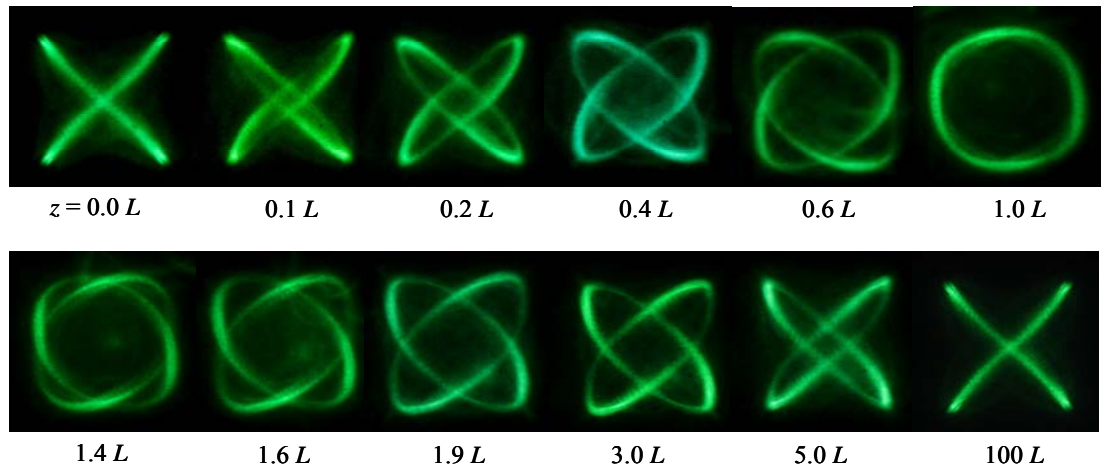


Fig. 5.2.1 Experimental setup for the generation of 3D coherent waves.

(a)



(b)

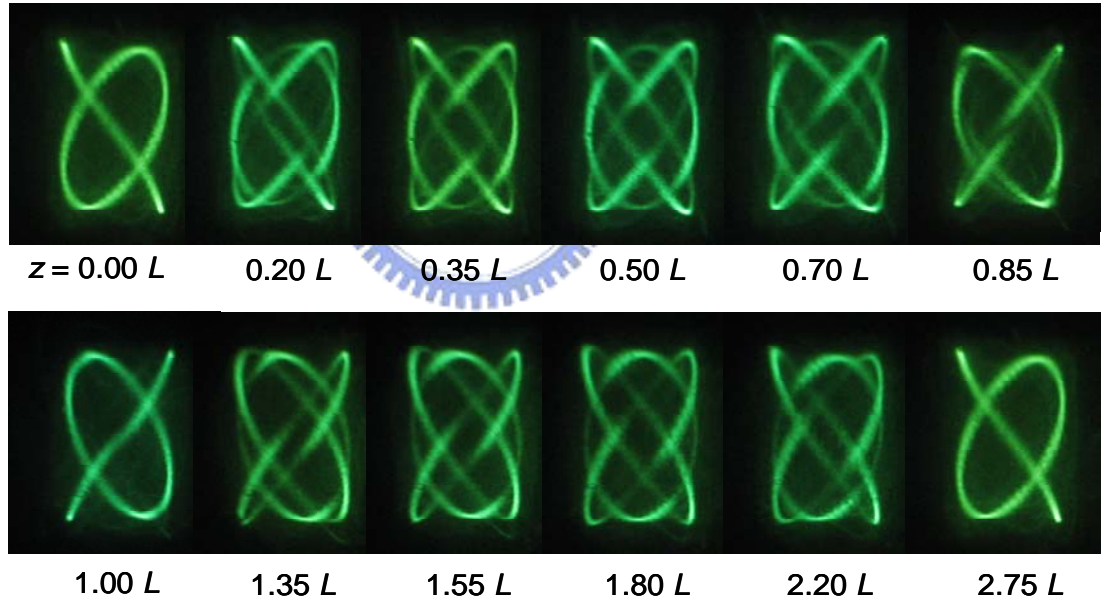


Fig. 5.2.2 (a) Experimental tomographic transverse patterns for the range from beam waist to far field with  $\Omega = 1/4$ ,  $(p, q) = (2, 2)$ . The pump position is at (0.29 mm, 0.30 mm); (b) Experimental tomographic transverse patterns for the range from beam waist to  $z = 2.75L$  with  $\Omega = 1/3$ ,  $(p, q) = (3, 3)$ . The pump position is at (0.23 mm, 0.30 mm).

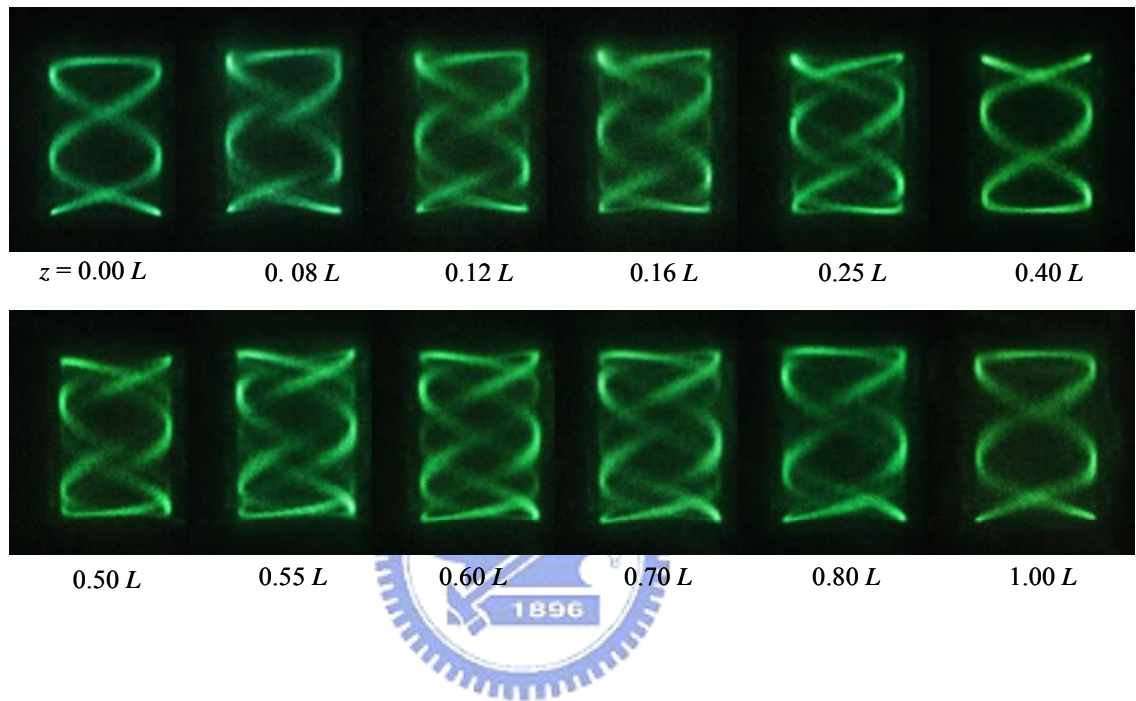
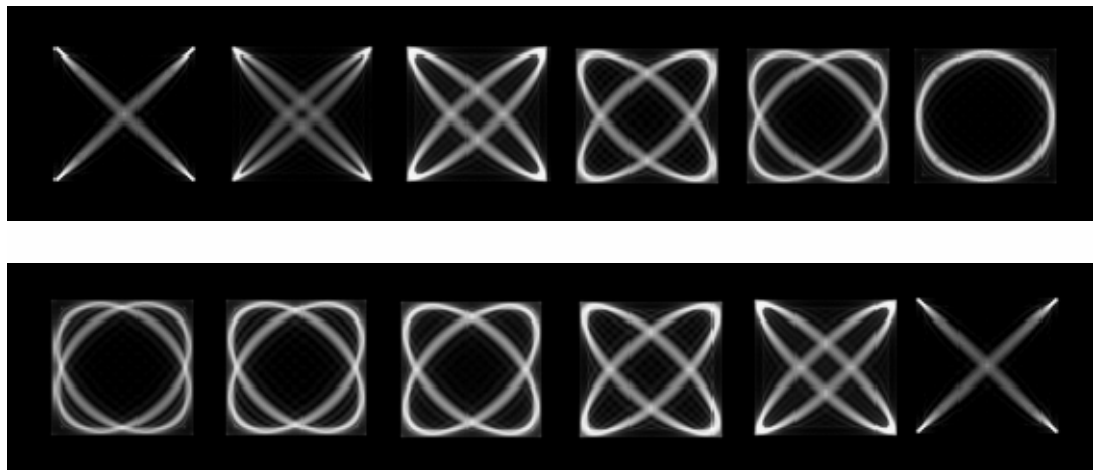


Fig. 5.2.3 Experimental tomographic transverse patterns for the range from beam waist to far field with  $\Omega = 2/7$ ,  $(p, q) = (2, 5)$ . The pump position is at (0.22 mm, 0.32 mm).

(a)



(b)

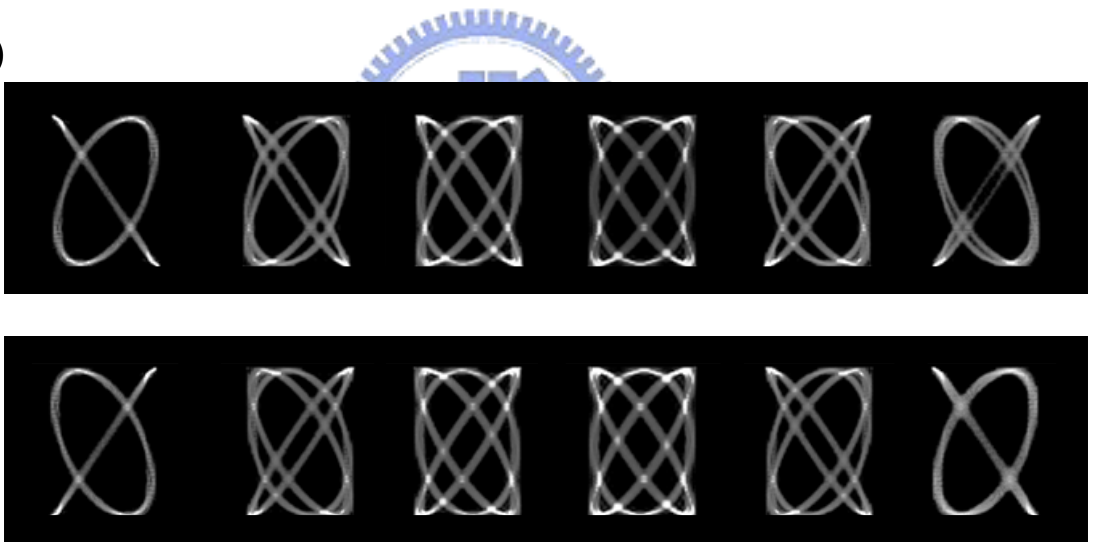


Fig. 5.2.4 (a) Numerical tomographic transverse patterns corresponding to Fig. 5.2.2 (a) with Eq. (5.2.1) and the parameters of  $(m_o, n_o) = (110, 110)$ ,  $(p, q) = (2, 2)$ ,  $P/Q = 1/4$ ,  $\phi_o = 0$  and  $M = 13$ . (b) (a) Numerical tomographic transverse patterns corresponding to Fig. 5.2.2 (b) with Eq. (5.2.1) and the parameters of  $(m_o, n_o) = (60, 140)$ ,  $(p, q) = (3, 3)$ ,  $P/Q = 1/3$ ,  $\phi_o = 0$  and  $M = 8$ .

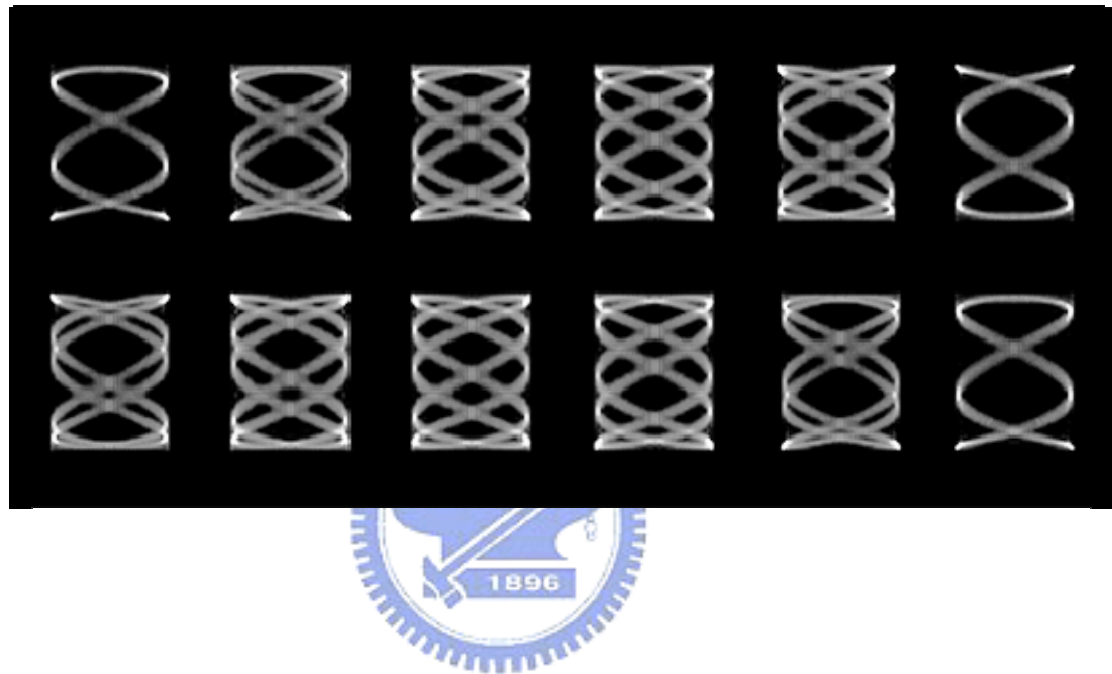


Fig. 5.2.5 Numerical tomographic transverse patterns corresponding to Fig. 5.2.3 with Eq. (5.2.1) and the parameters of  $(m_o, n_o) = (60, 130)$ ,  $(p, q) = (2, 5)$ ,  $P/Q = 2/7$ ,  $\phi_o = 0$  and  $M = 5$ .

Based on thorough experiments and numerical analysis, the stereographic structures of linked and knotted coherent waves are completely deduced to originate from a superposition of two degenerate 3D coherent states. With the representation of quantum coherent states, the 3D coherent waves localized on the Lissajous parametric surfaces can be described as

$$\psi_{m_o, n_o, l_o}^{p, q, s}(x, y, z) = \frac{1}{\sqrt{M+1}} \sum_{k=0}^M e^{ik\phi_o} \Phi_{m_o+pk, n_o+qk, l_o+sk}^{(HG)}(x, y, z) \quad , \quad (5.2.1)$$

where the parameter  $\phi_o$  is the relative phase between the adjoining Hermite-Gaussian (HG) modes  $\Phi_{m, n, l}^{(HG)}(x, y, z)$  which are given by

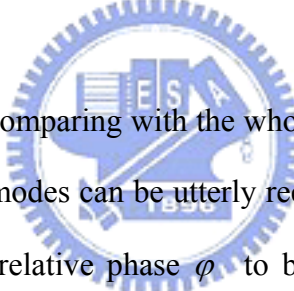
$$\Phi_{m, n, l}^{(HG)}(x, y, z) = \frac{1}{\sqrt{2^{m+n-1} \pi m! n!}} \frac{1}{w(z)} H_m\left(\frac{\sqrt{2} x}{w(z)}\right) H_n\left(\frac{\sqrt{2} y}{w(z)}\right) e^{\left[-\frac{x^2+y^2}{w(z)^2}\right]} \times e^{i(m+n+1) \tan^{-1}\left(\frac{z}{z_R}\right)} e^{-i\left(\frac{\pi z}{L}\right) \left[l+(m+n+1)\frac{P}{Q}\right] \left[\frac{x^2+y^2}{2(z^2+z_R^2)}+1\right]} \quad , \quad (5.2.2)$$

where  $m$  and  $n$  are the indices of  $x$  and  $y$  coordinates,  $l$  is the longitudinal mode index,  $w(z) = w_o \sqrt{1 + (z/z_R)^2}$ ,  $w_o$  is the beam radius at the waist,  $L$  is the effective cavity length and  $z_R$  is the Rayleigh range. We can abbreviate  $\psi_{m_o, n_o, l_o}^{p, q, s}(x, y, z)$  to be  $\psi_{m_o, n_o}^{p, q}(x, y, z)$  because the indices  $s$  and  $l_o$  obey the equations  $s + (p+q)(P/Q) = 0$  and  $l_o + (m_o + n_o + 1)(P/Q) = 2\lambda/L$ , respectively, where  $\lambda$  is the lasing wavelength. Note that the cases of  $p+q=0$  mean no longitudinal-transverse coupling and can not be allowed. With the spatial features of stationary coherent states in the 2D quantum harmonic oscillator [33-36], we can obtain that the 3D coherent waves  $\psi_{m_o, n_o}^{p, q}(x, y, z)$  are well concentrated on

the parametric surface:  $x(\vartheta, z) = \sqrt{m_o} w(z) \cos [q\vartheta - \phi(z)/p]$  and  $y(\vartheta, z) = \sqrt{n_o} w(z) \cos(p\vartheta)$ , where  $0 \leq \vartheta \leq 2\pi$ ,  $-\infty \leq z \leq \infty$ , and the  $z$ -dependent phase factor is given by  $\phi(z) = (q + p) \tan^{-1}(z/z_R) + \phi_o$ . Note that the phase factor  $\phi(z)$  comes from the Gouy-phase difference between the HG modes with distinct transverse orders. Although the phase factor  $\phi_o$  can be experimentally manipulated, we focus on the cases of  $\phi_o = 0$  hereafter for convenience.

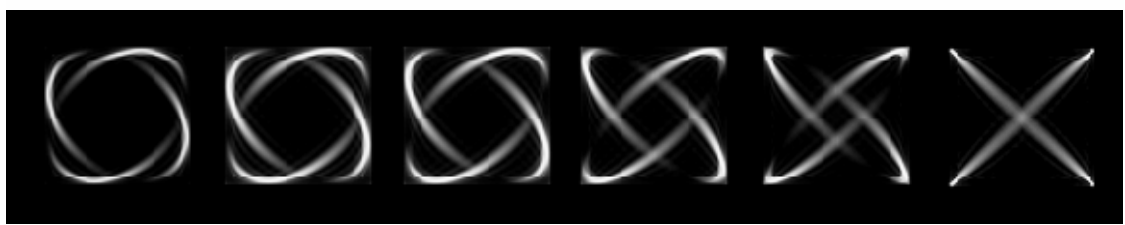
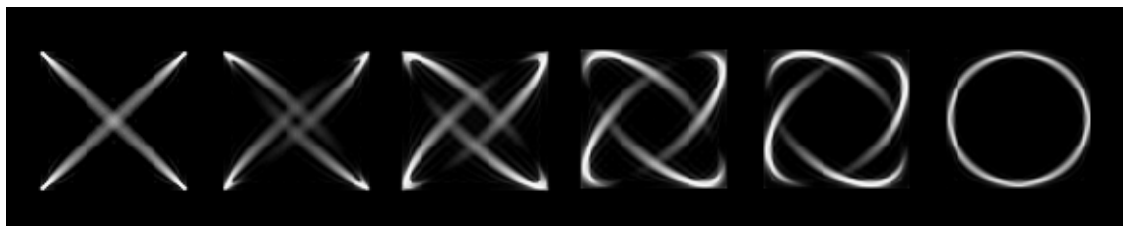
In terms of the 3D coherent waves of Eq. (5.2.1), a superposition of two degenerate 3D coherent states with the nearest neighbors can be generally expressed as

$$\Psi_{m_o, n_o}^{p, q}(x, y, z; \varphi) = \left[ \psi_{m_o, n_o}^{p, q}(x, y, z) + e^{-i\varphi} \psi_{m_o+1, n_o-1}^{p, q}(x, y, z) \right] / \sqrt{2} \quad , \quad (5.2.3)$$



where  $\varphi$  is the relative phase. Comparing with the whole experimental results, we substantiate that linked and knotted lasing modes can be utterly reconstructed with the superposition state of Eq. (5.2.3) and setting the relative phase  $\varphi$  to be  $\pm\pi/2$ . Figures 5.2.6 illustrates the numerical transverse patterns calculated with Eq. (5.2.3) and the parameters of: (a)  $(m_o, n_o) = (110, 110)$ ,  $M = 13$ , and  $\varphi = \pi/2$ , (b)  $(m_o, n_o) = (60, 140)$ ,  $M = 8$ , and  $\varphi = \pi/2$  corresponding to the experimental results shown in Fig. 5.2.2 (a) and (b), respectively. Excellent agreement validates the superposition states  $\Psi_{m_o, n_o}^{p, q}(x, y, z; \pm\pi/2)$  can entirely reconstruct the intriguing stereographic features of linked and knotted wave patterns. More importantly, the analytical representation enables us to discover the inherent properties of linked and knotted coherent waves. We henceforth concentrate on exploring the AM densities of the linked and knotted optical waves because of their applications in atomic trapping, tweezers, and imaging [26-29].

(a)



(b)

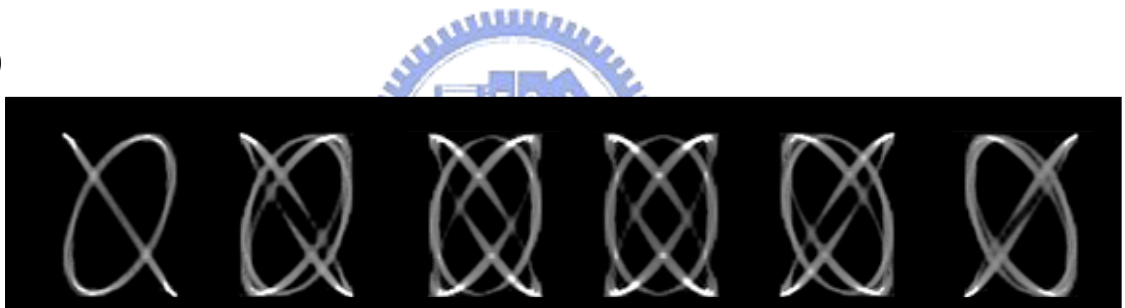


Fig. 5.2.6 (a) Numerical tomographic transverse patterns corresponding to Fig. 5.2.2 (a) with Eq. (5.2.3) and the parameters of  $(m_o, n_o) = (110, 110)$ ,  $(p, q) = (2, 2)$ ,  $P/Q = 1/4$ ,  $\varphi = \pi/2$  and  $M = 13$ .  
 (b) (a) Numerical tomographic transverse patterns corresponding to Fig. 5.2.2 (b) with Eq. (5.2.3) and the parameters of  $(m_o, n_o) = (60, 140)$ ,  $(p, q) = (3, 3)$ ,  $P/Q = 1/3$ ,  $\varphi = \pi/2$  and  $M = 8$ .

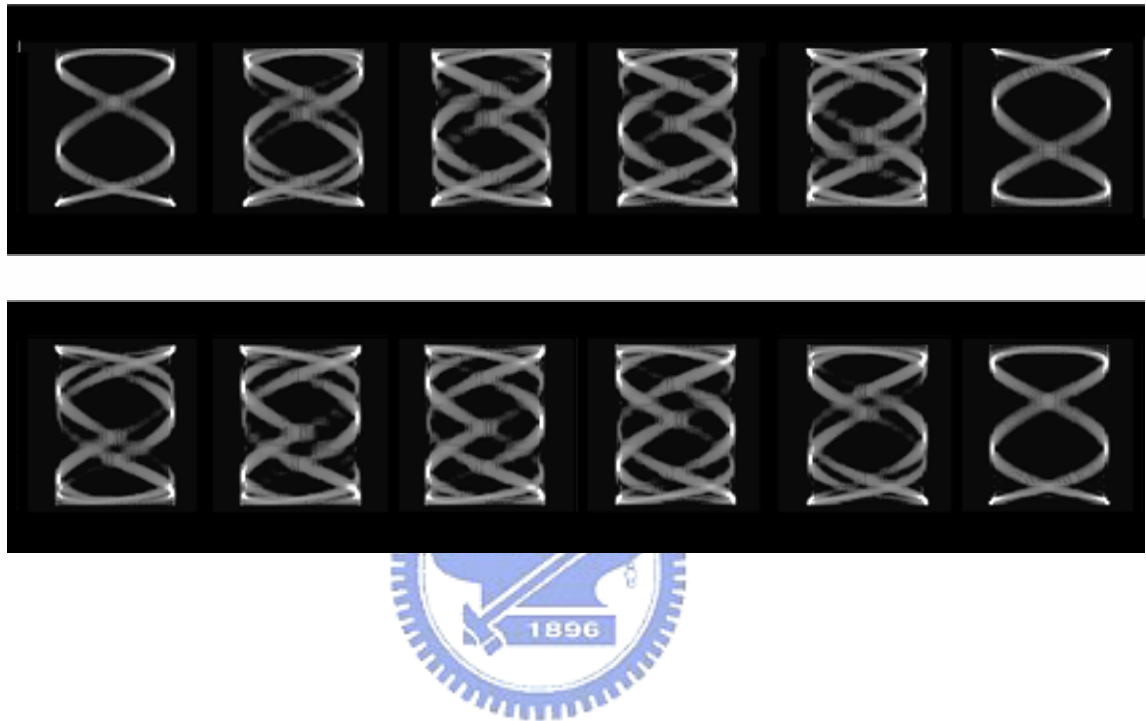
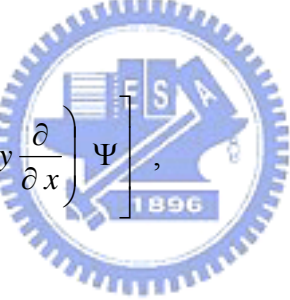


Fig. 5.2.7 Numerical tomographic transverse patterns corresponding to Fig. 5.2.3 with Eq. (5.2.3) and the parameters of  $(m_o, n_o) = (60, 130)$ ,  $(p, q) = (2, 5)$ ,  $P/Q = 2/7$ ,  $\varphi = \pi/2$  and  $M = 5$ .

### 5.2.2 Analyses of Angular Momentum for Two Degenerate Coherent States

The linear momentum density  $\vec{p}$  and AM density  $\vec{j}$  of a light beam can be calculated from the electric,  $\vec{E}$ , and magnetic,  $\vec{B}$ , fields, such as  $\vec{p} = \varepsilon_0 \langle \vec{E} \times \vec{B} \rangle$  and  $\vec{j} = \vec{r} \times \vec{p}$  [24-25], where  $\varepsilon_0$  is the permittivity of vacuum. The optical AM contains spin and orbital AM densities that are related to the circular polarization and the spatial distribution of the optical beam, respectively. In the paraxial approximation, experimental linked and knotted coherent waves are measured to be linearly polarized beams that can be expressed as  $\vec{E} = \hat{x} \Psi$ , where the unit vector  $\hat{x}$  is right on the  $c$ -axis of the gain medium. As a consequence, the z-component of the orbital AM density for a linearly polarized light beam is given by

$$\ell_z = \frac{\varepsilon_0}{2\omega} \text{Im} \left[ \Psi^* \left( x \frac{\partial}{\partial y} - y \frac{\partial}{\partial x} \right) \Psi \right], \quad (5.2.4)$$


where  $\omega$  is the angular frequency and  $\text{Im}$  denotes the imaginary part of the expression.

Figure 5.2.8 depicts the numerical results for the orbital AM densities obtained with Eq. (5.2.4) and the parameters of  $(m_o, n_o) = (110, 110)$ ,  $(p, q) = (2, 2)$ ,  $P/Q = 1/4$ , and  $M = 13$  corresponding to experimental wave patterns shown in Figs. 5.2.2 (a). The regions of maximum AM density can be clearly divided into four parts that exhibit to rotate with propagation. Furthermore, it is worth noting that some regions of the AM density have the opposite sign to the average AM of the whole beam, even though their overall contribution is extremely smaller than the global value. Unlike the LG modes that are the orbital AM eigenmodes [24-25], the orbital AM densities of linked and knotted coherent waves are not precisely matching to the local energy densities. Recently, Zambrini and Barnett [37] have numerically shown the possibility to engineer independently the local densities of optical AM

and energy. Nevertheless, in the present experiment the regions of maximum AM density almost coincide with the regions with maximum energy density.

Efficiently generating the average AM is of practical significance for numerous applications. Hence, it is essentially meaningful to consider the average AM per photon in linked and knotted coherent waves. Although the transverse patterns of the present coherent waves depend on the propagation distance from the laser cavity, the average AMs are constant at different longitudinal planes. With the quantum operator, the z-component of the orbital AM for a normalized linearly polarized light beam  $\Psi$  can be expressed as  $L_z = \langle \Psi | \hat{L}_z | \Psi \rangle$ ,

where  $\hat{L}_z = -i\hbar [x(\partial/\partial y) - y(\partial/\partial x)]$ . With the orthogonal properties of the eigenfunctions of the 2D quantum harmonic oscillator, we can verify that  $L_z = \langle \psi_{m_o, n_o}^{p, q} | \hat{L}_z | \psi_{m_o, n_o}^{p, q} \rangle = 0$ , i.e. the  $L_z$  values of the 3D coherent waves  $\psi_{m_o, n_o}^{p, q}$  are zero.

Although the average angular momentums of the single 3D coherent waves are zero, linked and knotted waves arising from the superposition of two degenerate 3D coherent states can possess very large  $L_z$  values. In order to derive the  $L_z$  value for experimental linked and knotted waves, we first use the annihilation and creation operators to show the result:

$$\left\langle \Phi_{m_o, n_o}^{HG} + e^{-i\varphi} \Phi_{m_o+1, n_o-1}^{HG} \middle| \hat{L}_z \middle| \Phi_{m_o, n_o}^{HG} + e^{-i\varphi} \Phi_{m_o+1, n_o-1}^{HG} \right\rangle = 2\hbar\sqrt{m_o+1}\sqrt{n_o} \sin \varphi. \quad (5.2.5)$$

With Eq. (5.2.5) and after some algebra, the  $L_z$  values for the wave functions in Eq. (5.2.3) can be derived to be

$$\left\langle \Psi_{m_o, n_o}^{p, q} \middle| \hat{L}_z \middle| \Psi_{m_o, n_o}^{p, q} \right\rangle = \left( \frac{\hbar}{M+1} \right) \sqrt{\left( \sum_{k=0}^M m_o + pk + 1 \right) \cdot \left( \sum_{k=0}^M n_o + qk \right)} \sin \varphi. \quad (5.2.6)$$

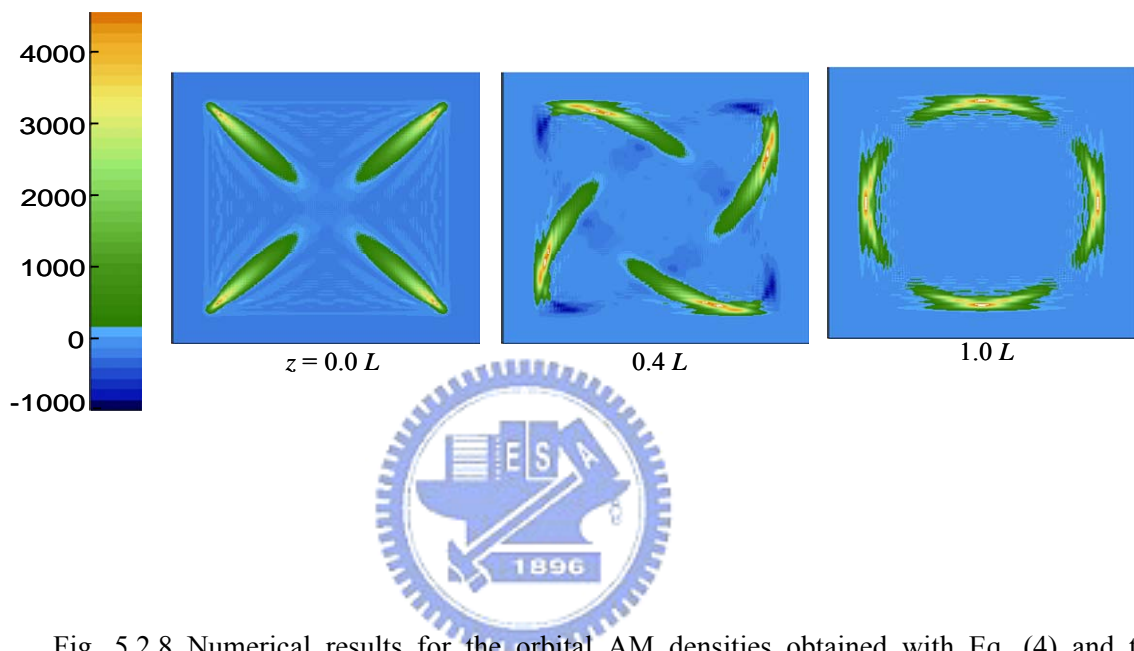


Fig. 5.2.8 Numerical results for the orbital AM densities obtained with Eq. (4) and the parameters of  $(m_o, n_o) = (110, 110)$ ,  $(p, q) = (2, 2)$ ,  $P/Q = 1/4$ , and  $M = 13$  corresponding to experimental wave patterns shown in Fig. 5.2.2(a)

Since the indices  $m_o$  and  $n_o$  are generally much greater than the absolute numbers of  $pM$  and  $qM$ , the  $L_z$  values in Eq. (5.2.6) can be approximately to  $\hbar\sqrt{m_o n_o} \sin\varphi$ . The factor  $\sqrt{m_o n_o}$  indicates the geometric mean of the transverse orders and is nearly proportional to the Fresnel number  $Fr$  of the laser cavity. The Fresnel number  $Fr$  in the present microchip laser can be in the range of 10-1000. As analyzed above, linked and knotted coherent waves have been confirmed to correspond to the relative phase of  $\varphi = \pm\pi/2$ . Therefore, the average AM per photon can be approximated as  $Fr \cdot \hbar$  and their values in the present experiment can be estimated to be greater than  $1000\hbar$ . To be brief, experimental linked and knotted coherent waves are the most efficient states in producing huge orbital AM in the set of the superposition states  $\Psi_{m_o, n_o}^{p, q}(x, y, z; \varphi)$  of Eq. (5.2.3).

### 5.2.3 Summary



In summary, we have successfully used the representation of the 3D coherent states to deduce the analytical wave functions for experimental linked and knotted lasing modes which can be straightforwardly generated in large-Fresnel-number microchip lasers with longitudinal-transverse coupling. The analytical expression enables us to explore the orbital AM densities. Moreover, we also manifest that experimental linked and knotted coherent waves have the largest AMs per photon in the set of the superposition states and the maximum value is as large as  $1000\hbar$ . Since links and knots are widely encountered in many branches of science [38-41], the present findings certainly provide some insights into various classical and quantum waves in the mesoscopic regime.

## REFERENCES

- [1] A. Ya. Bekshaev, and M. S. Soskin, Opt. Commun. **271**, 332 (2007).
- [2] L. Allen, M. W. Beijersbergen, R. J. C. Spreeuw, and J. P. Woerdman, Phys. Rev. A **45**, 8185 (1992).
- [3] A. T. O'Neil, I. MacVicar, L. Allen, and M. J. Padgett, Phys. Rev. Lett. **88**, 053601 (2002).
- [4] K. Staliūnas, G. Šlekys, and C. O. Weiss, Phys. Rev. Lett. **79**, 2658 (1997).
- [5] F. T. Arecchi, G. Giacomelli, P. L. Ramazza, and S. Residori, Phys. Rev. Lett. **67**, 3749 (1991).
- [6] A.M. Zhabotinsky. Dokl. Akad. Nauk, SSSR, **157**, 392 (1964).
- [7] M. Howard and A. D. Rutenberg, Phys. Rev. Lett. **90**, 128102 (2003).
- [8] S. Rüdiger, D. G. Míguez, A. P. Muñozuri, F. Sagués, and J. Casademunt, Phys. Rev. Lett. **90**, 128301 (2003).
- [9] L. Yang and I. R. Epstein, Phys. Rev. Lett. **90**, 178303 (2003).
- [10] V. K. Vanag and I. R. Epstein, Phys. Rev. E **67**, 066219 (2003).
- [11] S. Wasserman, J. Dungan, and N. Cozzarelli, Science **229**, 171 (1985).
- [12] E. Ercolini, F. Valle, J. Adamcik, G. Witz, R. Metzler, P. De Los Rios, J. Roca, and G. Dietler, Phys. Rev. Lett. **98**, 058102 (2007).
- [13] M. Brambilla, F. Battipede, L. A. Lugiato, V. Penna, F. Prati, C. Tamm, and C. O. Weiss, Phys. Rev. A **43**, 5090 (1991).
- [14] D. Dangoisse, D. Hennequin, C. Lepers, E. Louvergneaux, and P. Glorieux, Phys. Rev. A **46**, 5955 (1992).
- [15] E. Cabrera, O. G. Calderón, S. Melle, and J. M. Guerra, Phys. Rev. A **73**, 053820 (2006).
- [16] T. H. Lu, Y. F. Chen, and K. F. Huang, Phys. Rev. E **75**, 026614 (2007).
- [17] J. F. Nye and M. V. Berry, Proc. R. Soc. A **336**, 165-90 (1974).
- [18] M. S. Soskin, V. N. Gorshkov, M. V. Vasnetsov, J. T. Malos, and N. R. Heckenberg, Phys.

Rev. A **56**, 4064 (1997).

- [19] A. N. Alexeyev, T.A. Fadeyeva, A.V. Volyar, and M. S. Soskin, *Semicond. Phys. Quantum Electron. Optoelectron.* **1**, 82 (1998).
- [20] M. V. Berry, M. R. Dennis and M. S. Soskin, *J. Opt. A: Pure Appl. Opt.* **6**, S155 (2004).
- [21] R. A. Beth, *Phys. Rev.* **50**, 115 (1936).
- [22] R. Zambrini and S. M. Barnett, *Phys. Rev. Lett.* **96**, 113901 (2006).
- [23] A. Ya. Bershaev and M .S. Soskin, *Opt. Commun.* **271**, 332 (2007).
- [24] L. Allen, M. W. Beijersbergen, R. J. C. Spreeuw, and J. P. Woerdman, *Phys. Rev. A* **45**, 8185 (1992).
- [25] A. T. O'Neil, I. MacVicar, L. Allen, and M. J. Padgett, *Phys. Rev. Lett.* **88**, 053601 (2002).
- [26] P. Galajda and P. Ormosa, *Appl. Phys. Lett.* **78**, 249 (2001).
- [27] N. B. Simpson, K. Dholokia, L. Allen and M. J. Padgett, *Opt. Lett.* **22**, 52 (1997).
- [28] J. E. Curtis and D. G. Grier, *Phys. Rev. Lett.* **90**, 133901 (2003).
- [29] M. E. J. Friese, J. Enger, H. Rubinsztein-Dunlop, and N. R. Heckenberg, *Phys. Rev. A* **54**, 1593 (1996).
- [30] Y. F. Chen, T. H. Lu, K. W. Su, and K. F. Huang, *Phys. Rev. Lett.* **96**, 213902 (2006).
- [31] Y. F. Chen and Y. P. Lan, *Phys. Rev. A* **66**, 053812 (2002).
- [32] Y. F. Chen, C. H. Jiang, Y. P. Lan, and K. F. Huang, *Phys. Rev. A* **69**, 053807 (2004).
- [33] Y. F. Chen and K. F. Huang, *J. Phys. A* **36**, 7751 (2003).
- [34] A. J. Makowski, *J. Phys. A* **38**, 2299 (2005).
- [35] Y. F. Chen, T. H. Lu, K. W. Su, and K. F. Huang, *Phys. Rev. E* **72**, 056210 (2005).
- [36] K. J. Górska, A. J. Makowski, and S. T. Dembiński, *J. Phys. A* **39**, 13285 (2006).
- [37] R. Zambrini and S. M. Barnett, *Opt. Express* **15**, 15214 (2007).
- [38] J Leach, M R Dennis, J Courtial and M J Padgett, *New Journal of Phys.* **7**, 55 (2005).
- [39] A. T. Winfree, *Physica D* **84**, 126 (1995).

- [40] A. Malevanets and R. Kapral, Phys. Rev. Lett. **77**, 767 (1996).
- [41] P. Y. Lai, Y. J. Sheng, and H. K. Tsao, Sumners, Phys. Rev. Lett. **87**, 175503 (2001).



# Chapter 6

## Summary and Future Work

The various interesting patterns have been realized by use of the precise microchip laser cavity. With the transversely isotropic gain medium, the various polarization-resolved patterns can be generated and the GCSs theoretically reconstructed the experimental results. Therefore off-axis pumping scheme leads to the high-order three-dimensional coherent states which are localized on the three-dimensional Lissajous parametric surfaces. Furthermore superposition of three-dimensional coherent states results in the three-dimensional interference patterns which spatially localized on the Lissajous parametric surface. Importantly, the 3D coherent optical waves are demonstrated to carry large angular momentum. In chapter 4 the most complicated pattern is investigated in detail with the interesting and important polarization singularities, *V* points, *C* lines, and *L* surfaces. The polarization singularities can be revealed with the theoretical results perfectly.

However the various plentiful patterns have been showed and analyzed in the contents, the main target of our research will focus on the improvement of the Fresnel number in the laser cavity to study the super-high order coherent waves. We can demonstrate the eigenfunction of the laser cavity with the quantum mechanics and show the classical-like periodic orbits corresponding to classical world. The Fresnel number of the patterns which we had studied is about 20 to 1000. If we can enlarge the gain medium and the off-axis pumping radius, the Fresnel number can be increased substantially. The situation we can expect is that the patterns will be more colorful and complex than the patterns with small Fresnel number. Until now, the mathematical software is restricted to some limit of calculation results. It will be difficult to reconstruct the super-high order coherent waves. Therefore we will focus on the

classical theoretical analysis to help to study the formation of the various patterns. With the research of the formation of patterns the connection between microscopic and macroscopic can be explored deeply. The world of the physics is so wonderful, and then we should challenge ourselves to reach the limit what we can to see the beautiful of the physical world.



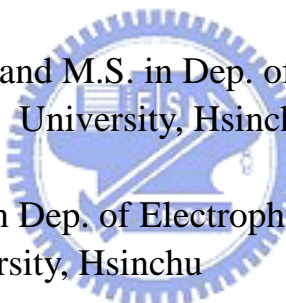
# Curriculum Vitae

## Personal Data

|  |                        |
|--|------------------------|
| Name: Ting-Hua Lu  | Birthday: Aug. 18,1982 |
| Nationality: Taiwan (R.O.C.)   | Birthplace: Kaohsiung  |
| Telephone (M): 886-928-205053  | Sex: Female            |
| E-mail: <a href="mailto:epspotlight@hotmail.com">epspotlight@hotmail.com</a> |                        |

## Education

|             |   |
|-------------|---|
| 2004 ~ 2008 | Ph.D. and M.S. in Dep. of Electrophysics, National Chiao Tung University, Hsinchu |
| 2000 ~ 2004 | B.E. in Dep. of Electrophysics, National Chiao Tung University, Hsinchu           |
| 1997 ~ 2000 | National FengHsin Senior High School, Kaohsiung                                   |



## Work Experience

|             |   |
|-------------|---|
| 2004 ~ 2008 | T.A. of Exercising of Physics and Quantum Mechanics |
|-------------|---|

## Speciality

Laser physics and Quantum physics

# Publication List

## (A) Journal papers:

1. T. H. Lu, Y. F. Chen, and K. F. Huang, “Spatial morphology of macroscopic superposition of three-dimensional coherent laser waves in degenerate cavities“, Phys. Rev. A 77, 013828 (2008)
2. T. H. Lu, Y. F. Chen, and K. F. Huang, “Generalized hyperboloid structures of polarization singularities in Laguerre-Gaussian vector fields“, Phys. Rev. A 76, 063809 (2007)
3. C. C. Chen, K. W. Su, T. H. Lu, C. C. Liu, Y. F. Chen, and K. F. Huang, “Generation of two-dimensional chaotic vector fields from a surface-emitting semiconductor laser: Analysis of vector singularities”, Phys. Rev. E 76, 026219 (2007)
4. C. C. Chen, C. C. Liu, K. W. Su, T. H. Lu, Y. F. Chen, and K. F. Huang, “Statistical properties of experimental coherent waves in microcavity lasers: Analogous study of quantum billiard wave functions”, Phys. Rev. E 75, 046202 (2007)
5. T. H. Lu, Y. F. Chen, and K. F. Huang, ”Generation of polarization-entangled optical coherent waves and manifestation of vector singularity patterns”, Phys. Rev. E 75, 026614 (2007)
6. Y. F. Chen, T. H. Lu, and K. F. Huang, “Hyperboloid structures formed by polarization singularities in coherent vector fields with longitudinal-transverse coupling”, Phys. Rev. Lett. 97, 233903 (2006)
7. C. C. Liu, T. H. Lu, Y. F. Chen, and K. F. Huang, “Wave functions with localizations on classical periodic orbits in weakly perturbed quantum billiards”, Phys. Rev. E 74, 046214 (2006)
8. Y. F. Chen, T. H. Lu, K. W. Su, and K. F. Huang, “Devil’s staircase in three-dimensional coherent waves localized on Lissajous parametric surfaces”, Phys. Rev. Lett. 96, 213902 (2006)
9. Y. F. Chen, K. W. Su, T. H. Lu, and K. F. Huang, “Manifestation of weak localization and long-range correlation in disordered wave functions from conical second harmonic generation”, Phys. Rev. Lett. 96, 033905 (2006)
10. Y. F. Chen, T. H. Lu, and K. F. Huang, “Observation of spatially coherent polarization

vector fields and visualization of vector singularities”, Phys. Rev. Lett. 96, 033901 (2006)

11. Y. F. Chen, T. H. Lu, K. W. Su, and K. F. Huang, “Quantum signatures of nonlinear resonances in mesoscopic system: efficient extension of localized wave function”, Phys. Rev. E 72, 056210 (2005)

## (B) Conference:

1. T. H. Lu, C. C. Chen, Y. F. Chen, and K. F. Huang, “Generalized hyperboloid structures of polarization singularities in coherent vector fields with longitudinal-transverse coupling”, Annual Meeting of the Physical Society of the Republic of China, paper PE-71 (2008) (壁報論文獎優選)
2. T. H. Lu, C. C. Chen, Y. F. Chen, and K. F. Huang, “Generation of polarization-entangled optical vector fields and visualization of vector singularity patterns”, Annual Meeting of the Physical Society of the Republic of China, paper cE-03 (2008)

